Evaluation of the enhanced thermal fluid conductivity for gas flow through structured packed pebble beds

T.L. Kgame

Dissertation submitted in partial fulfilment of the requirements for the degree of Magister in Mechanical Engineering at the North-West University – ***Potchefstroom Campus***.

Study Leader: Prof. P.G. Rousseau

Potchefstroom

2010

ACKNOWLEDGEMENTS

I would like to first thank God, in the name of Jesus Christ, our Lord, for helping me to complete my studies.

I would like to express my gratitude to Professor Rousseau for his guidance through this study. His incredible mentorship had enhanced my engineering skills and grown me to be a better academic researcher.

Special thanks to the M-Tech Industrial for letting me use the HPTU experimental data and the opportunity to be a test engineer of the plant.

I would like to thank my parents for giving me the opportunity to study; I was able to battle out all the challenges through their support.

This work is dedicated to my family Monica, Atlegang and Itumeleng.

2 Timothy 3:14 ***But you remain in the things which you have learned and have been assured of, knowing from whom you have learned them.***

ABSTRACT

The High Pressure Test Unit (HPTU) forms part of the Pebble Bed Modular Reactor (PBMR) Heat Transfer Test Facility (HTTF). One of the test sections that forms part of the HPTU is the Braiding Effect Test Section (BETS). This test section allows for the evaluation of the so-called 'braiding effect' that occurs in fluid flow through a packed pebble bed. The braiding effect implies an apparent enhancement of the fluid thermal conductivity due to turbulent mixing that occurs as the flow criss-crosses between the pebbles. The level of enhancement of the fluid thermal conductivity is evaluated from the thermal dispersion effect. The so-called thermal dispersion quantity K_r is equivalent to an effective Peclet number Pe_{eff} based on the inverse of the effective thermal conductivity k_{eff}.

This thesis describes the experiments carried out on three different BETS test sections with pseudo-homogeneous porosities of 0.36, 0.39 and 0.45, respectively. It also provides the values derived for the enhanced fluid thermal conductivity for the range of Reynolds numbers between 1,000 and 40,000.

The study includes the following:

- Compilation of a literature study and theoretical background.
- An uncertainty analysis to estimate the impact of instrument uncertainties on the accuracy of the empirical data.
- The use of a Computational Fluid Dynamics (CFD) model to simulate the heat transfer through the BETS packed pebble bed.
- Application of the CFD model combined with a numerical search technique to extract the effective fluid thermal conductivity values from the measured results.
- The assessment of the results of the experiments by comparing it with the results of other investigations found in the open literature.

The primary outputs of the study are the effective fluid thermal conductivity values derived from the measured data on the HPTU plant.

The primary variables that were measured are the temperatures at radial positions at different axial depths inside the bed and the total mass flow rate through the test section.

The maximum and minimum standard uncertainties for the measured data are 10.80% and 0.06% respectively.

The overall effective thermal conductivities that were calculated at the minimum and maximum Reynolds numbers were in the order of 1.166 W/mK and 38.015 W/mK respectively. A sensitivity study was conducted on the experimental data and the CFD data. A maximum uncertainty of 5.92 % was found in the calculated effective thermal conductivities.

The results show that relatively high values of thermal dispersion quantities or effective Peclet numbers are obtained for the pseudo-homogeneous packed beds when compared to randomly packed beds. Therefore, the effective thermal conductivity is low and it can be concluded that the radial mixing in the structured packing is low relative to the mixing obtained in randomly packed beds.

Key words: effective thermal conductivity, thermal dispersion quantity, Peclet number, turbulent mixing, radial mixing, pseudo-homogeneous packed beds, randomly packed beds

TABLE OF CONTENTS

LIST OF FIGURES

LIST OF TABLES

NOMENCLATURE

Symbols

3D	Three dimensional	[-]
A'	Quantiy used in the calculation for the discharge coefficient C	[-]
A	Area	[m^2]
A_{fs}	Interfacial area between the fluid phase and the solid phase	[m^2]
a	The period of the function in Equation (H.2)	[-]
$b0_0, b0_1, b0_2, b0_3$	3rd order polynomial constants derived from Viscosity and Density REFPROP data at different pressures and temperatures	[-]
$b1_0, b1_1, b1_2, b1_3$	3rd order polynomial constants derived from Viscosity and Density REFPROP data at different pressures and temperatures	[-]
$b2_0, b2_1, b2_2, b2_3$	3rd order polynomial constants derived from Viscosity and Density REFPROP data at different pressures and temperatures	[-]
$b3_0, b3_1, b3_2, b3_3$	3rd order polynomial constants derived from Viscosity and Density REFPROP data at different pressures and temperatures	[-]
b	The amplitude of the function in Equation (H.2)	[-]
b	Vector function for the temperature gradient transformation between phased-averaged and averaged temperature in Equation (2.15)	[m]
Bi	Biot number	[-]
C	Discharge coefficient	[-]
c	The temperature zero point of the curve function in Equation (H.2)	[-]
c_1	The intercept value of the previous calibration (before the test)	[-]
c_2	The intercept value of the current calibration (after the test)	[-]
c_p	Heat capacity for constatnt pressure	[kJ/kgK]
c_v	Heat capacity for constatnt volume	[kJ/kgK]
D	Diameter	[m]
d	The bed radius zero point of the curve function in Equation (H.2)	[-]

D1	Axial length of the test section	[m]
D2	Width length of the test section	[m]
D3	Height length of the test section	[m]
$D1_{top}$	Depicts vertical position for top layer thermocouples	[m]
$D1_{bottom}$	Depicts vertical position for the bottom layer thermocouples	[m]
d_1	The width of the two plates placed perpendicular on the back plate	[m]
$D3'$	The full length of the back plate	[m]
$D_{\text{outer braiding}}$	Braiding (hot gas) pipe outer diameter	[m]
d_{or}	Orifice diameter	[m]
D_p	Particle diameter	[m]
$\mathbf{D_e}$	Total effective thermal diffusivity tensor	[m^2/s]
$D_{e,z}$	Approximation of $\mathbf{D_e}$ in the longitudinal direction	[m^2/s]
$D_{e,r}$	Approximation of $\mathbf{D_e}$ in the transverse or radial () direction	[m^2/s]
$\mathbf{D^d}$	Dispersion tensor in Equation (2.15)	[m^2/s]
E_{rel}	Relative error solution associated with the grid indendence solution of the CFD grid	[-]
$E(k)$	Calculated error E as the function of the guessed thermal conducticitity k in Eqaution (J.1)	[-]
$F(k)$	Derivative function of $E(k)$ in Equation (J.2)	[-]
$E^{++} = F(k^{++})$	Error calculated at the guessed over-perturbed k^{++}	[-]
$E^{--} = F(k^{--})$	Error calculated at the guessed under-perturbed k^{--}	[-]
$error_{EXPERIMENTAL\,FIT}$	minimized errors calculated in Equation (H.4)	[-]
f_i and f_{i+1}	Solutions on two successively refined meshes for Equation (K.1) $(i-th\ and\ (i+1)-th\ meshes)$	[-]
G	- Gas mass flux	[kg/m^2.s]
g	Gravity constant	[m/s^2]
h	Height	[m]
$h = c_p T$	Thermal enthalpy in Equation (6.1)	[J/kg]

h_0	Total enthalpy	[J/kg]
$\mathbf{I}$	Unit tensor in Equation (2.15)	[-]
j	The number of spacers for Equation (4.14) calculation	[-]
k	Thermal conductivity	[W/m·K]
k_{beff}^{o}	Pebble bed effective thermal conductivity with motionless fluid (molecular conduction) in Equatio (2.7)	[W/m K]
k^{d}	Associated with the effective thermal diffusivity in Equation (2.16) and Equation (2.17)	[m^2/s]
k_1	First guessed thermal conductivity in Equation (J.2)	[W/mK]
Δk	The amount by which k_1 is decreased or increased in Equation (J.2)	[W/mK]
$\delta k = \alpha \cdot k$	Intervals used to perturb the guessed k	[W/mK]
$k^{new} = k + \Delta k$	The new value of k	[W/mK]
k^{--}	Under-perturbed value of the guessed k for full interval δk	[W/mK]
k^{-}	Under-perturbed value of the guessed k for the half interval $\frac{1}{2}\delta k$	[W/mK]
k^{++}	Over-perturbed value of the guessed k for full interval δk	[W/mK]
k^{+}	Over-perturbed value of the guessed k for the half interval $\frac{1}{2}\delta k$	[W/mK]
k_o	The pebble bed static gas effective thermal conductivity	[W/m·K]
$k_{coverage\ factor}$	Accounts for the coverage factor in the uncertainty calculation	[-]
K	Dispersion quantity	[-]
$K_{1,h}$	Slope parameter in Equation (2.12)	[-]
$K_{2,h}$	Damping parameter in Equation (2.12)	[-]
$\mathbf{L}_{\mathbf{t}}^{*}$	Tortuosity tensor in Equation (2.15)	[-]
$L_{t,z}^{*}$	Longitudinal approximation of the tortuosity tensor $\mathbf{L}_{\mathbf{t}}^{*}$	[-]
$L_{t,r}^{*}$	Transverse or radial approximation of the tortuosity tensor $\mathbf{L}_{\mathbf{t}}^{*}$	[-]
$\dot{m}$	Mass flow rate	[kg/s]
m_1	The gradient value of the previous calibration (before the test)	[-]

m_2	The gradient value of the current calibration (after the test)	[-]
n	The number of spheres in a string for Equation (4.14) calculation	[-]
n	Unit normal vector directed from the fluid phase into the solid phase	[-]
n_h	Curvature parameter for Equation (2.12)	[-]
n_p	The number of spheres inside the packed bed	[-]
N_{CV}	number of control volumes discretisized in a radial direction of the flow field in the CFD grid	[-]
N_{Pe_m}	Refers to the modified Peclet number, Pe_m	[-]
p_1	Static pressure (measured upstream to the orifice plate)	[Pa]
p_2	Static pressure (measured downstream to the orifice plate)	[Pa]
p	Pressure	[Pa]
$\overline{p}$	Average pressure	[Pa]
Pe	Péclet number	[-]
$\left(Perc\,Diff_{BedTransverse}\right)_{RadialLine1}$	percentage difference in temperature at a particular bed tranverse position $BedTransverse$ at the Radial line 1 $\left(RadialLine1\right)$ in Figure G-8 and Table G-3 between averaged temperature of for all five Radial lines	[%]
Pr	Prandtl number	[-]
q	Heat transfer	[J/kg]
R	Radius	[m]
R^2	A value from Equation (H.5) to evaluated polynomial fit	[%]
r	Radial coordinate	[m]
r^p	Ratio of with which successive meshes is refined at the $p-th$ order	[-]
Re	Reynolds number	[-]
Re_D	Reynolds number for the the pipe	[m]
s	The length of the spacers for Equation (4.14) calculation	[-]
s_h	Energy source term	[J/kg]
SSE	Quantity associated with the calculation of R^2 and number of fitted points N	[-]

SST	Quantity associated with the calculation of R^2 and number of fitted points N	[-]
t	Time	[s]
T	Temperature	[K]
$\overline{T}$	Average temperature	[K]
$\left(T_{BedTransverse}\right)_{RadialLine1}$	The temperature calculated at a particular bed tranverse position $BedTransverse$ on the Radial line 1 $\left(RadialLine1\right)$ in Figure G-8 and Table G-3	[K]
$\left(\overline{T}_{BedTransverse}\right)_{RadialLine1...5}$	the average temperature calculated at a particular bed tranverse position $BedTransverse$ over all five Radial lines $\left(RadialLine1...5\right)$	[K]
u	Interstertial velocity	[m/s]
$\mathbf{u}'$	Vectorial spatial deviation component of the fluid velocity	[m/s]
u_o	Superficial velocity	[m/s]
u_r, u_z	Directional components of the fluid velocity in the radial and axial coordinate directions respectively	[m/s]
$u(\ )$	Uncertainty quantity	[-]
V	Velocity	[m/s]
w_ϕ	the final uncertainty in the calculated variable ϕ	[-]
x	Transverse coordinate	[m]
x_j, x_i	Cartesian coordinates with $i, j = 1,2,3$ as defined in Equation (6.1)	[m]
$x_1, x_2, \ldots, x_n$	Indicates measured independent variables associated with measured variable ϕ	[-]
y	Vertical coordinate	[m]
z	Axial coordinate	[m]

Greek symbols

α	used in $\delta k = \alpha \cdot k$ to perturb the guessed k	[-]
α_f	Fluid thermal diffusivity in Equation (2.15)	[m^2/s]

β	Diameter ratio = d_{or}/D_{OrPipe}	[-]
ε	Porosity in Equation (2.1)	[-]
ε	Expansion coefficient in Equation (4.29)	[-]
$\bar{\varepsilon}$	Average porosity of the packed bed	[-]
κ	Isentropic expansion ratio	[-]
μ	Viscosity	[kg/s·m]
ρ	Density	[kg/m^3]
τ_{ij}	Strain tensor in Equation (6.1)	[Pa]
ϕ	Measured variable	
$\bar{\phi}$	Average value of the measured or calculated variable	

$\alpha\beta$ Represent the function of the fluid flow rate and the geometric properties of a packed bed system in Equation (2.9) [-]

ϕ_f The results for a measured variable ϕ that are calculated as a function of the independent variables $x_1, x_2, \ldots, x_n$ in Equation (4.5).

Subscripts

1b,2b,...,Nb	Indicates series of braiding temperature values measured for N points or effective thermal conductivities due to a temperament in the braiding profile
[1],[2],[3],[4]	Measured or calculated values at experimental tests: Test Run 1, Test Run 2, Test Run 3 and Test Run 4 respectively
200 and 201	Measurement done using instrument number 200 and 201 respectively
[-]	Non-dimensional
BedTransverse	Associated with bed tansverse position at the particular radial line in Figure G-8 and Table G-3
beff	Bed effective property
BED TRANSVERSE POSITION	Associated with the bed transverse position
BETS036	Attributed to the test section BETS036
BETS039	Attributed to the test section BETS039

BETS045	Attributed to the test section BETS045
BotLayer	Associated with the bottom layer of measurements
bottom	The Bottom row of the thermocouples
braiding	The braiding (hot gas) pipe property
braiding gas	The braiding gas
braiding profile	The braiding profile
braiding profile$_N$	The normalized braiding profile
Cold gas	Cold gas
cold gas in	Measurement done for the inlet cold gas
EXPERIMENTAL	Values extracted from the experimental data
EXPERIMENTAL FIT	Asociaated with the fitted experimental data
CFD	Values calculated from the CFD program simulations
CFD temperature profile	Contributed due to the CFD temperature profile
Drift	Drift
Experimental temperature profile	Contributed due to the Experimental temperature profile
eff	Effective
eax	Effective axial
er	Effective radial
f	Fluid
feff	Fluid effective property
Final	Final value
g	Gas
Hot gas	Hot gas
Hot gas in	Measurement done for the inlet hot gas
i	Indicates number of the grid (mesh) points tested in sequence
Instr	Instrument
lm	Lateral mixing
m	Modified
max	Maximum
min	Minimum

Or	Orifice
OrPipe	Orifice pipe
p	Particle
pfc	Pebble surface to fluid convection
POLINOMIAL FIT	Polynomial fit
r	Radial direction
$(RadialLine1...5)$	Associated with the Radial line 1 to Radial line 5 in in Figure G-8 and Table G-3
$-r_{BED\,TRANSVERSE\,POSITION}$	Associated with the left-hand side of the bed vertical line when viewed from the top
$+r_{BED\,TRANSVERSE\,POSITION}$	Associated with the right-hand side of the bed vertical line when viewed from the top
radiation	Radiation
s	Solid
stat	Statistical variance
$symm$	Associated with symmetrical value for the bottom or top layer of measurement
$symm1, symm2, ..., symmN$	Associated with symmetry values calculated respectively at fitted points $1, 2, ..., N$
test section	Test section
test section in	Test section inlet
t	Packed bed
turbulent mixing	Turbulent mixing
TopLayer	Associated with the top layer of measurements
total gas	Total gas
total gas in	Total gas in
z	Axial direction

ACRONOMYNS

BETS	Braiding Effect Test Section
BETS036	Braiding Effect Test Section with homogeneous porosity of *0.36*
BETS039	Braiding Effect Test Section with homogeneous porosity of *0.39*
BETS045	Braiding Effect Test Section with homogeneous porosity of *0.45*
CFD	Computational Fluid Dynamics
EES	Engineering Equation Solver
FT	Flow Transmitter
FV	Finite Volume
HPTU	High Pressure Test Unit
HTTF	Heat Transfet Test Facility
HX	Heat Exchanger
PBMR	Pebble Bed Modular Reactor
P&ID	Process and Instrumentation Diagram
PDT	Pressure Differential Transmitter
PT	Pressure Transmitter
SANAS	South African National Accreditation System
TT	Temperature Transmitter

1. INTRODUCTION

1.1. Background

The study of heat transfer parameters in packed pebble beds plays an important role in the design and performance evaluation. Investigations have been done using different experimental and modelling procedures to validate or deduce various heat transfer correlations for packed beds. These correlations, which can be either attributed to the fluid flow phenomena or to the heat transfer phenomena inside the bed, typically involve the following:

- The maximum and minimum operating conditions inside the bed (temperature, pressure and flow rate).
- The state mode for both the flowing fluid and the packed particles (gaseous phase, liquid phase and solid phase).
- The heat transfer mechanisms inside the bed (conduction, convection and radiation).
- The type of fluid and the packed particle material.
- The geometric forms of the bed and the packed particles.

However, these correlations may be modelled theoretically, whereby the conservation equations (mass, energy and momentum equations) are either based on:

- Either the fluid flow properties or the packed particle properties (pseudo-homogeneous models (De Wasch and Froment ,1972), or
- Both the fluid flow and the packed particles properties (pseudo-heterogeneous models (De Wasch and Froment ,1971, Dixon and Cresswell, 1979).

The use of the energy equation that is based on these models has created many arguments regarding the equivalence of these models for the steady-state conditions and transient state conditions inside the bed (Berninger and Vortmeyer, 1982, Schaefer and Vortmeyer,1982, and Dixon and Cresswell, 1979, 1982 and 1986)).

However, many authors have used the steady-state energy equation for the packed bed to

predict a particular temperature field inside the packed bed (Kunii *et al.,* 1960, Gunn and Khalid, 1975). The pre-calculated temperature field is usually adjusted to the experimental temperature field by characterizing a particular effective heat transfer parameter that is associated with the heat transfer mechanism in the field.

The temperature field is always associated with the particular region inside the bed in which the authors have a specific interest in their investigations. For instance, the following heat transfer parameters are associated with a particular region inside the bed as the fluid flows across the bed:

- *Heat transfer coefficient*

The heat transfer coefficient is associated with the convection heat transfer between the fluid and either the packed particle or the wall of the packed bed enclosure. The temperature field of interest is at the surface of the pebble or at the surface of the wall of the packed bed enclosure, and the intermediate fluid temperature near these surfaces, as seen in the works of Kunii and Suzuki (1967), Gunn and Khalid (1975), and Martin and Nilles (1993).

- *Thermal conductivity*

The effective thermal conductivity is associated with both the radiation and conduction heat transfers, and the fluid flow conductivity inside the bed. Conduction heat transfer occurs between the packed bed wall and the packed particle, and between the packed particle and the other surrounding packed particles. Radiation heat transfer also occurs in the same manner, but between the surfaces of the packed particles and also the packed bed wall. The temperature field of interest for the conduction heat transfer is within the packed particles and the packed bed wall, whereas for the radiation heat transfer, the latter is at the material surfaces of the packed particles and the packed bed wall. However, the radiation heat transfer depends on the properties of a surface as discussed in Van Antwerpen and Greyvenstein (2006).

Thermal conductivity is also associated with the dispersion heat transfer that occurs due to the lateral or turbulent mixing as the fluid criss-crosses between the packed particles as noted in Van Antwerpen and Greyvenstein (2006). The temperature field is in the

working fluid or in the packed particle as seen in the initial deduction of Kunii and Yagi (1957) (it is also continued in Endo *et al.*, 1964). The combined effect of the three thermal conductivities associated with each of the three heat transfer phenomena is known as the packed bed effective thermal conductivity. The heat transfer phenomena are illustrated in Figure 1-1.

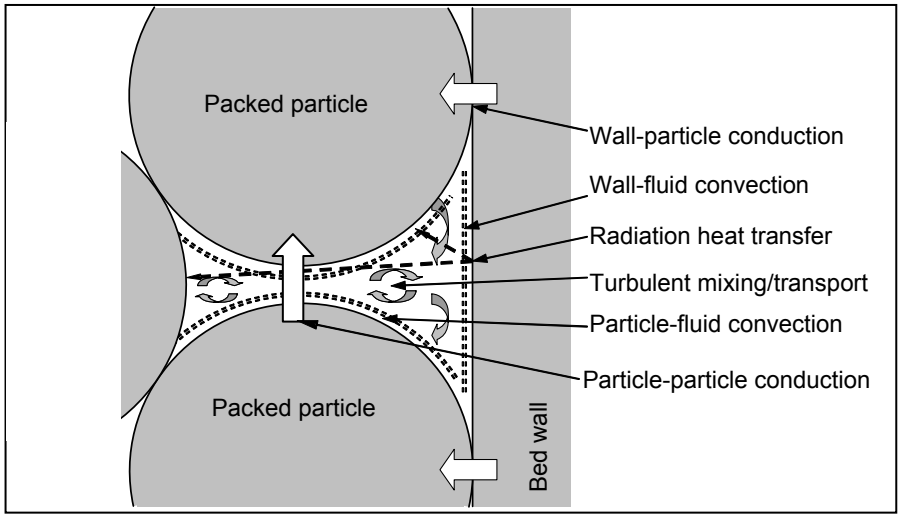

Figure 1-1: The summary of heat transfer phenomena in the packed bed.

1.2. Purpose of this study

The packed bed effective thermal conductivity is usually determined experimentally by forcing steady flow of a fluid through a cylindrical packed bed, heated or cooled circumferentially (Wakao and Yagi, 1959, Kunii *et al.*, 1960, Endo *et al.*, 1964, De Wasch and Froment, 1972, Gunn and Khalid, 1975), or by heating a fraction of the flow at the centreline of the bed (Bauer, 1977). The data of the axisymmetric two–dimensional temperature field are then compared with the quasi (pseudo)–homogeneous theoretical model which assumes a plug flow. By comparing the temperature profiles of the theoretical model with that of experimental data, the effective transverse thermal conductivity can be determined (Finlayson and Li, 1977).

This thesis presents the so-called steady-state separate effects tests done to determine the enhanced fluid thermal conductivity due to turbulent mixing in a structured packed pebble bed. This enhanced fluid thermal conductivity is coined as the ‘braiding effect’. The study will also present and discuss the derivation of the enhanced thermal

conductivities via the numerical analysis to correlate the braiding effect. The braiding effect is understood from the previous studies as the thermal dispersion (Krischke *et al.,* 2000, Nasr, *et al.*, 1994, Kuo and Tien, 1988, and Cheng and Vortmeyer, 1988).

In the thermal-fluid simulation models of the Pebble Bed Modular Reactor (PBMR) core, a diffusive model is assumed for thermal dispersion. In the bulk flow inside the packed bed, a more accurate calculation for thermal dispersion is by taking its effect perpendicular to the flow direction as noted in Van Antwerpen (2007).

However, it should be noted that dispersion in terms of the mass distribution is determined from the fluid concentration levels, i.e. by keeping track of the location of chemical species inside a packed bed in a great detail. Therefore, dispersion in terms of the mass distribution is called mass dispersion. The current study evaluates dispersion in terms of the temperature distribution associated the conductive heat transfer, i.e. by keeping track of the temperature field inside the packed bed. By Fourier's law, the conductive heat transfer is proportional to the thermal conductivity; therefore by keeping track of the temperature field inside the packed bed, the effective thermal conductivity inside the packed bed has to be monitored. Therefore dispersion in terms of the temperature distribution is called thermal dispersion.

It is noted in Kaviany (1991) that generally the dispersion effect has an anisotropic behaviour, and this can be confirmed from the works of Gunn and Pryce (1969) where mass dispersion was separately determined from both the radial and axial mixing. Also, the authors were able to determine that dispersion effect is notably influenced by the packing order inside the packed bed. The experimental setup for the current study enables measurement of temperature distribution in a transverse direction (or radial direction in cylindrical bed). The packing order inside the bed is structured packing with rhombohedral arrangement.

1.3. Impact of this study

The objective of this study is to extract effective thermal conductivities from the experiments that were carried out in three Braiding Effect Test Sections (BETS) with respective pseudo-homogeneous porosities of 0.36, 0.39 and 0.45. Hence the bed was structured bed. The thermal effective conductivities serve to correlate thermal dispersion inside the packed bed (the theory is well presented in Chapter 6). The purpose of the thermal dispersion modelling in the PBMR is to increase the accuracy of the temperature field calculation in the fluid side.

Though, it is noted in Kaviany (1991) that the dispersion effect in a packed bed is affected by the packing order, experiments were systematically carried out for three packed beds, with pseudo-homogeneous porosities and the same thermal boundary conditions.

1.4. Outline of the thesis

Chapter 2 presents a literature study regarding the thermal dispersion modelling. It discusses the original deduction and formulation history of the fluid effective thermal conductivity inside the packed bed. It also gives the relationship between the thermal fluid conductivity and thermal dispersion.

Chapter 3 gives a description of the experimental setup.

Chapter 4 gives the uncertainty analysis in the measured and calculated variables from the experimental data.

Experimental results are given in Chapter 5. For each Reynolds number (1000 to 40,000), four experiments were conducted to ensure repeatability in the data. Hence, the given results are the average values over the four experimental test data sets.

Chapter 6 gives the simulation method and the calculated results. The simulated results were done for two coordinate systems i.e., the Cartesian coordinate system (Cartesian

grid) and the cylindrical coordinate system (cylindrical grid). The chapter also gives the uncertainty in the calculated effective thermal fluid conductivity for the maximum and minimum Reynolds number (*Re*). This is done for the BETS039 and BETS045 test sections. This is because the overall maximum and minimum effective thermal conductivities were extracted from the experimental data for these test sections at the maximum and minimum Reynolds number (Table 6-4), summarized as follows:

- *BETS039 at Re=40,000*
- *BETS045 at Re=1000*

The chapter also compares the current work with the previous work that dealt with the dispersion work.

Chapter 7 gives conclusions and recommendations for a further work.

2. LITERATURE STUDY

2.1. Preview

The energy conservation equation for the fluid temperatures within the pebble bed is given by the following heat transport equation (Rousseau (2005)):

$$\begin{aligned}&\frac{\partial}{\partial t}\left(\varepsilon\rho h_0\right)+\frac{1}{r}\frac{\partial}{\partial r}\left(\varepsilon\rho h_0 u_r\right)+\frac{\partial}{\partial z}\left(\varepsilon\rho h_0 u_z\right)=\frac{\partial}{\partial t}\left(\varepsilon p\right)\\&+\frac{1}{r}\frac{\partial}{\partial r}\left(\varepsilon r k_{feff}\frac{\partial T}{\partial r}\right)+\frac{\partial}{\partial z}\left(\varepsilon k_{feff}\frac{\partial T}{\partial z}\right)+\varepsilon\rho\left(g_r u_r+g_z u_z\right)+q_{pfc}\end{aligned} \tag{2.1}$$

With:

ε - Pebble bed porosity.

ρ - Fluid density.

h_0 - Total enthalpy.

r - Radial co-ordinate direction.

z - Axial co-ordinate direction.

u_r, u_z - Directional components of the fluid velocity in the radial and axial coordinate directions respectively.

p - Static pressure in the fluid.

T - Static temperature in the fluid.

k_{feff} - Fluid effective conductivity (including the effects of turbulent mixing).

g_r, g_z - Gravitational acceleration components in the radial and axial coordinate directions respectively.

q_{pfc} - Pebble surface to fluid convection heat transfer.

Equation (2.1) represents the relationship between convective heat transport, i.e. the movement of heat by means of fluid movement and conductive heat transport (Van Antwerpen and Greyvenstein (2006)), where:

$\frac{1}{r}\frac{\partial}{\partial r}\left(\varepsilon\rho h_0 u_r\right)$ and $\frac{\partial}{\partial z}\left(\varepsilon\rho h_0 u_z\right)$ are the convective terms, and

$\frac{1}{r}\frac{\partial}{\partial r}\left(\varepsilon r k_{feff}\frac{\partial T}{\partial r}\right)$ and $\frac{\partial}{\partial z}\left(\varepsilon k_{feff}\frac{\partial T}{\partial z}\right)$ are the diffusive (conductive) terms.

It is noted in Van Antwerpen (2007) that dispersion is a convective heat transfer mechanism that appears as enhanced diffusive heat transfer in all directions. Therefore, the change in the magnitude of fluid thermal conductivity affects the modelling of dispersion (see Equation (2.1)).

The relative significance of convective heat transport versus conductive heat transport is quantified with the Peclet number (*Pe*). The Peclet number is defined in terms of the superficial velocity u_o. However, its calculation may either be based on:

- the pebble bed static gas effective thermal conductivity k_o, or
- the pebble bed solid effective thermal conductivity k_s, or
- the pebble bed radiation effective thermal conductivity k_r, or
- the fluid effective thermal conductivity k_{feff}, or
- the fluid (molecular) thermal conductivity k_g.

The Peclet number based on the fluid (molecular) conductivity k_g is calculated as follows:

$$Pe = \frac{\rho c_p u_o D_p}{k_g} \tag{2.2}$$

With:

$u_o = \varepsilon u$, whereby u is an interstitial gas velocity.

c_p Heat capacity for constatnt pressure

D_p - Pebble diameter.

If we assume that the flow is steady, fully developed in the axial direction, that there is no internal heat generation and that the effects of gravity are negligible, Equation (2.1) will reduce to:

$$\frac{\partial}{\partial z}\left(\varepsilon\rho h_0 u_z\right)=\frac{1}{r}\frac{\partial}{\partial r}\left(\varepsilon r k_{feff}\frac{\partial T}{\partial r}\right)+\frac{\partial}{\partial z}\left(\varepsilon k_{feff}\frac{\partial T}{\partial z}\right) \tag{2.3}$$

Furthermore, if the packed pebble bed porosity is pseudo-homogeneous and the ideal gas law is employed with constant density, specific heat capacity c_p and thermal conductivity, Equation (2.3) may be rewritten again, as follows:

$$\rho u_z c_p\frac{\partial T}{\partial z}=k_{feff}\frac{1}{r}\frac{\partial}{\partial r}\left(r\frac{\partial T}{\partial r}\right)+k_{feff}\frac{\partial^2 T}{\partial z^2} \tag{2.4}$$

Equation (2.4) can be written for a pseudo homogeneous pebble bed (i.e. mixed solid and fluid temperature) as follows:

$$Gc_p\frac{\partial T}{\partial z}=k_{er}\frac{1}{r}\frac{\partial}{\partial r}\left(r\frac{\partial T}{\partial r}\right)+k_{eax}\frac{\partial^2 T}{\partial z^2} \tag{2.5}$$

Where:

$G=\rho u_z$ - Gas mass flux.

k_{er} - Pebble bed effective radial thermal conductivity.

k_{eax} - Pebble bed effective axial thermal conductivity.

At the intermediate and high flow rates (i.e. high Peclet numbers) thermal conduction in the axial direction will be negligible compared to convective transport and therefore Equation (2.5) reduces to:

$$Gc_p\frac{\partial T}{\partial z}=k_{er}\frac{1}{r}\frac{\partial}{\partial r}\left(r\frac{\partial T}{\partial r}\right) \tag{2.6}$$

The literature covered here will present theoretical models and experimental methods that predict and provide correlations for k_{er}. The focus will be on studies that impose the use of particles with minimal thermal conduction; usually the ratio $\left(\frac{k_{er}}{k_g}\right)$ is calculated.

2.2. Literature

The packed pebble bed effective thermal conductivity formulation is separated into two terms. The one term is independent of the fluid flow (molecular thermal conduction) and the other is dependent on the lateral mixing of the fluid (convective contribution) in the packed pebbles or particles (Kunii and Yagi (1957)). It was initially represented as follows:

$$\frac{k_{beff}}{k_g} = \frac{k^o_{beff}}{k_g} + \frac{\left(k_{beff}\right)_{lm}}{k_g} \tag{2.7}$$

Where:

k_{beff} - Pebble bed effective thermal conductivity with flowing fluid.

k^o_{beff} - Pebble bed effective thermal conductivity with motionless fluid (molecular conduction).

$\left(k_{beff}\right)_{lm}$ - Pebble bed effective thermal conductivity caused by fluid lateral mixing.

k_g - Molecular thermal conductivity of the gas.

The experimental methods used in packed bed studies to determine the effective radial thermal conductivity introduced governing boundary conditions to minimize the term $k_{eax}\frac{\partial^2 T}{\partial z^2}$ in Equation (2.5) and to approximately convert Equation (2.7) to incorporate $\left(\frac{k_{er}}{k_g}\right)$, i.e.,

$$\left(\frac{k_{er}}{k_g}\right) = \frac{k^o_{beff}}{k_g} + \frac{\left(k_{er}\right)_{lm}}{k_g} \tag{2.8}$$

Where:

$\left(k_{er}\right)_{lm}$ - Pebble bed effective radial thermal conductivity caused by fluid lateral mixing.

The lateral mixing term in Equation (2.8) was correlated, using earlier works (Ranz (1952)) that related it with what was called the modified Peclet number:

$$\frac{(k_{er})_{lm}}{k_g} = \alpha\beta N_{Pe_m} \tag{2.9}$$

Where:

$\alpha\beta$ - represent the function of the fluid flow rate and the geometric properties of a packed bed.

N_{Pe_m} - refers to the modified Peclet number, Pe_m.

Endo *et al.* (1964)) employed the radial temperatures measurement method to investigate the adequacy of the model of lateral mixing in cylindrical packed beds in liquid – solid systems similarly to the gas – solid systems (Packed systems of both glass spheres and steel balls with average porosity of 0.4 were used). Cold water was circulated through the bed. The bed was simultaneously being heated circumferentially by a steam heating jacket in the counter flow direction of the cold water. The authors fitted Equation (2.8) through the data obtained from the experiments conducted on test sections of with ratios of: $0.0517 \leq {D_p}/{D_t} \leq 0.106$, at Peclet numbers that were ranging between 10 and 800 with, ${D_p}/{D_t}$ the diametric ratio of the packed solid particles (D_p) to that of the test section (D_t).

A similar experimental procedure for the measurement of the radial temperature profile was employed to separately study the effective radial thermal conductivity k_{er} (Schlünder and Zehner, 1973). Experiments were conducted by injecting hot nitrogen gas axially at the centre line of an insulated packed bed into the colder nitrogen gas passing through the test section. The packed materials used, were mono-dispersed spherical balls of foamed styropor, ceramic, steatite, steel and copper.

The authors (Schlünder and Zehner, 1973) introduced the quantity K that was experimentally determined to describe the influence of the lateral mixing (Schlünder (1966)). This quantity, that is different for radial and axial thermal conductivity, is also

dependent on the geometric conditions of the packing system and was correlated as follows for radial thermal dispersion:

$$K_r = 8 \bullet \left[2 - \left(1 - 2\frac{D_p}{D_t} \right)^2 \right] \tag{2.10}$$

Equation (2.10) has a limiting value of 8 for an infinite bed consisting of spherical particles, therefore, Equation (2.9) can be rewritten as follows (Schlünder and Zehner, 1973):

$$\frac{\left(k_{er}\right)_{lm}}{k_g} = \frac{Pe}{K_r} \tag{2.11}$$

An analysis was done to determine the influence of the particle form, size and size distribution along the mixing length on the packed bed effective radial thermal conductivity (Bauer and Schlünder, 1978a), specifically looking at Equation (2.11). The numerical investigation focused on about 2500 experiments conducted by the same authors (Schlünder and Zehner, 1973, and Zehner, 1972). From the analysis it was deduced that the influence of lateral mixing on the effective radial thermal conductivity could be calculated from the geometrical data. It was assumed that the thermal conductivities of the various sub-flows in the packed bed were directly proportional to their mixing lengths, and therefore the overall turbulent flow in the packing was replaced by the superposition of individual turbulent flows.

Krischke *et al.* (2000) conducted a comprehensive re-evaluation of available experimental data and presented a simple and consistent set of coefficients for both thermal and mass dispersion. For radial dispersion coefficients inside the cylindrical tube (packed bed) the authors used the correlation that was previously formulated by Cheng and Vortmeyer (1988) for the effective radial thermal conductivity:

$$k_{er}\left(r\right) = k_{beff}^{o} + K_{1,h} Pe \frac{u}{u_o} f\left(R - r\right) k_g \tag{2.12}$$

with:

$$f\left(R-r\right)=\begin{cases}\left(\dfrac{R-r}{K_{2,h}}\right)^{n_h} & for \quad 0<R-r\le K_{2,h}D_p \\ 1 & for \quad K_{2,h}D_p<R-r\le R\end{cases} \tag{2.13}$$

where:

$k_{er}\left(r\right)$ - effective radial thermal conductivity as function of radial direction,

R - tube radius,

$K_{1,h}$ - slope parameter in Equation (2.12),

$f\left(R-r\right)$ - function that varies with the tube radius in the radial direction in Equation (2.13)

$K_{2,h}$ - damping parameter in Equation (2.12),

n_h - curvature parameter for Equation (2.12)

Similarly, Cheng and Vortmeyer (1988) formulated the radial mass dispersion coefficient correlation with the same form as Equation (2.12). The parameters $K_{1,h}$, $K_{2,h}$ and n_h were determined by comparing the model (Equation (2.2)) with the experimental data in the literature. Figure 2-1 shows the plot of the radial effective conductivity $k_{er}\left(r\right)$ over the dimensionless distance from the wall $\left(R-r\right)/D_p$ and according to Krischke *et al.* (2000), the quantities $K_{1,h}$, $K_{2,h}$ and n_h have the following meaning:

- slope parameter $K_{1,h}$ determines the rate of increase of the effective radial conductivity with the flow velocity,
- damping parameter $K_{2,h}$ sets in multiples of the particle diameter D_p the point after which $k_{er}\left(r\right)$ begins to decline towards the wall, and
- the exponent n_h determines the curvature of the damping function.

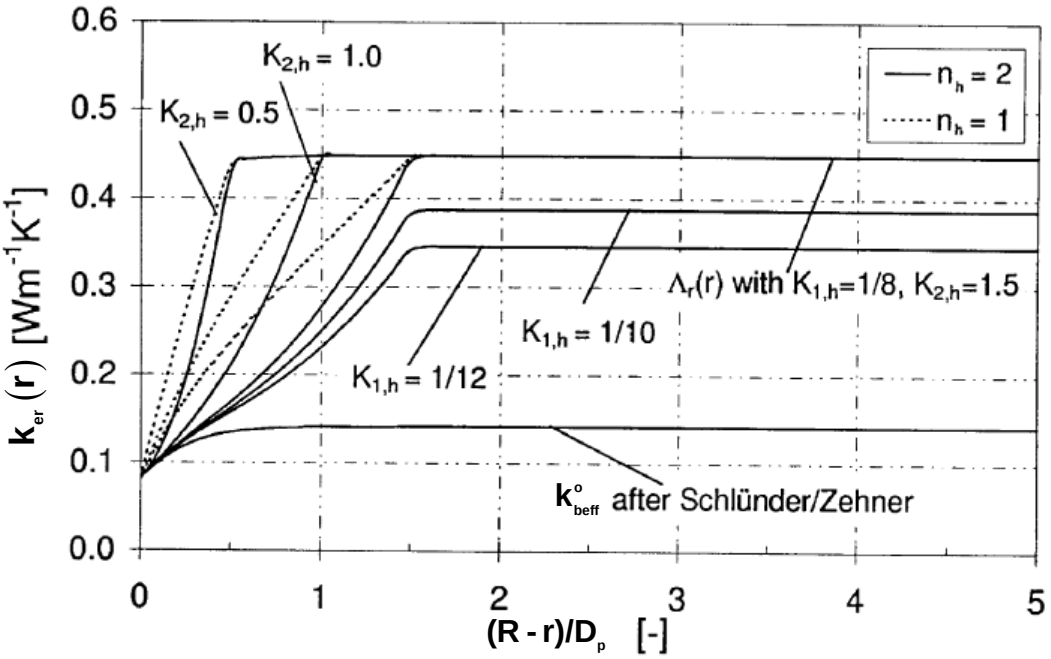

Figure 2-1: Radial effective thermal conductivity with n_h, $K_{1,h}$ and $K_{2,h}$ as parameters (Krischke *et al*, 2000).

Two types of experimental procedures were considered i.e., injection experiments, and wall-heated or wall-cooled packed beds (at constant wall temperature). These experimental procedures were respectively adopted by Schlünder and Zehner (1973) and Endo *et al.* (1964) as was previously noted and discussed at the beginning of this section.

Consequently, Krischke *et al.* (2000) evaluated the works of Schlünder and Zehner (1973) and Bauer (1977) and the following boundary conditions were set for thermal dispersion calculations for injection experiments:

- temperature is set to the injection temperature at the inlet,
- no temperature change with respect to the axial length at the outlet,
- no temperature change with respect to the radial length (transverse) at the centre of a packed bed, and
- no temperature change with respect to the radial length (transverse) at the wall of the packed bed.

With regards to the wall heated or wall-cooled the authors set the so-called, real boundary condition of the first kind, whereby the wall temperature is set to a constant heating or cooling media temperature. Other boundary condition remained similar to the injection experiments. Most of the authors used air with a few using ammonia and nitrogen gases; and as stated before, packings of mono-dispersed spherical particles with low solid thermal conductivity were used.

Krischke *et al.* (2000) found it difficult and potentially inaccurate to determine $K_{1,h}$, $K_{2,h}$ and n_h by using multi-parametric optimization because $K_{1,h}$ may vary depending on $K_{2,h}$, instead of definite, explicit values of each parameter. So, each parameter was evaluated on its own with a more structured and sequential approach.

$K_{1,h}$ was determined from the thermal injection experiments by minimizing error between the simulated temperatures profiles (both at the outlet and inlet) and the measured the temperatures profiles. In the Bauer (1977) injection experiments, the outlet temperature profiles shows that temperature spread is depicted at the centre of the bed than at the walls; this implies that the other two parameters ($K_{2,h}$ and n_h) would have less effect by the virtue of boundary conditions set for Equation (2.13). Figure 2-2 shows the results of the simulated reciprocal values of $K_{1,h}$ plotted against the packed bed diameter ratio D_t/D_p. Reciprocal values of $K_{1,h}$ (also called radial Peclet number Pe_r in the previously stated literature of Schlünder (1966), Bauer (1966), Schlünder and Zehner (1973), and Zehner (1972)) was reported to depended on the diametric ratio D_t/D_p. This implies that $1/K_{1,h}$ has the same meaning and implication as K_r from Equation (2.10) which has the limit of 8 as seen in Figure 2-2. Figure 2-2 also shows that re-evaluated experimental data produced values between 7 and 10 which scatter around the limiting value.

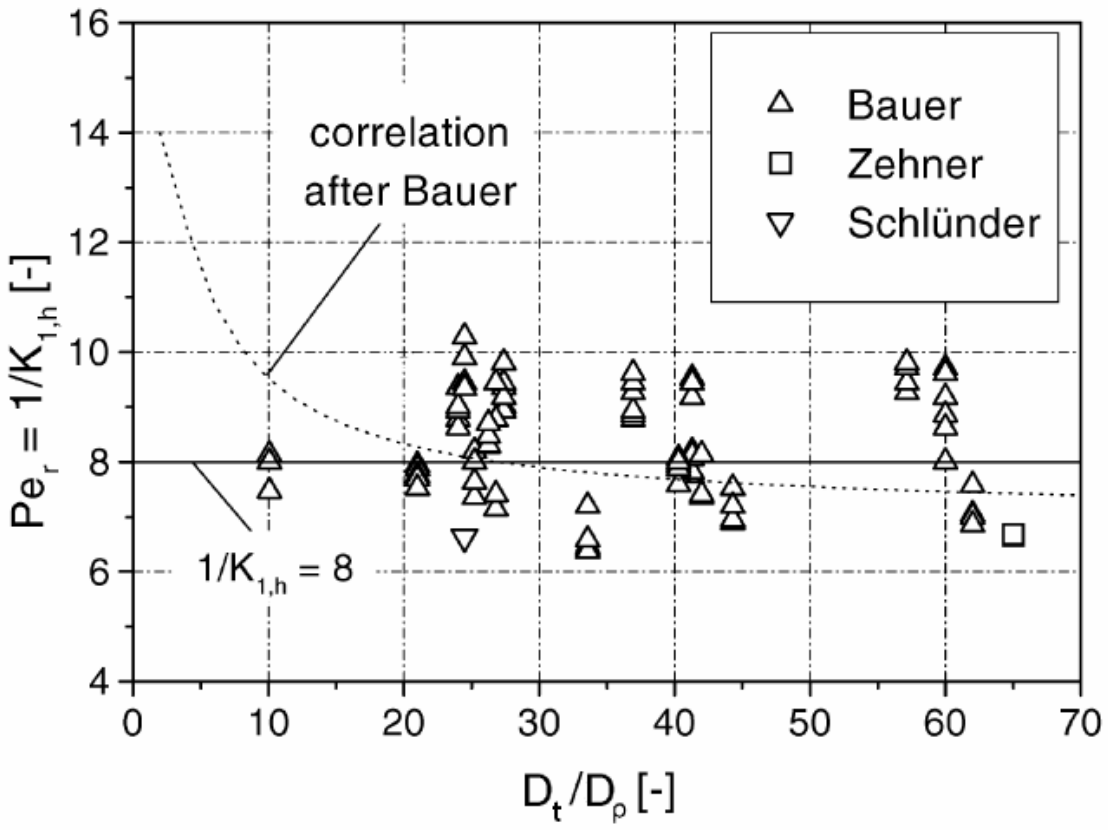

Figure 2-2: Reciprocal values of the slope parameter $K_{1,h}$ as obtained from the re-evaluation done by Krischke *et al* (2000) (Krischke *et al*, 2000).

Krischke *et al.* (2000) calculated $K_{2,h}$ and n_h from the experiments with constant wall temperature. The slope parameter was kept at $1/K_{1,h} = 8$. Many experimental data showed a very sharp temperature gradient near the wall, and therefore the curvature parameter was accurately computed as $n_h = 2$ which implies a quadratic drop of the part of the radial effective thermal conductivity induced by the fluid flow in the vicinity of the wall (Equation (2.13) and Equation (2.12)). Therefore one parametric optimization for damping parameter $K_{2,h}$ was suitable for $1/K_{1,h} = 8$ and $n_h = 2$. The simulated results have shown that the damping parameter approaches $K_{2,h} = 0.44$ at high Reynolds numbers; and it exponentially increases at low Reynolds numbers. Krischke *et al.* (2000) recommended the use of $K_{2,h} = 0.44$ because of the error in the calculation of

k_{beff}^{0} without the fluid flow. The authors could not determine the dependence of $K_{2,h}$ on the diametric ratio D_t/D_p or on the axial position.

For both experiments the optimized values and functions by Krischke *et al.* (2000) for Equation (2.13), which is applicable to the effective radial thermal conductivity $k_{er}(r)$ correlation in Equation (2.12), are summarized as follows:

$$\begin{aligned} n_h &= 2 \\ K_{2,h} &= \frac{1}{8} \\ K_{2,h} &= 0.44 + 4\exp\left(-\frac{\mathrm{Re}}{70}\right) \end{aligned} \tag{2.14}$$

With $\mathrm{Re} = \rho u_0 D_p / \mu$ and μ the dynamic viscosity of the fluid. The values for the parameters Equation (2.14) are valid for:

- Bed to particle diameter ratio: $5.5 \le D_t/D_p \le 65.0$
- Reynolds number: $24 \le \mathrm{Re} \le 2740$

Figure 2-3 shows the comparison between the results of Krischke *et al.* (2000), Cheng and Vortmeyer (1988), Cheng and Hsu (1986) and Kuo and Tien (1989) for the effective radial thermal conductivity $k_{er}(r)$ for Re=50. It is seen that the only correlation that is close to the current work of Krischke *et al.* (2000) is the correlation by Cheng and Hsu (1986) which gave $K_{1,h} = \frac{1}{8.3}$

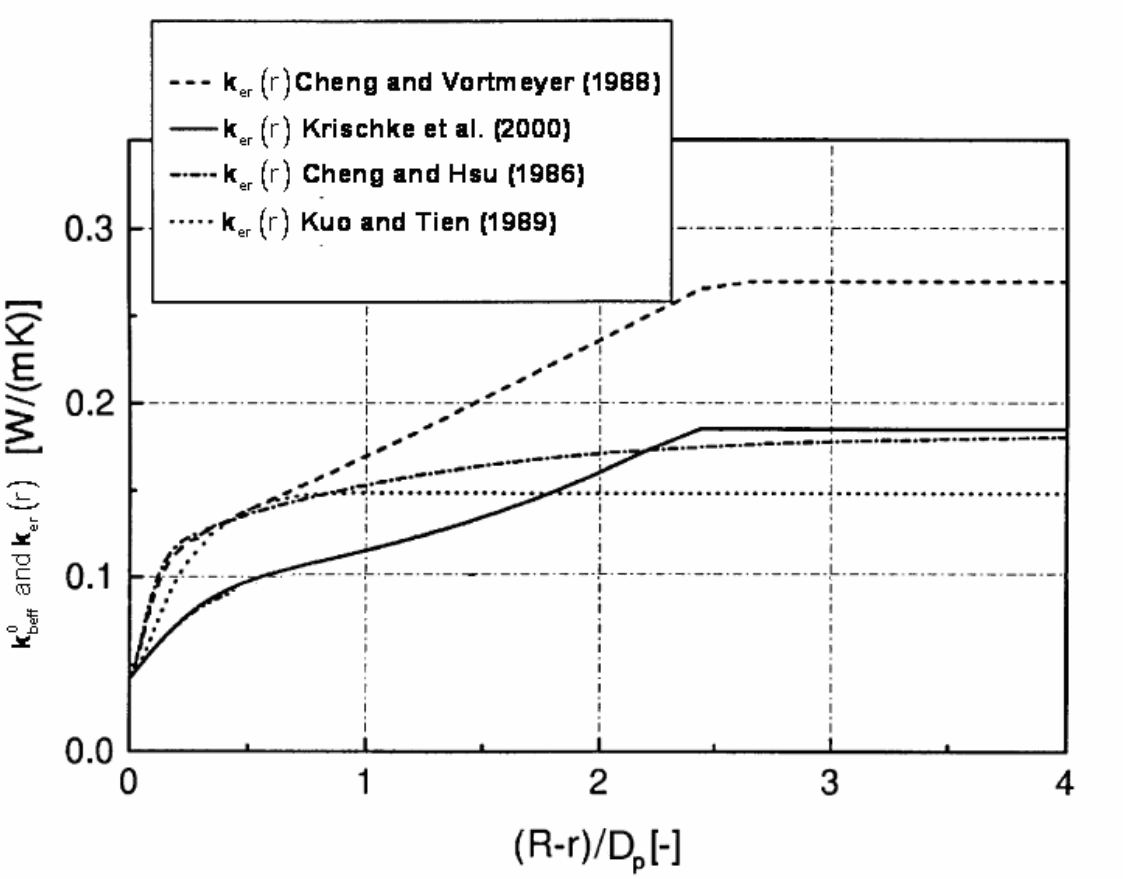

Figure 2-3: Comparison of work of Krischke *et al.* (2000) and other works (Krischke *et al*, 2000).

Mass dispersion coefficients were re-evaluated with tracer injection experiments by fitting measured data of the concentration levels inside packed beds in the mass transport equation (similarly to the formulation of Equation (2.1)). It was found that the mass dispersion is limited to 8. Krischke *et al.* (2000) also found no dependence on the diametric ratio and the axial position.

Kaviany (1991) examined the so-called fluid hydrodynamic dispersion inside a tube due to molecular diffusion for both turbulent and laminar flow. The examination was extended to the flow inside a packed bed (or tube) with particles of zero solid thermal conductivity i.e. $k_s = 0$. Both packed beds with random and structured packings were used. Kaviany (1991) theorized that, due to the multidimensionality of the temperature and velocity fields, the thermal dispersion coefficient must be presented as a tensor. The

heat transport equation given in Equation (2.1) was expanded for $k_s = 0$ and the so-called total effective thermal diffusivity tensor $\mathbf{D_e}$ was formulated as follows:

$$\mathbf{D_e} = \varepsilon \alpha_f \left(\mathbf{I} + \mathbf{L_t^*} \right) + \varepsilon \mathbf{D^d} \tag{2.15}$$

Where:

$\alpha_f = \dfrac{k_g}{\rho c_p}$ - fluid thermal diffusity,

$\mathbf{I} = \begin{bmatrix} 1 & 0 & 0 \\ 0 & 1 & 0 \\ 0 & 0 & 1 \end{bmatrix}$ - unit tensor,

$\mathbf{D^d} = -\dfrac{1}{V_f} \int_{V_f} \mathbf{u}' \mathbf{b} \, \mathrm{d}V$ - dispersion tensor,

$\mathbf{u}'$ - vectorial spatial deviation component of the fluid velocity,

$\mathbf{b}$ - vector function that transforms the gradient of the intrinsic phase-averaged temperature into the local variation of the deviation from the averaged temperature,

V_f - volume occupied by the fluid,

$\mathrm{d}V$ - derivative over volume V of the packed bed,

$\mathbf{L_t^*} = -\dfrac{1}{V_f} \int_{A_{fs}} \mathbf{n} \mathbf{b} \, \mathrm{d}A$ - tortuosity tensor,

$\mathbf{n}$ - unit normal vector directed from the fluid phase into the solid phase,

A_{fs} - interfacial area between the fluid phase and the solid phase,

$\mathrm{d}A$ - derivative over area volume A,

Kaviany (1991) compiled the work from Carbonell *et al.* (1983) who compared the experimental work from Gunn and Pryce (1969) and the numerical work from Carbonell *et al.* (1983). Numerical results were compared with the results the experiments that were conducted with packed beds with ordered and random packings of spheres with the following geometries and properties (Gunn and Pryce (1969)):

- Ordered or structured packing of polythene spheres,

  - Simple cubic arrangement with porosity of $\varepsilon = 0.48$.
  - Rhombohedral arrangement with porosity of $\varepsilon = 0.26$.
- Random packing of closely graded glass ballotini of $\varepsilon = 0.37$, and
- Experiments were conducted at minimum and maximum Reynolds numbers of 0.02 and 420.

It is seen from Equation (2.15) that the total effective dispersion thermal diffusivity $\mathbf{D_e}$ has tensorial formulation. In their numerical work, Carbonell *et al.* (1983) used finite element approximations for both the longitudinal ($D_{e,z}$) and the transverse or radial ($D_{e,r}$) directions. $D_{e,z}$ and $D_{e,r}$ are respectively formulated in Equation (2.16) and Equation (2.17).

$$D_{e,z} = \frac{k_{beff,z}}{k_g} + \frac{k_z^d}{k_g} = 1 + \mathrm{L}_{\mathrm{t,z}}^* + \frac{\rho c_p}{k_g} D_z^d \qquad (2.16)$$

$$D_{e,r} = \frac{k_{beff,r}}{k_g} + \frac{k_r^d}{k_g} = 1 + \mathrm{L}_{\mathrm{t,r}}^* + \frac{\rho c_p}{k_g} D_r^d \qquad (2.17)$$

Where:

$\frac{k_{beff,z}}{k_g} = 1 + \mathrm{L}_{\mathrm{t,z}}^*$ and $\frac{k_{beff,r}}{k_g} = 1 + \mathrm{L}_{\mathrm{t,r}}^*$ - the stagnant fluid phase effective thermal diffusivity components,

$\mathrm{L}_{\mathrm{t,z}}^*$ and $\mathrm{L}_{\mathrm{t,z}}^*$ - tortuosity tensor components, and

$\frac{k_z^d}{k_g} = \frac{\rho c_p}{k_g} D_z^d$ and $\frac{k_r^d}{k_g} = \frac{\rho c_p}{k_g} D_r^d$ - the mixing fluid phase effective thermal diffusivity components,

Kaviany (1991) showed comparisons between the predicted results of Carbonell *et al.* (1983) and Gunn and Pryce (1969) for the longitudinal total effective thermal diffusivity $D_{e,z}$ as shown in Figure 2-4. The experiments shown are were for a structured packing of simple cubic arrangement of polythene spheres with a porosity of $\varepsilon = 0.48$, and a random packing of graded glass ballotini with a porosity of $\varepsilon = 0.37$.

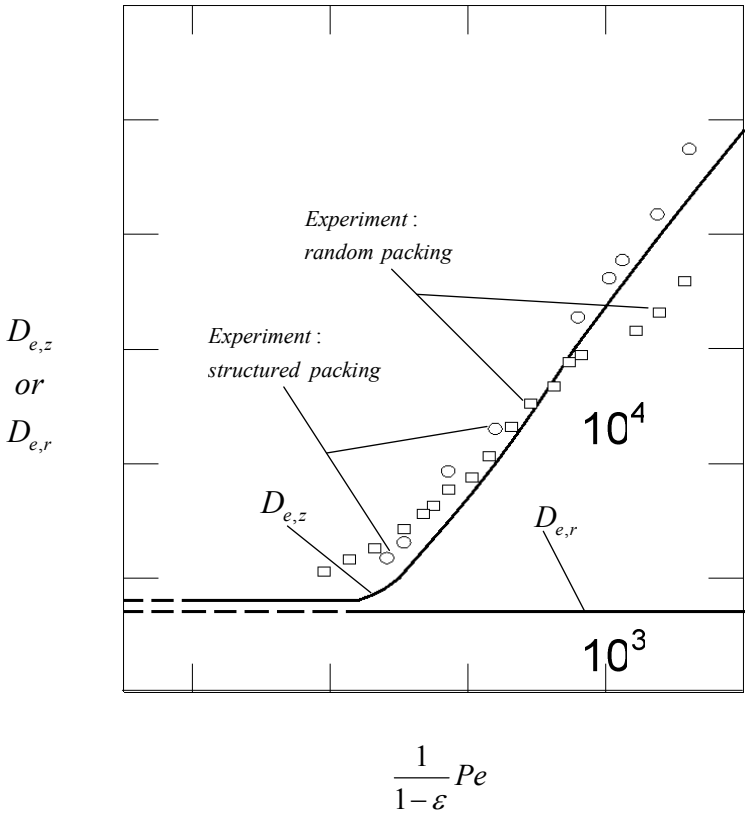

Figure 2-4: Predicted results of Carbonell *et al.* (1983) compared with the experimental results of Gunn and Pryce (1969) (Kaviany, 1991).

It is evident from the experimental results in Figure 2-4 that the packing structure of the bed i.e. ordered versus random, has an influence on $D_{e,z}$. The experimental results also indicate that the random packing has a negligible influence on $D_{e,z}$ for $\frac{1}{1-\varepsilon}Pe<1$; and for $100<\frac{1}{1-\varepsilon}Pe<1$, the experimental values for both beds with the random packing and structured packing are close to each other.

Kaviany (1991) reported that no data were available for the transverse total effective thermal diffusivity $D_{e,r}$. It is however, important to note the findings from Gunn and Pryce (1969) (for the same experiments which were evaluated by Carbonell *et al.* (1983)). The authors, conducted a numerical analysis on the radial mixing by determining the radial dispersion coefficient using diffusion and mixing models for the beds with ordered packing, and none of these latter models could describe the dispersion

phenomena. Their experimental results showed that the fluid in voids of the packed bed with an ordered structure was not well mixed as compared to the fluid in voids of the packed bed with a random structure.

Gunn and Pryce (1969) analysed mass dispersion for a packed bed with a random structure for the radial mixing experiments. The authors found that as the Reynolds number increases the Peclet number (based on the mass dispersion) settled around the value of 10. Figure 2-5 shows the Peclet number – Reynolds number relationship for spheres of ballotini with different diameters.

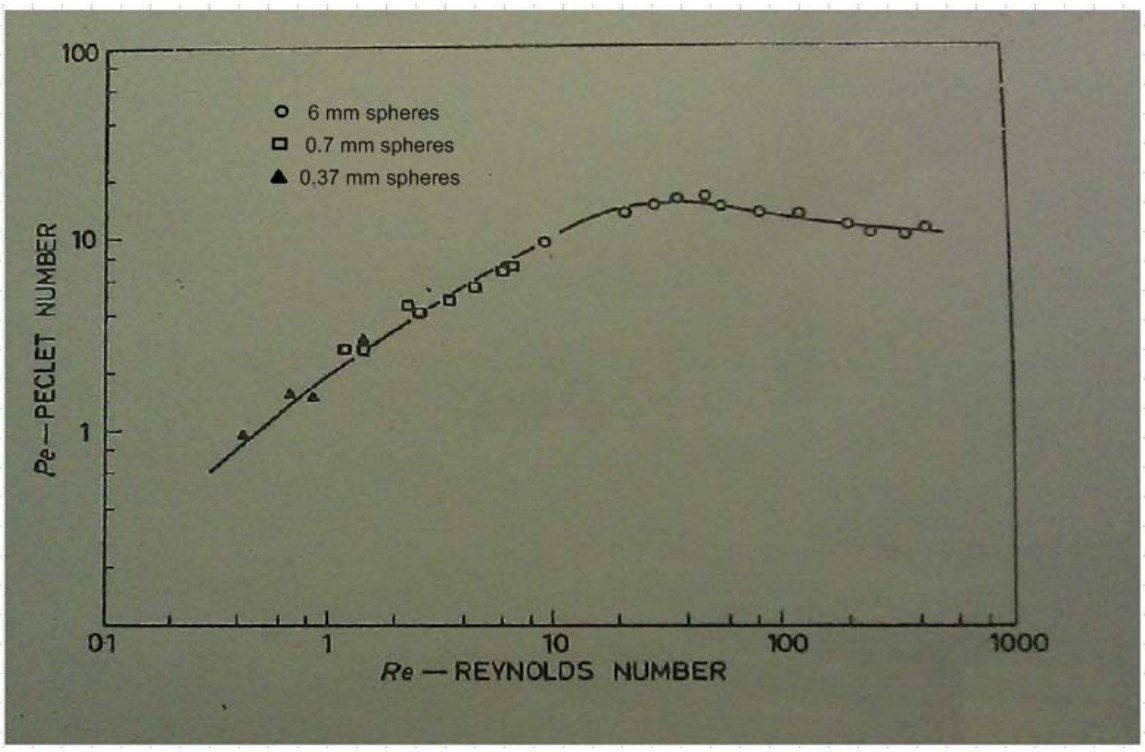

Figure 2-5: Peclet number based on the mass dispersion coefficient as the Reynolds number increases (Gunn and Pryce, 1969).

Gunn and Khalid (1975), and Kunni and Ono (1968) used the wall heated experimental method to determine the radial thermal conductivities. The authors used randomly packed beds of solid particles with both relatively low thermal solid conductivity (celite and glass) and relatively high thermal solid conductivity (steel and nickel). The geometry was varied for $3.3 \le {D_t}/{D_p} \le 190.5$. The authors further calculated the Peclet number based on

the effective radial thermal conductivity at higher Reynolds numbers to eliminate the axial conduction effects.

Dixon and Cresswell (1979) derived a theory for determining both the effective axial and radial thermal conductivities for a randomly packed bed. They assessed the work of Gunn and Khalid (1975) and Kunni and Ono (1968) by taking into account the effect of thermal solid conductivity. Their model calculations, which gave 25% and 50 % accuracy respectively for low thermal conductivity packing and high thermal conductivity packing, also predicted the effective radial Peclet number below 10 at high Reynolds numbers.

2.3. Remarks

The experimental procedures which were adopted by Endo *et al.* (1964), and Schlünder and Zehner (1973) have been widely used to evaluate the thermal dispersion based on the fluid thermal conductivity (Equations (2.8), (2.10), and (2.11)).

The re-evaluation by Krischke *et al.* (2000) re-evaluation of the Cheng and Vortmeyer (1988) expressions considered both the thermal dispersion and mass dispersion in terms of the direction of a packed bed (axial and radial (for the cylindrical beds) or transverse (for the Cartesian beds). Equation (2.12) gives an expression for the radial thermal dispersion which implies dependence in terms of radial direction of the packed bed. Although not presented here, mass dispersion in terms of the radial direction has a similar expression. No dependency was detected on both the diametric ratio D_t/D_p and the axial position inside the bed, but the following remarks are made with regards to Figure 2-3:

- From Krischke *et al.* (2000), the effective radial thermal conductivity $k_{er}(r)$ increases sharply for $R-r \le \frac{1}{2}D_p$ and increases less sharply for $\frac{1}{2}D_p \le R-r \le 2\frac{1}{2}D_p$ where afterwards where it becomes constant.

- From the correlations by Cheng and Hsu (1986) and Kuo and Tien (1989) , the effective radial conductivity $k_{er}(r)$ increases rapidly for $R-r \le \frac{1}{8}D_p$ and then increases very sharply to a constant value at about $R-r = 3\frac{1}{2}D_p$. An exception is seen in the Kuo and Tien (1989) correlation where from $R-r \le \frac{1}{4}D_p$, $k_{er}(r)$ increases more sharply than the rest of the correlations and become constant at $R-r \le 2\frac{1}{2}D_p$.

Marivoet *et al*. (1974) were able to relate the porosity profile inside the randomly packed bed with the transverse or radial length of the randomly packed bed. The authors found that the porosity in the random packing is equal to one at the wall because of the point contact between the wall and the particle. The profile then decreases to about 0.4 for measurements done in the range of four to five particle diameter distances from the wall. For the same range the porosity values forms a profile with a damped oscillation. The measured porosities became constant values that range between 0.36 and 0.37 towards the centre of the bed. Packed particles of uniform size and shape where used.

The following remarks can be made to relate the work of Krischke *et al.* (2000) to the work of Marivoet *et al*. (1974):

- Krischke *et al.* (2000) (Figure 2-3), shows that the calculated effective thermal conductivity $k_{er}(r)$ is constant for more than two and halve diameters distance $\left(R-r \ge 2\frac{1}{2}D_p\right)$ from the wall. Marivoet *et al*. (1974) recorded constant values of porosities inside the packed for more than five particle diameter distances $\left(R-r \ge 5D_p\right)$ from the wall.
- In general, Krischke *et al.* (2000) (and other works depicted in Figure 2-3), showed that the effective thermal conductivity $k_{er}(r)$ increases from the minimum value (away from the wall) before it reaches a constant maximum

value. Marivoet *et al*. (1974) recorded a porosity of 1 to 0.4 for a distance of $R - r \leq 4D_p$ away from the wall.

- It is however important to note that, the mixing between injected hot gas and the apparent cold gas, only start from the centre of the bed.

From these remarks, it can be deduced that the fluid effective radial thermal conductivity varies with the porosity values.

Therefore, keeping the above remarks in mind, the current work attempts to systematically investigate dispersion effects for three different pseudo-homogeneous porosities in the packed bed (BETS036, BETS039 and BETS045). The packing in the test section was constructed with spherical particles (poly-acrylline balls) with a negligible solid conduction. This implies that the calculated bed effective thermal conductivity is based only on the fluid thermal conductivity. Experiments were also conducted using a procedure similar to that adopted by Schlünder and Zehner (1973), whereby two temperature profiles were measured at two axial positions. The hot gas is injected in the surrounding cold gas at the same inlet velocity. Experimental setup and procedures are outlined in the next chapter. With these experimental attributes:

1. CFD models representing geometries for the three test sections were constructed in the CFD' pre-processor (Figure 6-5),
2. boundary conditions were set for the temperatures and velocities of the injected hot gas and the surrounding cold gas on the constructed geometries,
3. for a guessed effective thermal conductivity and with the set boundary conditions, CFD simulations were done for all the three conservations of matter, i.e. mass, momentum and energy,
4. from these CFD simulations, transverse temperatures profiles are extracted at two axial positions of the same axial length as the experimental measurements (Figure 6-5),
5. the CFD transverse temperature profiles are compared to the experimentally measured transverse temperature profiles,
6. for this comparison, a criteria is set to determine if the guessed effective thermal conductivity is correct

7. a search routine is developed and implemented in the CFD program to determine the guessed effective thermal conductivity by repeating steps 3–6, and
8. steps 2–7 are done for different Reynolds numbers (Figure 6-7),.

Chapter 6 outlines the all the theoretical background and assumptions used for the CFD simulations.

However, it can be expected to find low mixing in the radial or transversal direction, because of homogeneous porosity as prompted in Gunn and Pryce (1969) experimental results.

2.4. Summary

This chapter showed the advances that were made by the previous authors in the study of dispersion effects in the packed beds. The authors investigated the effect of radial dispersion on the bed effective radial thermal conductivity. It should be noted that the thermal dispersion effect is coined by the term ‘braiding’ effect.

This study systematically investigates the impact of porosity by using structured packed beds with different pseudo-homogeneous porosities. The experiments in the study also isolated the fluid thermal conductivity from the solid thermal conductivity by using packed particles with negligible solid thermal conductivity.

3. EXPERIMENTAL SETUP

3.1. Test facility

The High Temperature Test Facility (HTTF) experimental facility is situated at North-West University, Potchefstroom Campus, Potchefstroom in South Africa. The High Pressure Test Unit (HPTU) plant of this facility was operated from June 2006 to February 2008. The HPTU was designed and developed by M-Tech Industrial (Pty) Ltd. The company gave the author access to the HPTU and several of the design documents for the purpose of this study.

The HPTU tests that are relevant to this study are the steady-state separate effects tests to determine the effective fluid heat conduction due to turbulent mixing at different porosities (Braiding Effect Test Sections BETS 0.36, BETS 0.39 and BETS 0.45).

The following sections will provide an overview of the test facility and test sections relevant to this study.

3.2. HPTU plant

The HPTU plant has two cycles that are running concurrently while in operation, namely the gas cycle and cooling water cycle as shown in Figure 3-1. The three dimensional (3D) model of the gas cycle is also shown in Figure 3-2 with pipe interconnections between the components. The components of the two cycles are discussed henceforth.

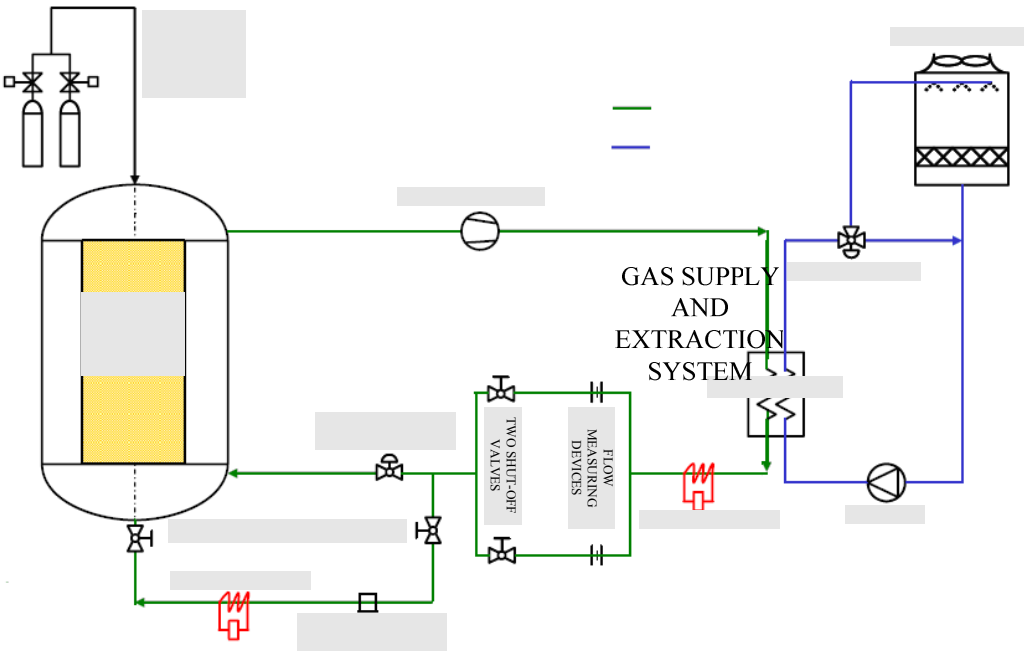

Figure 3-1: Schematic representation of the HPTU plant layout: gas and cooling water cycles.

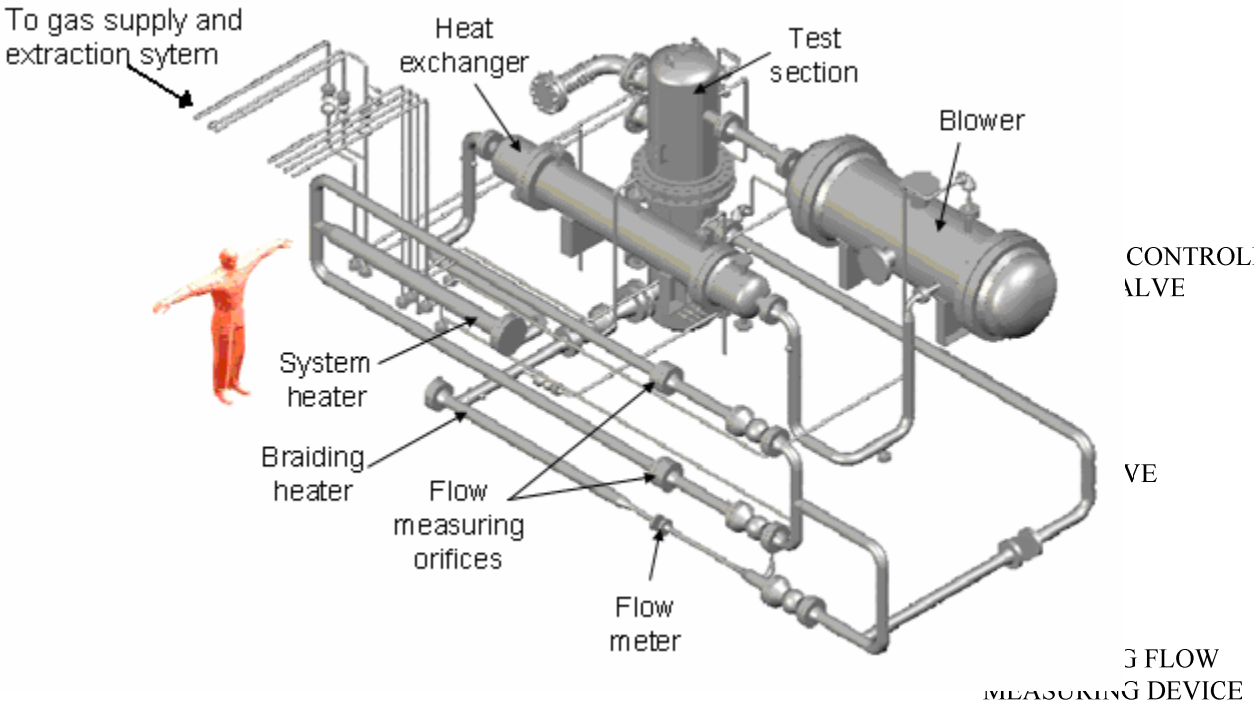

Figure 3-2: 3D model of the HPTU plant (only gas cycle).

Gas supply and extraction system

The gas cycle works with the nitrogen gas. The pressure in the gas cycle is controlled by the gas supply and extraction system. The system is also used to evacuate the nitrogen gas for maintenance purposes.

Blower system

After being supplied at the required pressure, nitrogen gas flows through the blower system which circulates the gas through the cycle. The blower system consists of a motor coupled to two blowers that are connected in series as shown in Figure 3-3.

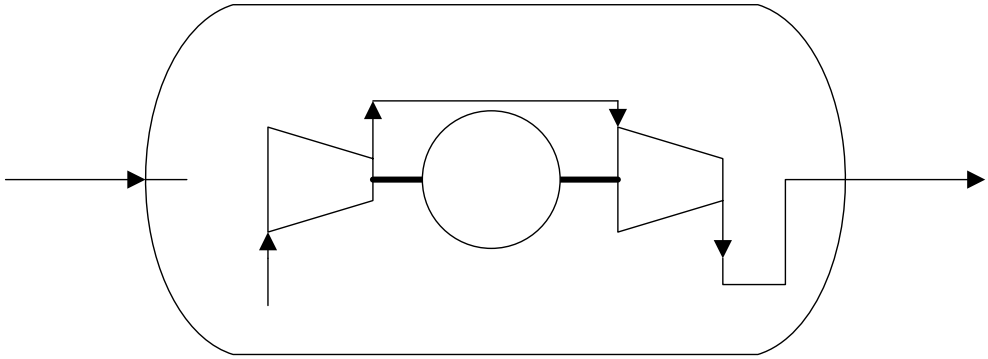

Figure 3-3: Schematic representation of the blower system.

The blowers are placed in a pressure vessel since the maximum working pressure of the system is 5*MPa*. This is to reduce the pressure difference over the blower wall and to enable the use of less expensive blowers. The inlet of the blower system (1) is open to the inside of the pressure vessel, as well as the inlet to the first blower. The second blower outlet leads out of the pressure vessel at point (2).

Heat Exchanger

The nitrogen temperature will rise gradually throughout the cycle. This is due to the compression through the blower system and the heating elements in the gas stream. It is thus necessary to maintain the correct temperature during experiments.

(1)

Blower 1 Motor

Therefore, the nitrogen gas is cooled through the exchange of heat with cooling water by means of a shell-and-tube heat exchanger, points (2) and (3) in Figure 3-4. The designed heat transfer duty of the heat exchanger is 34kW. In order for the heat exchanger not to extract too much heat from the nitrogen gas, a bypass temperature-controlled system is used in the cooling water cycle.

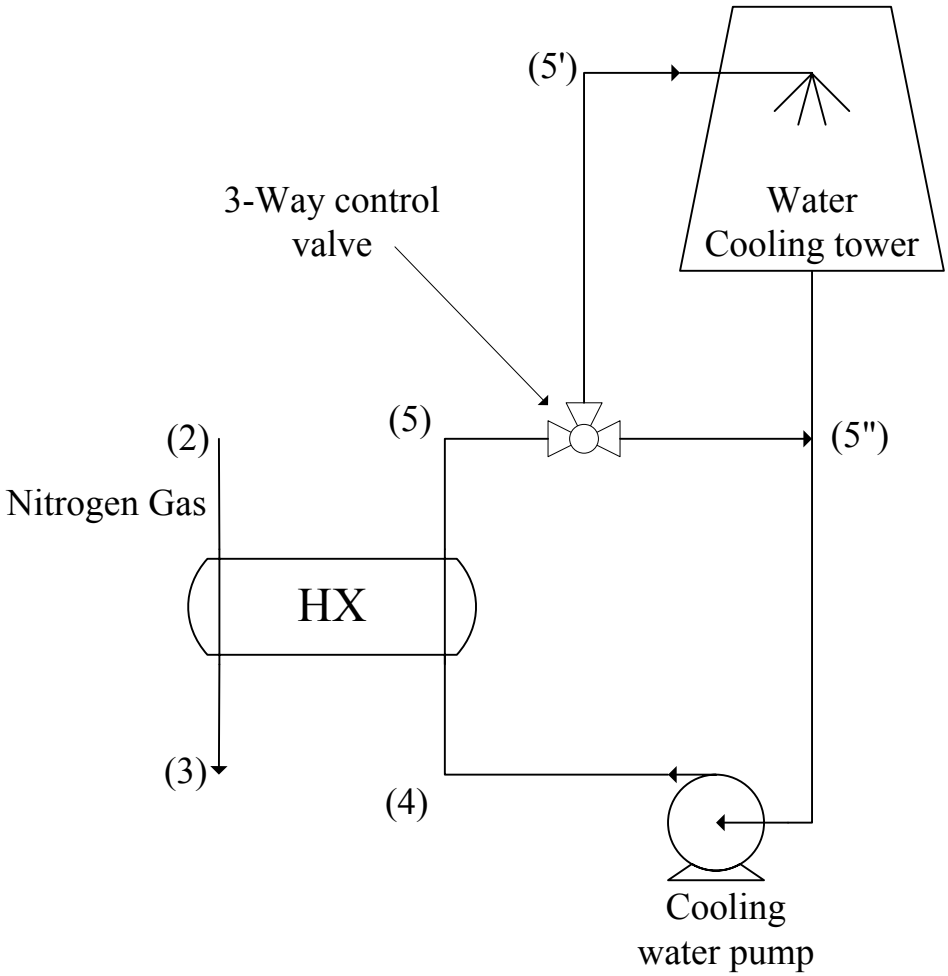

Figure 3-4: Schematic layout of the heat exchanger-cooling water cycle.

Also shown in Figure 3-4 is the heat exchanger cooling water cycle. The three-way control valve is controlled by the nitrogen outlet temperature at point (3). The controller maintains the outlet temperature (3) to the set ambient temperatures by bypassing a certain fraction of the heated water from point (5) to the cooled water at point (5"). Thus

the water entering the heat exchanger is not all cooled in the cooling tower and as a result the water temperature entering the heat exchanger (4) can be controlled.

System heater

To further help with temperature control a 20kW inline flanged system heater is installed at the outlet of the heat exchanger.

Main flow measuring devices

From the outlet of the system heater, flow measuring devices are implemented to measure the fluid mass flow rate. This system consists of two 4" pipe channels that can be opened or closed independent of each other. Each pipe channel consists of a shut-off valve to open or close the channel, an orifice plate and the necessary pressure and temperature instrumentation. From the measurements of this instrumentation, the flow rate can be determined.

The reason for the implementation of two independent orifice measuring stations is because of the wide range in mass flows to be measured. As a result, different orifice plates are necessary to cover an upper and lower Reynolds number range. Hence, the pipe system combined with two shut-off valves makes it easy to measure different flow rates.

System control valve

After the system total mass flow rate has been measured, the gas entering the test section is controlled, depending on the type of experiment being conducted. For the braiding experiments the system control valve is set so that a pre-determined amount of flow passes through the braiding line.

Braiding flow measuring device

The braiding flow pipe is also 4" in diameter. A flow transmitter is installed to measure the braiding mass flow rate.

Braiding heater

The braiding flow temperature has to be at least +40 ˚C higher than the main flow temperature. For this requirement, a 6*kW* inline flanged system heater is installed on the upstream side of the second shut-off valve on the braiding line (Figure 3-1).

Test section pressure vessel

The different test sections used in the HPTU were designed such that they can be exchanged with relative ease with another in the test section pressure vessel. Figure 3-5 illustrates the placement of the test section inside the pressure vessel.

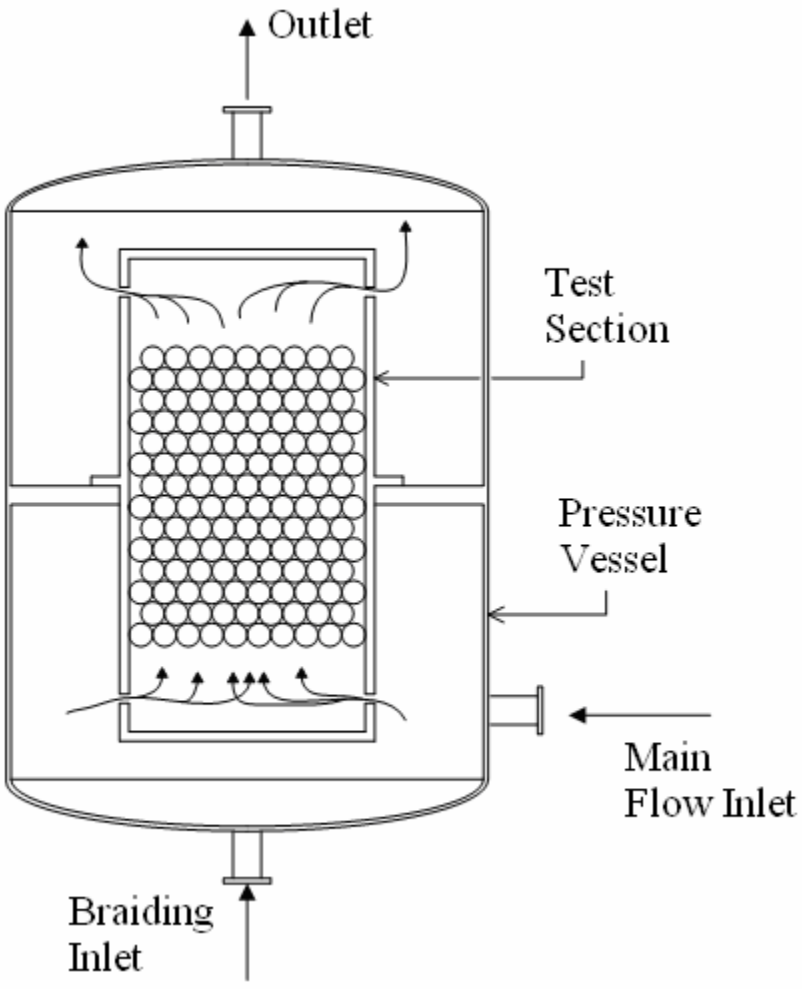

Figure 3-5: Placement of the test section into the pressure vessel.

3.3. HPTU BETS test sections

Figure 3-6 shows the schematic diagram of a BETS test section. The three test sections have been constructed similarly; the only difference is in terms of the porosity. Therefore, the schematical diagram shown in the figure is for all three test sections, namely BETS036, BETS039 and BETS045.

Figure 3-6 shows two layers of thermocouples that measure the transverse temperature distribution in the test section at different axial positions. The test section was constructed such that the heated fluid was introduced just below the pebbles in a symmetrical manner. The heated fluid is also referred to as the braiding gas as indicated in the figure.

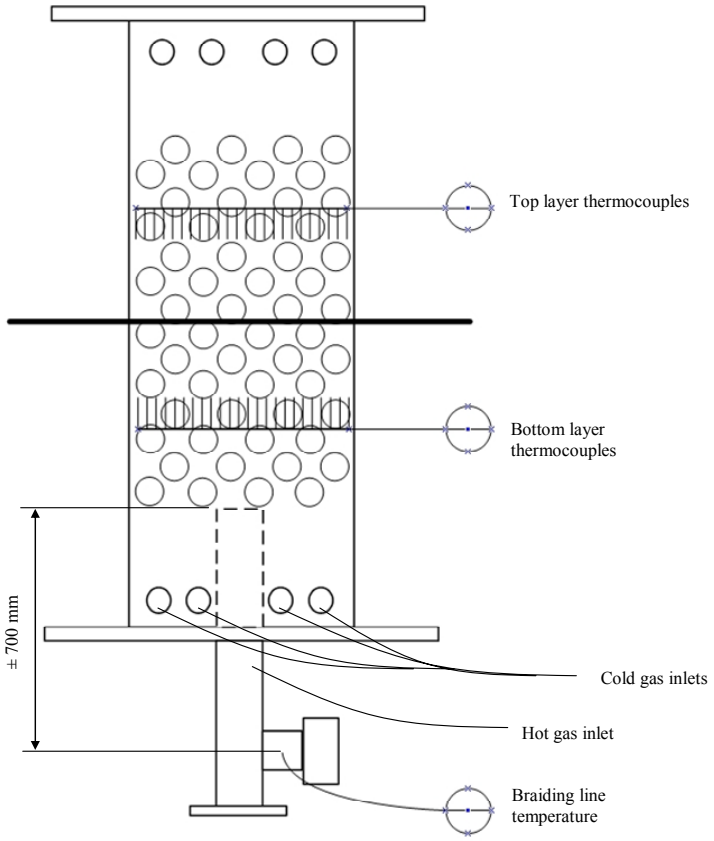

Figure 3-6: Schematic diagram of a BETS test section.

3.4. Instrumentation and measurement

The instrumentation and measurement on the gas cycle and the test sections are discussed hereafter.

3.4.1. *Gas Cycle*

Figure A-1 in APPENDIX A shows the P& ID diagram of the HPTU plant with the pressure, temperature and mass flow rate measuring devices indicated.

The following variables are measured:

- Test section inlet temperatures (Cold gas) (TT200 and TT201),
- Test section inlet pressure (PT 200, PT 201),
- Braiding line inlet mass flow (FT 230),
- Braiding inlet temperature (Hot gas) (TE 230),
- Inlet pressure of orifice station 220 (PT 220, PT 221),
- Inlet temperature of orifice station 220 (TT 222),
- Pressure drop across orifice station 220 (PDT 220, PDT 222),
- Inlet pressure of orifice station 221 (PT 223, PT 224),
- Inlet temperature of orifice station 221 (TT 223),
- Pressure drop across orifice station 221 (PDT 223, PDT 224),
- Total mass flow as calculated by LabVIEW[1],
- Bottom layer braiding profile temperatures (TT 390 to TT 408),
- Top layer braiding profile temperatures (TT 415 to TT 433).

3.4.2. *Test section*

The braiding profile temperature is measured at the two levels of measurement in the bed shown in Figure 3-6. The transverse and axial positioning of the thermocouples inside each of the three BETS packed beds will differ as the porosity changes. The three test sections with pseudo homogeneous porosities of 0.36, 0.39 and 0.45 have the following

[1] National instruments Labview version 7.1

notations BETS036, BETS039 and BETS045 respectively. The set of thermocouples at each level of measurement is collectively known as the layer of measurement.

The thermocouple installation positions inside BETS036, BETS039 and BETS045 are shown from Figure A-2 to Figure A-7 in APPENDIX A. Also shown in the figures are the distances of the axial positions for the bottom and top layers of measurement relative to the bottom of the test section.

For each BETS test section, the thermocouple designations are not the same as the designations in LabVIEW. The thermocouple designations in each test section are according to the tag numbering by the supplier. The LabVIEW designations are according to the channels that are used for the measurement transmissions. Thus for consistency the LabVIEW channel designations will be used for the thermocouple numbering as summarized in Table A-1.

The transverse positions of the various thermocouples are given in Table A-2 and Table A-3 in APPENDIX A. A negative value indicates that the thermocouple is positioned to the left of the vertical centre line as seen from the top of the test section, whilst the positive value indicates that the thermocouple is positioned to the right of the vertical centreline or on the centre line as seen from the top of the test section, as shown in Figure A-2 to Figure A-7.

The notation "over" indicates that the thermocouple is positioned above the horizontal centre line as seen from the top of the test section, whilst the notation "under" indicates that the thermocouple is positioned below the horizontal centre line as seen from the top of the test section, as shown in Table A-2 and Table A-3.

The axial or vertical positions of the layers are given in Table A-4.

3.5. Summary

The test facility that provides for the BETS experimental setup is available at the North-West University, Potchefstroom in South Africa. The HPTU plant has the main gas cycle and the cooling wate cycle, and both cyles are interconnected with the heat exchanger (Figure 3-4).

The temperature profiles are measured at two axial positions (Bottom layer thermocouples and top layer thermocouples in Figure 3-6). All the measurements under Section 3.4 of this Chapter were evaluated for uncertainy that is presented in the next chapter.

4. UNCERTAINTY ANALYSIS

4.1. Introduction

In general, uncertainty implies a parameter associated with the result of a measurement, or the combined result of several measurements that characterizes the dispersion of the values that can reasonably be expected (Van der Walt, 2008). Uncertainty is an alternative term to express error in the measurement.

According to Holman (1994) errors in a value that is being measured experimentally, can be distinguished due to two occurrences:

- **Fixed errors:** which will cause repeated readings to be in error by roughly the same amount but for some unknown reason, and
- **Random errors:** this may be caused by random electronic fluctuations in the apparatus or instruments, various influences of friction, etc.

Fixed errors are regarded as the uncertainty associated with the measuring instrument used. Random errors are regarded as the uncertainty associated with the statistical variance in the sample of measured values.

Measuring instruments were calibrated before and after a particular HPTU experimental test execution (Van Niekerk, 2008). According to the HPTU test plan, four test runs were done for each of the thirteen specified Reynolds numbers to ensure repeatability in the experimental results (Labuschagne, 2005). Due to seasonal changes, ambient conditions were not the same for all the four test runs. The ambient conditions were directly influenced by the seasonal changes which could in turn influence the measuring instruments. It was then necessary to re-calibrate the instruments between the tests which would lead to a "drift" in the measurements. This introduced another uncertainty associated with the drift analysis. The uncertainty analysis was, therefore, done on three defined uncertainties:

1) Instrument uncertainty,

2) Statistical variance, and

3) Drift uncertainty.

These uncertainties are discussed hereafter.

4.1.1. Instrument uncertainty

All secondary standard instruments were calibrated by a South African National Accreditation System (SANAS) accredited laboratory. These secondary standard instruments are used for the calibration of instruments used for experimental measurement. The HPTU instrument uncertainty was taken as the maximum between the calibrated and un-calibrated instrument uncertainty. In most cases the maximum between the two values was the un-calibrated uncertainty. Uncertainty in the secondary standard instruments was obtained from certificates supplied from the SANAS laboratory where that particular secondary standard instrument was calibrated. These uncertainties were generally given as an expanded uncertainty with a 95% confidence interval. Notation for the instrument uncertainty for a measured variable ϕ, is: $u_{Instr}(\phi)$.

4.1.2. Statistical variance

Steady-state measurements were done over a period of five minutes, whereby a measured variable was recorded twice in a second (Kaiser, 2008). This required a total of 600 data points to be measured over that period. The final measured value was the average of these 600 measured values. The standard deviation is associated with the average value of the sample. The standard deviation characterizes the dispersion of the measured variable and was used as the standard uncertainty in further calculations, to account for the statistical variance in the measured variable (Van der Walt, 2008). Notation for the statistical variance for a measured variable ϕ, is $u_{stat}(\phi)$.

4.1.3. Drift uncertainty

The calculation on the drift uncertainty is illustrated in Figure 4-1 (taken from (Van der Walt, 2008)). The actual and raw values are the measured values obtained from the secondary standard instrument and the HPTU instrument (under calibration),

respectively. Using regression, a slope and intercept could be determined in order to adjust the HPTU instrument to reflect the same measured value as the secondary standard instrument.

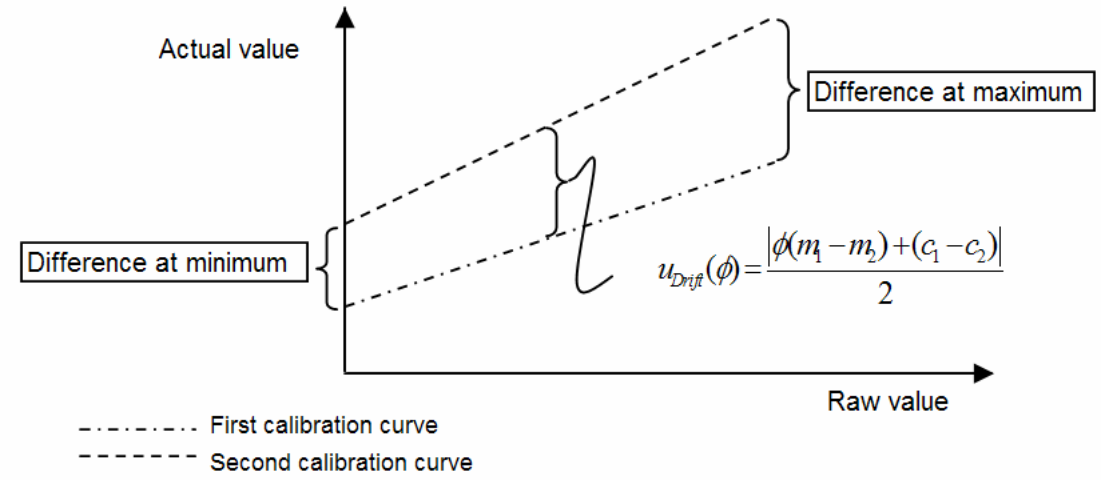

Figure 4-1: Calculation of drift uncertainty.

The actual drift uncertainty of the HPTU instrument was estimated for a coverage factor of $k_{coverage\ factor}$ = 2, which approximates a 95% confidence interval. This lead to a standard uncertainty of the drift of the HPTU instrument calculated as follows:

$$u_{Drift}(\phi)=\frac{|\phi(m_1-m_2)+(c_1-c_2)|}{2} \qquad (4.1)$$

Where:

ϕ = any variable that is a measured variable (i.e. the raw value as measured from the HPTU instrument before calibration constants are applied during experimental tests), for example pressure,

m_1 = the gradient of the previous calibration (before the test),

m_2 = the gradient of the current calibration (after the test),

c_1 = the intercept value of the previous calibration (before the test), and

c_2 = the intercept value of the current calibration (after the test).

4.2. Final uncertainty in the measured variable

The final uncertainty in the measured variable was either based on the maximum of the three stated uncertainties, or the combined effect of the three stated uncertainties.

4.2.1. Uncertainty based on the maximum values

The calculation of the final uncertainty for a measured variable ϕ, based on the maximum uncertainty of the three predefined uncertainties, is formulated as follows:

$$u(\phi)_{\max} = MAX\left(u_{Instr}(\phi), u_{Stat}(\phi), u_{Drif}(\phi)\right) \tag{4.2}$$

4.2.2. Uncertainty based on the combined effect

The calculation of the final uncertainty for a measured variable ϕ , based on the combined effect of the three predefined uncertainties, is formulated as follows:

$$u(\phi)_{comb} = \sqrt{\left[u_{Instr}(\phi)\right]^2 + \left[u_{Stat}(\phi)\right]^2 + \left[u_{Drif}(\phi)\right]^2} \tag{4.3}$$

4.3. Final uncertainty in the calculated variable

The uncertainty in a calculated variable is calculated by a procedure described by Holman (1994), with the uncertainty given by Equation (4.4).

$$w_\phi = \sqrt{\left(\frac{\partial \phi_f}{\partial x_1} u(x_1)\right)^2 + \left(\frac{\partial \phi_f}{\partial x_2} u(x_2)\right)^2 + \ldots + \left(\frac{\partial \phi_f}{\partial x_n} u(x_n)\right)^2} \tag{4.4}$$

Where:

ϕ_f = the results for a measured variable ϕ that are calculated as a function of the independent variables $x_1, x_2, \ldots, x_n$:

$$\phi_f = f(x_1, x_2, x_3, \ldots, x_n) \tag{4.5}$$

$u(x_1), u(x_2), \ldots, u(x_n)$ = the uncertainties in the independent variables $x_1, x_2, \ldots, x_n$, and

w_ϕ = the final uncertainty in the calculated variable ϕ.

It should be noted that the evaluation of the braiding effect will be based on the experimental data that was taken for four test runs. According to Kaiser (2008), repeatability was achieved for all important variables from the experimental data. Thus, the average value for four measured values was used in the CFD simulation. Therefore, the final uncertainty in the average values in the important variables was based on Equation (4.4). This method is outlined hereafter:

$$u\left(\bar{\phi}\right)=\sqrt{\left(\frac{\partial\phi_{[1]}}{\partial\bar{\phi}}\cdot u(\phi_{[1]})\right)^2+\left(\frac{\partial\phi_{[2]}}{\partial\bar{\phi}}\cdot u(\phi_{[2]})\right)^2+\left(\frac{\partial\phi_{[3]}}{\partial\bar{\phi}}\cdot u(\phi_{[3]})\right)^2+\left(\frac{\partial\phi_{[4]}}{\partial\bar{\phi}}\cdot u(\phi_{[4]})\right)^2} \quad (4.6)$$

Where,

$\bar{\phi}=\frac{\phi_{[1]}+\phi_{[2]}+\phi_{[3]}+\phi_{[4]}}{4}$ = the average value for the measured or calculated variable over the four test runs,

$\phi_{[1]}$ = the measured or calculated variable for test run 1,

$\phi_{[2]}$ = the measured or calculated variable for test run 2,

$\phi_{[3]}$ = the measured or calculated variable for test run 3,

$\phi_{[4]}$ = the measured or calculated variable for test run 4,

$\frac{\partial\phi_{[1]}}{\partial\bar{\phi}}=\frac{\partial\phi_{[2]}}{\partial\bar{\phi}}=\frac{\partial\phi_{[3]}}{\partial\bar{\phi}}=\frac{\partial\phi_{[4]}}{\partial\bar{\phi}}=\frac{1}{4}$ = the partial derivatives values, and

$u(\phi_{[1]}),u(\phi_{[2]}),u(\phi_{[3]}),u(\phi_{[4]})$ = the final uncertainties of the measured or calculated variables $\phi_{[1]},\phi_{[2]},\phi_{[3]},\phi_{[4]}$.

4.4. Uncertainties in the measured variable

The final uncertainties in the measured variables are either based on the maximum of the three stated uncertainties, or the combined effect of the three stated uncertainties.

4.4.1. Orifice stations measurements

4.4.1.1. Temperature

The statistical gas temperatures were measured at the two orifice stations for the calculation of the total mass flow rate (Figure A-1). The temperature at each orifice station was measured by one PT100 sensor:

- OR220: TT 222,
- OR221: TT 223.

The PT100 sensors had an un-calibrated uncertainty of ±0.25°C. However, the PT100 sensors were calibrated with a secondary standard instrument with an uncertainty of ±0.1°C. From Section 4.1.1 the instrument uncertainty was estimated with a coverage factor of $k_{\text{coverage factor}} = 2$ as:

- $u(T_{\text{total gas in}})_{Instr} = \frac{0.25}{2} = 0.125^{\circ} C$.

The two temperature sensors were calibrated before the tests (July 2007) and again after the tests had been performed (January 2008). The drift analysis was performed according to the procedure outlined in Van der Walt (2008). From the drift analysis performed, it was decided that the difference between the drifts at different temperatures was small enough to use the maximum drift throughout the uncertainty analysis.

Table 4-1 presents the amount of drift in the temperature that was encountered between the two calibration dates.

Table 4-1: Drift analysis of temperature sensors.

Sensor	Difference at intercept [°C]	Difference at maximum [°C]
TT222	-0.072944540	-0.053483303
TT223	0.035950839	-0.133272431

From Section 4.1.3 the drift uncertainty was estimated with a coverage factor of $k_{\text{coverage factor}} = 2$ as:

- $u(T_{or})_{drift} = \left|\frac{-0.133}{2}\right| = 0.067^{\circ} C$.

The standard variance of this temperature was incorporated in the viscosity and density calculations (*APPENDIX B: Fluid properties*) which were used for the calculations of the total mass flow rate and the overall Reynolds number. These values are summarized in

Table 4-2 and were calculated using Equation (4.6). It should be noted that all uncertainties are standard uncertainties and that when a particular orifice station is not used an "NA" is shown.

Table 4-2: Standard variances for temperature measurements at the orifice stations for all three test sections for all test runs.

	BETS036		BETS039		BETS045	
Reynolds Number	**OR220**	**OR221**	**OR220**	**OR221**	**OR220**	**OR221**
[-]	**[°C]**	**[°C]**	**[°C]**	**[°C]**	**[°C]**	**[°C]**
1000	NA	0.018	NA	0.020	NA	0.024
2000	NA	0.021	NA	0.025	NA	0.021
3000	NA	0.023	NA	0.022	NA	0.029
4000	NA	0.018	NA	0.028	NA	0.026
5000	NA	0.019	NA	0.020	NA	0.023
6000	NA	0.022	NA	0.021	NA	0.025
7000	NA	0.021	NA	0.023	NA	0.025
8000	NA	0.021	NA	0.024	NA	0.024
9000	NA	0.016	NA	0.019	NA	0.025
10000	NA	0.027	NA	0.020	NA	0.025
20000	NA	0.018	NA	0.019	NA	0.023
30000	0.023	0.019	0.023	0.020	0.023	0.022
40000	0.023	0.026	0.025	0.024	0.024	0.019

4.4.1.2. Pressure

Pressure measurements at both orifice stations were also needed for the total gas mass flow rate calculations. Two absolute pressure sensors were installed to measure the absolute gas pressure at each orifice station namely:

- OR220: PT 220, PT 221,
- OR221: PT 223, PT 224.

These instrument uncertainties were provided by the manufacturer. The two pressure sensors were calibrated with the secondary standard instruments that had the following claimed uncertainties:

- $0 < p \leq 400$ kPa ±1.6 kPa
- $400 < p \leq 6000$ kPa ±2 kPa

The maximum value between calibrated and un-calibrated instrument uncertainty was used for the final instrument uncertainty calculation. These values were estimated for a coverage factor of $k_{coverage\ factor} = 2$, which approximated a 95% confidence interval. This led to a standard instrument uncertainty of:

- $0 < p \leq 1600\,\text{kPa}$ $\quad u(p_{or})_{Instr} = \frac{1.6}{2} = 0.8kPa$
- $1600 < p \leq 6000\,\text{kPa}$ $\quad u(p_{or})_{Instr} = \frac{30}{2} = 15kPa$

The pressure sensors were calibrated while conducting the tests (in October 2007) and again after the tests had been performed (in January 2008). The drift of the pressure sensors was calculated using the procedure outlined in Van der Walt (2008). The drift was calculated at each pressure level measured because the drift varied significantly over the range of the four pressure transmitters when compared with the lowest pressure measured.

The values for the gradients and intercepts of the pressure transmitter, given at each orifice station, are shown in Table 4-3 and Table 4-4.

Table 4-3: The intercept and gradient values of the pressure sensor for OR-220.

	Current calibration constants		Previous calibrations constants	
Range [kPa]	**m_2 [kPa]**	**c_2 [kPa]**	**m_1 [kPa]**	**c_1 [kPa]**
100-1600	0.999820831	-12.71297368	1.00121224	-11.19042802
1600-5000	0.999693335	69.6847475	0.9992334	74.75435354

Table 4-4: The intercept and gradient values of the pressure sensor for OR-221.

	Current calibration constants		Previous calibrations constants	
Range [kPa]	**m_2 [kPa]**	**c_2 [kPa]**	**m_1 [kPa]**	**c_1 [kPa]**
100-1600	0.999017389	-0.03337115	1.000541094	-0.682722496
1600-5000	1.000299519	52.37266847	0.996072752	68.49996881

The final drift uncertainty $u(p_{or})_{Drift}$ at each pressure level is calculated by using Equation (4.1).

The statistical variance was also calculated with the standard deviation in the measured pressure values at the orifice stations as outlined in Section 4.1.2. It should be noted that all the uncertainties are standard uncertainties and that when a particular orifice station is not used an "NA" is shown in Table 4-5.

Table 4-5: Standard variances for pressure measurements in the orifice stations for all three test sections for all test runs.

	BETS036		BETS039		BETS045	
Reynolds Number	**OR220**	**OR221**	**OR220**	**OR221**	**OR220**	**OR221**
[-]	**[kPa]**	**[kPa]**	**[kPa]**	**[kPa]**	**[kPa]**	**[kPa]**
1000	NA	0.347	NA	0.252	NA	0.261
2000	NA	0.312	NA	0.219	NA	0.286
3000	NA	0.286	NA	0.277	NA	0.274
4000	NA	0.326	NA	0.343	NA	0.290
5000	NA	0.271	NA	0.283	NA	0.346
6000	NA	0.304	NA	0.332	NA	0.362
7000	NA	0.290	NA	0.299	NA	0.329
8000	NA	0.348	NA	0.359	NA	0.410
9000	NA	0.430	NA	0.378	NA	0.446
10000	NA	0.425	NA	0.436	NA	0.479
20000	NA	1.233	NA	1.275	NA	1.369
30000	1.718	1.474	1.558	1.329	1.717	1.493
40000	1.985	1.720	2.186	2.055	2.096	1.943

Values in Table 4-5 were calculated using Equation (4.6) for the average value over the four test runs.

4.4.1.3. Pressure drop

Pressure drop measurements across each orifice station were also needed for the total gas mass flow rate calculations. Three pressure differential transmitters were installed to measure the pressure drop across each orifice station, namely:

- OR220: PDT 220, PDT 222, PDT 224
- OR221: PDT 221, PDT 223, PDT 225

These instruments had the following ranges:

- PDT-220,221 $0 < \Delta p \leq 1\,\text{kPa}$ ±0.0015kPa
- PDT-222,223 $0 < \Delta p \leq 10\,\text{kPa}$ ±0.005kPa
- PDT-224,225 $3.5 < \Delta p \leq 50\,\text{kPa}$ ±0.025kPa

These instrument uncertainties were provided by the manufacturer. The pressure differential sensors were calibrated at a SANAS accredited laboratory, and had a claimed uncertainty of 0.4% of the measured value. The maximum value between calibrated and un-calibrated instrument uncertainty was used for the final instrument uncertainty calculation. These values were estimated for a coverage factor of $k_{\text{coverage factor}} = 2$, which approximated a 95% confidence interval. This led to a standard instrument uncertainty of:

- $u(\Delta p_{or})_{Instr} = \frac{0.4}{2} = 0.2\%$

The pressure differential sensors were calibrated while conducting the tests (in October 2007) and again after the tests had been performed (in January 2008). The drifts of the pressure sensors were calculated using the procedure outlined in Van der Walt (2008). The drift was calculated at each pressure level measured because the drift varied significantly over the range of the six pressure transmitters when compared with the lowest pressure drop measured.

The values for the gradients and intercepts of the pressure differential sensors, given at each orifice station, are shown in Table 4-6 and Table 4-7.

Table 4-6: Drift analysis of pressure differential sensors for OR 220.

Sensor	Difference at intercept [kPa]	Difference at maximum [kPa]
PDT-220	-0.000553358	-0.002909913
PDT-222	0.014580325	0.087045002
PDT-224	-0.023204702	0.217904823

Table 4-7: Drift analysis of pressure differetial sensors for OR 221.

Sensor	Difference at intercept [kPa]	Difference at maximum [kPa]
PDT-221	-0.0382949193	0.0343794400
PDT-223	0.0092970060	0.0846485699
PDT-225	0.0251671880	0.0299508620

The final drift uncertainty $u(\Delta p_{or})_{Drift}$ at each pressure level was calculated by using Equation (4.1).

The statistical variance was also calculated with the standard deviation in the measured pressure values at the orifice stations as outlined in Section 4.1.2. It should be noted that all the uncertainties are standard uncertainties and that when a particular orifice station is not used an "NA" is shown in Table 4-8.

Table 4-8: Standard variances for pressure drop measurements in the orifice stations for all three test sections for all test runs.

	BETS036		BETS039		BETS045	
Reynolds Number	**OR220**	**OR221**	**OR220**	**OR221**	**OR220**	**OR221**
[-]	**[kPa]**	**[kPa]**	**[kPa]**	**[kPa]**	**[kPa]**	**[kPa]**
1000	NA	0.002	NA	0.005	NA	0.005
2000	NA	0.003	NA	0.003	NA	0.003
3000	NA	0.003	NA	0.003	NA	0.003
4000	NA	0.004	NA	0.004	NA	0.004
5000	NA	0.003	NA	0.004	NA	0.004
6000	NA	0.004	NA	0.005	NA	0.005
7000	NA	0.005	NA	0.006	NA	0.005
8000	NA	0.006	NA	0.007	NA	0.006
9000	NA	0.006	NA	0.007	NA	0.006
10000	NA	0.016	NA	0.014	NA	0.013
20000	NA	0.017	NA	0.018	NA	0.018
30000	0.011	0.007	0.012	0.008	0.011	0.007
40000	0.020	0.018	0.019	0.018	0.018	0.015

The values in Table 4-8 were calculated from Equation (4.6) for the average value over the four test runs.

4.4.1.4. Orifice stations geometry

According to Van der Walt (2008), during the installation review of the orifice plates, twelve measurements of the pipe inside diameter were taken. The average pipe inside diameters for the two orifice plate stations D_{OrPipe} were found to be:

- OR220: D_{OrPipe} = 0.0972525 m
- OR221: D_{OrPipe} = 0.09721667 m

The standard deviations of the two pipes inside diameters were found to be:

- OR220: $u\left(D_{OrPipe}\right)$ = 4.97494E-5 m
- OR221: $u\left(D_{OrPipe}\right)$ = 2.64002E-5 m

The orifice diameters d_{or} were measured as

- OR220: d_{or} = 0.04839 ± 0.00005 m,
- OR221: d_{or} = 0.04834 ± 0.00005 m.

According to Van der Walt (2008), it is realistic to expect that orifice plates can be machined accurately to within 50 μm or 0.00005 m. It was assumed that, since the uncertainty was given without an associated confidence level, the extreme values were just as likely to occur as those close to the actual measured value. Therefore, a rectangular distribution was assumed, with a standard uncertainty of:

- $u(d_{or}) = \frac{0.00005}{\sqrt{3}} = 0.000028m$.

4.4.2. Thermal mass flow meter

The hot gas mass flow rate or the braiding mass flow rate was measured with a thermal mass flow meter (flow transmitter FT230 in Figure A-1). According to Kaiser (2008), the instrument uncertainty from the manufacturer was given as 0.6% of the measured value. It was assumed that since the uncertainty was given without an associated confidence

level, the extreme values were just as likely to occur as those close to the actual value. Therefore, a rectangular distribution was assumed, with a standard uncertainty of:

- $u\left(\dot{m}_{hot\cdot gas}\right)_{Instr} = \left(\frac{0.006}{\sqrt{3}}\right)\left(\dot{m}_{hot\cdot gas}\right) = 0.00346410162\left(\dot{m}_{hot\cdot gas}\right)^{\mathrm{kg}/\mathrm{s}}$.

The drift uncertainty in the thermal mass flow meter was taken as zero because it was only calibrated once by the manufacturer. However, an attempt was made to calibrate the instrument with one orifice station. But this method was found to be unreliable because the minimum mass flow rate that could be measured in the orifice station was 0.07 kg/s as opposed to the value for the thermal mass flow meter which was 0.0025 kg/s. This led to a significant amount of drift uncertainty of 13% which automatically increased the final uncertainty calculated for the hot gas mass flow rate.

The statistical variance was also calculated with the standard deviation of the measured mass flow rate in the thermal mass flow meter as outlined in Section 4.1.2.

The final uncertainty based on the combined effect (Equation (4.3)) for each of the test runs was considered as the conservative value for the uncertainty analysis. Therefore, the final uncertainty for the averaged value over the four test runs was calculated using Equation (4.6). These values are summarized in Table 4-9 for each of the three test sections, namely BETS036, BETS039 and BETS045.

Table 4-9: Final uncertainties of the hot gas inlet mass flow rates for all three BETS test sections.

	BETS036	BETS039	BETS045
Reynolds Number	Hot Gas	Hot Gas	Hot Gas
[-]	[kg/s]	[kg/s]	[kg/s]
1000	0.00003	0.00003	0.00003
2000	0.00003	0.00003	0.00003
3000	0.00005	0.00004	0.00005
4000	0.00007	0.00007	0.00008
5000	0.00012	0.00012	0.00008
6000	0.00013	0.00015	0.00011
7000	0.00015	0.00015	0.00017
8000	0.00016	0.00017	0.00020
9000	0.00016	0.00018	0.00022
10000	0.00022	0.00021	0.00023
20000	0.00038	0.00037	0.00032
30000	0.00084	0.00085	0.00041
40000	0.00097	0.00112	0.00054

4.4.3. Test section measurements

4.4.3.1. Cold gas temperature

The cold gas temperature at the inlet to the test sections was controlled at atmospheric temperature and measured with two PT100 sensors. The inlet temperature was calculated from:

$$T_{\text{cold gas in}} = \frac{T_{200} + T_{201}}{2} \tag{4.7}$$

The PT100 sensors had an un-calibrated uncertainty of ±0.25°C. However, the PT100 sensors were calibrated with a secondary standard instrument with an uncertainty of ±0.1°C. From Section 4.1.1 the instrument uncertainty was estimated with a coverage factor of $k_{\text{cov}erage\ factor} = 2$ as:

- $u(T_{\text{cold gas in}})_{Instr} = \frac{0.25}{2} = 0.125^{\circ}C$.

The two temperature sensors were calibrated before the tests (July 2007) and again after the tests had been performed (January 2008). The drift analysis was performed according to the procedure outlined in Van der Walt (2008). From the drift analysis performed, it was decided that the difference between the drifts at different temperatures was small enough to use the maximum drift throughout the uncertainty analysis.

Table 4-10 presents the amount of drift in the temperature that was encountered between the two calibration dates.

Table 4-10: Drift analysis of temperature sensors.

Sensor	Difference at intercept [°C]	Difference at maximum [°C]
TT200	-0.0133100	-0.2792639
TT201	-0.0460387	-0.2130353

From Section 4.1.1 the drift uncertainty was estimated with a coverage factor of $k_{coverage\ factor} = 2$ as:

- $u(T_{\text{cold gas in}})_{Drift} = \left|\frac{\text{-0.279}}{2}\right| = 0.140^{\circ}C$

Test section inlet temperature $T_{\text{test section in}}$ was recorded and used according to Equation (4.7), Therefore, the final uncertainty in the calculated variable can be estimated by using Holman (1994) (Equation (4.4)):

$$u(T_{\text{cold gas in}}) = \sqrt{\left(\frac{\partial T}{\partial T_{201}} \cdot u(T_{201})\right)^2 + \left(\frac{\partial T}{\partial T_{200}} \cdot u(T_{200})\right)^2} \tag{4.8}$$

Where:

$\frac{\partial T_{\text{test section in}}}{\partial T_{201}} = \frac{1}{2}$ = partial derivatives values from Equation (4.7),

$\frac{\partial T_{\text{test section in}}}{\partial T_{200}} = \frac{1}{2}$ = partial derivatives values from Equation (4.7), and

$u(T_{200}), u(T_{201})$ = uncertainties for measured temperatures with PT100 sensors: TT200 and TT201.

To encompass all the influences of the statistical variance in the uncertainty, Equation (4.9) was used to calculate the overall results:

$$u(T_{\text{cold gas in}})_{Stat} = MAX\left(\sqrt{\left(\frac{\partial T_{\text{cold gas in}}}{\partial T_{201}} \cdot u(T_{201})_{Stat}\right)^2 + \left(\frac{\partial T_{\text{cold gas in}}}{\partial T_{200}} \cdot u(T_{200})_{Stat}\right)^2}, u(T_{201})_{Stat}, u(T_{201})_{Stat}\right)$$

(4.9)

Where:

$u\left(T_{\text{cold gas in}}\right)_{Stat}$ = standard deviation in the recorded averages in the gas temperature measurements (Equation (4.7)),

$u(T_{200})_{Stat}$, $u(T_{201})_{Stat}$ = standard deviation for temperatures measured with PT100 sensors: TT200 and TT201.

The average value of the cold gas temperature $\overline{T}_{\text{cold gas in}}$ for all four test runs was used for the CFD simulation. Therefore, the final uncertainty was calculated using Equation (4.6). To be conservative in this step, the combined effect uncertainty in each cold gas temperature $T_{\text{cold gas in}}$ for each test run was used in the equation. These values were converted to the standard uncertainty percentage by dividing the final standard uncertainty (Equation (4.6)) with their respective averaged cold gas temperatures, i.e.:

- $\dfrac{u(T_{\text{cold gas in}})_{Final}}{\overline{T}_{\text{cold gas in}}} \times 100 \quad [\%]$
- $u(T_{\text{cold gas in}})_{Final}$ is calculated from Equation (4.6).

These values are summarized in Table 4-11 for each of the three test sections, namely BETS036, BETS 039 and BETS045.

Table 4-11: Final uncertainties of the cold gas inlet temperatures for all three BETS test sections.

	BETS036	BETS039	BETS045
Reynolds Number	Cold Gas	Cold Gas	Cold Gas
[-]	[%]	[%]	[%]
1000	0.647	0.583	0.572
2000	0.649	0.617	0.647
3000	0.693	0.627	0.659
4000	0.669	0.592	0.661
5000	0.708	0.618	0.660
6000	0.706	0.621	0.682
7000	0.709	0.621	0.686
8000	0.689	0.623	0.682
9000	0.666	0.626	0.680
10000	4.010	3.230	3.831
20000	0.654	0.598	0.700
30000	0.642	0.583	0.701
40000	0.610	0.562	0.717

The large value seen in the final uncertainties at the Reynolds number of 10000 was as a result of the large standard deviation values of the measured values from the TT201 thermocouple (Kaiser, 2008). A common experimental procedure about this measurement was that it was done while going up between the sytem pressures, i.e. for Test run 1 and Test run 3. The overall maximum and minimum final uncertainties of the BETS inlet cold gas temperature measurements were 4.010 % and 0.562 %, respectively.

4.4.3.2. Hot gas temperature

The hot gas inlet temperature measurement was performed with a thermocouples (TE 230) for which the un-calibrated uncertainty is given as ±1 °C. However, the thermocouple was calibrated at SANAS accredited laboratory to an uncertainty of ±0.6 °C (details in Kaiser (2008)).

As explained before, the instrument uncertainty was estimated with a coverage factor of $k_{coverage\ factor}$ = 2, which was the maximum between the calibrated and un-calibrated uncertainty:

- $u\left(T_{\text{Hot gas in}}\right)_{Instr} = \frac{1.0}{2} = 0.5°C$.

This thermocouple was also calibrated before the tests (July 2007) and again after the tests had been performed (January 2008). The drift analysis was performed according to the procedure outlined (Van der Walt, 2008).

The drift analysis was performed in a similar way as for the PT100 sensors. The maximum absolute value of the drift of all the temperature loops that were used in the braiding experiment was taken as the drift value for TE230 (Kaiser, 2008).

The uncertainties of the drift measurements were estimated for a coverage factor of $k_{coverage\ factor} = 2$, which approximates a 95% confidence interval. This leads to a standard uncertainty of the instrumentation drift calculated as:

- $u\left(T_{\text{Hot gas in}}\right)_{Drift} = \frac{0.777}{2} = 0.389^{\circ}C$

The statistical variance for the hot gas temperature recorded with this thermocouple was calculated by using a standard deviation from the recorded results as explained in Section 4.1.2.

The average value of the hot gas temperature $\overline{T}_{\text{Hot gas in}}$ for all four test runs was used for the CFD simulation. Therefore, the final uncertainty was calculated using Equation (4.6). To be conservative in this step, the combined effect uncertainty in each hot gas temperature $T_{\text{Hot gas in}}$ at each test run was used in the equation. These values are converted to the standard uncertainty percentage by dividing the final standard uncertainty (Equation (4.6)) with their respective averaged hot gas temperatures, i.e.:

- $\frac{u(T_{\text{Hot gas in}})_{Final}}{\overline{T}_{\text{Hot gas in}}} \times 100 \quad [\%]$
- $u(T_{\text{Hot gas in}})_{Final}$ is calculated from Equation (4.6).

These values are summarized in Table 4-12 for each of the three test sections, namely BETS036, BETS 039 and BETS045.

Table 4-12: Final uncertainties of the hot gas inlet temperatures for all three BETS test sections.

	BETS036	BETS039	BETS045
Reynolds Number	Hot Gas	Hot Gas	Hot Gas
[-]	[%]	[%]	[%]
1000	0.570	0.554	0.546
2000	0.570	0.543	0.565
3000	0.560	0.550	0.595
4000	0.559	0.553	0.600
5000	0.567	0.582	0.634
6000	0.576	0.597	0.692
7000	0.571	0.578	0.741
8000	0.572	0.571	0.734
9000	0.568	0.564	0.729
10000	0.565	0.551	0.708
20000	0.556	0.545	0.608
30000	0.562	0.549	0.620
40000	0.572	0.554	0.624

The overall maximum and minimum final uncertainties of the BETS inlet hot gas temperature measurements are 0.741 % and 0.543 % respectively.

4.4.3.3. Gas pressure

Two absolute pressure sensors were installed to measure the absolute gas pressure in the test sections namely:

- PT-200 $0 < p \leq 1600$ kPa ±1.6 kPa
- PT-201 $0 < p \leq 6000$ kPa ±30 kPa

These instrument uncertainties were provided by the manufacturer. The two pressure sensors were calibrated with the secondary standard instruments that had the following claimed uncertainties:

- $0 < p \leq 400$ kPa ±1 kPa
- $400 < p \leq 6000$ kPa ±2 kPa

The maximum value between calibrated and un-calibrated instrument uncertainty was used for the final instrument uncertainty calculation. These values were estimated for a coverage factor of $k_{coverage\ factor} = 2$, which approximated a 95% confidence interval. This lead to a standard instrument uncertainty of:

- $0 < p \leq 1600$ kPa $u(p)_{Instr} = \frac{1.6}{2} = 0.8\ kPa$
- $1600 < p \leq 6000$ kPa $u(p)_{Instr} = \frac{30}{2} = 15\ kPa$

The pressure sensors were calibrated while conducting the tests (in October 2007) and again after the tests had been performed (in January 2008). The drifts of the pressure sensors were calculated using the procedure outlined in Van der Walt (2008). The drift was calculated at each pressure level measured because the drift varied significantly over the range of the two pressure transmitters when compared with the lowest pressure measured.

The values for the gradients and intercepts of the pressure transmitters are given in Table 4-13.

Table 4-13: The intercept and gradient values of the pressure indicators.

	Current calibration constants		Previous calibrations constants	
Range kPa]	**m_2 [kPa]**	**c_2 [kPa]**	**m_1 [kPa]**	**c_1 [kPa]**
0-1600	0.999510519	0.008919963	1.000386136	0.384088217
1600-5000	0.999500229	3.105728458	0.998723404	4.198001902

The final drift uncertainty $u(p)_{Drift}$ at each pressure level was calculated using Equation (4.1).

The statistical variance was also calculated with the standard deviation in the measured pressure values as outlined in Section 4.1.2. For the CFD simulation, the average pressure of the four test runs was used; therefore, the final uncertainty calculation was formulated by using Equation (4.6). These values were converted to the standard uncertainty percentage by dividing the final standard uncertainty (using Equation (4.6)) with their respective averaged pressures, i.e.:

- $\frac{u(p)_{Final}}{\overline{p}} \times 100 \quad [\%]$,
- $u(p)_{Final}$ is calculated using Equation (4.6).

These values are summarized in Table 4-14 for each of the three test sections, namely BETS036, BETS039 and BETS045.

Table 4-14: Final standard uncertainties of the total gas inlet pressures for all three BETS test sections.

	BETS036	BETS039	BETS045
Reynolds Number	Total Gas	Total Gas	Total Gas
[-]	[%]	[%]	[%]
1000	0.442	0.440	0.444
2000	0.234	0.252	0.240
3000	0.160	0.155	0.157
4000	0.121	0.120	0.123
5000	0.099	0.099	0.105
6000	0.088	0.092	0.090
7000	0.076	0.077	0.079
8000	0.070	0.072	0.071
9000	0.065	0.064	0.064
10000	0.060	0.061	0.063
20000	0.378	0.379	0.379
30000	0.255	0.254	0.254
40000	0.202	0.202	0.202

The overall maximum and minimum final uncertainties of the BETS inlet gas pressure measurements are 0.444 % and 0.06 % respectively.

4.4.3.4. Braiding temperature profile

The braiding temperature profile measurements were obtained with the thermocouples indicated in Figure A-2 to Figure A-7 for which the un-calibrated uncertainty was given as ±1 °C. However, the thermocouples were calibrated at a SANAS accredited laboratory to an uncertainty of ±0.6 °C (details in Kaiser (2008)).

The braiding thermocouples were originally calibrated from 50 °C to 80 °C. After the installation of the thermocouples in the bed, it was noticed that the calibration range was too high. Consequently, the thermocouples were recalibrated with a curve fit method using the test section inlet and outlet temperature measurements as secondary standard instruments.

The maximum difference between the actual (PT100s) and displayed temperature (Braiding temperature thermocouples) was used as the curve fit uncertainty for the thermocouples. The maximum uncertainties for the calibration curves of all the

thermocouples were calculated and are summarized in Table 4-15 for all three test sections. These values are given with a coverage factor of $k_{coverage\ factor} = \sqrt{3}$, which is a rectangular confidence distribution.

Table 4-15: Curve fit uncertainties for the braiding temperature profile thermocouples for all three BETS test sections.

Curve fit uncertainty		
BETS036	**BETS039**	**BETS045**
[°C	**[°C]**	**[°C]**
0.289	0.886	1.221

The maximum difference between the calibrated (curve-fitting uncertainties) and the un-calibrated uncertainties as the final instrument uncertainties are summarized in Equation (4.10) for all three test sections. The uncertainties were estimated with a coverage factor of $k_{coverage\ factor} = 2$, which approximated 95% confidence interval.

$$\begin{aligned} u\left(\left(T_{\text{braiding profile}}\right)_{BETS036}\right)_{Instr} &= \frac{1}{2} = 0.5\ °C \\ u\left(\left(T_{\text{braiding profile}}\right)_{BETS039}\right)_{Instr} &= \frac{1}{2} = 0.5\ °C \\ u\left(\left(T_{\text{braiding profile}}\right)_{BETS045}\right)_{Instr} &= \frac{1.221}{2} = 0.6105\ °C \end{aligned} \tag{4.10}$$

The braiding profile thermocouples were calibrated before the tests (in July 2007) and again after the tests had been performed (in January 2008). The drift of each thermocouple was calculated using the procedure outlined in Van der Walt (2008). To be conservative in the drift analysis a maximum value for all 19 thermocouples was used as the final drift uncertainty (Kaiser, 2008).

The uncertainties of the drift measurement were estimated for a coverage factor of $k_{coverage\ factor} = 2$, which approximates a 95% confidence interval. This lead to a standard uncertainty of the instrumentation drift which was calculated for all three BETS test sections in Equation (4.11).

$$u\left(\left(T_{\text{braiding profile}}\right)_{BETS036}\right)_{Drift} = \frac{1.334}{2} = 0.667^{\circ}C$$
$$u\left(\left(T_{\text{braiding profile}}\right)_{BETS039}\right)_{Drift} = \frac{1.5}{2} = 0.750^{\circ}C \qquad (4.11)$$
$$u\left(\left(T_{\text{braiding profile}}\right)_{BETS045}\right)_{Drift} = \frac{1.385}{2} = 0.692^{\circ}C$$

The average value of the braiding temperature profile $\overline{T}_{\text{braiding profile}}$ for all four test runs was used for the CFD simulation. Therefore, the final uncertainty was calculated using Equation (4.6). To be conservative in this step, the combined effects uncertainty in each of the braiding temperature profile $\overline{T}_{\text{braiding profile}}$ at each test run was used in the equation. These values were converted to the standard uncertainty percentage by dividing the final standard uncertainty (Equation (4.6)) with their respective averaged hot gas temperatures, i.e.:

- $\frac{u\left(\overline{T}_{\text{braiding profile}}\right)_{Final}}{\overline{T}_{\text{braiding profile}}} \times 100 \quad [\%]$
- $u\left(\overline{T}_{\text{braiding profile}}\right)_{Final}$ was calculated from Equation (4.6).

These values are summarized in Table C- 1 to Table C- 6 for each of the three test sections, namely BETS036, BETS039 and BETS045 and range between 1.5 % and 10.508 % for the three test sections. These values are referenced to the transverse positioning of their respective thermocouples inside the bed. These transverse positions can be referenced to the particular thermocouple in Table A-2 and Table A-3.

4.4.3.5. Test section geometry

Figure 4-2 shows the BETS packing structure geometry.

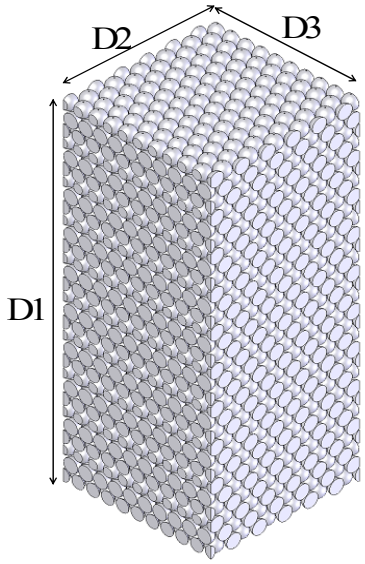

Figure 4-2: BETS packed structure geometry (Kaiser, 2008).

The inlet flow area for both hot and cold gas is shown in Figure 4-3.

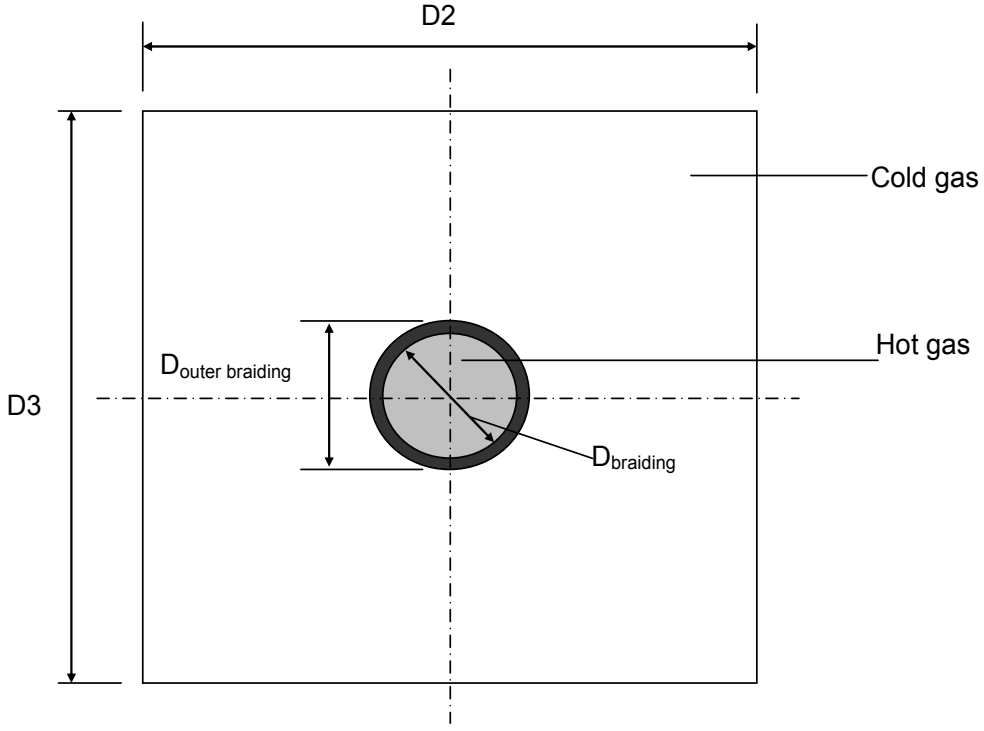

Figure 4-3: Inlet flow cross-section.

Table 4-16 gives a summary of the indicated dimensions of the packed bed geometry with their respective porosities.

Table 4-16: Summary of the BETS test section geometric data.

Geometry	Test Section		
	BETS036	BETS039	BETS045
Porosity [-]	0.352	0.389	0.448
D1 [mm]	741.1	756.46	781.7
D2 [mm]	300	300	300
D3 [mm]	300	300	300
$D_{braiding}$[mm]	77	77	77
$D_{outer\ braiding}$[mm]	79.58	79.58	79.58
Pebble diameter [mm]	28.575	28.575	28.575

The width $D2$ has an uncertainty of 0.025 mm. It was assumed that since the uncertainty was given without an associated confidence interval, the extreme values were just as likely to occur as those close to the actual measured value. Therefore, a rectangular distribution was assumed, with a standard uncertainty of:

- $u(D2) = \frac{0.000025}{\sqrt{3}} = 1.443E-5$ m

The depth $D3$ was calculated as follows:

$$D3 = D3' - 2 \cdot d_1 \tag{4.12}$$

Where:

$D3'$ = the full length (302.975 mm) of the back plate with an uncertainty of 0.025 mm (refer to Figure A-2 to Figure A-7),

d_1 = the width of the two plates (1.525 mm) placed perpendicular on the back plate. The uncertainty of the plate thickness is 0.025 mm.

The uncertainty for the calculated height $D3$ was determined as follows when a rectangular distribution was assumed:

$$
\begin{aligned}
u(D3) &= \sqrt{\left(\frac{\partial D3}{\partial D3'}\cdot u(D3')\right)^2 + \left(\frac{\partial D3}{\partial d_1}\cdot u(d_1)\right)^2} \\
&= \sqrt{\left((1)\cdot\left(\frac{0.025}{\sqrt{3}}\right)\right)^2 + \left((-2)\cdot\left(\frac{0.025}{\sqrt{3}}\right)\right)^2} \\
&= 3.228E-5 \text{ m}
\end{aligned}
\tag{4.13}
$$

The uncertainty in the length of the bed was calculated from the total number of spheres and spacers on a string. The packing structure was made of balls that were attached to these strings. The number of balls and spacers on a string were 10 balls and 9 spacers (Kaiser, 2008).

The length $D1$ was calculated as follows:

$$D1 = n\cdot D_p + j\cdot s \tag{4.14}$$

Where:

D_p = the diameter (28.575 mm) of the packed spheres (poly-vinyl chloride (acryline) balls); the balls were machined accurately to within 0.01 mm,

n = the number of spheres in a string,

j = the number of spacers, and

s = the length of the spacers; the spacers were machined accurately to within 0.05 mm.

The uncertainty for the calculated height $D1$ was determined as follows when a rectangular distribution was assumed:

$$
\begin{aligned}
u(D1) &= \sqrt{\left(\frac{\partial D1}{\partial d_p}\cdot u(d_p)\right)^2 + \left(\frac{\partial D1}{\partial s}\cdot u(s)\right)^2} \\
&= \sqrt{\left(n\cdot u(d_p)\right)^2 + \left(j\cdot u(s)\right)^2} \\
&= \sqrt{\left(10\cdot\frac{0.00001}{\sqrt{3}}\right)^2 + \left(9\cdot\frac{0.00005}{\sqrt{3}}\right)^2} \\
&= 2.661E-4 \text{ m}
\end{aligned}
\tag{4.15}
$$

The calculated uncertainties in Equations (4.12) and (4.15) are for the packing structures for all three BETS test sections.

The test section cross-sectional area $A_{test\ section}$ is calculated as follows (from Figure 4-2):

$$A_{test\ section} = D2 \cdot D3 \tag{4.16}$$

The uncertainty for the calculated test section cross-sectional area $A_{test\ section}$ was determined as follows:

$$\begin{aligned} u\left(A_{test\ section}\right) &= \sqrt{\left(\frac{\partial A_{test\ section}}{\partial D2}\cdot u\left(D2\right)\right)^2 + \left(\frac{\partial A_{test\ section}}{\partial D3}\cdot u\left(D3\right)\right)^2} \\ &= \sqrt{\left(D2\cdot u\left(D2\right)\right)^2 + \left(D3\cdot u\left(D3\right)\right)^2} \\ &= \sqrt{\left(0.299925\cdot 1.443E-5\right)^2 + \left(0.299975\cdot 3.228E-5\right)^2} \\ &= 1.060E-5\ \mathrm{m}^2 \end{aligned} \tag{4.17}$$

The average porosity was calculated using SolidWorks 2005 in which the drawings were compiled. There was, however, an uncertainty associated with the porosity of the actual test section. The porosity of the bed is defined as follows:

$$\overline{\varepsilon} = 1 - \frac{n_p \cdot V_p}{V_{test\ section}} \tag{4.18}$$

Where:

$V_p = \frac{4}{3}\pi D_p^3$ = volume of the packed spherical balls,

n_p = number of packed spherical balls in the test section, and

$V_{test\ section} = A_{test\ section} \cdot D1$ = volume of the test section.

The uncertainty of the calculated average porosity $\overline{\varepsilon}$ is determined as follows:

$$u\left(\overline{\varepsilon}\right) = \sqrt{\left(\frac{\partial \overline{\varepsilon}}{\partial n_p}\cdot u\left(n_p\right)\right)^2 + \left(\frac{\partial \overline{\varepsilon}}{\partial V_p}\cdot u\left(V_p\right)\right)^2 + \left(\frac{\partial \overline{\varepsilon}}{\partial V_{test\ section}}\cdot u\left(V_{test\ section}\right)\right)^2} \tag{4.19}$$

The first term in Equation (4.19) is equal to zero (0) since the number of balls in the test section is exactly determined according to the SolidWorks 2005 drawings.

The uncertainty of the calculated volume of the ball V_p was determined as follows when a rectangular distribution was assumed:

$$\begin{aligned} u\left(V_p\right) &= \sqrt{\left(\frac{\partial V_p}{\partial d_p}\cdot u\left(D_p\right)\right)^2} \\ &= \left(\left(4\cdot\pi\cdot 0.028575^2\right)\cdot\left(\frac{0.00001}{\sqrt{3}}\right)\right) \\ &= 3.949E-8\ \mathrm{m}^3 \end{aligned} \tag{4.20}$$

The uncertainty of the calculated volume of the test section $V_{test\ section}$ was determined as follows when a rectangular distribution was assumed:

$$\begin{aligned} u\left(V_{test\ section}\right) &= \sqrt{\left(\frac{\partial V_{test\ section}}{\partial A_{test\ section}}\cdot u\left(A_{test\ section}\right)\right)^2 + \left(\frac{\partial V_{test\ section}}{\partial D1}\cdot u\left(D1\right)\right)^2} \\ &= \sqrt{\left(D1\cdot u\left(A_{test\ section}\right)\right)^2 + \left(A_{test\ section}\cdot u\left(D1\right)\right)^2} \\ &= \sqrt{1.1236E-10\cdot D1^2 + 5.731E-10} \end{aligned} \tag{4.21}$$

Therefore, incorporating Equations (4.20) and (4.21) into Equations (4.19) lead to the following formulation of the average porosity $\bar{\varepsilon}$ which was dependent on the length of the bed:

$$\begin{aligned} u\left(\bar{\varepsilon}\right) &= \sqrt{\left(\frac{\partial \bar{\varepsilon}}{\partial n_p}\cdot u\left(n_p\right)\right)^2 + \left(\frac{\partial \bar{\varepsilon}}{\partial V_p}\cdot u\left(V_p\right)\right)^2 + \left(\frac{\partial \bar{\varepsilon}}{\partial V_{test\ section}}\cdot u\left(V_{test\ section}\right)\right)^2} \\ &= \sqrt{\left(-\frac{n_p}{V_{test\ section}}\cdot u\left(V_p\right)\right)^2 + \left(\frac{n_p\cdot V_p}{V_{test\ section}^2}\cdot u\left(V_{test\ section}\right)\right)^2} \end{aligned} \tag{4.22}$$

Incorporating the necessary values from Table 4-16 in Equation (4.22) lead to the following uncertainties for the average porosity in each test section:

$$\begin{aligned} u\left(\bar{\varepsilon}\right)_{BETS036} &= 0.0019427 \\ u\left(\bar{\varepsilon}\right)_{BETS039} &= 0.0017002 \\ u\left(\bar{\varepsilon}\right)_{BETS045} &= 0.0016440 \end{aligned} \tag{4.23}$$

4.4.3.6. Braiding temperature profile thermocouple positioning

The braiding temperature profile thermocouple positioning was important because this will ensure that a consistent measurement over the four test runs was achieved. The transverse and vertical positions of the thermocouples are shown in Table A-2, Table A-3 and Table A-4. No tolerance was given with regard to this values but according to Kaiser (2008), it is realistic to expect that during installation an error of 5 mm [2] in the position could have been made. It was, therefore, assumed that, since the uncertainty was given without an associated confidence interval, the extreme values were just as likely to occur as those close to the actual measured value. Therefore, a rectangular distribution was assumed, with a standard uncertainty of:

- $u(D1_{top}) = u(D1_{bottom}) = \frac{0.005}{\sqrt{3}} = 2.89E-3$ m
- $u(r) = \frac{0.005}{\sqrt{3}} = 2.89E-3$ m

Where:

r = depicts a transverse position as measured in the test section.

$D1_{top}$ = depicts vertical position for top layer thermocouples in Figure 3-6.

$D1_{bottom}$ = depicts vertical position for the bottom layer thermocouples in Figure 3-6.

4.5. Uncertainties in the derived variables

4.5.1. Inflow area

4.5.1.1. Hot gas inflow area

The hot gas inflow area is indicated in Figure 4-3 and is calculated as follows:

$$A_{hot \cdot gas} = \frac{\pi D_{hot \cdot gas}^2}{4} \tag{4.24}$$

The hot gas diameter (braiding line inside diameter in Figure 3-5) i.e. $D_{hot \cdot gas}$ is:

[2] From a conversation with R de Bruyn, the engineer who was responsible for the manufacturing of the test sections

- $D_{hot\cdot gas} = 77 \pm 0.05\,mm$

It was assumed that since the uncertainty was given without an associated confidence level that the extreme values were just as likely to occur as those close to the actual value. Therefore, a rectangular distribution was assumed, with a standard uncertainty of:

- $u\left(D_{hot\cdot gas}\right) = \dfrac{0.00005}{\sqrt{3}} = 2.88675\text{E-}05$ m

Therefore, the uncertainty for the calculated hot gas inflow area $A_{hot\cdot gas}$ was determined as follows when a rectangular distribution was assumed:

$$\begin{aligned} u\left(A_{hot\cdot gas}\right) &= \sqrt{\left(\frac{\partial A_{hot\cdot gas}}{\partial D_{hot\cdot gas}} u\left(D_{hot\cdot gas}\right)\right)^2} \\ &= \left(\frac{\partial A_{hot\cdot gas}}{\partial D_{hot\cdot gas}} u\left(D_{hot\cdot gas}\right)\right) \\ &= \frac{2\pi}{4} D_{hot\cdot gas} \cdot u\left(D_{hot\cdot gas}\right) \\ &= \frac{\pi}{2}\left(\frac{77}{1000}\right)\left(2.8867\,E-05\right) \\ &= 3.4915\text{E-}06 \text{ m}^2 \end{aligned} \tag{4.25}$$

4.5.1.2. Cold gas inflow area

The cold gas inflow area is indicated in Figure 4-3 and was calculated as follows:

$$A_{cold\cdot gas} = A_{test\,section} - A_{hot\cdot gas} \tag{4.26}$$

Therefore, the uncertainty for the calculated cold gas inflow area $A_{cold\cdot gas}$ was determined as follows when a rectangular distribution was assumed:

$$\begin{aligned} u\left(A_{cold\cdot gas}\right) &= \sqrt{\left(\frac{\partial A_{cold\cdot gas}}{\partial A_{test\,section}} \cdot u\left(A_{test\,section}\right)\right)^2 + \left(\frac{\partial A_{cold\cdot gas}}{\partial A_{hot\,gas}} \cdot u\left(A_{hot\,gas}\right)\right)^2} \\ &= \sqrt{\left(1 \cdot 1.06054E\text{-}05\right)^2 + \left(-1 \cdot 7.21711E\text{-}07\right)^2} \\ &= 1.063E\text{-}05 \text{ m}^2 \end{aligned} \tag{4.27}$$

4.5.2. Fluid properties

Fluid properties were calculated from the temperature and pressure measurements. For this analysis the following fluid properties are important:

1) Density
2) Viscosity

These properties were obtained by fitting curves through REFPROP[3] data for temperature ranges between 10°C and 90°C while varying the pressure from 100 kPa to 5000 kPa. This method is outlined in *APPENDIX B: Fluid properties*.

For any one of the two mentioned fluid properties ϕ, the final uncertainty is calculated by Equation (4.4):

$$u\left[\phi\left(p,T\right)\right]=\sqrt{\left(\frac{\partial\phi}{\partial p}\cdot u\left(p\right)\right)^2+\left(\frac{\partial\phi}{\partial T}\cdot u\left(T\right)\right)^2} \tag{4.28}$$

For the BETS experiments, the stated fluid properties are used to calculate the following variables:

1. The cold and hot gases inlet mass flow rates ($\dot{m}_{cold\ gas}$ and $\dot{m}_{hot\ gas}$ respectively),
2. The cold and hot gases inlet velocities ($V_{cold\ gas}$ and $V_{hot\ gas}$ respectively), and
3. The total gas Reynolds number ($Re_{total\ gas}$).

4.5.3. Gas mass flow rate

4.5.3.1. Total gas mass flow rate

The total gas mass flow rate is based on the Reynolds number ($Re_{total\ gas}$) required at the inlet of the test section, and is calculated from the following equation:

$$\dot{m}_{total\ gas}=\frac{C\varepsilon}{\sqrt{1-\beta^4}}\frac{\pi}{4}d_{or}^2\sqrt{2\rho_1\Delta p_{or}} \tag{4.29}$$

Where the discharge coefficient C is formulated as follows (Van der Walt, 2008):

[3] REFPROP – Reference Fluid Thermodynamic and Transport Properties, NIST Standard Reference database 23, Version 7.

$$C = 0.5961 + 0.0261 \cdot \beta^2 - 0.216 \cdot \beta^8 + 0.000521 \cdot \left(\frac{10^6 \cdot \beta}{\mathrm{Re}_D} \right)^{0.7} + \left(0.0188 + 0.0063 A' \right) \cdot \beta^{3.5} \cdot \left(\frac{10^6}{\mathrm{Re}_D} \right)^{0.3}$$

with:

- $A' = \left(\frac{19000 \cdot \beta}{\mathrm{Re}_D} \right)^{0.8}$,
- $\beta = \frac{d_{or}}{D_{OrPipe}}$ = orifice station ratio (measurements thereof are explained in Section 4.4.1.4),
- Re_D = the pipe Reynolds number,

The expansion factor ε is calculated as:

$$\varepsilon = 1 - \left(0.351 + 0.256 \cdot \beta^4 + 0.93 \cdot \beta^8 \right) \cdot \left[1 - \left(\frac{p_2}{p_1} \right)^{1/\kappa} \right]$$

with:

- $\frac{p_2}{p_1}$ = ratio of the static pressure; measured downstream to the orifice plate (p_2) and measured upstream to the orifice plate (p_1),
- $\kappa = \frac{c_p}{c_v}$ = isentropic expansion ratio.

The fluid density ρ_1 is calculated using the correlations in *APPENDIX B: Fluid properties* with the use of the orifice station measurements measured at the downstream (Section 4.4.1). The pressure drop across the orifice plate was measured as explained in Section 4.4.1.

According to Van der Walt (2008) the standard uncertainty percentage in the total mass flow rate (4.29) is formulated as follows:

$$\frac{u(\dot{m}_{total\,gas})}{\dot{m}_{total\,gas}} = \sqrt{\left(\frac{u(C)}{C} \right)^2 + \left(\frac{u(\varepsilon)}{\varepsilon} \right)^2 + \left(\frac{2\beta^4}{1-\beta^4} \right)^2 \cdot \left(\frac{u(D_{OrPipe})}{D_{OrPipe}} \right)^2 + \left(\frac{2}{1-\beta^4} \right)^2 \left(\frac{u(d_{or})}{d_{or}} \right)^2 + \frac{1}{4} \left(\frac{u(\Delta p_{or})}{\Delta p_{or}} \right)^2 + \frac{1}{4} \left(\frac{u(\rho_1)}{\rho_1} \right)^2} \qquad (4.30)$$

Where:

$\frac{u(C)}{C}$ = 1.0% for $0.2 \leq \beta \leq 0.6$. The value used in the uncertainty analysis, however, is 1 % since an additional 0.5 % was added after the orifice installation review,

$\frac{u(\varepsilon)}{\varepsilon}$ = $3.5\frac{\Delta p}{\kappa \cdot p_1}$% (The uncertainty of the expansion factor),

$\frac{u(D_{OrPipe})}{D_{OrPipe}}$ = the orifice pipe diameter standard uncertainty percentage,

$\frac{u(d_{or})}{d_{or}}$ = the orifice plate diameter standard uncertainty percentage,

$\frac{u(\Delta p_{or})}{\Delta p_{or}}$ = the pressure drop across the orifice plate standard uncertainty percentage, and

$\frac{u(\rho_1)}{\rho_1}$ = the density standard uncertainty percentage.

The final uncertainty based on the combined effect (Equation (4.3)) for each of the test runs was considered as the conservative value for the uncertainty analysis. Therefore, the final uncertainty for the averaged value over the four test runs was calculated using Equation (4.6). These values were converted to the standard uncertainty percentage by dividing the final uncertainty using Equation (4.6) with their respective averaged total gas mass flow rates over the four test runs, i.e.:

- $\frac{u(\dot{m}_{total\,gas})_{Final}}{\dot{m}_{total\,gas}} \times 100 \quad [\%]$
- $u(\dot{m}_{total\,gas})_{Final}$ is calculated using Equation (4.6).

These percentage values are summarized in Table 4-17 for each of the three test sections, namely BETS036, BETS039 and BETS045.

Table 4-17: Final uncertainty percentages of the total gas inlet mass flow rates for all three BETS test sections.

	BETS036	BETS039	BETS045
Reynolds Number	Total Gas	Total Gas	Total Gas
[-]	[%]	[%]	[%]
1000	0.903	0.915	0.793
2000	0.761	0.757	0.763
3000	0.634	0.630	0.633
4000	0.582	0.579	0.581
5000	0.556	0.555	0.556
6000	0.541	0.541	0.542
7000	0.533	0.533	0.533
8000	0.527	0.527	0.528
9000	0.523	0.523	0.524
10000	0.524	0.521	0.519
20000	0.545	0.484	0.546
30000	0.386	0.386	0.387
40000	0.394	0.393	0.392

The overall maximum and minimum final uncertainty percentages of the BETS inlet total gas mass flow rate measurements are 0.915 % and 0.386 %, respectively.

4.5.3.2. Cold gas mass flow rate

The total mass flow rate is the sum of both the hot gas and cold gas mass flow rates ($\dot{m}_{cold\ gas}$ and $\dot{m}_{hot\ gas}$). Therefore, the cold gas mass flow rate was calculated as follows:

$$\dot{m}_{cold\ gas} = \dot{m}_{total\ gas} - \dot{m}_{hot\ gas} \tag{4.31}$$

The associated standard uncertainty in the cold gas mass flow rate $\dot{m}_{cold\ gas}$ was calculated from Equation (4.4) as follows:

$$u\left(\dot{m}_{cold\ gas}\right) = \sqrt{\left(\frac{\partial \dot{m}_{cold\ gas}}{\partial \dot{m}_{total\ gas}} u\left(\dot{m}_{total\ gas}\right)\right)^2 + \left(\frac{\partial \dot{m}_{cold\ gas}}{\partial \dot{m}_{hot\ gas}} u\left(\dot{m}_{hot\ gas}\right)\right)^2} \tag{4.32}$$

Where:

$$\frac{\partial \dot{m}_{cold\ gas}}{\partial \dot{m}_{total\ gas}} = 1,$$

$$\frac{\partial \dot{m}_{cold\ gas}}{\partial \dot{m}_{hot\ gas}} = -1,$$

$u\left(\dot{m}_{total\,gas}\right)$ = the total gas mass flow rate standard uncertainty, and

$u\left(\dot{m}_{hot\,gas}\right)$ = the hot gas mass flow rate standard uncertainty.

The final uncertainty based on the combined effect (Equation (4.3)) for each of the test runs was considered as the conservative value for the uncertainty analysis. Therefore, the final uncertainty for the averaged value over the four test runs was calculated by using Equation (4.6). These values were converted to the standard uncertainty percentage by dividing the final uncertainty using Equation (4.6) with their respective averaged cold gas mass flow rates over the four test runs, i.e.:

- $\frac{u(\dot{m}_{cold\,gas})_{Final}}{\dot{m}_{cold\,gas}} \times 100 \quad [\%]$
- $u(\dot{m}_{cold\,gas})_{Final}$ was calculated using Equation (4.6).

These percentage values are summarized in Table 4-18 for each of the three test sections, namely BETS036, BETS 039 and BETS045.

Table 4-18: Final uncertainty percentages of the cold gas inlet mass flow rates for all three BETS test sections.

	BETS036	BETS039	BETS045
Reynolds Number	**Cold Gas**	**Cold Gas**	**Cold Gas**
[-]	**[%]**	**[%]**	**[%]**
1000	0.948	0.961	0.822
2000	0.798	0.793	0.799
3000	0.664	0.661	0.663
4000	0.611	0.607	0.610
5000	0.584	0.583	0.583
6000	0.569	0.568	0.569
7000	0.560	0.560	0.560
8000	0.554	0.554	0.554
9000	0.549	0.549	0.550
10000	0.550	0.548	0.545
20000	0.572	0.508	0.572
30000	0.409	0.409	0.406
40000	0.416	0.416	0.412

The overall maximum and minimum final uncertainty percentages of the BETS inlet cold gas mass flow rate measurements are 0.961 % and 0.406 %, respectively.

4.5.4. Gas velocity

4.5.4.1. Cold gas velocity

The cold gas velocity is calculated using the following equation:

$$\dot{m}_{cold\ gas} = \left[\rho V A\right]_{cold\ gas}$$
$$V_{cold\ gas} = \left[\frac{\dot{m}}{\rho A}\right]_{cold\ gas} \tag{4.33}$$

Where:

$\rho_{cold\ gas}$ = the density as calculated using correlations given in *APPENDIX B: Fluid properties*, using the pressure of the test section and the hot gas inlet temperature,

$A_{cold\ gas}$ = the inflow area of the cold gas to the test section, calculated using Equation (4.26),

$\dot{m}_{cold\ gas}$ = the cold gas mass flow rate, calculated using Equation (4.31).

The uncertainty in the cold gas velocity is, therefore, calculated using Equation (4.4) as follows:

$$u\left(V_{cold\ gas}\right) = \sqrt{\left(\frac{\partial V_{cold\ gas}}{\partial \dot{m}_{cold\ gas}} u\left(\dot{m}_{cold\ gas}\right)\right)^2 + \left(\frac{\partial V_{cold\ gas}}{\partial \rho_{cold\ gas}} u\left(\rho_{cold\ gas}\right)\right)^2 + \left(\frac{\partial \dot{m}_{cold\ gas}}{\partial A_{cold\ gas}} u\left(A_{cold\ gas}\right)\right)^2} \tag{4.34}$$

Where:

$$\frac{\partial V_{cold\ gas}}{\partial \dot{m}_{cold\ gas}} = \left[\frac{1}{\rho A}\right]_{cold\ gas},$$

$$\frac{\partial V_{cold\ gas}}{\partial \rho_{cold\ gas}} = -\left[\frac{\dot{m}}{\rho^2 \cdot A}\right]_{cold\ gas},$$

$$\frac{\partial \dot{m}_{cold\ gas}}{\partial A_{cold\ gas}} = -\left[\frac{\dot{m}}{\rho \cdot A^2}\right]_{cold\ gas},$$

$u\left(\dot{m}_{cold\ gas}\right)$ = the total gas mass flow rate standard uncertainty using Equation (4.32),

$u\left(\rho_{cold\ gas}\right)$ = the density standard uncertainty calculated using Equation (4.28), and

$u\left(A_{cold\ gas}\right)$ = the cold gas inflow area standard uncertainty as calculated using Equation (4.27).

The final uncertainty based on the combined effect (Equation (4.3)) for each of the test runs was considered the conservative value for the uncertainty analysis. Therefore, the final uncertainty for the averaged value over the four test runs was calculated by using Equation (4.6). These values were converted to the standard uncertainty percentage by dividing the final uncertainty using Equation (4.6) with their respective averaged cold gas velocities over the four test runs, i.e.:

- $\frac{u\left(V_{cold\ gas}\right)_{Final}}{V_{cold\ gas}} \times 100 \quad [\%]$
- $u\left(V_{cold\ gas}\right)_{Final}$ was calculated using Equation (4.6).

These percentage values are summarized in Table 4-19 for each of the three test sections, namely BETS036, BETS039 and BETS045.

Table 4-19: Final uncertainty percentages of the cold gas inlet velocity for all three BETS test sections.

	BETS036	BETS039	BETS045
Reynolds Number	**Cold Gas**	**Cold Gas**	**Cold Gas**
[-]	**[%]**	**[%]**	**[%]**
1000	2.101	2.123	1.639
2000	1.666	1.666	1.456
3000	1.370	1.357	1.191
4000	1.247	1.241	1.086
5000	1.187	1.185	1.036
6000	1.154	1.153	1.006
7000	1.132	1.133	0.989
8000	1.119	1.119	0.977
9000	1.108	1.108	0.968
10000	1.109	1.102	0.960
20000	1.375	1.267	1.202
30000	0.969	0.952	0.840
40000	0.927	0.929	0.803

The overall maximum and minimum final uncertainty percentages of the BETS inlet cold gas mass flow rate measurements are 2.123% and 0.803%, respectively.

4.5.4.2. Hot gas velocity

The hot gas velocity was calculated using the following equation:

$$\dot{m}_{hot\,gas} = \left[\rho V A\right]_{hot\,gas}$$
$$V_{hot\,gas} = \left[\frac{\dot{m}}{\rho A}\right]_{hot\,gas} \tag{4.35}$$

Where:

$\rho_{hot\,gas}$ = the density as calculated in *APPENDIX B: Fluid properties*, using the pressure of the test section and the hot gas inlet temperature,

$A_{hot\,gas}$ = the inflow area of the hot gas to the test section, calculated using Equation (4.24),

$\dot{m}_{hot\,gas}$ = the hot gas mass flow rate, measured with the thermal mass flow meter as explained in Section 4.4.2.

The uncertainty in the cold gas velocity was, therefore, calculated using Equation (4.4) as follows:

$$u\left(V_{hot\,gas}\right) = \sqrt{\left(\frac{\partial V_{hot\,gas}}{\partial \dot{m}_{hot\,gas}} u\left(\dot{m}_{hot\,gas}\right)\right)^2 + \left(\frac{\partial V_{hot\,gas}}{\partial \rho_{hot\,gas}} u\left(\rho_{hot\,gas}\right)\right)^2 + \left(\frac{\partial V_{hot\,gas}}{\partial A_{hot\,gas}} u\left(A_{hot\,gas}\right)\right)^2} \tag{4.36}$$

Where:

$$\frac{\partial V_{hot\,gas}}{\partial \dot{m}_{hot\,gas}} = \left[\frac{1}{\rho A}\right]_{hot\,gas},$$

$$\frac{\partial V_{hot\,gas}}{\partial \rho_{hot\,gas}} = -\left[\frac{\dot{m}}{\rho^2 \cdot A}\right]_{hot\,gas},$$

$$\frac{\partial \dot{m}_{hot\,gas}}{\partial A_{hot\,gas}} = -\left[\frac{\dot{m}}{\rho \cdot A^2}\right]_{hot\,gas},$$

$u\left(\dot{m}_{hot\,gas}\right)$ = the hot gas mass flow rate standard uncertainty as explained in Section 4.4.2,

$u\left(\rho_{hot\,gas}\right)$ = the density standard uncertainty calculated using Equation (4.28), and

$u\left(A_{hot\,gas}\right)$ = the hot gas inflow area standard uncertainty calculated using Equation (4.25).

The final uncertainty based on the combined effect (Equation (4.3)) for each of the test runs was considered the conservative value for the uncertainty analysis. Therefore, the final uncertainty for the averaged value over the four test runs was calculated by using Equation (4.6). These values were converted to the standard uncertainty percentage by dividing the final uncertainty using Equation (4.6) with their respective averaged hot gas velocities over the four test runs, i.e.:

- $\dfrac{u\left(V_{hot\,gas}\right)_{Final}}{V_{hot\,gas}} \times 100 \quad [\%]$
- $u\left(V_{hot\,gas}\right)_{Final}$ was calculated from Equation (4.6).

These percentage values are summarized in Table 4-20 for each of the three test sections, namely BETS036, BETS039 and BETS045.

Table 4-20: Final uncertainty percentages of the hot gas inlet velocity for all three BETS test sections.

	BETS036	BETS039	BETS045
Reynolds Number	**Cold Gas**	**Cold Gas**	**Cold Gas**
[-]	**[%]**	**[%]**	**[%]**
1000	2.420	2.161	1.979
2000	1.285	1.346	1.121
3000	1.390	1.061	1.286
4000	1.484	1.332	1.593
5000	1.882	1.858	1.178
6000	1.813	2.000	1.467
7000	1.776	1.773	1.554
8000	1.607	1.694	1.609
9000	1.463	1.622	1.573
10000	1.773	1.655	1.595
20000	1.670	1.672	1.295
30000	2.254	2.218	1.022
40000	1.936	2.157	0.964

The overall maximum and minimum final uncertainty percentages of the BETS hot gas inlet velocity measurements are 2.420% and 0.964%, respectively.

4.6. Summary

The uncertainty analysis in the measured and calculated variables was investigated. This was made over the four test runs. Table 4-21 summarizes variables that are important in the calculation of the effective fluid conductivity; their associated maximum and minimum standard uncertainty percentages are also presented. These percentages were done for all three test sections.

Table 4-21: Final uncertainty percentages of the measured and calculated variables that are important in the simulation.

	BETS036		BETS039		BETS045	
	Maximum	Minimum	Maximum	Minimum	Maximum	Minimum
Variable	[%]	[%]	[%]	[%]	[%]	[%]
Test section inlet pressure	0.442	0.060	0.440	0.061	0.444	0.065
Cold gas temperature	4.010	0.610	3.230	0.562	3.831	0.572
Hot gas temperature	0.576	0.556	0.597	0.543	0.741	0.546
Cold gas velocity	2.101	0.927	2.123	0.929	1.639	0.803
Hot gas velocity	2.420	1.285	2.218	1.061	1.979	0.964
Top braiding temperature profile	4.531	2.334	4.178	2.202	4.280	1.871
Bottom braiding temperature profile	5.145	1.990	4.697	2.008	10.804	1.500

The overall maximum and minimum final uncertainty percentages of these variables are 10.804% and 0.060%, respectively. The next chapter will present experimental results for these variables.

5. EXPERIMENTAL RESULTS

5.1. Introduction

Four test runs were conducted for each BETS test section for the range of Reynolds numbers between 1,000 and 40,000. This implies that four sets of experiments were conducted for a particular Reynolds number and porosity. From these four sets, an averaged data set was calculated, which was used as input data to the CFD calculation of the effective fluid thermal conductivity. This was also done in the uncertainty analysis in the previous chapter.

This chapter will present the experimental results for the variables which served as the input data to the CFD calculation. These variables were briefly discussed in the summary of the previous chapter and are listed as follows:

- Test section inlet pressure,
- Cold gas temperature,
- Hot gas temperature,
- Cold gas velocity,
- Hot gas velocity,
- Top braiding temperature profile, and
- Bottom braiding temperature profile.

The inlet temperatures and mass flow rate measurements were required to meet the following test requirements:

1. The braiding gas temperature had to be more than 40 °C warmer than the cold gas temperature, and
2. Both gas streams had to have the samel superficial velocity at the inlet of the bed (*APPENDIX D: Inlet superficial velocity*); to minimize the pressure drop in both streams due to convection.

5.2. Inlet gas pressure

The inlet gas pressure was measured at the inlet of the test section and would, therefore, be the same for both the hot and cold gas flows. The gas pressure was increased from one experiment to another to achieve the required Reynolds number. The average values of the inlet gas pressure measurements over the four test runs of each BETS test section were calculated as input variables to the CFD solution. These values are summarized in Table 5-1 for each Reynolds number that was intended. The tests were limited to the maximum pressure of 3800*kPa* because the thermal mass flow meter could only measure accurately up to this pressure level.

Table 5-1: Average values of the total gas pressure for all three BETS test sections.

	BETS036	BETS039	BETS045
Reynolds Number	Total Gas	Total Gas	Total Gas
[-]	[kPa]	[kPa]	[kPa]
1000	100.8611	100.6111	100.8770
2000	200.9430	200.7561	201.1302
3000	300.8580	300.5022	300.9436
4000	400.6812	400.6793	400.7676
5000	501.0973	500.6478	500.1593
6000	600.7658	600.4628	600.1094
7000	700.2610	699.9763	700.6685
8000	800.3625	800.3143	800.4549
9000	900.5735	900.6523	900.5877
10000	1000.2185	1000.6700	1000.9242
20000	2001.0211	2000.8069	2000.7705
30000	2999.7813	3000.4902	2999.6587
40000	3799.2372	3800.7236	3798.2826

5.3. Inlet gas temperature

The average values of the inlet gas temperature measurements over four test runs of each BETS test section were calculated as input variables to the CFD solution. These average values are summarized in Table 5-2.

Table 5-2: Average values of the inlet gas temperatures for all three BETS test sections.

	BETS036		BETS039		BETS045	
Reynolds Number	Braiding Gas	Cold Gas	Braiding Gas	Cold Gas	Braiding Gas	Cold Gas
[-]	[˚C]	[˚C]	[˚C]	[˚C]	[˚C]	[˚C]
1000	57.0349	14.8640	58.1015	16.5194	59.4761	16.7865
2000	57.3333	14.6898	59.5975	15.5883	57.2730	14.9135
3000	57.5203	13.8288	58.6158	15.3272	56.7720	14.4999
4000	57.4628	14.2813	58.9234	16.2053	57.5357	14.5713
5000	57.0084	13.5692	58.8162	15.4556	56.4558	14.6092
6000	55.7776	13.4654	57.8852	15.3823	55.9968	14.0667
7000	56.0767	13.4544	57.9546	15.3689	55.5924	14.0051
8000	56.1078	13.8781	58.4756	15.3990	57.1338	14.0935
9000	56.4816	14.2854	57.8639	15.3075	57.8217	14.1096
10000	56.8421	13.7753	58.5547	15.4208	58.1486	14.0512
20000	57.7282	14.6245	59.6524	16.0153	57.7959	13.8004
30000	57.4703	14.9250	58.8132	16.5260	56.8716	13.7934
40000	56.5631	15.6822	58.9703	17.2651	55.3655	13.5182

5.4. Inlet gas velocities

The average values of the inlet gas velocity (superficial velocity) over four test runs for each of the BETS test sections were calculated as input variables to the CFD solution. These average values are summarized in Table 5-3.

Table 5-3: Average values of the inlet gas velocities for all three BETS test sections.

	BETS036		BETS039		BETS045	
Reynolds Number	Braiding Gas	Cold Gas	Braiding Gas	Cold Gas	Braiding Gas	Cold Gas
[-]	[m/s]	[m/s]	[m/s]	[m/s]	[m/s]	[m/s]
1000	0.5283	0.5263	0.5360	0.5283	0.5361	0.5292
2000	0.5289	0.5238	0.5290	0.5267	0.5316	0.5231
3000	0.5193	0.5220	0.5356	0.5285	0.5243	0.5242
4000	0.5295	0.5251	0.5314	0.5309	0.5257	0.5253
5000	0.5251	0.5218	0.5325	0.5287	0.5280	0.5270
6000	0.5249	0.5228	0.5261	0.5294	0.5242	0.5256
7000	0.5233	0.5233	0.5306	0.5293	0.5237	0.5255
8000	0.5249	0.5247	0.5291	0.5303	0.5271	0.5257
9000	0.5307	0.5262	0.5310	0.5299	0.5310	0.5260
10000	0.5269	0.5257	0.5384	0.5318	0.5308	0.5261
20000	0.5364	0.5324	0.5389	0.5382	0.5311	0.5298
30000	0.5400	0.5379	0.5564	0.5532	0.5375	0.5344
40000	0.5731	0.5734	0.5934	0.5779	0.5736	0.5657

5.5. Braiding temperature profile

The braiding temperature profile for any of the two layers of measurement that are indicated in Figure 3-6 was directly influenced by the gas inlet temperatures. This is because the cold gas inlet temperature was controlled close to or equal to the ambient temperature. The ambient temperature value varied for the different tests due to seasonal temperature changes. For a particular point in a layer of measurement, a non–dimensional number was derived as a function of the gas inlet temperatures (cold gas flow and hot gas flow) and the measured temperature at that point (braiding profile temperature).

This number was calculated as follows:

$$T_{[-]} = \frac{\left(T_{\text{braiding profile}} - T_{\text{cold gas in}}\right)}{\left(T_{\text{hot gas in}} - T_{\text{cold gas in}}\right)} \cdot 100 \qquad (5.1)$$

Where:

$T_{\text{hot gas in}}$ = the hot or braiding gas inlet temperature,

$T_{\text{cold gas in}}$ = the cold gas inlet temperature, and

$T_{\text{braiding profile}}$ = the braiding temperature profile.

For a particular BETS test section a non-dimensional temperature value was calculated using Equation (5.1) and averaged over the four test runs. This average value was used to calculate the so-called normalized braiding profile temperature (Equation (5.2)), by using the average inlet gas temperatures ($\overline{T}_{\text{hot gas in}}$ and $\overline{T}_{\text{cold gas in}}$).

$$T_{braiding\ profile_N} = \frac{\overline{T}_{[-]}}{100} \times \left(\overline{T}_{\text{hot gas in}} - \overline{T}_{\text{cold gas in}}\right) + \overline{T}_{\text{cold gas in}} \qquad (5.2)$$

Where:

$\overline{T}_{[-]}$ = the average non-dimensional braiding profile temperature over the four test runs,

$\overline{T}_{\text{hot gas in}}$ = the average hot gas inlet temperature over the four test runs,

$\overline{T}_{\text{cold gas in}}$ = the average cold gas inlet temperature over the four test runs, and

$T_{braiding\ profile_N}$ = normalized braiding temperature profile.

The average values of the non-dimensional braiding temperature profiles for all three test sections are summarized in Table E-1 to Table E-6. The average values of the normalized braiding temperature profiles for all three test sections are summarized in Table F- 1 to Table F- 6.

5.6. Summary

The experimental results that were used as the input data to the CFD solution were presented in this chapter. These results were averaged over the four sets of test runs for each BETS test section. Two experimental requirements stated at the end of Section 5.1 were met for the gas inlet temperatures and velocities. These requirements can be confirmed in the values that are given in Table 5-2 and Table 5-3 for all three BETS test sections.

A non-dimensional number was introduced in the braiding temperature profile to lessen the influence of climate change in the temperature profiles. This was done by formulating the so-called normalized braiding temperature profiles (Equations (5.1) and (5.2)).

5.7. Remarks

The input data for the CFD simulation was obtained from the following variables at a particular Reynolds number:

1. The BETS packed bed geometry (Table 4-16),
2. Cold gas and braiding gas inlet absolute pressures (Table 5-1),
3. Cold gas and braiding gas inlet velocities (Table 5-2),
4. Cold gas and braiding gas inlet temperatures (Table 5-3),
5. Two polynomial equations for the two curves fitted through normalized braiding temperature profiles (top and bottom layer measurements Table F- 1 to Table F- 6) (Equation (H.3) in Appendix H),
6. Thermocouple installed positions at the top and bottom layer measurement positions.

The next chapter presents the results of the CFD and simulations and methodology used to calculate the enhanced fluid thermal conductivity value obtained from the experimental data.

6. SIMULATION METHOD AND RESULTS

6.1. Background theory

The thermal fluid simulation method that was used in the packed bed follows the pseudo homogeneous modelling approach with the following assumptions:

- Solid and fluid temperatures are assumed to be the same.
- Single phase energy equation (Equation (6.5)) for fluid and solid because the packed materials have a negligible thermal conductivity.

The commercial CFD code used for simulation is Flo++[4]. This code was used to predict the steady-state transverse temperature profile across the packed bed.

The equation for the conservation of energy equation in Flo++[4] is solved in the form of a transport equation for static temperature. The temperature equation is obtained from the enthalpy equation which is solved by taking the temperature as a dependent variable. The steady-state enthalpy equation is defined as (Flo++[4]):

$$\frac{\partial}{\partial x_j}\left(\rho u_j h\right) = k_{eff}\frac{\partial}{\partial x_j}\left(\frac{\partial T}{\partial x_j}\right) + u_j\frac{\partial p}{\partial x_j} + \tau_{ij}\frac{\partial u_i}{\partial x_j} + s_h \qquad (6.1)$$

Where:

x_j, x_i = Cartesian coordinates ($i, j = 1,2,3$),

ρ = fluid density,

u_j = velocity component in direction x_j ,

$h = c_p T$ = thermal enthalpy,

c_p = constant pressure specific heat at temperature T ,

k_{eff} = thermal conductivity assumed to be constant because the working fluid is considered to be isotropic,

[4] ©Copyright 1999, Softflo cc. www.softlo.com. Flo++ Home Page and Documentation Information.

p = static pressure,

τ_{ij} = strain tensor, and

s_h = energy source term.

The convention of the notation used in Equation (6.1) is that $i\,or\,j = 1$ corresponds to the *x*-direction, $i\,or\,j = 2$ corresponds to the *y*-direction and $i\,or\,j = 3$ corresponds to the *z*-direction.

The following must be noted in going forward:

- The total net flow of the mass flow rate in and out of the test section at a particular Reynolds number for the steady state conditions remains the same; therefore the continuity equation becomes, $\frac{\partial}{\partial x_j}\left(\rho\, u_j\right) = 0$ i.e., only convective term remains in the equation.
- Pressure drop effects due to the porous media are not considered in the momentum equation, i.e. the flow is taken to be in a hollow pipe or tube. This stance is taken to account for the turbulent mixing, due to the presence and resistance of the packed particles, only to the fluid thermal conductivity. Presumably, there are no leaks in the system. Therefore the effects of the pressure and viscous forces are minimal. The effects of the body forces due to gravity are also negligible.
- Values of the terms, $u_j \frac{\partial p}{\partial x_j}$ and $\tau_{ij} \frac{\partial u_i}{\partial x_j}$, in Equation (6.1) will have a minimal influence to the final solution because they represent contributions from the effects of the pressure and viscous forces respectively.

The energy source term s_h will be zero as there is negligible internal heat transfer to the flow field. Equation (6.1) can be rewritten as follows (for analysis):

$$\frac{\partial}{\partial x_j}\left(\rho\, u_j h\right) = k_{eff} \frac{\partial}{\partial x_j}\left(\frac{\partial T}{\partial x_j}\right) \qquad (6.2)$$

Differentiating by parts on the left hand side of Equation (6.2) yields:

$$h\frac{\partial}{\partial x_j}\left(\rho u_j\right)+\rho u_j\frac{\partial h}{\partial x_j}=k_{eff}\frac{\partial}{\partial x_j}\left(\frac{\partial T}{\partial x_j}\right) \tag{6.3}$$

But for steady state conditions $\frac{\partial}{\partial x_j}\left(\rho u_j\right)=0$, therefore:

$$\rho u_j\frac{\partial h}{\partial x_j}=k_{eff}\frac{\partial}{\partial x_j}\left(\frac{\partial T}{\partial x_j}\right) \tag{6.4}$$

With $h=c_pT$ Equation (6.4) then finally becomes:

$$\rho u_j c_p\frac{\partial T}{\partial x_j}=k_{eff}\frac{\partial}{\partial x_j}\left(\frac{\partial T}{\partial x_j}\right) \tag{6.5}$$

Equation (6.5) is the conservative form of the (simplified) equation of the conservation of energy; Equation (2.6) is the non-conservative form of the energy equation which was obtained from the literature.

Density ρ in Equation (6.5) is estimated by using the ideal gas equation. The thermal conductivity k_{eff} is assumed to be isotropic, i.e. uniform in all direction despite the fact that the dispersion effect is in the bed transverse direction (anisotropic). The gas thermal conductivity account for the effects of turbulent mixing, hence it is calculated as effective thermal conductivity.

6.2. CFD grid

The inflow area in Figure 4-3 can be subdivided into four sub-domains as shown in Figure 6-1.

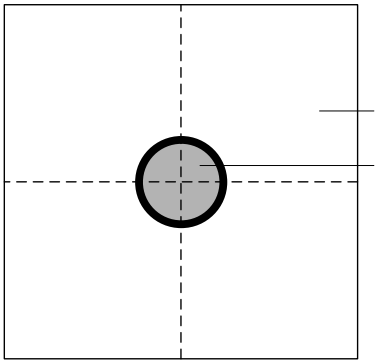

2

Figure 6-1: Gas inflow area subdivided into four equal portions.

It is shown in Appendix G, that any sub-domain in Figure 6-1 will have the same solution for the braiding temperature profiles when extracted along any axial line in the bed. Therefore, the CFD grid used represents only a quarter of the volume of the original BETS test section, in order to increase the speed of the CFD solver to obtain the solution.

4

It is also shown in Appendix G, that any of the sub-domains in Figure 6-1 (e.g. sub-domain 1) can be divided in symmetrical halves as shown in Figure 6-2. That also yields the same braiding temperature profiles solution when extracted along any axial line in the bed.

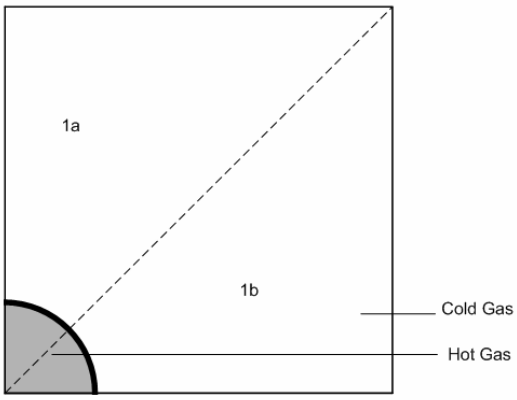

Figure 6-2: Quarter portion of the gas inflow area subdivided into two equal portions.

Therefore, the final volume representation of the test section was 1/8 of the total volume as shown in Figure 6-3.

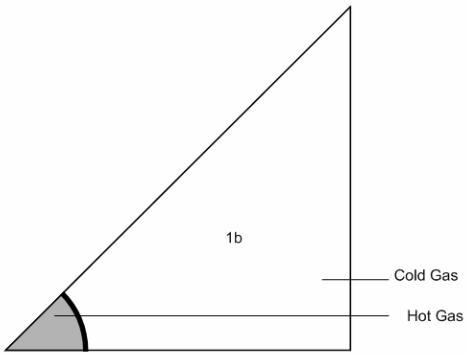

Figure 6-3: 1/8 portion of the gas inflow area.

The applied CFD code uses the finite volume (FV) spatial discretization method. This implies that the flow field is discretisized in all directions (x_1, x_2 *and* x_3 in Equation (6.5) or z *and* r in Equation (2.6)). This method also generates a structured grid whereby the temperature values at the centres of the discretisized control volumes (CVs) are calculated, i.e. a co-located grid is used. The centres are indicated as discrete points in the structured grid as shown in Figure 6-4. The three dimensional (3D) grid is shown in Figure 6-5 with the physical dimensions as re-casted from Figure 4-2 and Figure 4-3.

It must be noted that the temperature profile from the CFD temperature solution can be extracted along any of the radial lines indicated in Figure 6-4. This is evident from the fact that, for a particular vertical axial position in the bed, the temperature profiles along all the indicated radial lines have the same form of shape as shown in Appendix G (refer to Figure G-9 and values in Table G-3).

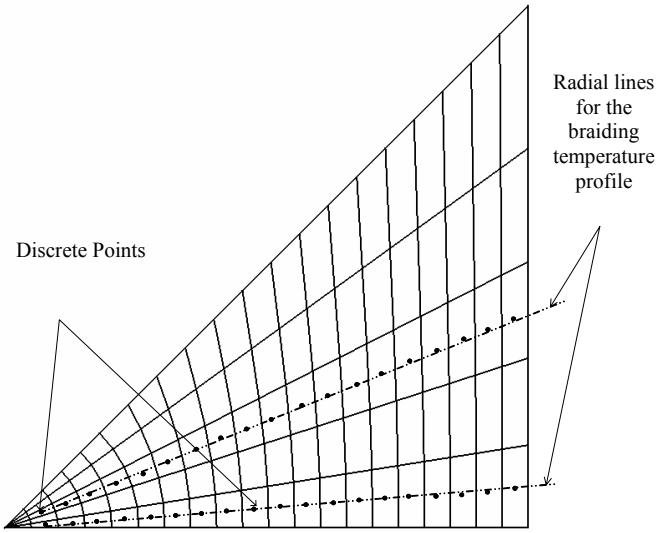

Figure 6-4: Discrete points in the structured grid of the gas inflow area of the BETS test section.

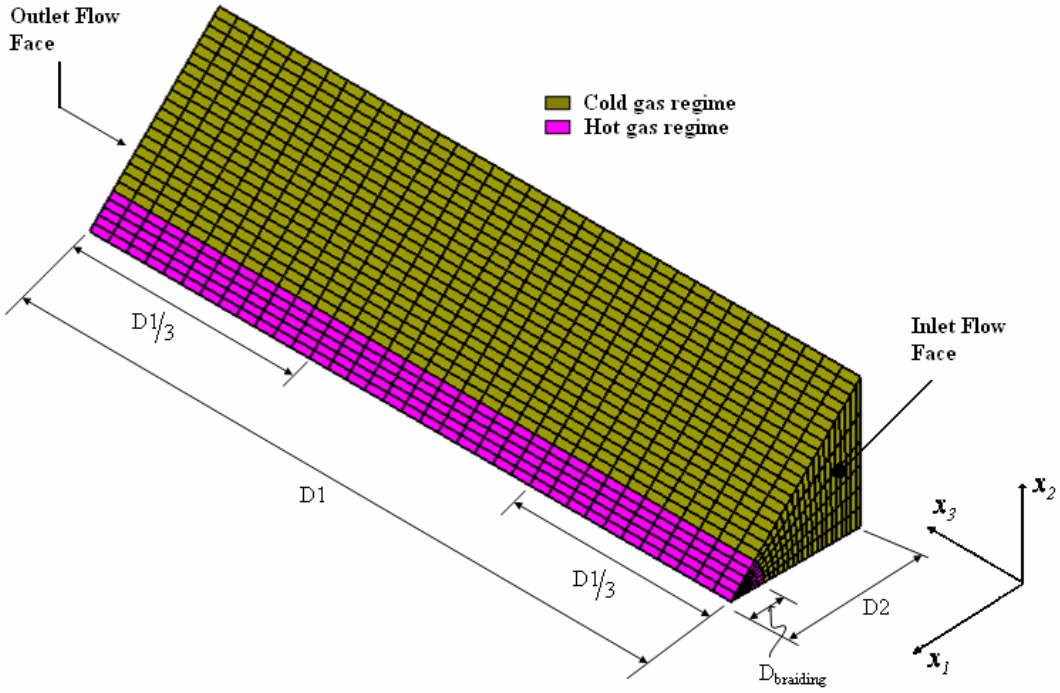

Figure 6-5: Three dimensional (3D) grid for the 1/8 portion of the BETS structure.

The following must also be noted with Figure 6-5:

- Values of D1, D2 and $D_{braiding}$ are stipulated in Table 4-16.

- Temperature profile from the CFD temperature solution was extracted along the axial direction (x_3-direction) of the grid at D1/3 distance from the outlet, and D1/3 distance from the inlet; these values were respectively compared with the experimentally measured temperature values in the test sections using top layer thermocouples and bottom layer thermocouples. Values for D1/3 values are shown from Figure A-2 to Figure A-7 in Appendix A for BETS036, BETS039 and BETS045.
- The final choice for the grid resolution was done in the grid dependence study discussed in Appendix K. The well known Richardson extrapolation (Roache (1998)) was used; this method uses the so-called a 'relative solution error', E_{rel} which gives the normal change in the solution (temperature solution in this case) should the mesh be refined in the next step. Equation (K.1) gives the formulation thereof. The main heat transfer mechanisms that are active are those of heat convection and heat conduction for axial direction and transverse direction, respectively. Four cases on grid refinement were investigated and are explained hereafter:
    - **Base case:** refinements for both angular (azimuthal) and transverse direction were kept constant whilst the refinement in the axial direction was varied (Table K-2) and QUICK differencing scheme was used; the axial temperature profile started to become stable at grid point 6 (as seen in Figure K-2 and Figure K-3 for 91 grid points in the axial direction), and also the relative solution error is less than 0.5 % at grid point 6 (Figure K-4 to Figure K-7),
    - **Transverse refinement:** refinements for both angular (azimuthal) and axial directions were kept as in Table K-2 whilst the number of cells in the transverse direction was varied; the relative solution error is less than 0.5 % at grid point 6 (Figure K-4 to Figure K-7),
    - **Angular or Azimuthal refinement:** refinements for both azimuthal and axial directions were kept constant whilst the refinement in the transverse

direction was varied; the relative solution error is less than 0.5 % at grid point 6 (Figure K-4 to Figure K-7), and

- **UPWIND differencing scheme:** refinement in the base case was used whilst UPWIND convection discretization scheme; the relative solution error is less than 0.5 % at grid point 6 (Figure K-4 to Figure K-7).

It was therefore enough to use Grid point 6 which has the following number of cells (Table K-2):

- *5 cells* : Angular or azimuthal direction
- *18 cells* Transverse direction
- *91 cells*: Axial direction.

Simulations were done for the Cartesian grid that resembled the BETS geometric properties as shown in Figure 6-4 and Figure 6-5. However, simulations were also done on a cylindrical grid because the real PBMR packed reactor is cylindrical. The simulated results on the two grids were compared to see the variation between results obtained for the two geometries.

The cylindrical grid had the same number of cells and the Cartesian grid, though the transverse direction was purely cylindrical. Figure 6-6 shows the discretisized CVs with their cell centres on the flow area of the grid.

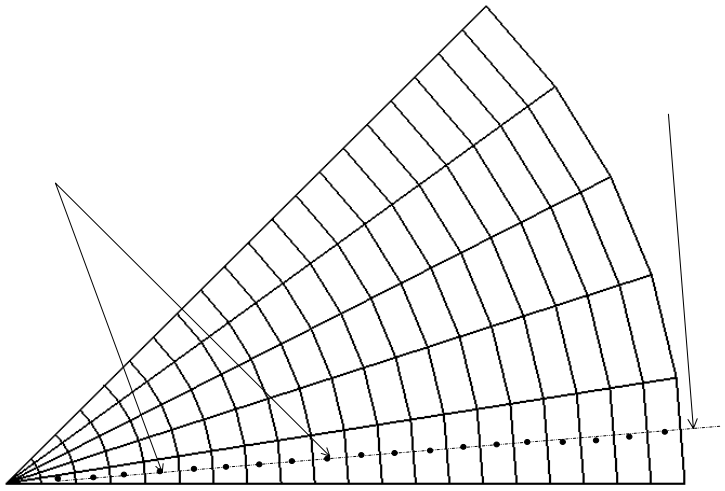

Figure 6-6: Discrete points in cylindrical grid.

6.3. Simulation method

The simulation method is summarized in Figure 6-7. The primary outputs of the simulation method procedure were effective thermal conductivities at Reynolds numbers between 1 000 and 40 000 for porosities 0.36 (BETS036), 0.39 (BETS039) and 0.45 (BETS045). The blocks for these attributes are filled with a grey colour in Figure 6-7.

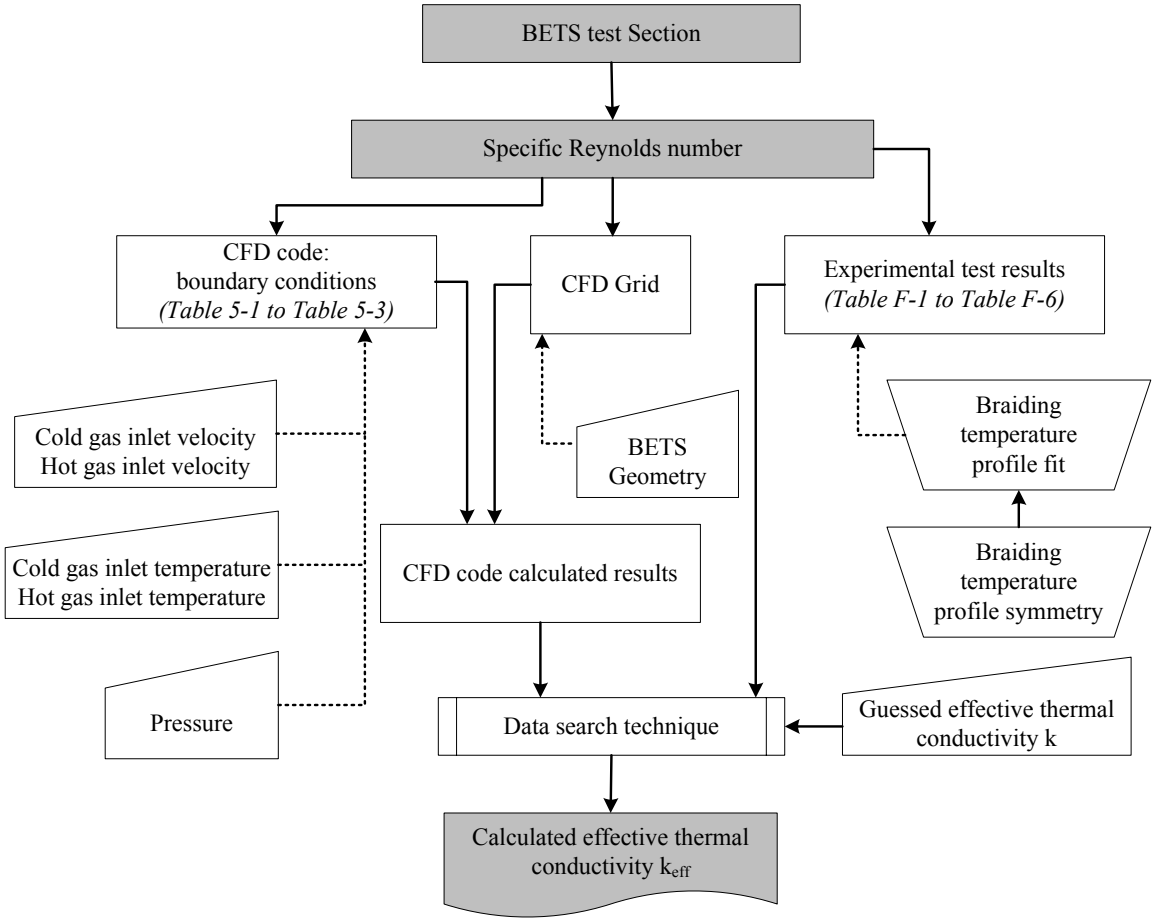

Figure 6-7: Summary of the simulation method.

The following must be noted with reference to Figure 6-7 for specific Reynolds number experimental results that were conducted for a particular test section:

- The boundary values for the CFD code were set by using the input data from Table 5-1 to Table 5-3.
- The CFD grid (from Figure 6-5 and/or Figure 6-6) was set by using the BETS geometry in Table 4-16.

- The CFD code calculated results were temperature profile from the temperature solution as explained in Section 6.2.
- The experimental test results were experimental braiding temperature profiles that were reworked for correct comparison with the CFD results by performing the following:
    - Braiding temperature profile symmetry
    - Braiding temperature profile polynomial fit

  These two re-workings that are stated above are explained in detail in the Appendix H and Appendix I.
- The data search technique compares both the CFD braiding temperature profile and the experimental braiding temperature profile by guessing the effective thermal conductivity.

6.3.1. Braiding temperature profile symmetry

Theoretically, the radial diffusion between the cold gas and braiding gas is symmetric across the bed i.e. the temperature transverse distribution will be the same in the outward direction of the bed centreline. This is also evident from the CFD generated temperature transverse distribution results in Figure G-7 in Appendix G that are shown to prove volume independence in the braiding temperature profile.

The symmetry in the braiding temperature profile for test in the three test sections is evaluated in Appendix I. The symmetry is formulated in Equation (I.1) whereby the calculated value must range between 0 (zero) and 1 (one); which respectively indicates the worst and best symmetry in the measured profile. The calculated values are shown in Table I-1, and they range between 0.93 and 0.99 for all the tests in the three test sections.

Hence, to demonstrate, the experimental braiding temperature profile for BETS036 test section at Reynolds number of 10 000 the bottom layer is measured as given in Table F-1 and after symmetry calculations it is then transformed to Table 6-1.

Table 6-1: The experimental data for BETS036 at Reynolds number of 10 000.

BOTTOM LAYER MEASUREMENT	
Bed transverse position	**Temperature Profile**
[m]	[K]
0.02	309.88
0.033	301.50
0.036	306.40
0.048	295.12
0.065	290.61
0.078	289.40
0.094	287.90
0.108	287.70
0.124	287.60
0.139	287.50

6.3.2. Braiding temperature profile polynomial fit

The formulation of the braiding temperature profile polynomial fit is explained in Appendix H. As an example again, the data shown in Table 6-1 is plotted and fitted in Figure 6-8.

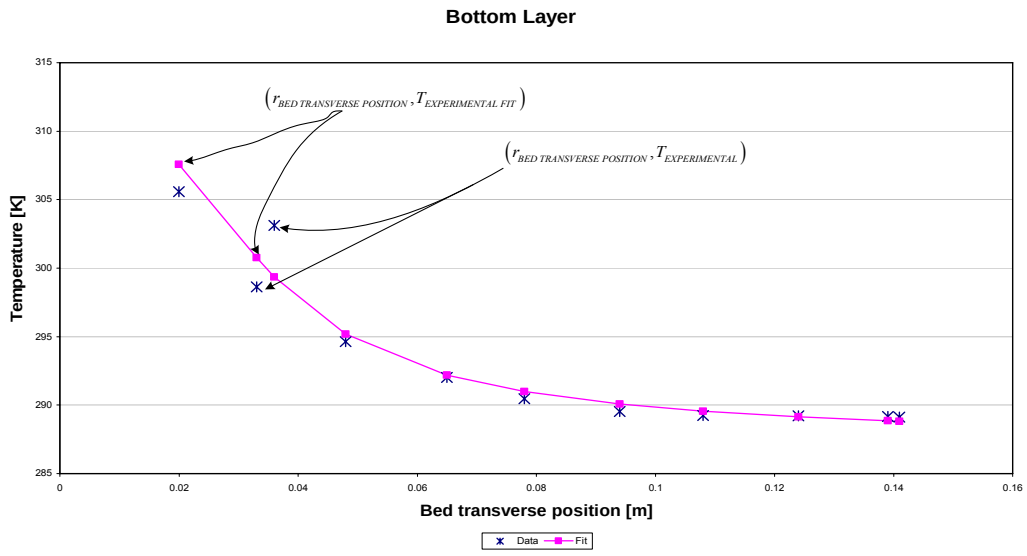

Figure 6-8: Braiding temperature profile plot for BETS036 at the Reynolds number of 10 000: experimental data and experimental fit.

The polynomial equation for the experimental data is shown in Equation (6.6); the optimized constants a,b,c,d that were obtained are given in Table 6-2:

$$T_{EXPERIMENTAL\,FIT} \cong \frac{1}{a}\arctan\left(\frac{d - r_{BED\,TRANSVERSE\,POSITION}}{b}\right) + c \qquad (6.6)$$

The optimized constants in Table 6-2 were calculated by minimizing the difference (errors) between the BETS measured temperature values $T_{EXPERIMENTAL}$ and the calculated temperature values in Equation (6.6).

Table 6-2: The optimized constants for the BETS036 bottom layer experimental data at the Reynolds number of 10 000.

Constants	Values
a	0.0870407
b	0.014898544
c	303.7650086
d	0.031964811

6.3.3. Data search technique

The data search technique in Appendix J shows the calculation of the error E between the experimental results and the CFD simulation for a particular guessed thermal conductivity k. Figure J-2 shows the flow diagram that is used in formulating E as a function of k, i.e., $E(k)$. Graphs in Figure J-3 and Figure J-4 are used to formulate Δk, which is the amount that k must increase or decrease to get a minimum $E(k)$.Figure J-5 shows the search routine that was implemented in the CFD code, to obtain Δk and the routine is again given in Figure 6-9. The new themal conductivity $k^{new} = k + \Delta k$ is set to $k^{new} = k_{eff}$ if $\partial E(k)/\partial k \ll$ than a maximum allowable value. The value of k is perturbed at $\delta k = \alpha \cdot k$ to initiate Equation (J.3). The pertubation intervals are controlled at $0 < \alpha < 0.1$ to keep the perturbed values as small as possible; simulations has shown that $\alpha = 0.00625$ is suitable for all the calculations. Simulations have also shown that $\partial E(k)/\partial k = 0.001$ is enough for the required $k^{new} = k_{eff}$ condition.

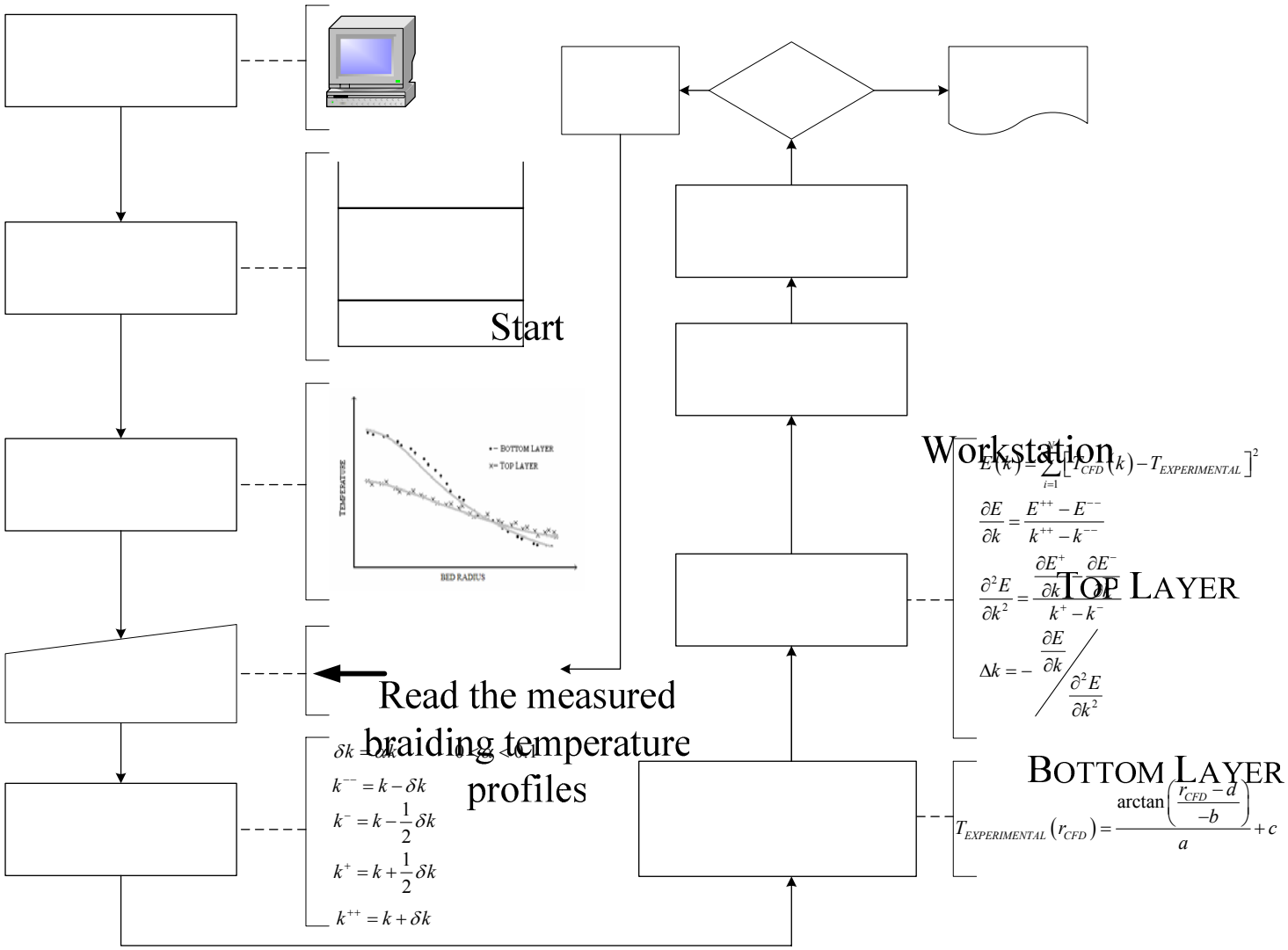

Figure 6-9: Illustration of the search routine that was implemented in the CFD program.

6.4. Simulation results

The test results for all the Reynolds numbers were simulated on the Cartesian grid. Simulations were also done for the cylindrical grid, but only selected cases, specifically for low and high Reynolds numbers, as indicated in Table 6-3.

Table 6-3: Summary of the simulation matrix for the experiments simulated using different flow field grid.

	BETS036		BETS039		BETS045	
Reynolds Number	Cartesian grid	Cylindrical grid	Cartesian grid	Cylindrical grid	Cartesian grid	Cylindrical grid
[-]	[˚C]	[˚C]	[˚C]	[˚C]	[˚C]	[˚C]
1000	√	√	√	√	√	√
2000	√	√	√	√	√	√
3000	√	×	√	×	√	×
4000	√	×	√	×	√	×
5000	√	×	√	×	√	×
6000	√	√	√	√	√	√
7000	√	×	√	×	√	×
8000	√	×	√	×	√	×
9000	√	×	√	×	√	×
10000	√	√	√	√	√	√
20000	√	√	√	√	√	√
30000	√	×	√	×	√	×
40000	√	√	√	√	√	√

The symbols "√" and "×" respectively indicate that the CFD simulation was done for the experiment or the CFD simulation was not done for the experiment. It should be reiterated that the cylindrical grid simulations were done to see the difference between the two grids due to the apparent four corners shown in Figure 6-10. If there were significant disparities, the conclusion could be made that the results are not applicable to the cylindrical bed. Otherwise, for insignificant disparities the current results are also applicable to the cylindrical bed.

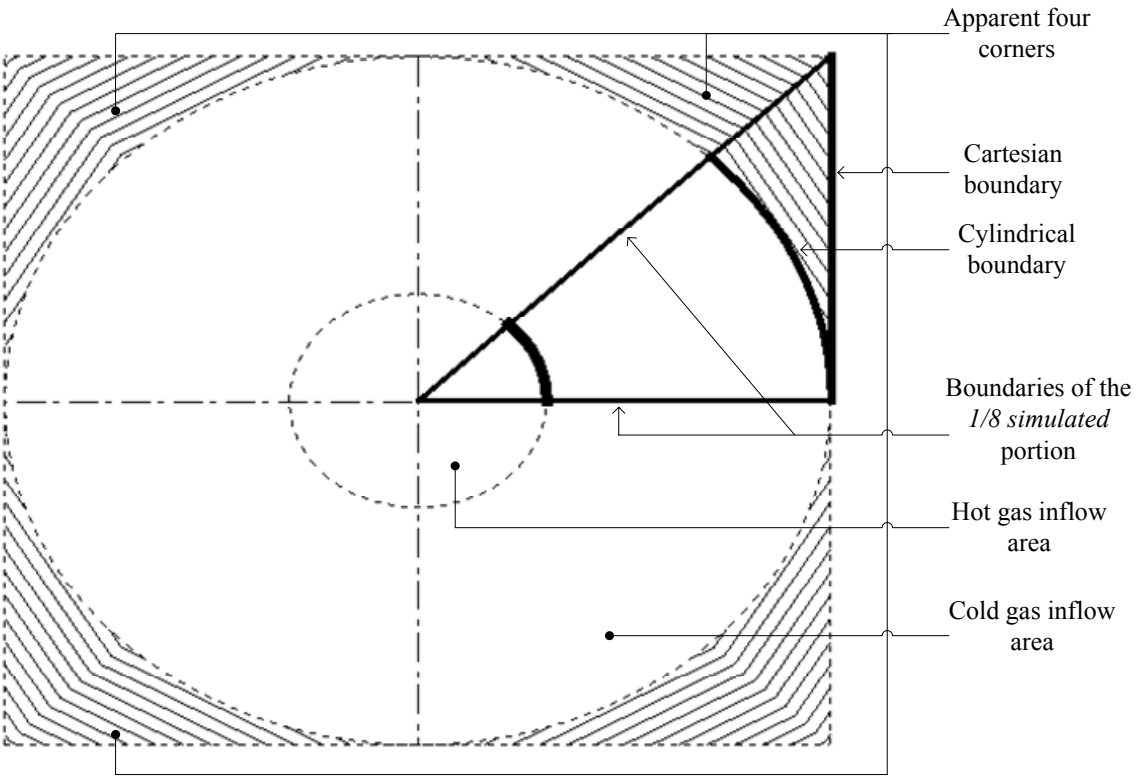

Figure 6-10: Integrated sketch of the gas inflow areas, identified boundaries and apparent corners between the Cartesian boundary and the cylindrical boundary.

6.4.1. Cartesian Grid

Table 6-4 shows the calculated results of the effective thermal conductivities obtained from the CFD simulations using the Cartesian grid for the three test sections using the search routine in Figure 6-9.

Table 6-4: Simulations results of the effective thermal conductivities using the Cartesian grid.

	BETS036	BETS039	BETS045
Reynolds Number	Effective thermal conductivity k_{eff}	Effective thermal conductivity k_{eff}	Effective thermal conductivity k_{eff}
[-]	[W/m K]	[W/m K]	[W/m K]
1000	1.208	1.449	1.166
2000	2.329	2.748	1.704
3000	3.007	3.951	2.259
4000	3.786	3.689	2.538
5000	4.198	4.577	3.030
6000	5.215	5.320	3.496
7000	4.998	6.645	3.914
8000	5.822	7.332	4.807
9000	6.794	8.676	5.609
10000	7.227	9.499	6.298
20000	14.250	18.542	12.339
30000	22.365	27.769	17.438
40000	31.657	38.015	26.259

Figure 6-11 shows the comparison between the calculated effective conductivities in the CFD simulations for the three test sections as a function of the Reynolds number. In general, there's linear relationship between the calculated values and the Reynolds number. The results in the figure show that the values are quite close to each other between the 1000 and 10 000 Reynolds number for the three porosities. The values tend to deviate significantly from each other between 20 000 and 40 000 Reynolds number, with BETS039 at maximum, and BETS045 at minimum at each Reynolds number. The maximum and minimum values calculated are 38.015 W/mK and 1.1657 W/mK respectively.

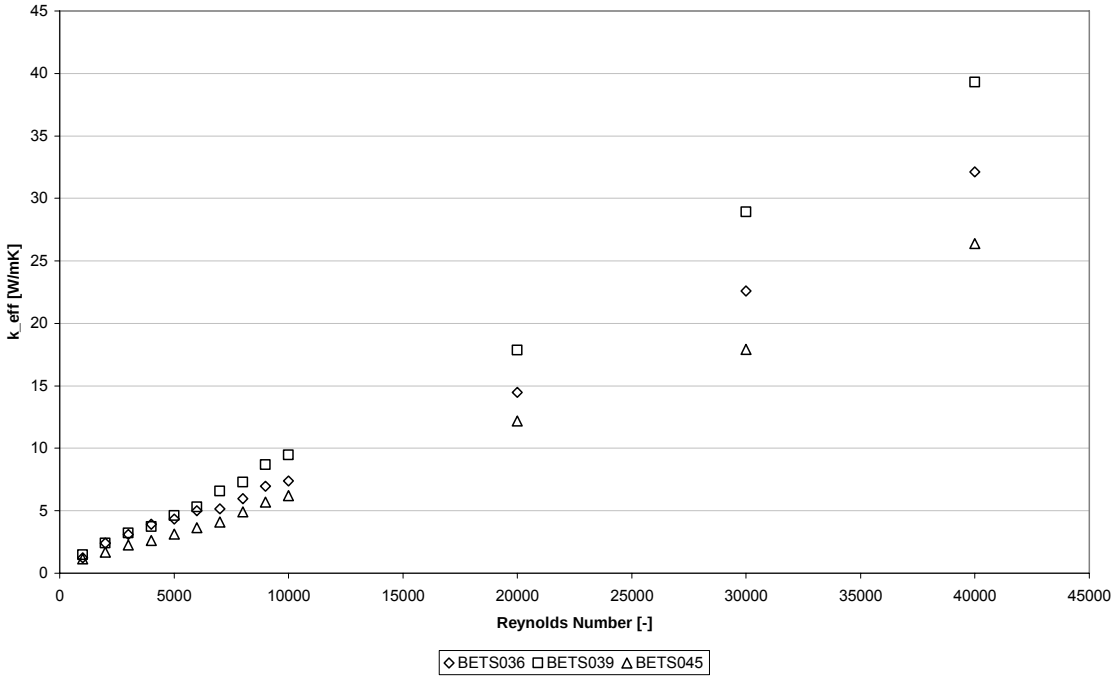

Figure 6-11: Effective thermal conductivities comparison as the porosity changes.

6.4.2. Cylindrical grid

It is stated in Appendix K that the results simulated using the Cartesian mesh proved to be sufficient for the solution that is grid independent. Because the experimental test sections have square cross sections, the Cartesian grid is a better representation of the geometry.

Table 6-5 shows the calculated results of the effective thermal conductivities obtained from the CFD simulations using the cylindrical grid for the three test sections. Comparing the results in Table 6-4 and Table 6-5 it can be seen that there is a negligible difference between the results obtained from the simulations performed on the two grids. It can therefore be concluded that the area of the flow field in the four corners apparently (Figure 6-10) has a very small influence on the values of k_{eff} .

Table 6-5: Simulations results of the effective conductivities using the cylindrical grid.

	BETS036	BETS039	BETS045
Reynolds Number	Effective thermal conductivity k_{eff}	Effective thermal conductivity k_{eff}	Effective thermal conductivity k_{eff}
[-]	[W/m K]	[W/m K]	[W/m K]
1000	1.2818	1.4214	1.0433
5000	4.3176	4.4567	2.9722
10000	7.3902	9.8053	5.8805
40000	32.2524	38.2487	21.9002

The maximum and minimum values calculated are 38.2487 *W/mK* and 1.0433 *W/mK*, respectively.

6.4.3. Temperature profiles

The temperature profiles play an important role in the evaluation of the effect of dispersion on the fluid effective thermal conductivity k_{eff} for a packed bed. The theory and methodology followed here have been developed and discussed in Appendix H; it is also partially discussed in Section 6.3: Simulation method. Figure 6-12 and Figure 6-13 show the temperature profiles for the BETS045 CFD (simulated) data and experimental data.

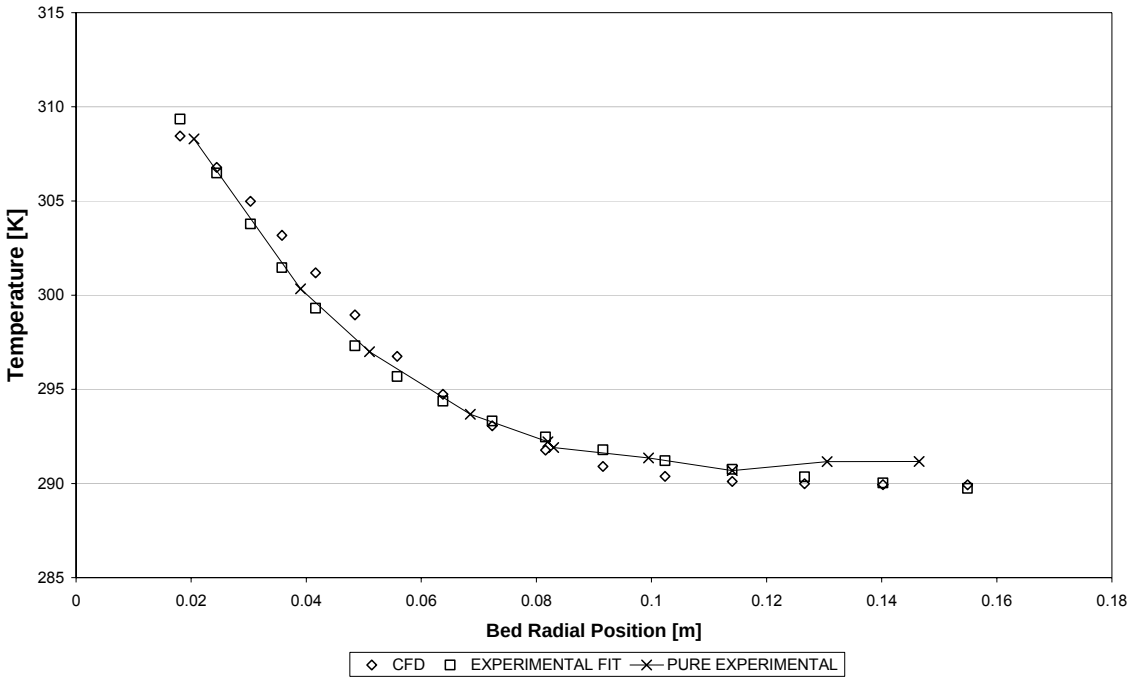

Figure 6-12: Bottom temperature profile for BETS045 at 1000 Reynolds Number.

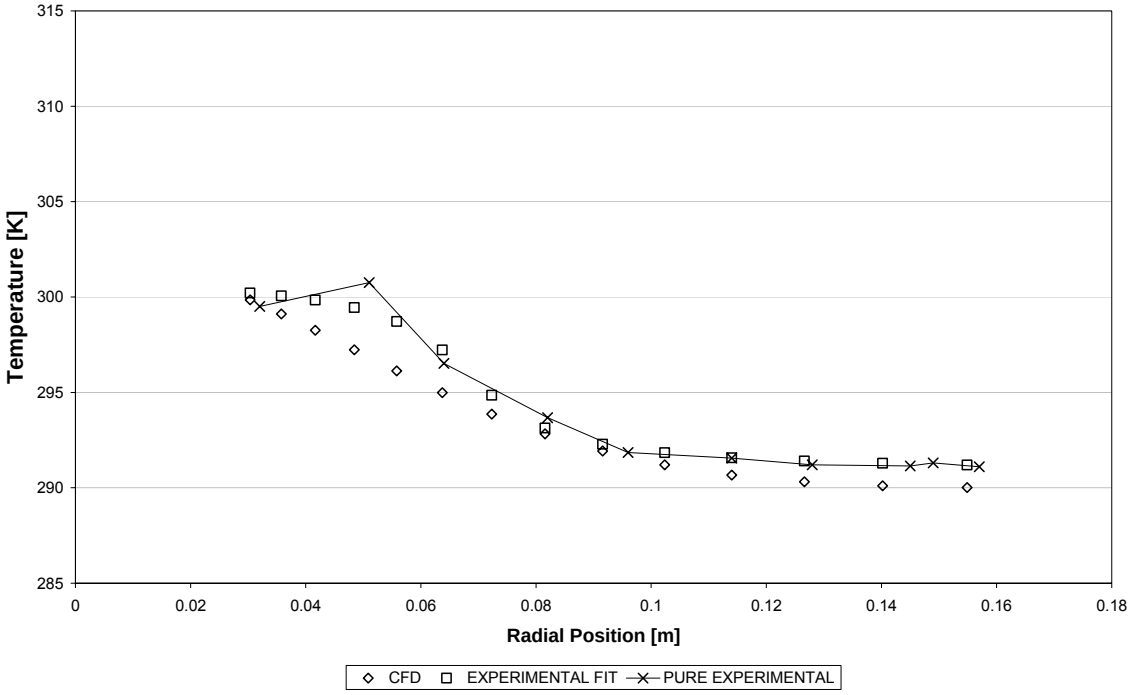

Figure 6-13: Top temperature profile for BETS045 at 1 000 Reynolds Number.

In the two figures, the good agreement between the CFD data and the experimental data is seen. These agreements are evaluated or quantified by calculating the so-called R-squared value R^2 for the fit between the CFD temperature profile and the experimental temperature profile. The R^2 value, which is given in Equation (6.7), is used to evaluate the fit between (with reference toFigure 6-12 and Figure 6-13):

- the experimental fit (as described in Appendix H), and
- the CFD results (as determined through the search routine in Figure 6-9.

For a good fit the R^2 value must be close to unity (1).

For the calculated temperature values $T_{EXPERIMENTAL\,FIT}$ and the CFD extracted temperatures T_{CFD} (in Figure 6-12 and Figure 6-13) , the R^2 value is calculated as follows:

$$R^2 = 1 - \frac{SSE}{SST} \tag{6.7}$$

Where:

$$SSE = \sum_N \left(T_{CFD} - T_{EXPERIMENTAL\,FIT} \right)^2,$$

$$SST = \left(\sum_{N} T^2_{EXPERIMENTAL\ FIT} \right) - \frac{\left(\sum_{N} T_{EXPERIMENTAL\ FIT} \right)^2}{N},$$

N = number of fitted points at the bottom or top layer measurement.

R^2 values that are calculated using Equation (6.7) are shown in Figure 6-14 to Figure 6-16 for each Reynolds number for the three test sections. It is seen that all the runs have good agreement except for the BETS045 top temperature profiles.

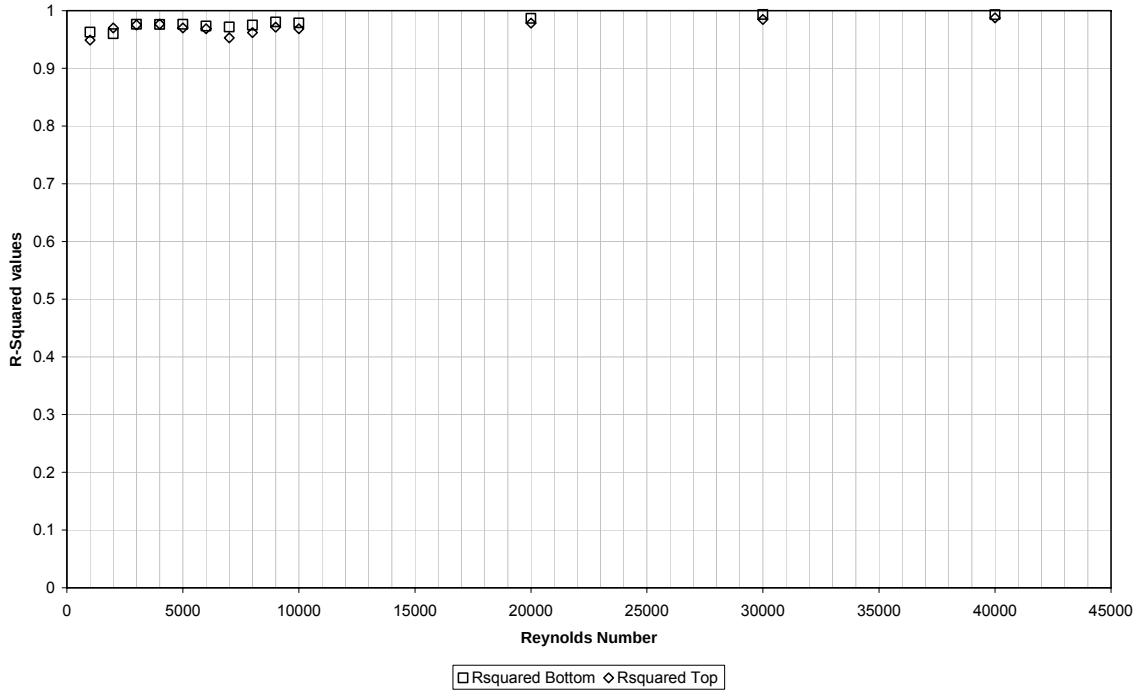

Figure 6-14: R^2 **-**values between BETS036 braiding temperature profile experimental results and the CFD braiding temperature profile results.

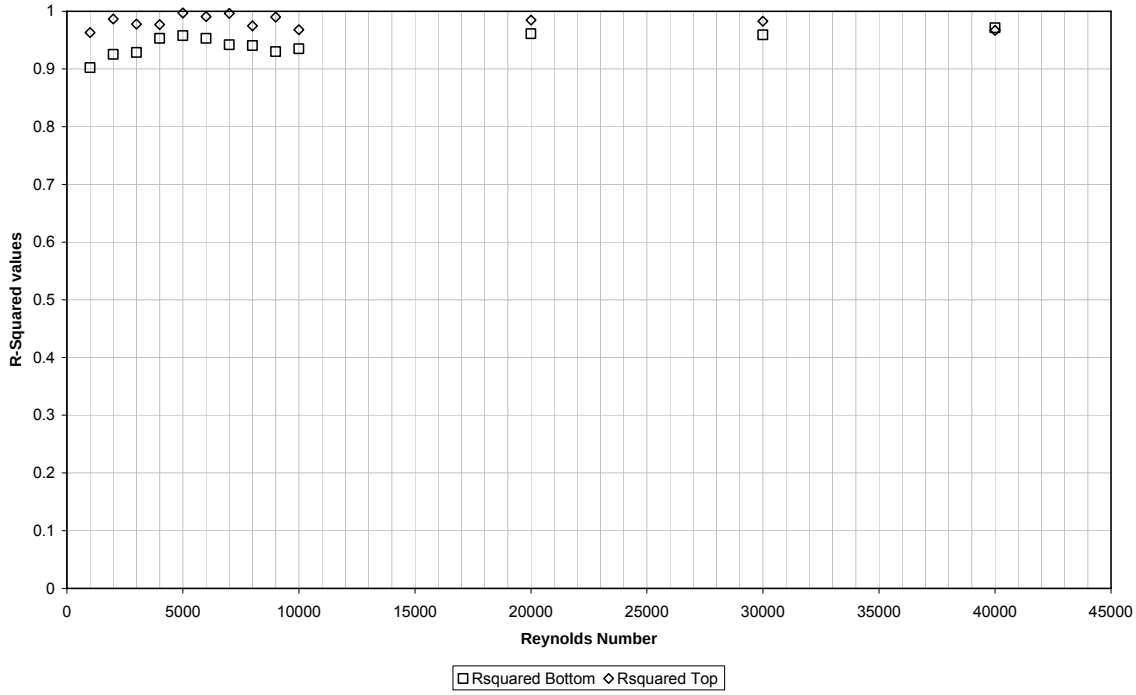

Figure 6-15: R^2 **-**values between BETS039 braiding temperature profile experimental results and the CFD braiding temperature profile results.

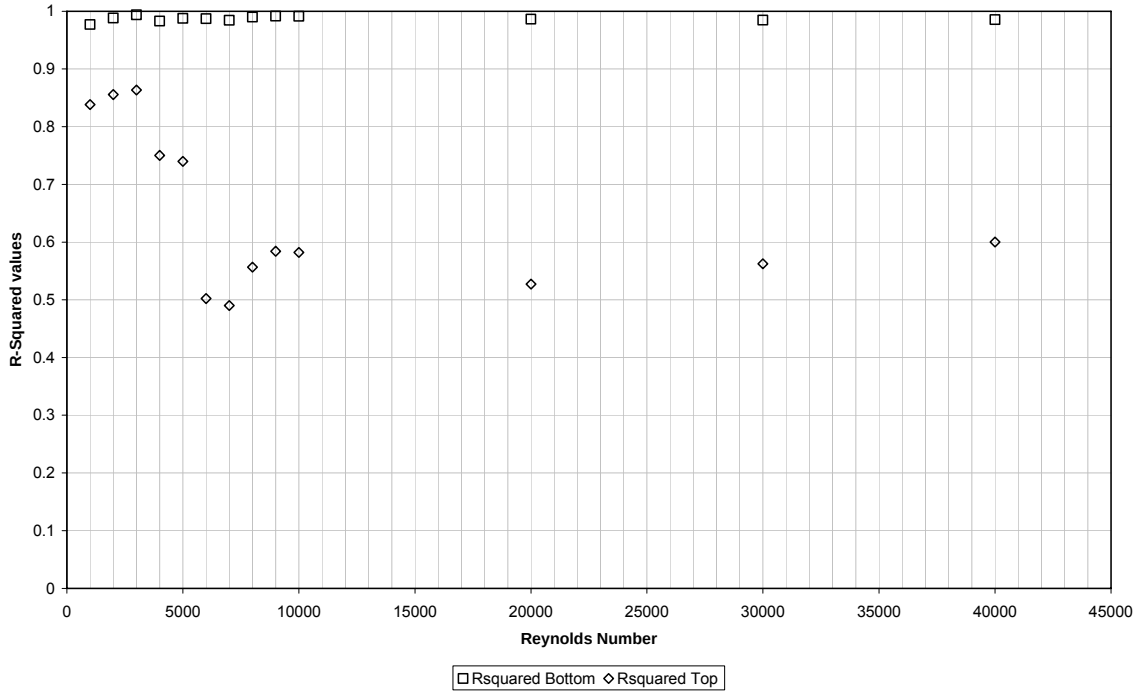

Figure 6-16: R^2 -values between BETS045 braiding temperature profile experimental results and the CFD braiding temperature profile results.

R^2-values for BETS045 at the top layer show that there is a large disparity between the CFD results and the experimental results. The values indicate a maximum of 0.7 and a minimum of 0.49 between 4 000 Reynolds number and 40 000 Reynolds number at the top layer.

However, the results show that there is a good agreement between the CFD results and the experimental results at the bottom layer. Hypothetically, the effective thermal conductivity is isotropic and the dispersion effect is anisotropic which applies for all the levels in the axial direction. Therefore the results for the BETS045 test section are in contrary to this hypothesis. A possible reason could be that wrong measurement were made at the top layer.

6.5. *Uncertainty in the effective conductivity calculation*

The calculated effective thermal conductivity k_{eff} in the CFD simulations is a function of the braiding temperature profiles, i.e.:

$$k_{eff} = f\left(T_{1b}, T_{2b}, ..., T_{Nb}\right) \tag{6.8}$$

With:

$T_{1b}, T_{2b}, ..., T_{Nb}$ = the braiding temperature measurements at the top and bottom layers.

According to Equation (4.4), the uncertainty in the calculated variable k_{eff} can be estimated as follows:

$$u\left(k_{eff}\right) = \sqrt{\left(\frac{\partial k_{eff}}{\partial T_{1b}} u\left(T_{1b}\right)\right)^2 + \left(\frac{\partial k_{eff}}{\partial T_{1b}} u\left(T_{2b}\right)\right)^2 + \ldots + \left(\frac{\partial k_{eff}}{\partial T_{Nb}} u\left(T_{Nb}\right)\right)^2} \tag{6.9}$$

With:

$u\left(T_{1b}\right), u\left(T_{2b}\right), ..., u\left(T_{Nb}\right)$ = final uncertainties for each temperature that was measured in the braiding profile at the top and bottom layers, and

$\frac{\partial k_{eff}}{\partial T_{1b}}, \frac{\partial k_{eff}}{\partial T_{1b}}, \ldots, \frac{\partial k_{eff}}{\partial T_{Nb}}$ = partial derivatives which are interpreted as the change in the effective conductivity k_{eff}, due to the change in any one of the temperatures that was measured in the braiding profile at the top and bottom layers.

Equation (6.9) was evaluated for the temperature profiles that were measured in the BETS experiments or determined with the CFD simulations. The partial derivatives can therefore be obtained by varying the braiding profile temperature within their respective uncertainty bands or by perturbing each point in the profile with a conservative value (± 1°C was used in this case). The former case is imposed onto the experimental data by changing the polynomial fit constants that are described in Appendix H. For the latter case the values for $u(T_{1b}), u(T_{2b}), ..., u(T_{Nb})$ were taken as the difference between the experimental temperature profile and the CFD temperature at each point that was perturbed.

The final uncertainty for each temperature that was measured on the braiding profile was estimated from the non-dimensional values used to normalise the braiding profiles (Appendix F). The final uncertainty was estimated as follows:

$$u\left(T_{braiding\ profile_N}\right) = \sqrt{\begin{array}{l}\left(\frac{\partial T_{braiding\ profile_N}}{\partial \overline{T}_{[-]}} u\left(\overline{T}_{[-]}\right)\right)^2 + \\ \left(\frac{\partial T_{braiding\ profile_N}}{\partial \overline{T}_{braiding\ gas}} u\left(\overline{T}_{braiding\ gas}\right)\right)^2 + \\ \left(\frac{\partial T_{braiding\ profile_N}}{\partial \overline{T}_{cold\ gas}} u\left(\overline{T}_{cold\ gas}\right)\right)^2\end{array}} \qquad (6.10)$$

Where:

$\overline{T}_{[-]}$ = the average non-dimensional braiding profile temperature,

$\overline{T}_{braiding\ gas}$ = the average braiding gas inlet temperature,

$\overline{T}_{cold\ gas}$ = the average gas inlet temperature,

$T_{braiding\ profile_N} = \overline{T}_{[-]} \times \left(\overline{T}_{braiding\ gas} - \overline{T}_{cold\ gas} \right) + \overline{T}_{cold\ gas}$ = normalized braiding temperature profile.

Therefore values for $u\left(T_{1b}\right), u\left(T_{2b}\right), ..., u\left(T_{Nb}\right)$ in Equation (6.9) are formulated as follows for calculations:

$$\begin{aligned} u\left(T_{Nb}\right) &= u\left(T_{braiding\ profile_N}\right)_{Nb} \\ u\left(T_{Nb}\right) &= \left| T_{CFD} - T_{EXPERIMENTAL} \right|_{Nb} \end{aligned} \tag{6.11}$$

For illustrative purposes, the calculated effective conductivity $\left(k_{eff}\right)_{Nb}$ due to the change in the braiding temperature $u\left(T_{Nb}\right)$ is formulated as follows:

$$\left(k_{eff}\right)_{Nb} = f\left(T_{1b}, T_{2b}, ..., T_{Nb} \pm u\left(T_{Nb}\right)\right) \tag{6.12}$$

For clarity, the *Nb* point temperature value in the braiding temperature profile was formulated as follows:

$$\begin{aligned} T_{Nb} &= \left(T_{braiding\ profile_N}\right)_{Nb} \\ &= \left(\overline{T}_{[-]}\right)_{Nb} \times \left(\overline{T}_{braiding\ gas} - \overline{T}_{cold\ gas}\right) + \overline{T}_{cold\ gas} \end{aligned} \tag{6.13}$$

It can therefore be seen that the uncertainties in the other temperature measurements at the inlet of the test section are included in the overall uncertainty calculation of the effective thermal conductivity.

The change in the calculated effective thermal conductivity $\left(\Delta k_{eff}\right)_{Nb}$, due to the change in the braiding temperature $u\left(T_{Nb}\right)$, is formulated as follows:

$$\left(\Delta k_{eff}\right)_{Nb} = \left| \left(k_{eff}\right)_{Nb} - k_{eff} \right| \tag{6.14}$$

The partial derivatives in Equation (6.9) could be calculated as follows:

$$\frac{\partial k_{eff}}{\partial T_{Nb}} = \frac{\left(\Delta k_{eff}\right)_{Nb}}{\Delta T_{Nb}} \tag{6.15}$$

With:

$$\Delta T_{Nb} = T_{Nb} \pm u\left(T_{Nb}\right).$$

The final uncertainty in k_{eff} was calculated as follows:

$$u\left(k_{eff}\right)_{Final} = \sqrt{\left(u\left(k_{eff}\right)_{\substack{Experimental\\Temperature\\Profile}}\right)^2 + \left(u\left(k_{eff}\right)_{\substack{CFD\\Temperature\\Profile}}\right)^2} \tag{6.16}$$

With:

$u\left(k_{eff}\right)_{\substack{Experimental\\Temperature\\Profile}}$, $u\left(k_{eff}\right)_{\substack{CFD\\Temperature\\Profile}}$ = calculated using Equation (6.9).

The following experimental tests were used to calculate the effective fluid thermal conductivity uncertainty:

- *BETS039 at Re = 40 000*

The maximum values of the calculated effective thermal conductivities for all test sections at the maximum Reynolds number were obtained for these tests. The tests were therefore chosen to calculate the uncertainty at the maximum Reynolds number.

- *BETS045 at Re = 1000*

The minimum values of the calculated effective thermal conductivities for all test sections at the minimum Reynolds number were obtained for these tests. The tests were therefore chosen to calculate the uncertainty at the minimum Reynolds number.

Simulated results for Equation (6.12) to Equation (6.15) are shown from Table 6-6 to Table 6-9 and and the calculated uncertainties are summarized in Table 6-10.

Table 6-6: Simulations results for Equation (6.12) to Equation (6.15) used in the effective thermal conductivities uncertainties calculations at the maximum Reynolds number = 40 000 (Experimental measurements).

k_{eff}	Nb	$\left(k_{eff}\right)_{Nb}^{+}$	$\left(k_{eff}\right)_{Nb}^{-}$	$u\left(T_{Nb}\right)=u\left(T_{braiding\ profile_N}\right)_{Nb}$	$\frac{\partial k_{eff}}{\partial T_{Nb}}$	$\left(\frac{\partial k_{eff}}{\partial T_{Nb}}u\left(T_{Nb}\right)\right)^2$
[W/mK]	**[-]**	**[W/mK]**	**[W/mK]**	**[°C]**	**[W/mK^2]**	**[(W/mK)^2]**
38.015	**1**	39.193	39.142	1.201	0.021	6.585E-04
	2	38.971	39.127	1.314	0.060	6.119E-03
	3	39.570	39.575	1.440	0.002	6.553E-06
	4	39.113	39.578	1.362	0.171	5.400E-02
	5	39.351	39.041	1.181	0.131	2.406E-02
	6	39.904	38.553	1.231	0.549	4.561E-01
	7	39.082	39.019	1.369	0.023	1.002E-03
	8	38.546	39.676	1.695	0.333	3.189E-01
	9	39.193	39.041	1.175	0.065	5.796E-03
	10	40.355	40.359	1.291	0.001	3.716E-06
	11	38.213	38.100	1.128	0.050	3.156E-03
	12	38.125	38.047	1.129	0.034	1.493E-03
	13	38.258	38.128	1.185	0.055	4.210E-03
	14	38.216	38.213	1.524	0.001	3.011E-06
	15	38.175	38.240	1.195	0.027	1.062E-03
	16	38.216	38.213	1.129	0.002	3.011E-06
	17	38.157	38.213	1.128	0.025	7.755E-04
	18	38.193	38.284	1.249	0.036	2.070E-03
	19	37.254	38.486	1.402	0.439	3.793E-01
	20	38.110	38.122	1.212	0.005	3.446E-05
	21	38.287	38.288	1.132	0.000	2.813E-08
	22	37.916	38.287	1.129	0.165	3.449E-02

Table 6-7: Simulations results for Equation (6.12) to Equation (6.15) used in the effective thermal conductivities uncertainties calculations at the minimum Reynolds number = 1 000 (Experimental measurements).

k_{eff}	Nb	$\left(k_{eff}\right)_{Nb}^{+}$	$\left(k_{eff}\right)_{Nb}^{-}$	$u\left(T_{Nb}\right)=u\left(T_{braiding\ profile_N}\right)_{Nb}$	$\frac{\partial k_{eff}}{\partial T_{Nb}}$	$\left(\frac{\partial k_{eff}}{\partial T_{Nb}}u\left(T_{Nb}\right)\right)^2$
[W/mK]	**[-]**	**[W/mK]**	**[W/mK]**	**[°C]**	**[W/mK^2]**	**[(W/mK)^2]**
1.165	**1**	1.211	1.213	1.084	0.00092	1.000E-06
	2	1.200	1.169	1.132	0.01367	2.397E-04
	3	1.214	1.169	1.171	0.01905	4.975E-04
	4	1.213	1.205	1.102	0.00362	1.591E-05
	5	1.214	1.209	1.089	0.00220	5.736E-06
	6	1.203	1.206	1.090	0.00150	2.663E-06
	7	1.195	1.207	1.131	0.00541	3.746E-05
	8	1.200	1.209	1.158	0.00365	1.785E-05
	9	1.197	1.169	1.119	0.01253	1.965E-04
	10	1.117	1.156	1.114	0.01747	3.785E-04
	11	1.156	1.157	1.119	0.00042	2.157E-07
	12	1.157	1.160	1.253	0.00117	2.134E-06
	13	1.158	1.156	1.118	0.00058	4.222E-07
	14	1.159	1.156	1.120	0.00100	1.257E-06
	15	1.159	1.159	1.114	0.00001	9.470E-11
	16	1.149	1.139	1.114	0.00450	2.507E-05
	17	1.158	1.151	1.137	0.00267	9.240E-06
	18	1.129	1.175	1.204	0.01910	5.291E-04
	19	1.111	1.184	1.113	0.03272	1.328E-03

Table 6-8: Simulations results for Equation (6.12) to Equation (6.15) used in the effective thermal conductivities uncertainties calculations at the maximum Reynolds number = 40 000 (CFD calculations).

k_{eff}	Nb	$\left(k_{eff}\right)^{+}_{Nb}$	$\left(k_{eff}\right)^{-}_{Nb}$	$u\left(T_{Nb}\right)=\left\lvert T_{CFD}-T_{EXPERIMENTAL}\right\rvert_{Nb}$	$\frac{\partial k_{eff}}{\partial T_{Nb}}$	$\left(\frac{\partial k_{eff}}{\partial T_{Nb}}u\left(T_{Nb}\right)\right)^{2}$
[W/mK]	**[-]**	**[W/mK]**	**[W/mK]**	**[°C]**	**[W/mK^2]**	**[(W/mK)^2]**
38.015	**1**	37.600	38.433	1.139	0.4168	2.253E-01
	2	37.756	38.415	0.749	0.3298	6.096E-02
	3	37.919	38.112	1.084	0.0966	1.096E-02
	4	38.019	38.011	1.523	0.0043	4.308E-05
	5	38.069	37.961	1.402	0.0537	5.669E-03
	6	38.071	37.959	0.972	0.0560	2.961E-03
	7	38.063	37.968	0.617	0.0476	8.623E-04
	8	38.036	37.994	0.309	0.0208	4.121E-05
	9	38.026	38.004	0.310	0.0111	1.181E-05
	10	38.026	38.004	0.310	0.0111	1.181E-05
	11	37.525	38.515	2.544	0.4947	1.584E+00
	12	37.589	38.448	0.791	0.4294	1.155E-01
	13	37.589	38.448	2.574	0.4294	1.222E+00
	14	37.915	38.116	2.034	0.1003	4.163E-02
	15	37.996	38.036	0.278	0.0201	3.136E-05
	16	38.090	37.941	0.745	0.0742	3.063E-03
	17	38.081	37.950	0.773	0.0655	2.562E-03
	18	38.059	37.973	0.575	0.0431	6.131E-04
	19	38.039	37.993	0.070	0.0228	2.547E-06
	20	38.019	38.012	0.385	0.0034	1.723E-06
	21	38.017	38.015	0.664	0.0010	3.996E-07
	22	38.017	38.015	0.664	0.0010	3.996E-07

Table 6-9: Simulations results for Equation (6.12) to Equation (6.15) used in the effective thermal conductivities uncertainties calculations at the minimum Reynolds number = 1 000 (CFD calculations).

k_{eff}	Nb	$\left(k_{eff}\right)_{Nb}^{+}$	$\left(k_{eff}\right)_{Nb}^{-}$	$u\left(T_{Nb}\right)=\left\|T_{CFD}-T_{EXPERIMENTAL}\right\|_{Nb}$	$\frac{\partial k_{eff}}{\partial T_{Nb}}$	$\left(\frac{\partial k_{eff}}{\partial T_{Nb}}u\left(T_{Nb}\right)\right)^2$
[W/mK]	**[-]**	**[W/mK]**	**[W/mK]**	**[°C]**	**[W/mK^2]**	**[(W/mK)^2]**
1.165	**1**	1.183	1.148	0.363	0.01742	4.000E-05
	2	1.174	1.158	2.209	0.00826	3.330E-04
	3	1.168	1.164	2.235	0.00182	1.664E-05
	4	1.163	1.168	0.295	0.00213	3.933E-07
	5	1.162	1.169	0.349	0.00329	1.319E-06
	6	1.163	1.169	0.904	0.00292	6.962E-06
	7	1.164	1.168	1.089	0.00218	5.648E-06
	8	1.164	1.167	1.176	0.00148	3.038E-06
	9	1.165	1.167	1.184	0.00103	1.483E-06
	10	1.136	1.196	0.901	0.02973	7.179E-04
	11	1.157	1.175	1.884	0.00905	2.907E-04
	12	1.162	1.170	1.636	0.00375	3.753E-05
	13	1.162	1.169	0.374	0.00364	1.851E-06
	14	1.171	1.161	0.695	0.00489	1.153E-05
	15	1.162	1.170	0.881	0.00384	1.144E-05
	16	1.163	1.168	0.840	0.00249	4.386E-06
	17	1.164	1.167	0.645	0.00134	7.501E-07
	18	1.165	1.166	0.374	0.00060	5.023E-08
	19	1.166	1.166	0.183	0.00008	2.309E-10

All the uncertainties are summarised in Table 6-10 together with the final uncertainty as calculated with Equations (6.16) and (6.15). The final uncertainties in the effective thermal conductivities at the maximum and minimum Reynolds number are 5.693 % and 5.923 % respectively. These uncertainties are higher than the original target of ±4.5 % (Rousseau, 2005).

Table 6-10: Summary of all the effective thermal conductivities uncertainties calculations at the maximum and minimum Reynolds numbers with the final uncertainty.

	Experimental Measurements		CFD Calculations		Final Uncertainty	
Reynolds Number	$u\left(k_{eff}\right)$	$\frac{u\left(k_{eff}\right)}{k_{eff}}\times 100$	$u\left(k_{eff}\right)$	$\frac{u\left(k_{eff}\right)}{k_{eff}}\times 100$	$u\left(k_{eff}\right)_{Final}$	$\left(\frac{u\left(k_{eff}\right)}{k_{eff}}\right)_{Final}\times 100$
[-]	**[W/m K]**	**[%]**	**[W/m K]**	**[%]**	**[W/m K]**	**[%]**
1000	0.057	4.918	0.039	3.305	0.069	5.923
40000	1.137	2.991	1.810	4.761	2.137	5.623

6.6. Comparisons with the previous authors

Most authors separate the packed pebble bed effective thermal conductivity formulation into two terms (Bunnell *et al.* (1949), Schlünder and Zehner (1973), Borkink and Westerterp (1992), Al-Ali *et al.* (2000), Ding *et al.* (2006), Endo *et al.* (1964)). The one term is independent of the fluid flow (molecular thermal conduction) and the other is dependent on the lateral mixing of the fluid between the packed pebbles or particles (convective contribution).

From the literature, the lateral mixing term in Equation. (2.8) was found to be influenced by the geometric forms of the bed and the fluid flow rate. It was also found that its applicability (Endo *et al.* 1964) is not limited to either to the liquid – solid systems or to gas – solid systems. Typical correlations by previous authors presented the ratio of radial diffusive transport to convective transport for a specific packed bed geometry and particle type. By using Equation (2.2), the lateral mixing term in Equation (2.8) can be rewritten as follows for radial thermal dispersion:

$$\frac{\left(k_{er}\right)_{lm}}{k_g}=\frac{Pe}{K_r}=\frac{1}{K_r}\frac{\rho c_p u_o D_p}{k_g} \tag{6.17}$$

Based on the initial assumptions that were made for Equation (2.6), and hence Equation (6.5):

- the current study also takes the effects of lateral mixing into consideration with an isotropic effective thermal fluid conductivity k_{eff},

- the stagnant effect on the effective thermal conductivity k_{beff}^{o} due to the motionless fluid is not evaluated,
- the effective thermal fluid conductivity k_{eff} is however evaluated for the temperature profile that is predominantly in the transversal direction of a packed bed, and
- by the virtue of the transversal temperature distribution and therefore of the temperature field, the anisotropic behaviour of the thermal dispersion is in the transversal direction in the Cartesian bed (Figure 6-5) and in the radial direction in the cylindrical bed (Figure 6-6); it does not change for the two similar geometries that differs only due to the attributes shown in Figure 6-10 because of the little difference in the values of k_{eff} that were calculated using both geometries (Table 6-4 and Table 6-5).

It is therefore appropriate and relevant to compare the current results with the work that was discussed in the Literature survey (Chapter 2) which is based on the cylindrical packed beds.

The value of the thermal dispersion quantity or effect K_r (deemed to be transversal or radial) can be calculated by determining effective Peclet number Pe_{eff} based on the effective thermal conductivity k_{eff} in Table 6-4 , i.e:

$$Pe_{eff} = \frac{\rho c_p u_o D_p}{k_{eff}} \tag{6.18}$$

Therefore from Equation (6.17)

$$\begin{aligned} &\frac{k_{er}}{k_g} \approx \frac{(k_{er})_{lm}}{k_g} = \frac{k_{eff}}{k_g} = \frac{Pe}{K_r} = \frac{1}{K_r}\frac{\rho c_p u_o D_p}{k_g} \\ \Leftrightarrow \quad &\frac{k_{eff}}{k_g} = \frac{1}{K_r}\frac{\rho c_p u_o D_p}{k_g} \\ \therefore \quad &K_r = \frac{1}{k_{eff}}\rho c_p u_o D_p = Pe_{eff} \end{aligned} \tag{6.19}$$

The calculations for Equation (6.19) were done using the fluid properties from the Engineering Equation Solver (EES) program; values of the thermal dipersion quantity K_r or the effective Peclet number Pe_{eff} are given in Table 6-11. These values are plotted in Figure 6-17 against the Reynolds numbers for which they were calculated for the three respective test sections.

Table 6-11: Summary of the Peclet numbers based on the effective conductivities k_{eff} as the Reynolds number increases.

Reynolds Number	K_r		
	BETS036	BETS039	BETS045
1000	13.7141	11.5822	14.8258
2000	14.0820	14.1242	20.3644
3000	16.3949	15.9996	22.6277
4000	17.4651	18.3367	26.1215
5000	19.6174	18.6023	27.3701
6000	20.4486	19.3176	28.0751
7000	23.1533	18.2306	29.212
8000	22.8442	18.7694	27.8135
9000	22.1858	17.7899	27.1019
10000	23.1333	18.2788	27.5939
20000	23.9423	19.4661	28.2665
30000	23.2164	18.5691	29.1696
40000	22.0022	18.2578	26.7596

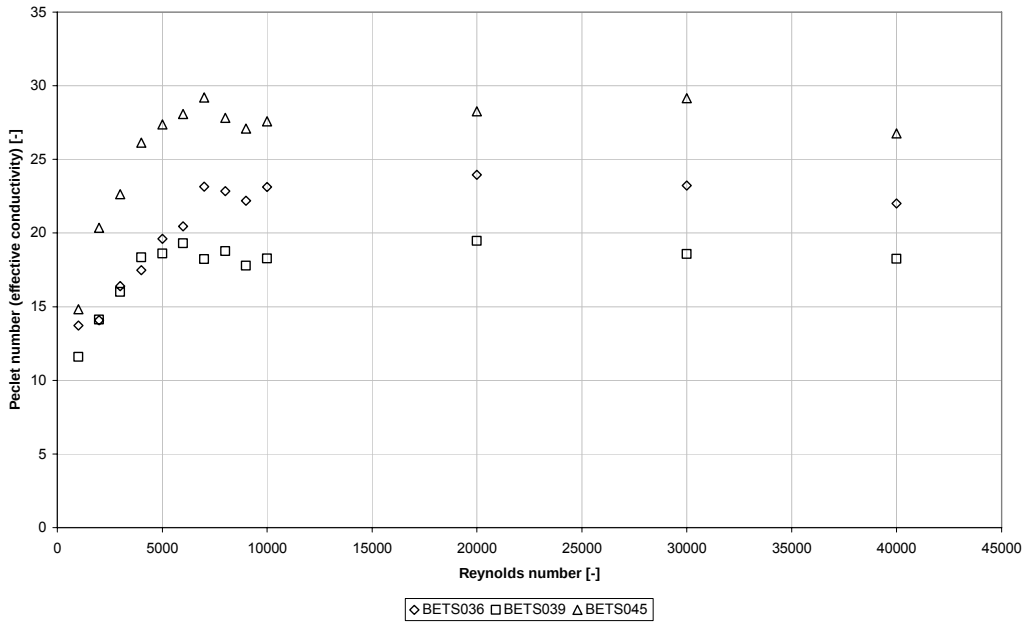

Figure 6-17: Peclet number Pe_{eff} based on the effective conductivities k_{eff} as the Reynolds number increases for all three test sections.

The following points can be made with the literature in hand:

- Figure 6-17 shows that, thermal disperion values are somewhat higher than the value of $K_r = 8$, which was firstly determined by Schlünder and Zehner (1973).
- The thermal dispersion values are however larger for the BETS045 with the homogeneous porosity of 0.45; this implies less enhancement of thermal conductivity as compared to the other test sections with smaller homogeneous porosities of 0.36 and 0.39. A Krishcke *et al.* (2000) evaluation (including other work as reevaluated in Figure 2-3) shows the same effect when considering the initial account that was given by Marivoet *et al*. (1974) about the radial porosity profile of the randomly packed bed.
- An assessment done by Kaviany (1991) on the work from Gunn and Pryce (1969), presented the axial dispersion for experiments that were conducted in the structured packed bed. It was deduced from Gunn and Pryce (1969) that the radial mass dispersion is undetermined because of the low mixing in the radial direction of the structured bed. However, Gunn and Pryce (1969) calculations for the radial

mass dispersion showed a similar trend as seen in the comparison that is done in Figure 6-18 with the current work. Mass dispersion correlation from the work of Krishcke *et al.* (2000) has the limiting value of 8.It is however, not within the scope of this work to relate the mass dispersion and the thermal dispersion, but the trend looks similar.

- Figure 6-19 shows the results of Dixon and Cresswell (1979) predictions, the current work (BETS036, BETS039, BETS045), Gunn and Khalid (1975), and Kunii and Ono (1968a). It is seen again that the structured bed exhibit high values of thermal dispersion quantities as compared to the randomly packed bed.

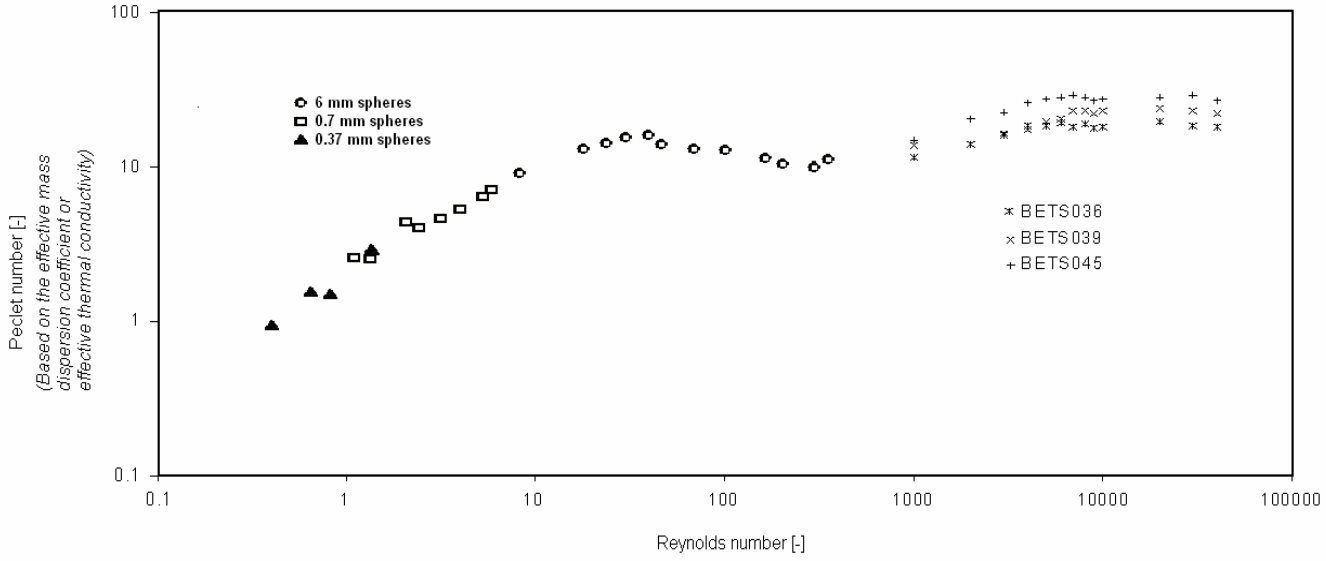

Figure 6-18: Comparison between the evaluation of the thermal disperision from current work and evaluation of the mass dispersion from Gunn and Pryce (1969).

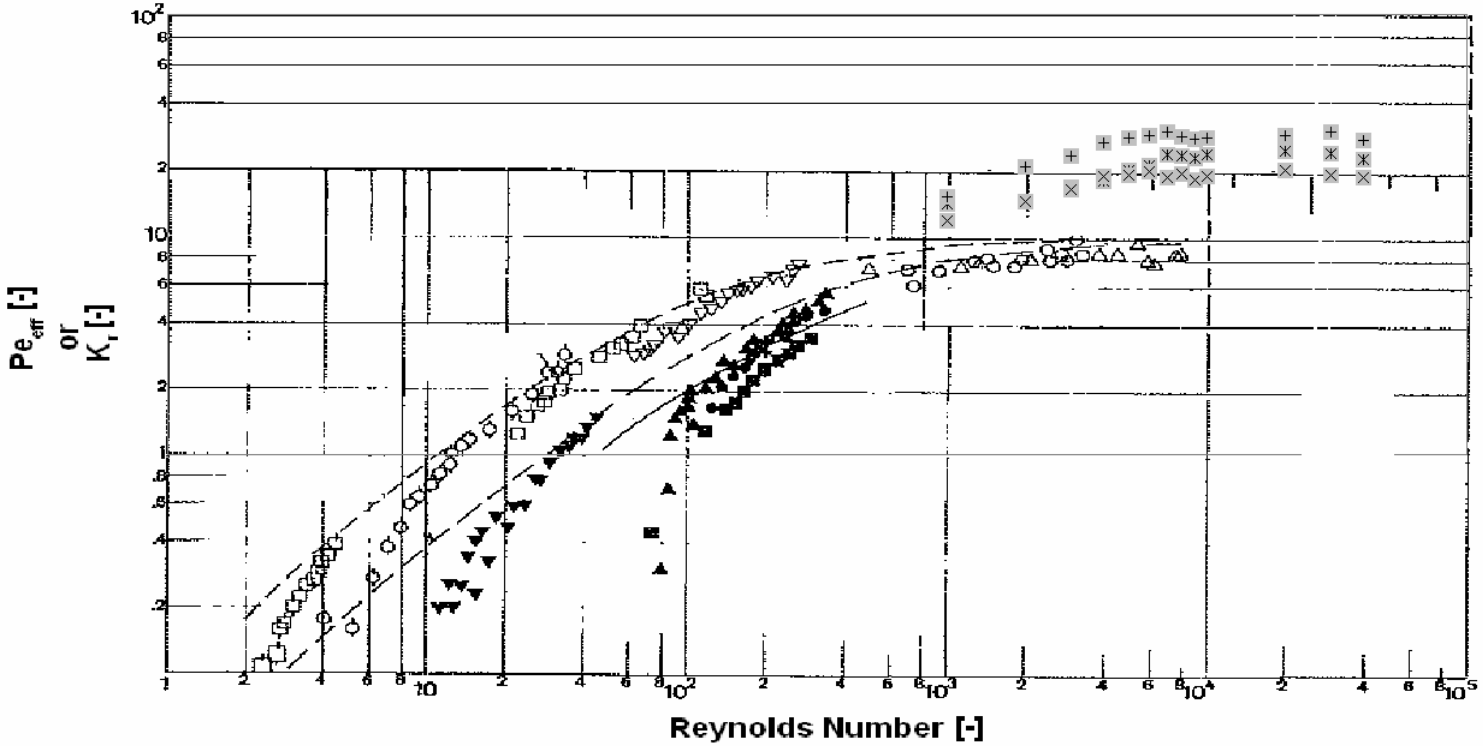

Symbol	Packing	d_t/d_p	Workers
●	6.8 mm nickel	14.0	Gunn and Khalid (1975)
■	6.4 mm steel	14.9	Gunn and Khalid (1975)
▼	1.0 mm lead	95.2	Gunn and Khalid (1975)
▲	7.0 mm lead	13.6	Gunn and Khalid (1975)
▽	6.0 mm glass	15.9	Gunn and Khalid (1975)
+	BETS045		
×	BETS039		

Symbol	Packing	d_t/d_p	Workers
□	0.5 mm glass	190.5	Gunn and Khalid (1975)
○	1.15 mm glass	82.8	Gunn and Khalid (1975)
□	3.0 mm glass	31.8	Gunn and Khalid (1975)
○	28 mm celite	5.0	Kunii and Ono (1968b)
△	42 mm celite	3.3	Kunii and Ono (1968b)
*	BETS036		
——	Dixon and Cresswell (1979)		

Figure 6-19: Comparison between the current work and the work from Gunn and Khalid (1975), and Kunii et al (1968).

6.7. Summary

This Chapter gave the background theory with regards to the CFD simulation and Figure 6-7 showed the simulation method used to calculate the effective conductivity k_{eff} from the experimental results. The use of the cylindrical grid in the CFD simulation bears negligible influence in the effective conductivity k_{eff} for all three BETS test sections. This can be seen in the results shown in Table 6-5 and Table 6-4. The final uncertainties in the effective thermal conductivities at the maximum and minimum Reynolds number are 5.693 % and 5.923 % respectively. These uncertainties are higher as compared to the original target of ±4.5 % (Rousseau, (2005)).

Many authors have predicted effective Peclet number (or thermal dispersion) to the value between 8 and 10 for randomly packed beds. This value is also obtained at relatively high Reynolds number (in the order of Re = 10000 in Figure 6-19). Theoretical prediction by Dixon and Cresswell (1969) also gives the values below 10. The mass dispersion value has also a limiting value that ranges between 8 and10 respectively, from the work by Krishcke *et al.* (2000) on the mass dispersion correlation and, the work results from Gunn and Pryce (1969) on the randomly packed bed (Figure 6-18).

6.8. Remarks

The calculations made in the current study, shows relatively high values of thermal dispersion (calculated as either K_r or Pe_{eff}). These values imply that convective heat transport dominates conductive heat transport.

Although they were able to determine that axial mass dispersion, Gunn and Pryce (1969) were not able to determine radial dipersion in the structured packed bed due to low radial mixing. Low radial mixing (and therefore low conductive heat transfer to account for the convective heat transfer) is seen in the current study for the structured packed bed.

Relationship between the findings by Krischke (2001) and Marievoet (1974) suggest that the thermal dispersion effect is influenced by the porosity in the packed bed. This situation is seen by high values of thermal dispersion quantities (K_r or Pe_{eff}) in Figure 6-17) in BETS045 packed bed (with high porosity) as compared to both BETS036 and BETS039 packed beds (with low values of porosity).

This study also seems to suggest that the thermal dispersion is affected by the porous structure through the porosity and the structuredness (unstructured or structured) of the packed bed.

7. CONCLUSIONS AND RECOMMENATIONS

7.1. Introduction

The aim of this work was to evaluate the enhanced thermal fluid conductivity from the experimental results for gas flow through a structured bed packed pebble beds. A CFD simulation was developed by using the geometric properties of the test sections and the experimental conditions at which the experiment were conducted. The enhancement of the thermal fluid conductivity was evaluated by calculating the effective Peclet numbers or thermal dispersion quantities (K_r or Pe_{eff}). These results were compared to the results that were found in the open literature.

7.2. Summary of the work

A good understanding in the dispersion effect was developed from the literature study of this work in Chapter 2. The chapter also highlighted the impact that can be made by this disstation in this field.

An overview of the test facility was presented in Chapter 3 with specific emphasis on the BETS experimental test setup employed for this study.

Chapter 4 outlined the uncertainty analysis in the experimental data. Generally, the final uncertainty in the experimental data is influenced by the errors in the measuring instruments and the fluctuations (noise) in the measured data. However, instruments that were used in the BETS experiments underwent calibration to ensure that correct data were measured. The instrument calibrations were done before the tests started and after the tests were completed. Re-calibrating the instruments highlighted a “drift” in measurements as tests progressed; this effect is regarded as drift uncertainty in the final uncertainty. The final uncertainty is calculated in terms of the measured variable or calculated variable from the measured data. The final measured variable uncertainty is either based in the combined effect from the three defined uncertainties or based in the maximum value in the three defined uncertainties.

Experimental results were presented in Chapter 5 showing that the tests were conducted under the specified requirements (Rousseau (2005)) for all three BETS test sections. The chapter also indicates the required variables needed in the CFD calculations.

Chapter 6 gave the simulation method that was implemented to calculate the effective thermal conductivities k_{eff} for all three BETS test sections. The current study evaluation results show a low thermal dispersion effect quantity as compared to the results found in the literature study.

7.3. Conclusions

This study was able to calculate the fluid effective thermal conductivities k_{eff} (Table 6-4) from the experimental results using the CFD model. In general, the CFD results that were produced agree well with the experimental results, except for the BETS045 packed bed. As stated a possible reason could be that a wrong measurement was made at the top layer measurement.

It was also shown that the results are practically insensitive to the cylindrical grid because the experiments were conducted using a Caretsian packed bed (Figure 4-2). The study estimated the uncertainties in the calculated effective conductivities k_{eff} which are summarised in Table 6-10. The maximum uncertainty calculated is 5.923 % which is slightly higher than the original target of ±4.5 % (Rousseau, (2005)).

The high values of thermal dispersion quantities (K_r or Pe_{eff}) implies that there is low conductive heat transfer as opposed to the convective heat transfer. Therefore radial mixing is low and this is attributed to the structured packing of the BETS test section. Therefore the effect of turbulent mixing in structured beds is concluded to be low as compared to randomly packed beds. This agrees with the observations of low pressure drop and shorter effective flow path as found in other investigations on the similar BETS structured bed (Pressure Drop Test Section) (du Toit (2008)).

7.4. Recommendations for further work

This study focussed on structured packed beds with pseudo-homogeneous porosity; the final correlation must be completed by doing simulations for the similar experimental work with an unstructured packed bed.

The study has shown a low thermal dispersion effect (enhanced effective conductivity in the structured bed as compared to the literature work that presented results for the unstructured bed. However, the scope for the HPTU plant experimental tests also included braiding effect tests for the randomly packed beds that are fully cylindrical. It is therefore recommended that this work be evaluated for those experiments for the final correlation to be used in the PBMR research. Furthermore, the current experimental setup can be developed to evaluate mass dispersion and thermal dispersion simulataneouly by aiding measurement of concentration levels inside the packed bed.

REFERENCES

- Al-Ali, H.H., Demirel, Y., Sharma, R.N., 2000. Technical Note: On the effective heat transfer parameters in a packed bed. International Journal of Heat and Mass Transfer 43, 327-332.
- Bauer, R., 1977. Effective radial heat conductivity of gas-flow through packed bed with particles of different form and large distribution. VDI – Research text 582.
- Bauer, R., Schlünder, E.U., 1978a. Effective radial thermal conductivity of packings in gas flow. Convective transport coefficient, Industrial Chemical Engineering – I. 18, 181.
- Berninger, R., Vortmeyer, D., 1982. Comments on the paper by Dixon and Cresswell (1979). AIChE 28, 353.
- Borkink, J.G.H., Westerterp, K.R., 1992. Influence of tube and particle diameter on heat transport in packed beds, AIChE **38**, 5, 703-715.
- Bunnell, D.G., Irvin, H.B., Olson, R.W., Smith, J.M., 1949. Effective thermal conductivities in gas-solid systems. Industrial and Engineering Chemistry Research and Development **41**, 1977-1998.
- Carbonell, R.G., Eidsath, A., Hermann, L.,R., Whitaker, S., 1983. Dispersion in Pulsed systems–III. Chemical Engineering Science 38, 1803–1816
- Cheng, P., Hsu, C. T., 1986. Applications of van Driest's mixing length theory to transverse thermal dispersion in forced convective flow through a packed bed. International Communications in Heat and Mass Transfer, 13(6), 613-625.
- Cheng, P., Vortmeyer, D., 1988. Transverse thermal dispersion and wall channelling in a porous bed with forced convective flow. Chemical Engineering Science 9, 2523–2532
- De Wasch, A.P., Froment, G.F., 1971. A two dimensional heterogeneous model for fixed bed catalytic reactors. Chemical Engineering Science 26, 629 – 634.

- De Wasch, A.P., Froment, G.F., 1972. Heat transfer in packed beds. Chemical Engineering Science 27, 567 – 576.
- Ding, Y., Wen, D., 2006. Heat transfer of gas flow through packed beds. Chemical Engineering Science 61, 3532 – 3542.
- Dixon, A.G., Cresswell, D.L., 1979. Theoretical prediction of effective parameters in packed beds. AIChE 25, 663–675.
- Dixon, A.G., Cresswell, D.L., 1982. Reply to comments made by Vortmeyer and Schaefer (1974), on Dixon and Cresswell (1979). AIChE 28, 511.
- Dixon, A.G., Cresswell, D.L., 1986. Effective heat transfer parameters for transient packed – bed models. AIChE 32, 809-819.
- Du Toit, C.G., HPTU Pressure Drop Tests Summary Report, M-Tech rep. HPTU002-0011, Rev 2, 2008.
- Endo, E., Kunii, D., Yagi, S., 1964. Heat transfer in packed beds through which water is flowing. International Journal of Heat and Mass Transfer 7, 333–339.
- Finlayson, B.A., Li, C.H., 1977. Heat transfer in packed beds: re – evaluation. Chemical Engineering Science 32, 1055 – 1066.
- Gunn, D.J., Khalid, M., 1975. Thermal dispersion and wall heat transfer in packed beds. Chemical Engineering Science 30, 261 – 267.
- Gunn, D.J., Pryce C., 1969. Dispersion in packed beds. Trans. Instn Chem. Engrs 47, T341-T350.
- Holman, J.P., Experimental methods for engineers, 6$^{th.}$ Ed., pp. 49-57, McGraw-Hill, Inc., ISBN 0-07-029666-9, 1994.
- Kaiser, W.H.K., HPTU BETS Test Reports, M-Tech rep. HPTU002-BETS036 rev 1, HPTU002-BETS039 rev. 1, HPTU002-BETS045 rev 1, 2008.
- Kaviany, M., Principles of Heat Transfer in Porous Media, Mechanical Engineering Series, Springer-Verlag, 1991.
- Krischke A., Tsotsas E, Vortmeyer D., Winterberg M., 2000. A simple and coherent set of coefficients for modelling of heat and mass transport with and without chemical reaction in tubes filled with spheres. Chemical Engineering Science 55, 967 – 979.

- Kunii, D., Suzuki, M., 1967. Particle-to-fluid heat and mass transfer in packed beds of fine particles. International Journal of Heat and Mass Transfer 10, 845–852.
- Kunni, D., Ono, N., 1968. Heat transfer from wall surroundings to pecked beds at high Reynolds number. Journal for Chemical Engineering (Japan) 1, pp 21.
- Kunii, D., Wakao, N., Yagi, S., 1960. Radially effective thermal conductivities in packed beds. Proc. of 1960 International Heat Transfer Conference, pp.742 – 749.
- Kunii, D., Yagi, S., 1957. Studies on effective thermal conductivities in packed beds. AIChE 3, 373–381.
- Kuo, S.M., Tien, C.L., 1988. ASME Proceedings of the 1988 National Heat Transfer Conference, ASME HTD 96, 629-634.
- Labuschagne, J.T., High pressure test unit thermal-fluid design report, M-Tech rep. HTTF001-0009.2, rev 3, 2005.
- Marivoet, J., Teodoroiu, P., Wajc, S.J., 1974. Porosity, velocity and temperature profiles in cylindrical packed beds. Chemical Engineering Science, 29, 1836.
- Martin, H., Nilles, M., 1993. Radiale Wärmeleitung in durschströmten Schüttungsrohren, Chemie Ingenieur Technik 65, pp1468-1477.
- Nasr, K.J., Ramadhyani, S., Viskanta, R. 1994. Numerical studies of forced convection heat transfer from a cylinder embedded in a packed bed. International Journal of Heat and Mass Transfer 38, 2353–2366.
- Ranz, W.E., 1952. Friction and transfer coefficients for single particles and packed beds. Chemical Engineering Progress 48, 247.
- Roache, P.J., Verification and Validation in Computational Science and Engineering, Hermosa Publishers, Albuquerque, New Mexico, 1998.
- Rousseau, P.G., Heat Transfer Test Facility Test Specification, M-Tech rep. HTTF001-0008.1, Rev 3, 2005.
- Schaefer, R.J., Vortmeyer, D., 1974. Equivalence of one – and two – phase models for heat transfer processes in packed beds: one dimensional theory. Chemical Engineering Science 29, 485.

- Schlünder, E.U., 1966 Wärme- und Stoffübertragung zwischen durchströmter Schüttungen und darin eingebetten Einzelkörpern, Chemie Ingenieur Technik 38, 767
- Schlünder, E.U., Zehner, P., 1973. Die effektive Wämeleitfähigkeit durschströmter Kugelschüttungen bei mäßigen und hohen Temperaturen Chemie Ingenieur Technik 45, 272.
- Van Antwerpen, H.J., 2007, Modelling a pebble bed high temperature gas-cooled reactor using a system-CFD approach. North-West University, Potchefstroom Campus, Department of Mechanical Engineering
- Van Antwerpen, H.J., Greyvenstein, G.P., 2006. High Temperature Gas-cooled Reactor Thermal-Fluid Analysis Lecture Notes. North-West University - Potchefstroom Campus, Postgraduate School for Nuclear Engineering.
- Van der Walt, A.J.K., Procedures for processing data, M-Tech rep. HPTU002-0028.2, rev 2, 2008.
- Van Niekerk, W., HPTU drift analysis results from January 2008 calibration, M-Tech rep. HPTU002-0018.2, rev A, 2008
- Versteeg, H.K., Malalasekera, W., An introduction to Computational Fluid Dynamics, The Finite Volume Method, Longman Group Ltd, 1998
- Wakao, N., Yagi, S., 1959. Heat and mass transfer from wall to fluid in packed beds. AIChE 5, 79 – 85.
- Zehner, P. (1972). Experimentelle und theoretische Bestimmung der effektiven Wämeleitfähigkeit durschströmter Kugelschüttungen bei mäßigen und hohen Temperaturen. Dissertation, University of Karlsruhe.

APPENDICES

APPENDIX A: Instrumentation and measurement

A.1 Gas and water cycles

Figure A-1 shows the instrumentation and measurements on the gas and water cycles for the HPTU plant. The two cycles are linked together through the heat exchanger to regulate the gas cycle temperature to the required level. The gas temperature is monitored at the outlet of the heat exchanger in the gas side (thermocouples TT-220 and TT-221), whilst the water temperature is monitored at the inlet of the heat exchanger in the water side (thermocouple TT-240).

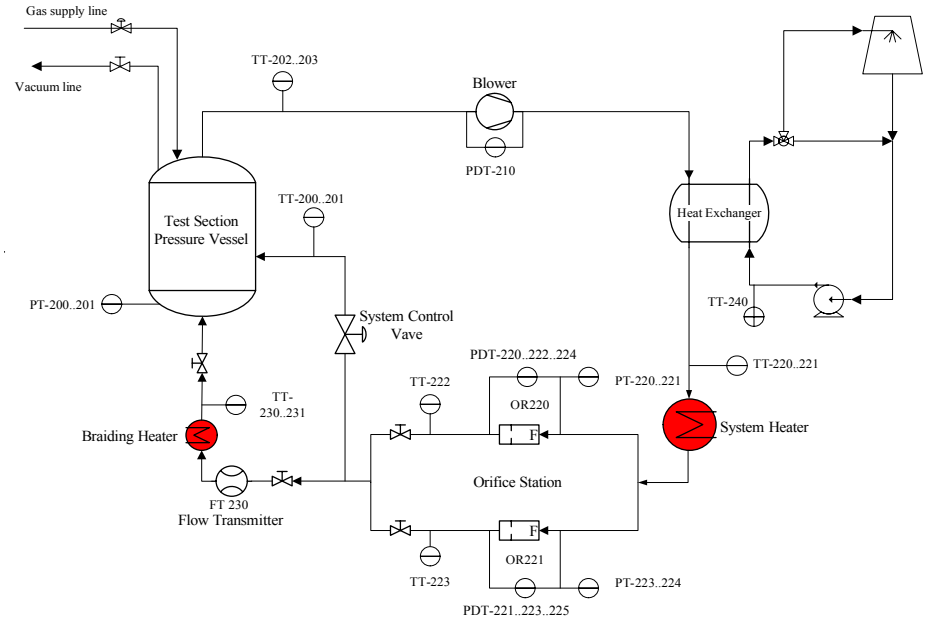

224

Figure A-1: P & ID diagram of the HPTU Plant.

A.2 Test sections

Figure A-2 to Figure A-7 shows the drawings for the top and side views of the test sections with their instrumentation and measurement. The top view drawings of the test section show the transverse positioning of the thermocouples to measure the braiding temperature profiles at the bottom and top layers. The side view drawings of the test section show the axial positioning of the thermocouples to measure the braiding temperature profiles at the bottom and top layers.

Table A-1 to Table A-4 shows the exact values for the transverse and axial positioning of the thermocouples as indicated in the test sections (Figure A-2 to Figure A-7).

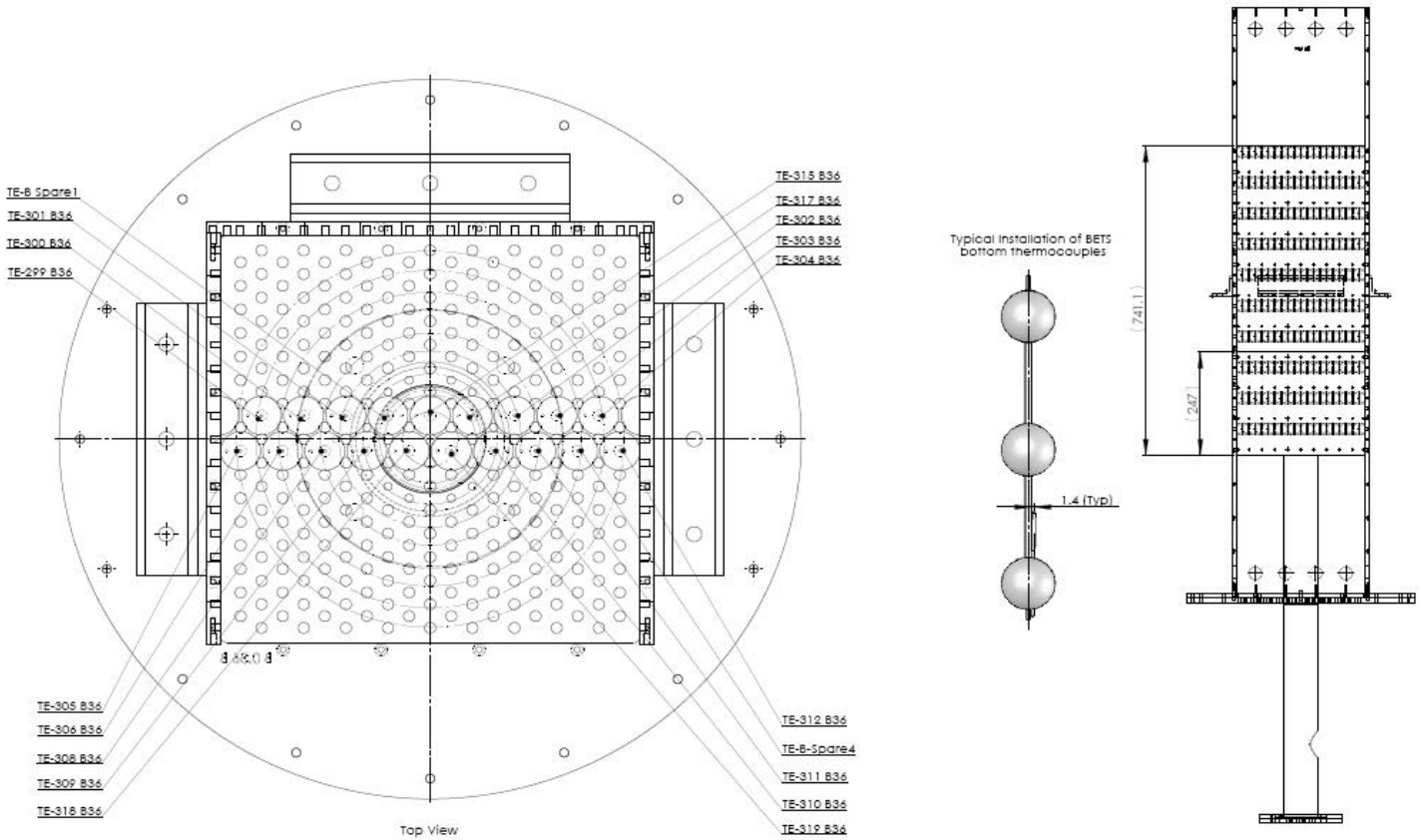

Figure A-2: BETS 036 Bottom Layer thermocouple installation positions.

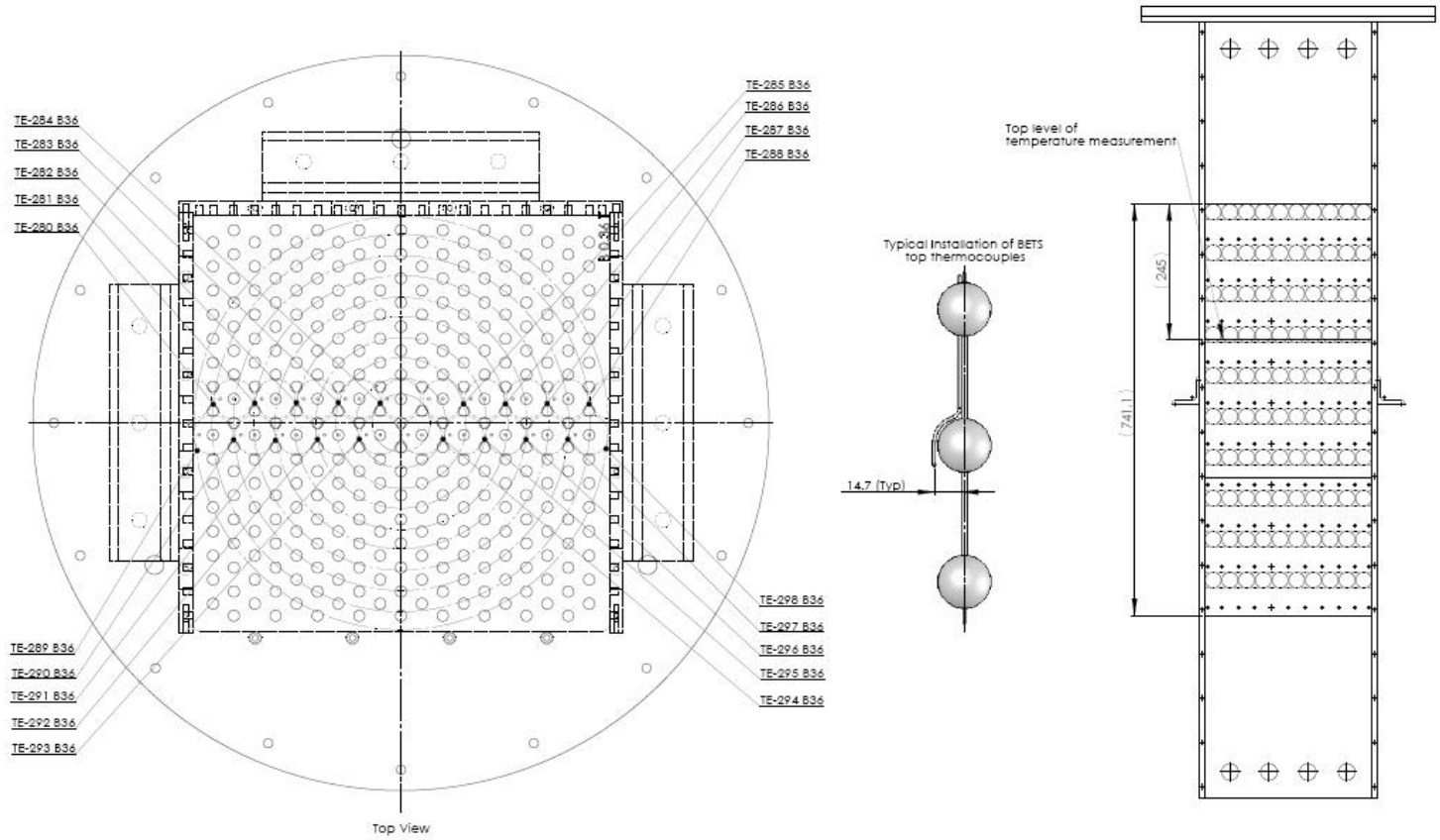

Figure A-3: BETS 036 Top Layer thermocouple installation positions.

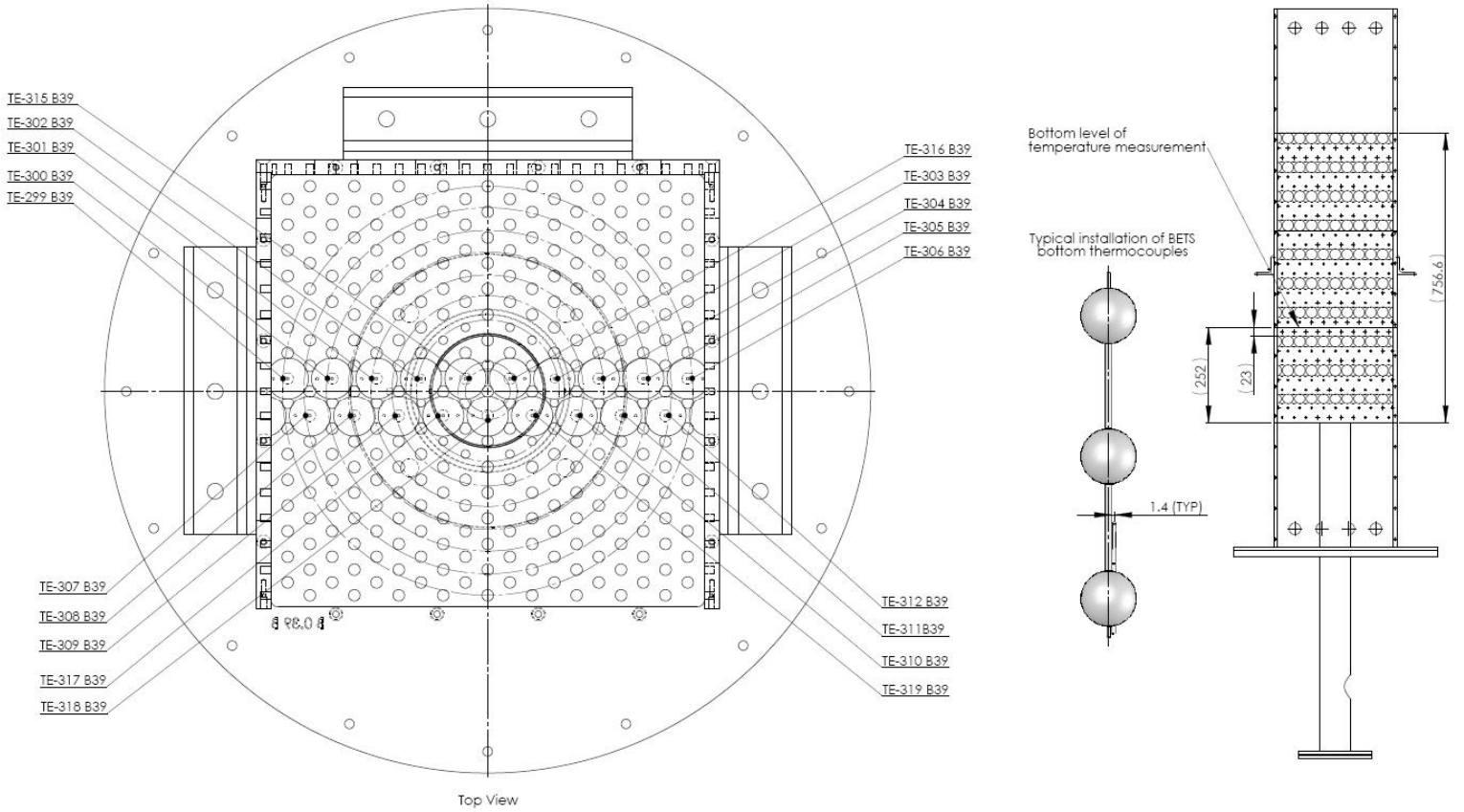

Figure A-4: BETS 039 Bottom Layer thermocouple installation positions.

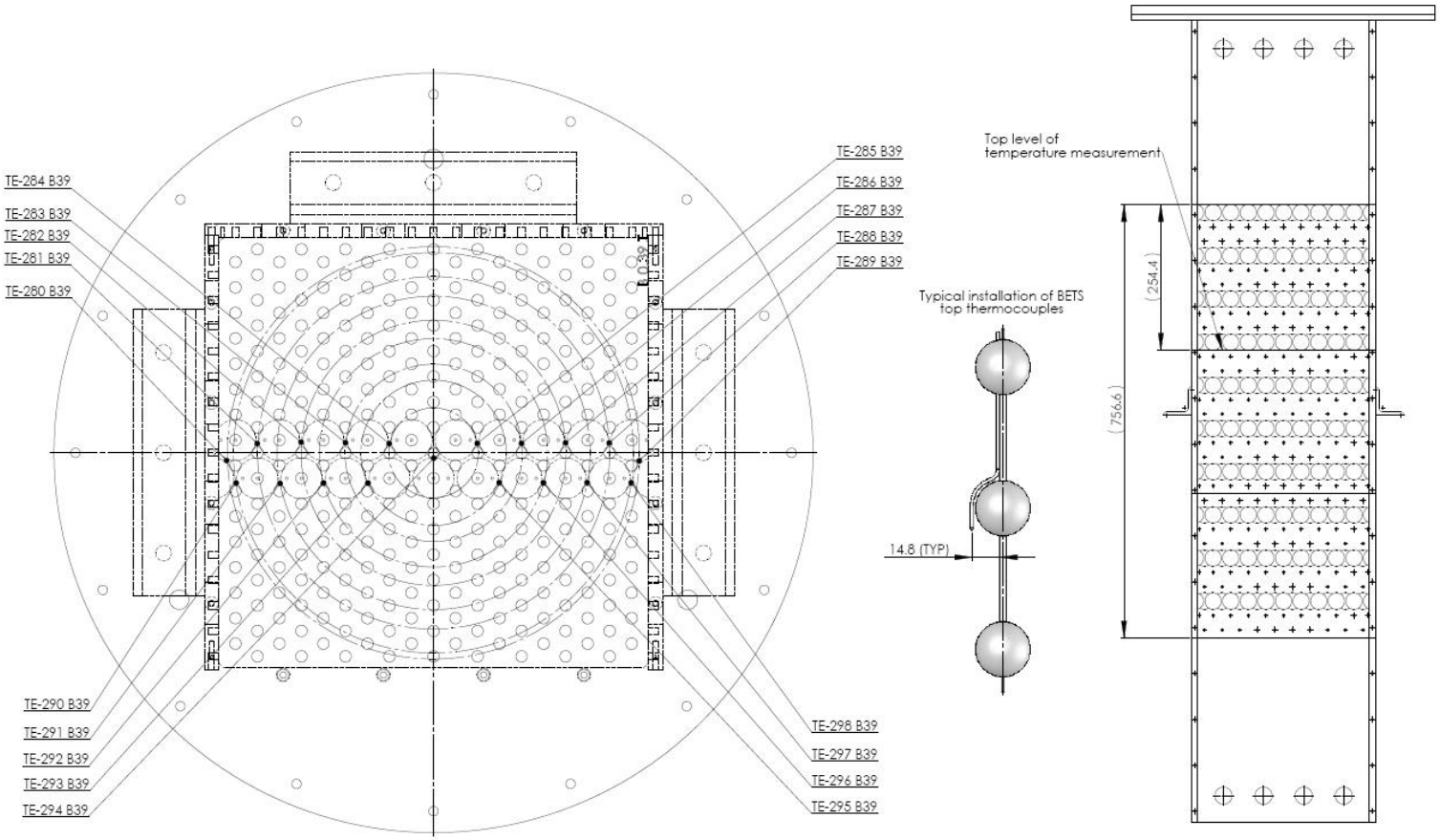

Figure A-5: BETS 039 Top Layer thermocouple installation positions.

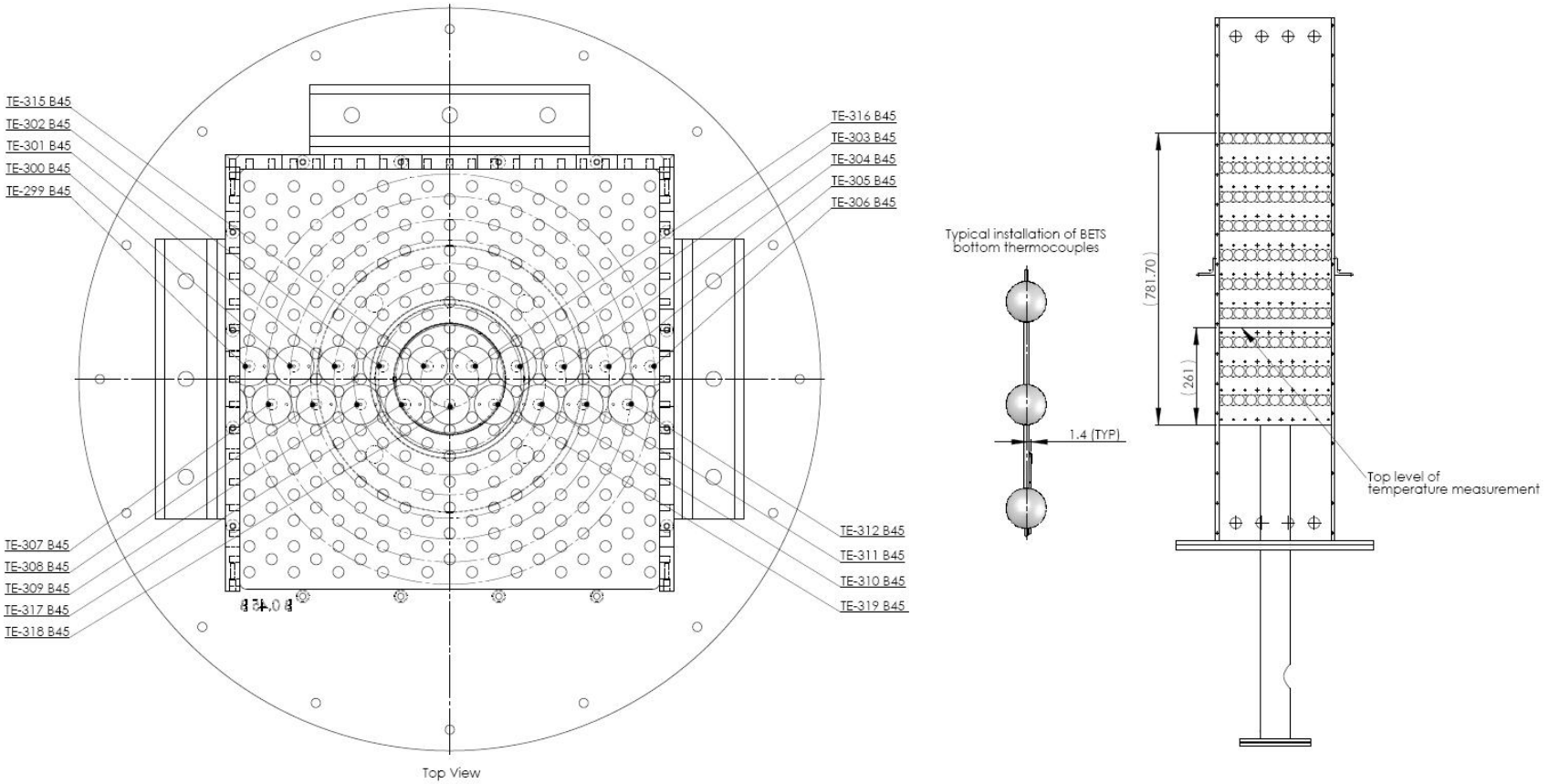

Figure A-6: BETS 045 Bottom Layer thermocouple installation positions.

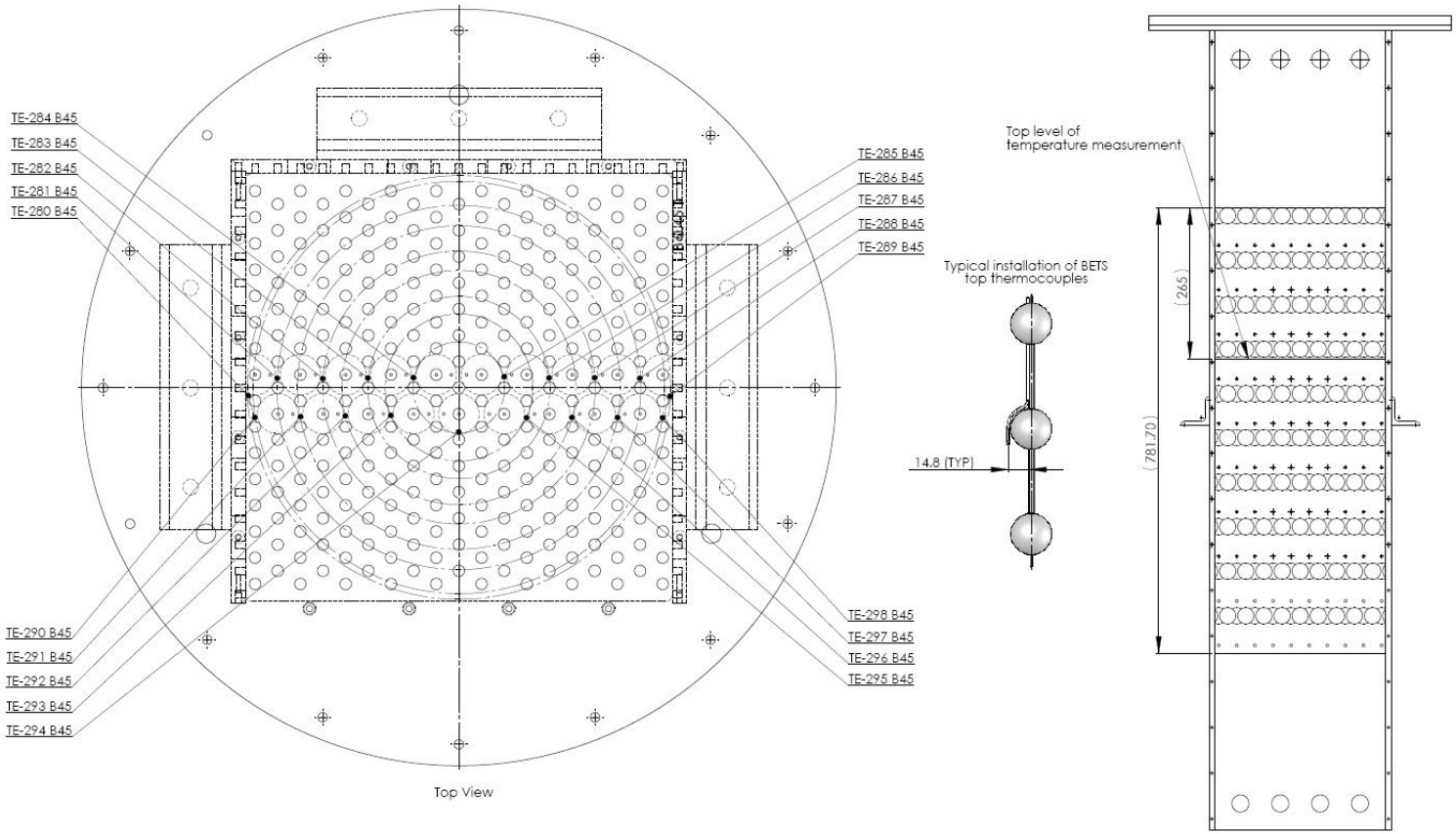

Figure A-7: BETS 045 Top Layer thermocouple installation positions.

Table A-1: Original designation of thermocouple tags and associated channel in LabVIEW.

LabVIEW Channel	BETS 0.36 original designation	BETS 0.39 original designation	BETS 0.45 original designation
TE-390	TE-280_B36	TE-280_B39	TE-280_B45
TE-391	TE-281_B36	TE-281_B39	TE-281_B45
TE-392	TE-282_B36	TE-282_B39	TE-282_B45
TE-393	TE-283_B36	TE-283_B39	TE-283_B45
TE-394	TE-284_B36	TE-284_B39	TE-284_B45
TE-395	TE-285_B36	TE-285_B39	TE-285_B45
TE-396	TE-286_B36	TE-286_B39	TE-286_B45
TE-397	TE-287_B36	TE-287_B39	TE-287_B45
TE-398	TE-288_B36	TE-288_B39	TE-288_B45
TE-399	TE-289_B36	TE-289_B39	TE-289_B45
TE-400	TE-290_B36	TE-290_B39	TE-290_B45
TE-401	TE-291_B36	TE-291_B39	TE-291_B45
TE-402	TE-292_B36	TE-292_B39	TE-292_B45
TE-403	TE-293_B36	TE-293_B39	TE-293_B45
TE-404	TE-294_B36	TE-294_B39	TE-294_B45
TE-405	TE-295_B36	TE-295_B39	TE-295_B45
TE-406	TE-296_B36	TE-296_B39	TE-296_B45
TE-407	TE-297_B36	TE-297_B39	TE-297_B45
TE-408	TE-298_B36	TE-298_B39	TE-298_B45
TE-415	TE-299_B36	TE-299_B39	TE-299_B45
TE-416	TE-300_B36	TE-300_B39	TE-300_B45
TE-417	TE-301_B36	TE-301_B39	TE-301_B45
TE-418	B_Spare1	TE-302_B39	TE-302_B45
TE-419	TE-315_B36	TE-315_B39	TE-315_B45
TE-420	TE-317_B36	TE-317_B39	TE-316_B45
TE-421	TE-302_B36	TE-303_B39	TE-303_B45
TE-422	TE-303_B36	TE-304_B39	TE-304_B45
TE-423	TE-304_B36	TE-305_B39	TE-305_B45
TE-424	TE-305_B36	TE-306_B39	TE-306_B45
TE-425	TE-306_B36	TE-308_B39	TE-307_B45
TE-426	TE-308_B36	TE-309_B39	TE-308_B45
TE-427	TE-309_B36	TE-317_B39	TE-309_B45

LabVIEW Channel	BETS 0.36 original designation	BETS 0.39 original designation	BETS 0.45 original designation
TE-428	TE-318_B36	TE-318_B39	TE-317_B45
TE-429	TE-319_B36	TE-319_B39	TE-318_B45
TE-430	TE-310_B36	TE-310_B39	TE-319_B45
TE-431	TE-311_B36	TE-311_B39	TE-310_B45
TE-432	B_Spare4	TE-312_B39	TE-311_B45
TE-433	TE-312_B36	TE-314_B39	TE-312_B45

Table A-2: Bottom layer thermocouple Radial Positioning in the test sections.

Bottom Layer Temperature Measurements				
Labview	Placement	r[mm] *(BETS036)*	r[mm] *(BETS039)*	r[mm] *(BETS045)*
TE-415	Over	-124	-142	-146.5
TE-416	Over	-94	-111	-114
TE-417	Over	-65	-80.5	-83
TE-418	Over	-36	-49	-51
TE-419	Over	-20	-15	-20.5
TE-420	Over	33	20	20.5
TE-421	Over	65	49	51
TE-422	Over	94	80.5	82
TE-423	Over	124	111	114
TE-424	Under	-139	141	146.5
TE-425	Under	-108	-127	130.5
TE-426	Under	-78	-96	-99.5
TE-427	Under	-48	-66	-68.5
TE-428	Under	-20	-39	-39
TE-429	Under	20	20.5	20.5
TE-430	Under	48	39	39
TE-431	Under	78	66	68.5
TE-432	Under	108	96	99.5
TE-433	Under	139	127	130.5

Table A-3: Top layer thermocouple Radial Positioning in the test sections.

Top Layer Temperature Measurements				
Labview	**Placement**	**r[mm]**	**r[mm]**	**r[mm]**
		(BETS036)	***(BETS039)***	***(BETS045)***
TE-390	Over	-136	-144	-148.5
TE-391	Over	-106	-123	-128
TE-392	Over	-76	-92	-95.5
TE-393	Over	-47	-62	-64
TE-394	Over	-21	-31	-32
TE-395	Over	47	31	32
TE-396	Over	76	62	64
TE-397	Over	106	92	95.5
TE-398	Over	136	123	128
TE-399	Under	-149	144	148.5
TE-400	Under	-121	-140	-144.5
TE-401	Under	-91	-109	-113.5
TE-402	Under	-61	-80	-82
TE-403	Under	-32	-51	-51
TE-404	Under	32	3.5	32
TE-405	Under	61	51	51
TE-406	Under	91	80	82
TE-407	Under	121	109	113.5
TE-408	Under	149	140	144.5

Table A-4: Thermocouple layers vertical positioning in the test sections.

Description	**Placement**	**Value [mm]**	**Value [mm]**	**Value [mm]**
		(BETS036)	***(BETS039)***	***(BETS045)***
Bottom Layer Temperature Measurements	$D1_{bottom}$	247	252	261
Top Layer Temperature Measurements	$D1_{top}$	496.1	502	516.7

APPENDIX B: Fluid properties

Adapted from Van der Walt (2008).

The Fluid properties of the nitrogen gas were obtained by fitting curves through REFPROP[5] data. The following fluid properties were used:

1) Viscosity
2) Density

These properties were obtained for different temperatures (10 °C, 15 °C, 20 °C, 25 °C, 30 °C, 35 °C, 40 °C, 50 , 60 °C, 70 °C, 80 °C, 90 °C) and different pressures (100 kPa, 200 kPa, 300 kPa, 400 kPa, 500 kPa, 600 kPa, 700 kPa, 800 kPa, 900 kPa, 1000 kPa, 2000 kPa, 3000 kPa, 4000 kPa, 5000 kPa) across the applicable range.

For each of these temperatures a plot as function of pressure was drawn and then a third or second order polynomial trend line derived for each temperature. The coefficients of the trend lines were then plotted as function of temperature. For each of the coefficients a third order polynomial trend line as function of temperature was derived. This resulted in the following equations for the fluid properties named above:

VISCOSITY (μ) [10 ˚C to 40 ˚C]

$$\mu \text{ [kg/m s]} = \left(b2_3 T^3 + b2_2 T^2 + b2_1 T + b2_0\right) p^2 + \left(b1_3 T^3 + b1_2 T^2 + b1_1 T + b1_0\right) p + \left(b0_3 T^3 + b0_2 T^2 + b0_1 T + b0_0\right)$$

Where:

$b2_3$ = -2.31556E-21

$b2_2$ = 5.91776E-19

$b2_1$ = -7.83363E-17

$b2_0$ = 6.5815E-15

[5] REFPROP – Reference Fluid Thermodynamic and Transport Properties, NIST Standard Reference database 23, Version 7.

$b1_3$ = -6.22222E-18

$b1_2$ = 1.96619E-15

$b1_1$ = -5.86961E-13

$b1_0$ = 1.67993E-10

$b0_3$ = 0

$b0_2$ = -3.25714E-11

$b0_1$ = 4.785E-8

$b0_0$ = 1.66207E-5

$T[^{\circ}C]$ = Temperature

$p[kPa]$ = Static pressure

VISCOSITY (μ) [40 ˚C to 90 ˚C]

$b2_3$ = -1.028180E-21

$b2_2$ = 4.005720E-19

$b2_1$ = -6.907740E-17

$b2_0$ = 6.434720E-15

$b1_3$ = -3.237420E-18

$b1_2$ = 1.741900E-15

$b1_1$ = -5.821660E-13

$b1_0$ = 1.679690E-10

$b0_3$ = 0

$b0_2$ = -2.804490E-11

$b0_1$ = 4.746540E-08

$b0_0$ = 1.662890E-05

DENSITY (ρ) [10 ˚C to 40 ˚C]

$$\rho\ [\mathrm{kg/m^3}] = \left(b3_3 T^3 + b3_2 T^2 + b3_1 T + b3_0\right) p^3 + \left(b2_3 T^3 + b2_2 T^2 + b2_1 T + b2_0\right) p^2 + \left(b1_3 T^3 + b1_2 T^2 + b1_1 T + b1_0\right) p + \left(b0_3 T^3 + b0_2 T^2 + b0_1 T + b0_0\right)$$

Where:

$b3_3$ = 3.4e-19

$b3_2$ = -2.32257e-16

$b3_1$ = 4.59236e-14

$b3_0$ = -3.73572e-12

$b2_3$ = -7.74489e-14

$b2_2$ = 1.67423e-11

$b2_1$ = -1.76353e-9

$b2_0$ = 5.78174e-8

$b1_3$ = -4.22222e-10

$b1_2$ = 1.58476e-7

$b1_1$ = -4.50004e-5

$b1_0$ = 1.23325e-2

$b0_3$ = -1.90620e-9

$b0_2$ = 2.79035e-7

$b0_1$ = -1.78122e-5

$b0_0$ = 4.19341e-4

$T[^{\circ}C]$ = Temperature

$p[kPa]$ = Static pressure

DENSITY (ρ) [40 ˚C to 90 ˚C]

$b3_3$ = 5.06333e-19

$b3_2$ = -2.35465e-16

$b3_1$ = 4.51444e-14

$b3_0$ = -3.70737e-12

$b2_3$ = -2.5714e-14

$b2_2$ = 9.796245e-12

$b2_1$ = -1.429574e-9

$b2_0$ = 5.208762e-8

$b1_3$ = -2.263333e-10

$b1_2$ = 1.308050e-7

$b1_1$ = -4.359402e-5

$b1_0$ = 1.230701e-2

$b0_3$ = -1.086530e-9

$b0_2$ = 2.710439e-7

$b0_1$ = -2.316224e-5

$b0_0$ = 6.167926e-4

APPENDIX C: Standard uncertainties in the braiding temperature profiles

Table C-1 to Table C-6 shows the standard uncertainties on the braiding temperature profiles at the at the top and bottom layers of measurements inside the packed bed for the three test sections.

Table C- 1: The standard uncertainties on the BETS036 braiding temperature profiles for the four test runs at the top layer measurement [%].

TOP LAYER MEASUREMENT [%]													
Bed Radius [mm]	Reynolds Number [-]												
	1000	**2000**	**3000**	**4000**	**5000**	**6000**	**7000**	**8000**	**9000**	**10000**	**20000**	**30000**	**40000**
-136	3.663	3.840	4.087	3.943	4.166	4.211	4.226	4.124	4.011	4.152	3.943	3.880	3.722
-106	3.689	3.859	4.100	3.966	4.184	4.229	4.241	4.132	4.016	4.154	3.972	3.909	3.745
-76	3.354	3.479	3.603	3.508	3.666	3.703	3.698	3.621	3.537	3.621	3.488	3.445	3.350
-47	3.108	3.175	3.084	2.953	3.031	3.047	3.031	2.996	2.947	2.987	2.838	2.837	2.833
-21	2.722	2.682	2.590	2.530	2.573	2.580	2.545	2.517	2.472	2.473	2.345	2.334	2.335
47	2.934	2.909	2.851	2.768	2.830	2.865	2.873	2.871	2.821	2.851	2.740	2.740	2.727
76	3.145	3.135	3.121	3.029	3.123	3.170	3.193	3.177	3.116	3.142	3.018	3.036	3.001
106	3.506	3.636	3.792	3.709	3.873	3.949	3.966	3.904	3.812	3.893	3.715	3.687	3.575
136	3.933	4.109	4.373	4.226	4.460	4.518	4.531	4.426	4.313	4.450	4.238	4.172	4.004
-149	3.568	3.768	4.020	3.874	4.097	4.140	4.157	4.053	3.943	4.077	3.878	3.811	3.656
-121	3.713	3.871	4.113	3.966	4.184	4.226	4.232	4.130	4.021	4.158	3.952	3.885	3.726
-91	3.635	3.787	3.989	3.861	4.061	4.101	4.109	4.026	3.936	4.060	3.907	3.857	3.719
-61	3.280	3.363	3.416	3.322	3.479	3.519	3.515	3.450	3.373	3.441	3.288	3.278	3.171
-32	2.762	2.756	2.713	2.685	2.767	2.802	2.790	2.758	2.703	2.726	2.596	2.584	2.556
32	2.804	2.803	2.770	2.723	2.824	2.872	2.880	2.833	2.799	2.876	2.777	2.780	2.751
61	3.264	3.316	3.364	3.344	3.379	3.428	3.453	3.305	3.245	3.304	3.157	3.152	3.102
91	4.006	4.119	4.284	4.139	4.322	4.374	4.387	4.287	4.184	4.291	4.050	4.000	3.876
121	3.725	3.884	4.127	3.992	4.209	4.259	4.273	4.172	4.062	4.191	3.982	3.922	3.775
149	3.841	4.060	4.335	4.183	4.425	4.474	4.490	4.383	4.268	4.411	4.199	4.134	3.967

Table C- 2: The standard uncertainties on the BETS036 braiding temperature profiles for the four test runs at the bottom layer measurement [%].

BOTTOM LAYER MEASUREMENT [%]													
Bed Radius [mm]	Reynolds Number [-]												
	1000	**2000**	**3000**	**4000**	**5000**	**6000**	**7000**	**8000**	**9000**	**10000**	**20000**	**30000**	**40000**
-124	4.181	4.324	4.588	4.432	4.676	4.724	4.730	4.617	4.498	4.643	4.426	4.351	4.172
-94	4.112	4.249	4.487	4.334	4.562	4.611	4.619	4.511	4.393	4.529	4.332	4.266	4.102
-65	3.730	3.898	4.031	3.929	4.190	4.289	4.379	4.353	4.139	4.346	3.982	3.879	3.787
-36	2.478	2.422	2.332	2.292	2.332	2.342	2.304	2.342	2.245	2.310	2.203	2.152	2.151
-20	2.418	2.326	2.212	2.173	2.181	2.189	2.160	2.144	2.128	2.119	1.990	2.012	2.055
33	3.058	3.022	2.990	2.919	2.879	3.111	3.194	3.150	3.207	3.074	3.099	2.803	2.725
65	3.768	3.885	4.035	3.925	4.078	4.417	4.367	4.413	4.241	4.291	3.953	3.898	3.657
94	4.125	4.281	4.538	4.390	4.638	4.697	4.714	4.604	4.484	4.627	4.410	4.340	4.173
124	4.031	4.185	4.445	4.293	4.530	4.578	4.589	4.483	4.366	4.508	4.296	4.228	4.055
-139	3.950	4.103	4.357	4.207	4.439	4.482	4.498	4.389	4.267	4.410	4.195	4.127	3.955
-108	4.313	4.442	4.699	4.537	4.783	4.827	4.837	4.718	4.594	4.742	4.524	4.455	4.283
-78	4.240	4.341	4.493	4.333	4.532	4.573	4.580	4.493	4.395	4.518	4.404	4.363	4.215
-48	3.711	3.799	3.856	3.728	3.835	3.842	3.827	3.754	3.670	3.746	3.559	3.538	3.474
-20	2.903	2.796	2.723	2.673	2.762	2.764	2.714	2.706	2.666	2.724	2.554	2.599	2.530
20	2.509	2.398	2.289	2.261	2.310	2.409	2.415	2.396	2.383	2.353	2.260	2.206	2.205
48	3.771	3.747	3.728	3.609	3.678	3.697	3.734	3.639	3.608	3.695	3.643	3.574	3.509
78	3.417	3.485	3.593	3.467	3.637	3.691	3.724	3.645	3.566	3.664	3.506	3.461	3.350
108	3.889	4.027	4.276	4.123	4.355	4.401	4.413	4.310	4.198	4.336	4.131	4.061	3.895
139	4.507	4.685	4.982	4.741	5.075	5.131	5.145	5.024	4.888	5.052	4.810	4.729	4.532

Table C- 3: The standard uncertainties of the BETS039 braiding temperature profiles for the four test runs at the top layer measurement [%].

TOP LAYER MEASUREMENT [%]													
Bed Radius [mm]	Reynolds Number [-]												
	1000	**2000**	**3000**	**4000**	**5000**	**6000**	**7000**	**8000**	**9000**	**10000**	**20000**	**30000**	**40000**
-144	3.538	3.745	3.756	3.582	3.757	3.779	3.804	3.821	3.832	3.812	3.690	3.584	3.460
-123	3.666	3.879	3.890	3.706	3.890	3.916	3.940	3.958	3.971	3.950	3.819	3.705	3.567
-92	3.741	3.940	3.913	3.717	3.860	3.887	3.920	3.943	3.973	3.951	3.852	3.752	3.609
-62	3.293	3.430	3.305	3.113	3.160	3.223	3.272	3.297	3.354	3.337	3.258	3.149	3.045
-31	2.824	2.800	2.689	2.599	2.630	2.683	2.710	2.728	2.790	2.771	2.701	2.654	2.597
31	2.690	2.648	2.564	2.467	2.486	2.537	2.551	2.559	2.575	2.558	2.414	2.430	2.409
62	3.144	3.238	3.182	3.052	3.158	3.202	3.235	3.243	3.266	3.235	3.090	3.079	2.953
92	3.651	3.854	3.862	3.684	3.844	3.874	3.897	3.911	3.934	3.906	3.769	3.703	3.549
123	3.846	4.061	4.078	3.891	4.082	4.110	4.138	4.156	4.178	4.151	4.023	3.917	3.771
144	3.469	3.671	3.687	3.514	3.689	3.714	3.737	3.751	3.770	3.747	3.631	3.522	3.392
-140	3.580	3.791	3.803	3.624	3.801	3.823	3.847	3.862	3.876	3.853	3.734	3.627	3.498
-109	3.683	3.882	3.877	3.684	3.849	3.870	3.888	3.907	3.929	3.899	3.778	3.680	3.559
-80	3.518	3.629	3.555	3.370	3.470	3.503	3.552	3.597	3.634	3.624	3.534	3.471	3.326
-51	2.957	2.955	2.846	2.719	2.762	2.795	2.806	2.830	2.869	2.847	2.664	2.598	2.534
3.5	2.538	2.470	2.369	2.278	2.278	2.322	2.312	2.294	2.325	2.322	2.202	2.230	2.232
51	3.218	3.308	3.255	3.112	3.162	3.203	3.213	3.184	3.222	3.175	2.982	2.963	2.916
80	3.725	3.884	3.888	3.742	3.916	3.971	3.994	4.018	4.063	4.025	3.936	3.845	3.697
109	3.634	3.833	3.853	3.677	3.864	3.893	3.919	3.937	3.956	3.932	3.814	3.702	3.564
140	3.787	4.006	4.020	3.831	4.021	4.047	4.076	4.091	4.109	4.086	3.954	3.837	3.697

Table C- 4: The standard uncertainties of the BETS039 braiding temperature profiles for the four test runs at the bottom layer measurement [%].

BOTTOM LAYER MEASUREMENT [%]													
Bed Radius [mm]	Reynolds Number [-]												
	1000	**2000**	**3000**	**4000**	**5000**	**6000**	**7000**	**8000**	**9000**	**10000**	**20000**	**30000**	**40000**
-142	3.991	4.208	4.237	4.034	4.229	4.256	4.280	4.296	4.313	4.286	4.152	4.028	3.880
-111	4.015	4.225	4.256	4.053	4.251	4.279	4.307	4.322	4.340	4.314	4.178	4.057	3.909
-80.5	4.057	4.239	4.225	4.024	4.282	4.395	4.529	4.624	4.551	4.604	4.178	4.050	3.914
-49	3.491	3.647	3.627	3.532	3.635	3.710	3.743	3.881	3.870	3.918	3.707	3.469	3.319
-15	2.319	2.233	2.154	2.083	2.044	2.070	2.074	2.068	2.113	2.085	2.008	2.033	2.031
20	2.316	2.216	2.175	2.140	2.108	2.268	2.390	2.322	2.421	2.390	2.447	2.240	2.179
49	2.946	2.974	2.957	2.840	2.941	3.152	3.110	3.236	3.201	3.137	2.950	3.009	2.769
80.5	3.862	4.061	4.075	3.867	4.009	4.020	4.022	4.026	4.041	3.995	3.805	3.733	3.593
111	3.873	4.074	4.109	3.917	4.104	4.135	4.161	4.175	4.196	4.170	4.040	3.928	3.783
141	3.755	3.950	3.981	3.798	3.982	4.006	4.032	4.043	4.062	4.038	3.909	3.793	3.654
-127	4.145	4.357	4.389	4.178	4.382	4.406	4.435	4.452	4.474	4.448	4.307	4.182	4.031
-96	4.251	4.445	4.461	4.258	4.451	4.489	4.518	4.544	4.570	4.530	4.347	4.238	4.100
-66	3.961	4.052	3.998	3.799	3.900	3.899	3.949	3.980	4.006	4.000	3.735	3.657	3.559
-39	3.526	3.533	3.479	3.376	3.476	3.488	3.470	3.521	3.553	3.615	3.396	3.401	3.224
20.5	2.738	2.616	2.504	2.410	2.426	2.532	2.550	2.524	2.569	2.527	2.399	2.353	2.328
39	3.193	3.237	3.223	3.140	3.137	3.167	3.198	3.177	3.211	3.195	3.109	3.069	3.068
66	2.980	3.017	2.971	2.842	2.945	2.983	2.986	2.978	2.996	2.943	2.736	2.687	2.634
96	3.649	3.802	3.799	3.618	3.784	3.808	3.826	3.838	3.859	3.824	3.707	3.631	3.495
127	4.344	4.567	4.601	4.384	4.604	4.633	4.661	4.675	4.697	4.673	4.521	4.387	4.222

Table C- 5: The standard uncertainties of the BETS045 braiding temperature profiles for the four test runs at the top layer measurement [%].

TOP LAYER MEASUREMENT [%]													
Bed Radius [mm]	Reynolds Number [-]												
	1000	**2000**	**3000**	**4000**	**5000**	**6000**	**7000**	**8000**	**9000**	**10000**	**20000**	**30000**	**40000**
-148.5	3.265	3.750	3.829	3.802	3.807	3.977	3.988	3.968	3.976	4.007	4.104	4.132	4.217
-128	3.231	3.692	3.768	3.736	3.743	3.910	3.923	3.903	3.913	3.942	4.045	4.074	4.160
-95.5	3.102	3.481	3.520	3.470	3.459	3.586	3.587	3.543	3.554	3.559	3.642	3.668	3.790
-64	2.465	2.554	2.513	2.452	2.441	2.475	2.472	2.415	2.415	2.401	2.414	2.399	2.535
-32	2.359	2.479	2.455	2.411	2.406	2.445	2.445	2.391	2.393	2.379	2.397	2.388	2.522
32	2.211	2.209	2.113	2.027	2.007	2.011	1.991	1.950	1.939	1.939	1.949	1.949	2.071
64	2.670	2.865	2.836	2.756	2.731	2.775	2.759	2.713	2.705	2.709	2.782	2.824	2.903
95.5	3.179	3.603	3.656	3.604	3.597	3.726	3.734	3.696	3.701	3.730	3.848	3.908	4.018
128	3.291	3.770	3.847	3.807	3.813	3.978	3.990	3.968	3.976	4.007	4.116	4.152	4.243
148.5	3.194	3.691	3.767	3.735	3.740	3.902	3.915	3.894	3.906	3.940	4.049	4.085	4.172
-144.5	3.260	3.734	3.810	3.779	3.783	3.953	3.963	3.941	3.952	3.982	4.076	4.105	4.197
-113.5	3.233	3.680	3.748	3.711	3.716	3.872	3.881	3.854	3.862	3.888	3.977	4.016	4.129
-82	2.962	3.313	3.376	3.352	3.365	3.485	3.489	3.455	3.458	3.481	3.559	3.571	3.680
-51	2.286	2.323	2.244	2.155	2.142	2.146	2.121	2.076	2.074	2.071	2.096	2.095	2.245
32	2.272	2.334	2.281	2.218	2.218	2.245	2.237	2.200	2.203	2.207	2.224	2.219	2.348
51	2.108	2.108	2.029	1.950	1.936	1.938	1.920	1.875	1.872	1.871	1.890	1.882	1.993
82	3.054	3.376	3.368	3.303	3.310	3.404	3.406	3.360	3.357	3.376	3.487	3.514	3.645
113.5	3.106	3.519	3.571	3.525	3.524	3.658	3.666	3.633	3.637	3.664	3.757	3.806	3.906
144.5	3.327	3.808	3.883	3.852	3.851	4.017	4.027	4.004	4.013	4.046	4.158	4.192	4.280

Table C- 6: The standard uncertainties of the BETS045 braiding temperature profiles for the four test runs at the bottom layer measurement [%].

BOTTOM LAYER MEASUREMENT [%]													
Bed Radius [mm]	Reynolds Number [-]												
	1000	**2000**	**3000**	**4000**	**5000**	**6000**	**7000**	**8000**	**9000**	**10000**	**20000**	**30000**	**40000**
-146.5	3.433	3.914	3.995	3.962	3.965	4.139	4.150	4.130	4.134	4.164	4.261	4.288	4.379
-114	3.462	3.930	4.010	3.978	3.984	4.155	4.168	4.150	4.157	4.185	4.286	4.316	4.408
-83	3.397	3.821	3.863	3.814	3.820	3.977	3.991	3.965	3.978	4.003	4.096	4.122	4.254
-51	2.610	2.730	2.691	2.618	2.589	2.632	2.598	2.530	2.536	2.521	2.518	2.496	2.670
-20.5	1.770	1.720	1.658	1.609	1.619	1.636	1.621	1.585	1.600	1.597	1.767	1.711	1.962
20.5	1.740	1.693	1.617	1.553	1.544	1.554	1.536	1.501	1.505	1.500	1.546	1.584	1.692
51	2.723	2.855	2.806	2.751	2.758	2.806	2.809	2.752	2.731	2.726	2.652	2.573	2.691
82	3.333	3.760	3.811	3.754	3.751	3.872	3.869	3.824	3.815	3.828	3.876	3.917	4.079
114	8.754	9.839	10.081	10.034	10.024	10.069	10.163	10.137	10.187	10.270	10.529	10.574	10.804
146.5	3.438	3.921	4.007	3.971	3.974	4.147	4.159	4.137	4.144	4.174	4.274	4.302	4.393
-130.5	3.579	4.064	4.150	4.117	4.121	4.302	4.312	4.290	4.297	4.329	4.428	4.457	4.549
-99.5	3.729	4.226	4.312	4.274	4.281	4.466	4.480	4.460	4.466	4.496	4.596	4.628	4.726
-68.5	3.249	3.605	3.626	3.578	3.586	3.701	3.702	3.666	3.675	3.694	3.752	3.757	3.905
-39	2.540	2.616	2.539	2.453	2.437	2.456	2.438	2.391	2.377	2.374	2.397	2.380	2.545
20.5	1.924	1.903	1.825	1.748	1.742	1.733	1.717	1.684	1.687	1.681	1.727	1.752	1.889
39	2.528	2.577	2.496	2.408	2.380	2.366	2.352	2.294	2.251	2.291	2.318	2.368	2.526
68.5	2.973	3.228	3.220	3.154	3.141	3.212	3.203	3.152	3.148	3.179	3.307	3.359	3.524
99.5	3.295	3.753	3.831	3.797	3.800	3.966	3.978	3.954	3.963	3.995	4.097	4.132	4.232
130.5	3.347	3.816	3.899	3.865	3.866	4.037	4.048	4.026	4.033	4.063	4.164	4.192	4.279

APPENDIX D: Inlet superficial velocity

For the steady-state measurements it is required that the cold gas and the hot gas superficial velocities should be equal. This requirement needed to be derived in terms of mass flow rates of the total incoming gas (braiding line and the cold gas line).

Considering Figure 3-6 it is required that:

$$\overline{\varepsilon} V_{hot\ gas} = \overline{\varepsilon} V_{cold\ gas} = u_o \tag{D.1}$$

This implies that:

$$\frac{\dot{m}_{hot\ gas}}{\rho_{hot\ gas} \cdot A_{hot\ gas}} = \frac{\dot{m}_{cold\ gas}}{\rho_{cold\ gas} \cdot A_{cold\ gas}} \tag{D.2}$$

The total incoming mass flow rate equals the sum of the hot and cold gas mass flow rates i.e.:

$$\dot{m}_{total\ gas} = \dot{m}_{cold\ gas} + \dot{m}_{hot\ gas} \tag{D.3}$$

The combination of the above equations (D.2 and D.3) leads to:

$$\begin{aligned} \dot{m}_{total} &= \left(1 + \frac{\rho_{cold\ gas} \cdot A_{cold\ gas}}{\rho_{hot\ gas} \cdot A_{hot\ gas}}\right) \cdot \dot{m}_{hot\ gas} \\ \dot{m}_{hot\ gas} &= \frac{\dot{m}_{total}}{\left(1 + \frac{\rho_{cold\ gas} \cdot A_{cold\ gas}}{\rho_{hot\ gas} \cdot A_{hot\ gas}}\right)} \end{aligned} \tag{D.4}$$

During the experimental test, the system control valve (Figure 3-1) was adjusted such that the Equation (D.4) was satisfied.

APPENDIX E: Non-dimensional braiding temperature profiles

Table E-1 to Table E-6 shows the non-dimentional braiding temperature profiles at the at the top and bottom layers of measurements inside the packed bed for the three test sections.

Table E-1: BETS036 averaged non-dimensional braiding temperature profiles calculated at the top layer of measurement.

TOP LAYER MEASUREMENT [%]													
Bed transverse position [mm]	Reynolds Number [-]												
	1000	**2000**	**3000**	**4000**	**5000**	**6000**	**7000**	**8000**	**9000**	**10000**	**20000**	**30000**	**40000**
-136	2.866	1.504	1.297	1.476	1.271	1.188	1.102	0.920	0.905	0.934	0.674	0.549	0.336
-106	3.793	2.429	2.183	2.326	2.129	2.096	2.011	1.917	1.949	1.955	1.495	1.386	1.255
-76	10.203	8.927	9.081	9.296	9.047	9.125	9.182	9.139	9.192	9.202	8.903	8.871	8.628
-47	18.650	19.291	21.604	22.161	22.246	22.782	22.966	22.922	22.810	22.836	24.214	24.124	23.169
-21	27.444	28.523	31.377	32.437	32.968	33.845	34.281	34.469	34.801	35.273	37.058	37.558	37.192
47	20.271	20.811	22.714	23.630	23.923	24.154	23.992	23.355	23.272	23.576	23.878	23.587	23.018
76	14.862	15.245	16.577	17.256	17.251	17.306	17.115	16.554	16.622	16.997	17.336	16.577	15.806
106	7.429	6.252	6.315	6.297	6.244	5.911	5.755	5.463	5.466	5.705	5.620	5.240	4.831
136	3.669	2.384	2.091	2.260	2.032	1.904	1.815	1.623	1.577	1.653	1.367	1.241	1.038
-149	3.070	1.438	1.152	1.358	1.128	1.061	0.952	0.783	0.762	0.813	0.536	0.438	0.197
-121	2.826	1.665	1.513	1.722	1.560	1.508	1.468	1.296	1.263	1.296	1.054	0.971	0.772
-91	4.882	3.648	3.587	3.777	3.577	3.572	3.519	3.309	3.208	3.197	2.569	2.344	2.053
-61	10.901	10.174	10.949	11.271	10.881	10.896	10.920	10.834	10.943	11.071	11.653	11.694	11.362
-32	23.104	23.489	25.371	25.419	25.253	25.548	25.475	25.564	25.770	26.140	27.270	27.529	27.590
32	22.903	23.174	24.751	25.260	24.793	25.046	24.699	24.470	24.260	24.135	23.839	23.630	23.127
61	13.225	12.748	13.609	13.020	14.170	14.079	13.874	14.826	14.790	14.965	15.078	14.850	14.444
91	6.163	5.397	5.663	6.047	6.019	5.983	5.857	5.778	5.780	5.878	6.196	6.093	5.865
121	3.561	2.349	2.113	2.248	2.075	1.977	1.868	1.695	1.678	1.755	1.548	1.414	1.130
149	3.385	1.695	1.355	1.532	1.279	1.196	1.102	0.906	0.849	0.926	0.616	0.460	0.197

Table E-2: BETS036 averaged non-dimensional braiding temperature profiles calculated at the bottom layer measurement.

BOTTOM LAYER MEASUREMENT [%]													
Bed transverse position [mm]	Reynolds Number [-]												
	1000	**2000**	**3000**	**4000**	**5000**	**6000**	**7000**	**8000**	**9000**	**10000**	**20000**	**30000**	**40000**
-124	2.713	1.852	1.746	1.906	1.716	1.659	1.634	1.471	1.415	1.488	1.171	1.082	0.893
-94	3.472	2.607	2.594	2.806	2.651	2.595	2.554	2.392	2.371	2.451	2.038	1.922	1.694
-65	9.788	8.186	8.615	8.804	8.565	8.812	8.948	8.987	9.235	9.016	8.470	8.632	8.011
-36	35.821	37.516	41.239	42.563	42.621	43.689	44.525	44.654	45.312	45.152	48.099	48.963	48.956
-20	45.022	48.498	52.901	54.675	55.378	56.833	57.740	57.813	58.030	58.470	62.499	62.505	61.548
33	25.189	26.071	28.731	30.992	32.322	31.840	32.834	30.868	30.555	33.812	36.184	36.295	36.718
65	9.259	8.256	8.948	9.030	9.154	8.431	7.872	8.005	7.801	8.092	9.054	10.367	10.534
94	3.764	2.735	2.568	2.733	2.452	2.323	2.215	2.040	2.016	2.069	1.779	1.677	1.440
124	2.992	1.980	1.825	1.994	1.789	1.732	1.662	1.471	1.425	1.500	1.169	1.056	0.874
-139	2.697	1.672	1.545	1.722	1.536	1.496	1.405	1.238	1.240	1.289	1.024	0.910	0.751
-108	3.006	2.287	2.240	2.444	2.258	2.239	2.195	2.061	2.050	2.094	1.769	1.634	1.401
-78	5.741	5.148	5.676	6.100	5.996	6.075	5.998	5.812	5.713	5.726	4.736	4.459	4.243
-48	13.794	12.966	13.980	14.926	15.101	15.593	15.887	16.157	16.319	16.459	16.930	17.299	17.029
-20	33.871	36.666	39.970	41.140	41.696	42.515	42.973	43.502	43.522	44.052	46.473	46.738	46.973
20	46.165	50.068	54.564	55.646	56.617	57.577	57.646	57.040	56.564	57.405	58.336	59.314	59.305
48	17.551	18.133	19.936	20.922	21.456	22.164	21.917	22.162	21.836	21.578	21.021	21.467	21.851
78	5.872	5.474	6.130	6.554	6.310	6.156	5.846	5.746	5.635	5.705	5.474	5.388	5.107
108	2.774	1.860	1.719	1.954	1.722	1.659	1.577	1.392	1.351	1.406	1.101	1.010	0.813
139	2.800	1.750	1.573	2.250	1.567	1.488	1.410	1.226	1.208	1.260	0.959	0.867	0.691

Table E-3: BETS039 averaged non-dimensional braiding temperature profiles calculated at the top layer of measurement.

TOP LAYER MEASUREMENT [%]													
Bed transverse position [mm]	Reynolds Number [-]												
	1000	**2000**	**3000**	**4000**	**5000**	**6000**	**7000**	**8000**	**9000**	**10000**	**20000**	**30000**	**40000**
-144	0.283	0.300	0.780	0.515	0.470	0.426	0.235	-0.002	0.100	0.049	-0.179	-0.273	-0.594
-123	0.116	0.130	0.585	0.353	0.306	0.275	0.084	-0.157	-0.073	-0.119	-0.309	-0.369	-0.629
-92	1.594	1.691	2.447	2.481	2.683	2.640	2.383	2.060	2.026	1.945	1.607	1.531	1.360
-62	11.856	12.782	14.745	15.028	15.755	15.207	14.471	13.935	13.392	13.250	13.317	14.579	14.713
-31	21.547	23.031	25.865	26.505	27.266	26.680	25.812	25.171	24.341	24.172	24.168	25.183	25.173
31	21.685	23.416	25.604	26.380	27.256	26.743	26.540	26.076	26.071	26.089	28.114	27.477	26.708
62	11.097	11.196	12.345	12.549	12.407	12.221	11.995	11.715	11.780	11.756	12.759	12.154	12.560
92	1.843	1.787	2.222	2.126	2.190	2.106	1.921	1.756	1.800	1.752	1.803	1.308	1.247
123	0.634	0.689	1.108	0.856	0.777	0.712	0.490	0.259	0.297	0.252	0.020	-0.151	-0.394
144	0.245	0.276	0.690	0.434	0.362	0.303	0.109	-0.107	-0.068	-0.114	-0.338	-0.419	-0.657
-140	0.320	0.310	0.798	0.558	0.518	0.486	0.280	0.060	0.157	0.103	-0.134	-0.227	-0.539
-109	0.440	0.590	1.190	1.104	1.161	1.156	1.022	0.794	0.848	0.830	0.581	0.387	0.002
-80	3.914	4.644	5.908	6.244	6.666	6.540	5.992	5.340	5.250	5.059	5.186	5.356	5.079
-51	15.541	16.952	19.451	20.460	21.036	21.080	20.676	20.064	19.747	19.808	22.197	23.573	23.810
3.5	25.410	27.942	31.157	32.562	33.951	33.855	34.060	33.651	33.382	33.640	35.249	34.578	32.911
51	10.126	10.416	11.794	12.125	12.975	12.716	12.783	12.788	12.610	13.029	14.549	14.373	13.671
80	5.435	5.523	6.094	5.803	5.552	5.267	5.052	4.663	4.501	4.549	4.081	4.016	4.054
109	0.613	0.707	1.099	0.824	0.709	0.623	0.391	0.157	0.201	0.162	-0.106	-0.184	-0.394
140	0.015	0.073	0.514	0.261	0.203	0.144	-0.073	-0.281	-0.227	-0.284	-0.470	-0.555	-0.845

Table E-4: BETS039 averaged non-dimensional braiding temperature profiles calculated at the bottom layer measurement.

BOTTOM LAYER MEASUREMENT [%]													
Bed transverse position [mm]	Reynolds Number [-]												
	1000	**2000**	**3000**	**4000**	**5000**	**6000**	**7000**	**8000**	**9000**	**10000**	**20000**	**30000**	**40000**
-142	0.604	0.722	1.094	0.908	0.853	0.808	0.632	0.422	0.499	0.457	0.251	0.219	-0.026
-111	0.490	0.690	1.034	0.849	0.788	0.740	0.538	0.326	0.388	0.352	0.142	0.060	-0.192
-80.5	2.264	2.565	3.367	3.396	3.369	3.280	3.118	2.874	2.891	2.898	3.214	3.043	2.582
-49	11.437	10.884	11.895	11.679	11.818	11.266	10.777	10.107	9.570	9.649	11.449	13.390	14.061
-15	45.137	48.289	52.242	54.590	56.943	57.155	57.016	56.434	55.777	56.045	57.678	58.086	57.687
20	41.194	44.559	48.367	50.403	51.345	50.739	50.052	49.020	48.602	48.761	50.986	50.779	50.639
49	17.998	18.631	20.515	20.879	20.459	19.970	19.340	18.886	18.745	18.979	20.185	20.165	21.898
80.5	2.527	2.561	3.061	3.152	3.406	3.522	3.534	3.381	3.496	3.637	4.180	3.908	3.916
111	0.635	0.833	1.143	0.919	0.877	0.788	0.593	0.395	0.430	0.390	0.164	0.057	-0.172
141	0.753	0.938	1.262	1.021	0.956	0.916	0.724	0.537	0.581	0.527	0.351	0.309	0.092
-127	0.646	0.869	1.218	1.047	0.983	0.960	0.758	0.535	0.584	0.527	0.334	0.267	0.017
-96	1.739	2.049	2.545	2.360	2.335	2.245	2.018	1.739	1.762	1.801	1.991	1.880	1.535
-66	6.859	7.644	9.020	9.667	9.999	10.327	9.946	9.578	9.607	9.547	11.159	11.902	11.597
-39	17.988	19.118	21.178	21.447	22.426	22.453	22.266	21.795	21.614	21.455	23.025	23.833	24.228
20.5	35.933	39.638	44.161	46.167	48.168	48.493	48.479	47.908	47.178	47.326	49.178	49.937	49.288
39	23.522	23.545	24.826	24.795	26.257	26.547	26.414	26.035	26.077	26.104	26.910	27.160	26.109
66	8.096	9.255	10.716	10.930	10.802	10.588	10.621	10.579	10.634	11.109	13.163	13.370	12.784
96	1.365	1.843	2.504	2.411	2.364	2.331	2.182	1.963	1.998	2.059	1.857	1.526	1.392
127	0.308	0.563	0.900	0.682	0.581	0.539	0.342	0.166	0.207	0.134	-0.039	-0.099	-0.304

Table E-5: BETS045 averaged non-dimensional braiding temperature profiles calculated at the top layer of measurement.

TOP LAYER MEASUREMENT [%]													
Bed transverse position [mm]	Reynolds Number [-]												
	1000	**2000**	**3000**	**4000**	**5000**	**6000**	**7000**	**8000**	**9000**	**10000**	**20000**	**30000**	**40000**
-148.5	2.919	1.826	2.046	2.093	2.016	1.729	1.795	1.699	1.564	1.431	1.209	1.025	1.047
-128	2.801	1.883	2.123	2.210	2.123	1.837	1.872	1.774	1.639	1.505	1.220	1.041	1.038
-95.5	4.916	4.440	4.977	5.295	5.465	5.345	5.522	5.624	5.409	5.418	5.217	5.172	4.887
-64	18.939	21.120	23.010	23.922	24.729	25.286	25.670	26.094	25.653	25.798	26.204	27.374	26.020
-32	19.661	20.871	22.383	22.895	23.545	23.983	24.339	24.704	24.265	24.358	24.652	25.687	24.349
32	25.374	29.667	33.494	35.761	37.292	38.466	39.552	39.851	39.424	39.276	39.806	40.628	38.099
64	11.905	12.666	14.141	15.204	15.927	16.560	17.093	17.299	17.167	17.014	17.461	17.652	16.804
95.5	4.022	3.259	3.674	3.998	4.080	4.031	4.141	4.166	4.013	3.840	3.333	2.886	2.659
128	3.159	2.124	2.351	2.523	2.448	2.195	2.242	2.152	2.013	1.873	1.550	1.307	1.269
148.5	3.477	2.064	2.286	2.385	2.304	2.055	2.103	2.019	1.840	1.671	1.339	1.089	1.088
-144.5	2.782	1.782	2.019	2.113	2.046	1.750	1.818	1.744	1.596	1.462	1.267	1.070	1.031
-113.5	3.060	2.251	2.548	2.701	2.632	2.421	2.488	2.444	2.306	2.198	2.013	1.744	1.507
-82	8.630	7.632	7.842	7.869	7.843	7.637	7.790	7.736	7.555	7.357	7.110	7.460	7.298
-51	23.453	26.607	29.744	31.715	33.178	34.197	35.359	35.576	35.256	35.014	34.797	35.720	33.323
32	22.245	24.575	26.932	28.094	28.750	29.302	30.088	29.796	29.293	29.156	29.425	30.397	28.810
51	27.216	31.289	34.788	36.870	38.330	39.553	40.706	40.919	40.420	40.267	40.589	41.613	39.368
82	8.875	8.536	9.602	10.163	10.225	10.348	10.506	10.567	10.415	10.217	9.490	9.476	8.928
113.5	4.517	3.698	4.127	4.387	4.422	4.275	4.358	4.344	4.213	4.041	3.740	3.384	3.218
144.5	2.854	1.875	2.137	2.237	2.201	1.968	2.042	1.968	1.825	1.666	1.333	1.106	1.111

Table E-6: BETS045 averaged non-dimensional braiding temperature profiles calculated at the bottom layer measurement.

BOTTOM LAYER MEASUREMENT [%]													
Bed transverse position [mm]	Reynolds Number [-]												
	1000	**2000**	**3000**	**4000**	**5000**	**6000**	**7000**	**8000**	**9000**	**10000**	**20000**	**30000**	**40000**
-146.5	2.713	1.852	1.746	1.906	1.716	1.659	1.634	1.471	1.415	1.488	1.171	1.082	0.893
-114	3.472	2.607	2.594	2.806	2.651	2.595	2.554	2.392	2.371	2.451	2.038	1.922	1.694
-83	9.788	8.186	8.615	8.804	8.565	8.812	8.948	8.987	9.235	9.016	8.470	8.632	8.011
-51	35.821	37.516	41.239	42.563	42.621	43.689	44.525	44.654	45.312	45.152	48.099	48.963	48.956
-20.5	45.022	48.498	52.901	54.675	55.378	56.833	57.740	57.813	58.030	58.470	62.499	62.505	61.548
20.5	25.189	26.071	28.731	30.992	32.322	31.840	32.834	30.868	30.555	33.812	36.184	36.295	36.718
51	9.259	8.256	8.948	9.030	9.154	8.431	7.872	8.005	7.801	8.092	9.054	10.367	10.534
82	3.764	2.735	2.568	2.733	2.452	2.323	2.215	2.040	2.016	2.069	1.779	1.677	1.440
114	2.992	1.980	1.825	1.994	1.789	1.732	1.662	1.471	1.425	1.500	1.169	1.056	0.874
146.5	2.697	1.672	1.545	1.722	1.536	1.496	1.405	1.238	1.240	1.289	1.024	0.910	0.751
-130.5	3.006	2.287	2.240	2.444	2.258	2.239	2.195	2.061	2.050	2.094	1.769	1.634	1.401
-99.5	5.741	5.148	5.676	6.100	5.996	6.075	5.998	5.812	5.713	5.726	4.736	4.459	4.243
-68.5	13.794	12.966	13.980	14.926	15.101	15.593	15.887	16.157	16.319	16.459	16.930	17.299	17.029
-39	33.871	36.666	39.970	41.140	41.696	42.515	42.973	43.502	43.522	44.052	46.473	46.738	46.973
20.5	46.165	50.068	54.564	55.646	56.617	57.577	57.646	57.040	56.564	57.405	58.336	59.314	59.305
39	17.551	18.133	19.936	20.922	21.456	22.164	21.917	22.162	21.836	21.578	21.021	21.467	21.851
68.5	5.872	5.474	6.130	6.554	6.310	6.156	5.846	5.746	5.635	5.705	5.474	5.388	5.107
99.5	2.774	1.860	1.719	1.954	1.722	1.659	1.577	1.392	1.351	1.406	1.101	1.010	0.813
130.5	2.800	1.750	1.573	2.250	1.567	1.488	1.410	1.226	1.208	1.260	0.959	0.867	0.691

APPENDIX F: Normalized braiding temperature profiles

Table F-1 to Table F-6 shows the normalized braiding temperature profiles at the at the top and bottom layers of transversal measurements inside the packed bed for the three test sections.

Table F- 1: BETS036 normalized braiding temperature profiles at the top layer measurement (recalculated from the average inlet gas temperatures and non-dimensional braiding temperatures).

TOP LAYER MEASUREMENT [˚C]													
Bed transverse position [mm]	Reynolds Number [-]												
	1000	**2000**	**3000**	**4000**	**5000**	**6000**	**7000**	**8000**	**9000**	**10000**	**20000**	**30000**	**40000**
-136	16.07	15.33	14.40	14.92	14.12	13.97	13.92	14.27	14.67	14.18	14.91	15.16	15.82
-106	16.46	15.73	14.78	15.29	14.49	14.35	14.31	14.69	15.11	14.62	15.27	15.51	16.20
-76	19.17	18.50	17.80	18.30	17.50	17.33	17.37	17.74	18.16	17.74	18.46	18.70	19.21
-47	22.73	22.92	23.27	23.85	23.23	23.11	23.24	23.56	23.91	23.61	25.06	25.19	25.15
-21	26.44	26.85	27.54	28.29	27.89	27.79	28.07	28.43	28.97	28.97	30.60	30.90	30.89
47	23.41	23.56	23.75	24.49	23.96	23.69	23.68	23.74	24.11	23.93	24.92	24.96	25.09
76	21.13	21.19	21.07	21.73	21.06	20.79	20.75	20.87	21.30	21.10	22.10	21.98	22.14
106	18.00	17.36	16.59	17.00	16.28	15.97	15.91	16.19	16.59	16.23	17.05	17.15	17.66
136	16.41	15.71	14.74	15.26	14.45	14.27	14.23	14.56	14.95	14.49	15.21	15.45	16.11
-149	16.16	15.30	14.33	14.87	14.06	13.91	13.86	14.21	14.61	14.13	14.86	15.11	15.76
-121	16.06	15.40	14.49	15.02	14.25	14.10	14.08	14.43	14.82	14.33	15.08	15.34	16.00
-91	16.92	16.25	15.40	15.91	15.12	14.98	14.95	15.28	15.64	15.15	15.73	15.92	16.52
-61	19.46	19.03	18.61	19.15	18.30	18.08	18.11	18.45	18.90	18.54	19.65	19.90	20.33
-32	24.61	24.71	24.91	25.26	24.54	24.28	24.31	24.67	25.16	25.03	26.38	26.64	26.96
32	24.52	24.57	24.64	25.19	24.34	24.06	23.98	24.21	24.52	24.17	24.90	24.98	25.14
61	20.44	20.13	19.77	19.90	19.72	19.42	19.37	20.14	20.53	20.22	21.12	21.24	21.59
91	17.46	16.99	16.30	16.89	16.18	16.00	15.95	16.32	16.72	16.31	17.30	17.52	18.08
121	16.37	15.69	14.75	15.25	14.47	14.30	14.25	14.59	14.99	14.53	15.29	15.53	16.14
149	16.29	15.41	14.42	14.94	14.13	13.97	13.92	14.26	14.64	14.17	14.89	15.12	15.76

Table F- 2: BETS036 normalized braiding temperature profiles at the bottom layer measurement (recalculated from the average inlet gas temperatures and non-dimensional braiding temperatures).

BOTTOM LAYER MEASUREMENT [˚C]													
Bed transverse position [mm]	Reynolds Number [-]												
	1000	**2000**	**3000**	**4000**	**5000**	**6000**	**7000**	**8000**	**9000**	**10000**	**20000**	**30000**	**40000**
-124	16.01	15.48	14.59	15.10	14.31	14.17	14.15	14.50	14.88	14.42	15.13	15.39	16.05
-94	16.33	15.80	14.96	15.49	14.72	14.56	14.54	14.89	15.29	14.83	15.50	15.74	16.37
-65	18.99	18.18	17.59	18.08	17.29	17.19	17.27	17.67	18.18	17.66	18.28	18.60	18.96
-36	29.97	30.69	31.85	32.66	32.08	31.95	32.43	32.74	33.41	33.22	35.36	35.76	35.70
-20	33.85	35.37	36.94	37.89	37.63	37.51	38.06	38.29	38.77	38.96	41.56	41.52	40.84
33	25.49	25.81	26.38	27.66	27.61	26.94	27.45	26.91	27.18	28.34	30.22	30.37	30.69
65	18.77	18.21	17.74	18.18	17.55	17.03	16.81	17.26	17.58	17.26	18.53	19.34	19.99
94	16.45	15.86	14.95	15.46	14.63	14.45	14.40	14.74	15.14	14.67	15.39	15.64	16.27
124	16.13	15.53	14.63	15.14	14.35	14.20	14.16	14.50	14.89	14.42	15.13	15.37	16.04
-139	16.00	15.40	14.50	15.02	14.24	14.10	14.05	14.40	14.81	14.33	15.07	15.31	15.99
-108	16.13	15.67	14.81	15.34	14.55	14.41	14.39	14.75	15.15	14.68	15.39	15.62	16.25
-78	17.29	16.89	16.31	16.92	16.17	16.04	16.01	16.33	16.70	16.24	16.67	16.82	17.42
-48	20.68	20.22	19.94	20.73	20.13	20.06	20.23	20.70	21.17	20.86	21.92	22.28	22.64
-20	29.15	30.33	31.29	32.05	31.68	31.45	31.77	32.25	32.65	32.75	34.66	34.81	34.89
20	34.33	36.04	37.67	38.31	38.16	37.83	38.02	37.97	38.15	38.50	39.77	40.16	39.93
48	22.27	22.42	22.54	23.32	22.89	22.84	22.80	23.24	23.50	23.07	23.69	24.06	24.62
78	17.34	17.02	16.51	17.11	16.31	16.07	15.95	16.30	16.66	16.23	16.98	17.22	17.77
108	16.03	15.48	14.58	15.13	14.32	14.17	14.13	14.47	14.86	14.38	15.10	15.35	16.01
139	16.04	15.44	14.52	15.25	14.25	14.10	14.06	14.40	14.80	14.32	15.04	15.29	15.96

Table F- 3: BETS039 normalized braiding temperature profiles at the top layer measurement (recalculated from the average inlet gas temperatures and non-dimensional braiding temperatures).

TOP LAYER MEASUREMENT [˚C]													
Bed transverse position [mm]	Reynolds Number [-]												
	1000	**2000**	**3000**	**4000**	**5000**	**6000**	**7000**	**8000**	**9000**	**10000**	**20000**	**30000**	**40000**
-144	16.64	15.72	15.66	16.43	15.66	15.56	15.47	15.40	15.35	15.44	15.94	16.41	17.02
-123	16.57	15.65	15.58	16.36	15.59	15.50	15.40	15.33	15.28	15.37	15.88	16.37	17.00
-92	17.18	16.33	16.39	17.27	16.62	16.50	16.38	16.29	16.17	16.26	16.72	17.17	17.83
-62	21.45	21.21	21.71	22.62	22.29	21.85	21.53	21.40	21.01	21.14	21.83	22.69	23.40
-31	25.48	25.72	26.52	27.53	27.28	26.72	26.36	26.24	25.67	25.85	26.56	27.18	27.76
31	25.54	25.89	26.41	27.47	27.27	26.75	26.67	26.63	26.40	26.67	28.28	28.15	28.40
62	21.13	20.52	20.67	21.57	20.84	20.58	20.48	20.45	20.32	20.49	21.58	21.67	22.50
92	17.29	16.37	16.29	17.11	16.41	16.28	16.19	16.16	16.07	16.18	16.80	17.08	17.79
123	16.78	15.89	15.81	16.57	15.79	15.68	15.58	15.51	15.43	15.53	16.02	16.46	17.10
144	16.62	15.71	15.63	16.39	15.61	15.51	15.42	15.35	15.28	15.37	15.87	16.35	16.99
-140	16.65	15.72	15.67	16.44	15.68	15.59	15.49	15.42	15.37	15.47	15.96	16.43	17.04
-109	16.70	15.85	15.84	16.68	15.96	15.87	15.80	15.74	15.67	15.78	16.27	16.69	17.27
-80	18.15	17.63	17.88	18.87	18.35	18.16	17.92	17.70	17.54	17.60	18.28	18.79	19.38
-51	22.98	23.05	23.75	24.95	24.58	24.34	24.17	24.04	23.71	23.96	25.70	26.49	27.20
3.5	27.09	27.89	28.81	30.12	30.18	29.77	29.87	29.89	29.51	29.93	31.40	31.15	30.99
51	20.73	20.17	20.43	21.38	21.08	20.79	20.81	20.91	20.67	21.04	22.36	22.60	22.97
80	18.78	18.02	17.97	18.68	17.86	17.62	17.52	17.41	17.22	17.38	17.80	18.22	18.96
109	16.77	15.90	15.80	16.56	15.76	15.65	15.54	15.47	15.39	15.49	15.97	16.45	17.10
140	16.53	15.62	15.55	16.32	15.54	15.44	15.34	15.28	15.21	15.30	15.81	16.29	16.91

Table F- 4: BETS039 normalized braiding temperature profiles at the bottom layer measurement (recalculated from the average inlet gas temperatures and non-dimensional braiding temperatures).

BOTTOM LAYER MEASUREMENT [˚C]													
Bed transverse position [mm]	Reynolds Number [-]												
	1000	**2000**	**3000**	**4000**	**5000**	**6000**	**7000**	**8000**	**9000**	**10000**	**20000**	**30000**	**40000**
-142	16.771	15.906	15.801	16.593	15.825	15.726	15.638	15.581	15.520	15.618	16.125	16.619	17.254
-111	16.723	15.892	15.775	16.568	15.797	15.697	15.598	15.539	15.473	15.573	16.077	16.552	17.185
-80.5	17.461	16.717	16.785	17.656	16.916	16.776	16.697	16.637	16.538	16.671	17.418	17.813	18.342
-49	21.275	20.378	20.476	21.194	20.580	20.171	19.958	19.753	19.380	19.583	21.011	22.188	23.129
-15	35.288	36.840	37.942	39.525	40.146	39.675	39.649	39.709	39.044	39.595	41.184	41.089	41.324
20	33.649	35.198	36.265	37.737	37.719	36.948	36.684	36.515	35.991	36.453	38.264	37.999	38.384
49	24.003	23.788	24.208	25.124	24.327	23.870	23.605	23.535	23.285	23.607	24.823	25.053	26.398
80.5	17.570	16.715	16.652	17.552	16.933	16.879	16.874	16.855	16.795	16.990	17.839	18.179	18.898
111	16.783	15.955	15.822	16.598	15.836	15.717	15.621	15.569	15.490	15.589	16.087	16.550	17.193
141	16.832	16.001	15.873	16.641	15.870	15.772	15.677	15.630	15.555	15.648	16.169	16.657	17.303
-127	16.788	15.971	15.854	16.653	15.882	15.790	15.692	15.629	15.556	15.648	16.161	16.639	17.272
-96	17.243	16.490	16.429	17.213	16.468	16.337	16.228	16.148	16.057	16.198	16.884	17.321	17.905
-66	19.371	18.952	19.232	20.335	19.791	19.772	19.605	19.525	19.396	19.539	20.885	21.559	22.102
-39	23.999	24.002	24.495	25.367	25.180	24.926	24.851	24.787	24.506	24.675	26.063	26.604	27.369
20.5	31.461	33.033	34.444	35.927	36.341	35.993	36.014	36.036	35.385	35.834	37.475	37.643	37.821
39	26.300	25.950	26.074	26.797	26.841	26.665	26.617	26.614	26.405	26.681	27.758	28.011	28.154
66	19.886	19.661	19.966	20.875	20.140	19.882	19.892	19.956	19.833	20.213	21.759	22.180	22.597
96	17.087	16.399	16.411	17.235	16.480	16.373	16.298	16.244	16.158	16.309	16.826	17.171	17.846
127	16.648	15.836	15.717	16.497	15.708	15.611	15.515	15.470	15.396	15.479	15.998	16.484	17.138

Table F- 5: BETS045 normalized braiding temperature profiles at the top layer measurement (recalculated from the average inlet gas temperatures and non-dimensional braiding temperatures).

TOP LAYER MEASUREMENT [˚C]													
Bed transverse position [mm]	Reynolds Number [-]												
	1000	**2000**	**3000**	**4000**	**5000**	**6000**	**7000**	**8000**	**9000**	**10000**	**20000**	**30000**	**40000**
-148.5	18.03	15.69	15.36	15.47	15.45	14.79	14.75	14.82	14.79	14.68	14.33	14.23	13.96
-128	17.98	15.71	15.40	15.52	15.50	14.84	14.78	14.86	14.83	14.72	14.34	14.24	13.95
-95.5	18.89	16.79	16.60	16.85	16.90	16.31	16.30	16.51	16.47	16.44	16.10	16.02	15.56
-64	24.87	23.86	24.23	24.85	24.96	24.67	24.68	25.32	25.32	25.43	25.33	25.59	24.41
-32	25.18	23.75	23.96	24.41	24.46	24.12	24.13	24.73	24.72	24.79	24.65	24.86	23.71
32	27.62	27.48	28.66	29.94	30.21	30.20	30.45	31.25	31.34	31.37	31.31	31.30	29.46
64	21.87	20.28	20.48	21.10	21.27	21.01	21.11	21.54	21.61	21.55	21.48	21.40	20.55
95.5	18.50	16.29	16.05	16.29	16.32	15.76	15.73	15.89	15.86	15.74	15.27	15.04	14.63
128	18.14	15.81	15.49	15.66	15.63	14.99	14.94	15.02	14.99	14.88	14.48	14.36	14.05
148.5	18.27	15.79	15.47	15.60	15.57	14.93	14.88	14.96	14.91	14.79	14.39	14.26	13.97
-144.5	17.97	15.67	15.35	15.48	15.47	14.80	14.76	14.84	14.81	14.70	14.36	14.25	13.95
-113.5	18.09	15.87	15.58	15.73	15.71	15.08	15.04	15.15	15.12	15.02	14.69	14.54	14.15
-82	20.47	18.15	17.81	17.95	17.89	17.27	17.24	17.42	17.41	17.30	16.93	17.01	16.57
-51	26.80	26.18	27.07	28.20	28.49	28.41	28.71	29.41	29.52	29.49	29.11	29.18	27.46
32	26.28	25.32	25.88	26.64	26.64	26.35	26.52	26.92	26.91	26.91	26.75	26.89	25.57
51	28.41	28.17	29.21	30.41	30.65	30.65	30.93	31.71	31.78	31.81	31.66	31.72	29.99
82	20.58	18.53	18.56	18.94	18.89	18.41	18.37	18.64	18.66	18.56	17.98	17.88	17.25
113.5	18.71	16.48	16.24	16.46	16.46	15.86	15.82	15.96	15.95	15.83	15.45	15.25	14.86
144.5	18.00	15.71	15.40	15.53	15.53	14.89	14.85	14.94	14.91	14.79	14.39	14.27	13.98

Table F- 6: BETS045 normalized braiding temperature profiles at the bottom layer measurement (recalculated from the average inlet gas temperatures and non-dimensional braiding temperatures).

BOTTOM LAYER MEASUREMENT [˚C]													
Bed transverse position [mm]	Reynolds Number [-]												
	1000	**2000**	**3000**	**4000**	**5000**	**6000**	**7000**	**8000**	**9000**	**10000**	**20000**	**30000**	**40000**
-146.5	17.99	15.78	15.45	15.59	15.57	14.92	14.88	14.95	14.94	14.83	14.49	14.40	14.10
-114	18.03	15.89	15.56	15.69	15.66	15.02	14.97	15.04	15.01	14.91	14.56	14.46	14.16
-83	18.76	16.67	16.50	16.70	16.67	16.02	15.96	16.07	16.02	15.92	15.56	15.47	14.99
-51	24.23	23.17	23.52	24.17	24.46	24.17	24.42	25.09	25.04	25.15	25.24	25.55	24.20
-20.5	35.51	36.58	37.86	39.06	38.97	38.75	38.89	39.89	39.69	39.52	38.17	37.77	35.32
20.5	35.34	36.44	38.06	39.74	40.03	40.04	40.19	41.31	41.24	41.15	39.92	39.09	36.60
51	23.46	22.37	22.79	23.28	23.28	22.90	22.83	23.35	23.51	23.60	24.66	25.86	25.09
82	19.06	16.89	16.66	16.92	16.93	16.41	16.42	16.62	16.65	16.61	16.43	16.28	15.65
114	17.03	15.15	14.79	14.86	14.87	14.81	14.67	14.71	14.64	14.52	14.16	14.10	13.80
146.5	18.06	15.83	15.49	15.63	15.62	14.96	14.92	15.00	14.98	14.87	14.52	14.43	14.13
-130.5	18.00	15.85	15.52	15.64	15.63	14.97	14.94	15.01	14.99	14.88	14.55	14.45	14.16
-99.5	18.18	16.04	15.72	15.86	15.84	15.17	15.13	15.20	15.18	15.07	14.75	14.65	14.35
-68.5	20.63	18.58	18.48	18.73	18.71	18.13	18.12	18.31	18.27	18.18	17.91	17.92	17.27
-39	27.03	26.18	26.97	27.99	28.16	27.99	28.24	28.89	29.00	29.04	28.93	29.38	27.76
20.5	34.59	35.00	36.45	38.10	38.32	38.53	38.93	39.79	39.96	39.74	38.88	38.44	35.83
39	27.34	26.83	27.82	29.08	29.42	29.60	29.96	30.78	30.86	30.95	30.20	30.37	28.48
68.5	20.43	18.81	18.85	19.27	19.35	18.94	18.99	19.33	19.34	19.22	18.49	18.27	17.37
99.5	18.22	16.00	15.67	15.81	15.80	15.14	15.10	15.18	15.15	15.03	14.66	14.54	14.20
130.5	18.02	15.81	15.47	15.61	15.60	14.94	14.90	14.98	14.96	14.85	14.49	14.39	14.10

APPENDIX G: Volume independent solution

This investigation was performed to determine the independence of the braiding temperature profile solution to the volume of the theoretical test section. The volume independent solution was done using a Cartesian grid which resembeled geometric properties of the BETS test section. .

Figure G-1 to Figure G-4 show the inlet flow test cross-sections corresponding to the volume sizes that were investigated. Also indicated in the figures are the radial lines along which the temperature profiles were calculated. Figure G-5 shows the three dimensional (3D) grid for the 1/8 portion of the BETS structure in Figure 3-6. Figure G-5 has the same axial length (D1) as the other volumes, i.e., full volume, halve volume and quarter volume. Temperature solutions were extracted at D1/3 distance from the outlet face (top level of measurement in Figure 3-6).

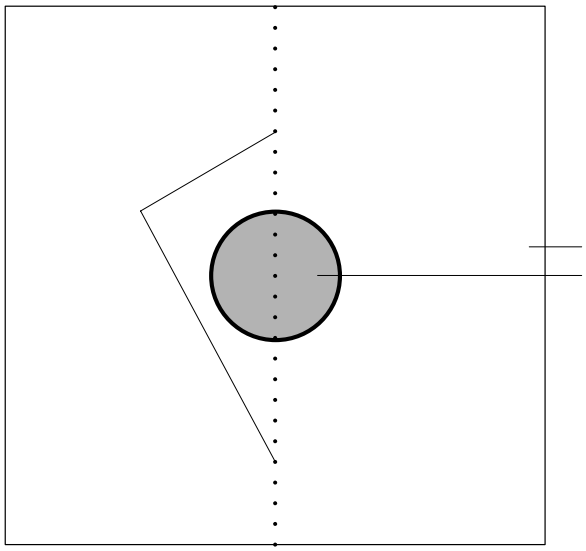

Figure G-1: The inlet flow cross-section of the full volume of the BETS test section.

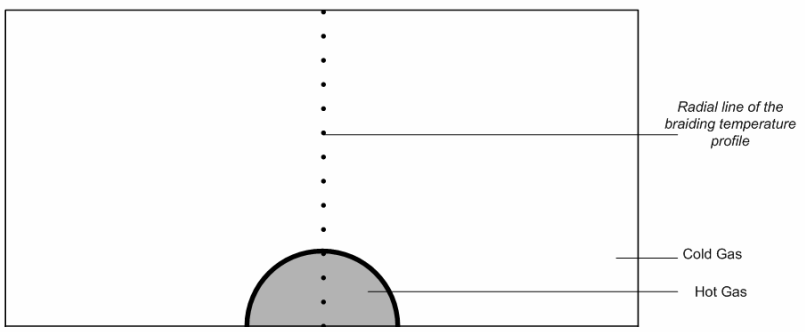

Figure G-2: The inlet flow cross-section of the halve volume of the BETS test section.

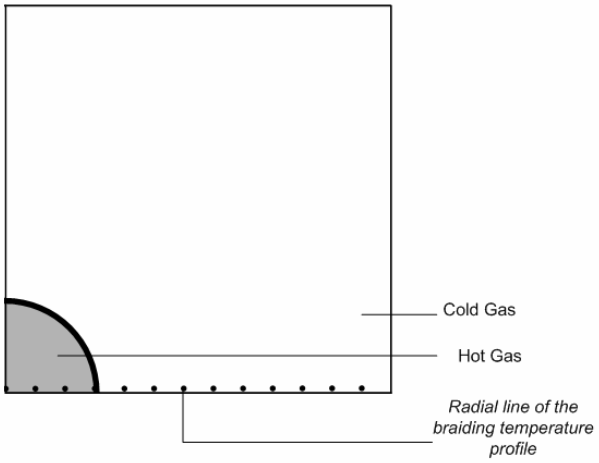

Figure G-3: The inlet flow cross-section of the quarter volume of the BETS test section.

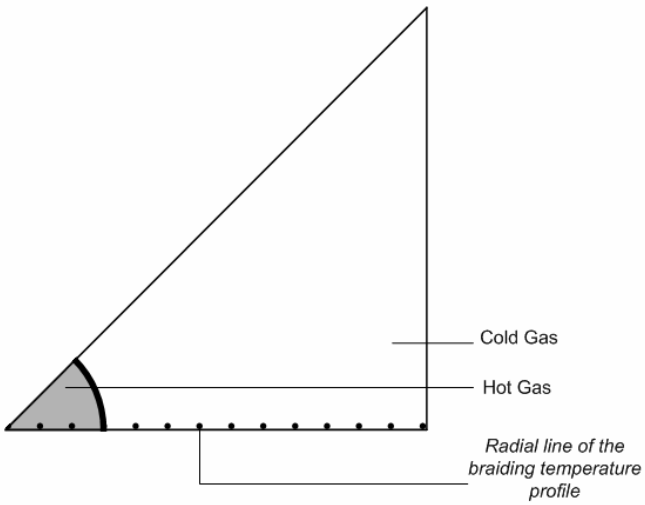

Figure G-4: The inlet flow cross-section of the 1/8 volume of the BETS test section.

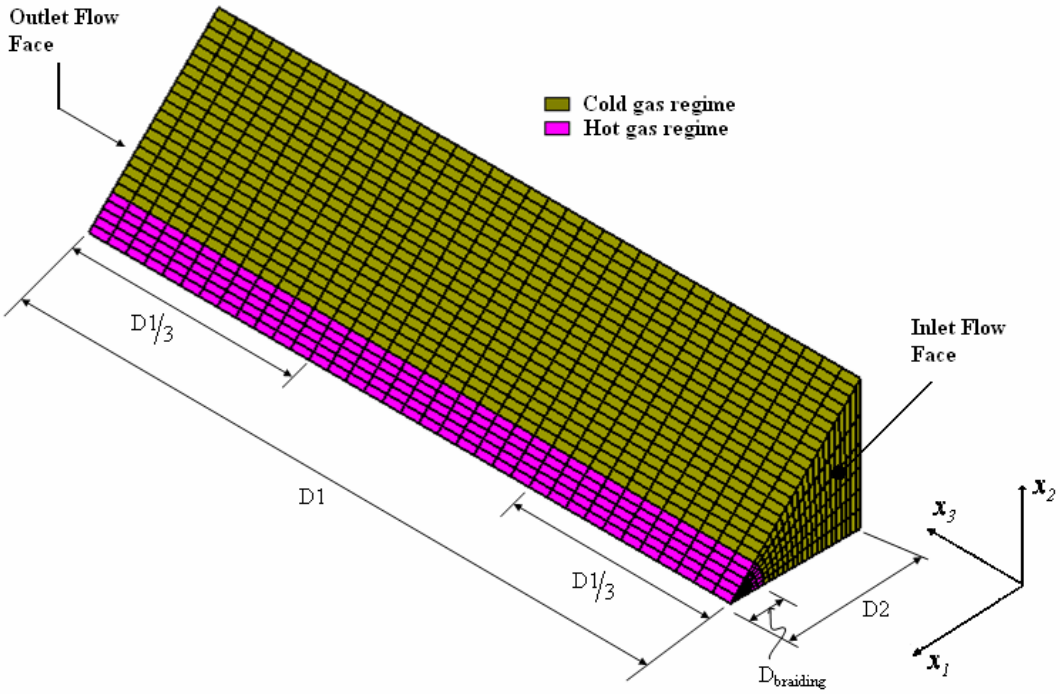

Figure G-5: Three dimensional (3D) grid of the (1/8) portion for the BETS structure.

Flo++[6] uses a finite volume (FV) spatial discretization, to generate the solution for the temperature distribution across the bed. This discretization method generates a structured grid whereby the temperature values at the centres of the discretisized control volumes (CVs) are calculated, i.e. a co-located grid is used. By applying the FV method, these volumes (Figure G-1 to Figure G-4) were divided into twenty (20) radial CVs and eighteen (18) circumferential CVs. For illustrative purposes, this will only be shown for the 1/8 total volume of the BETS test section as shown in Figure G-6.

[6] ©Copyright 1999, Softflo cc. www.softlo.com. Flo++ Home Page and Documentation Information.

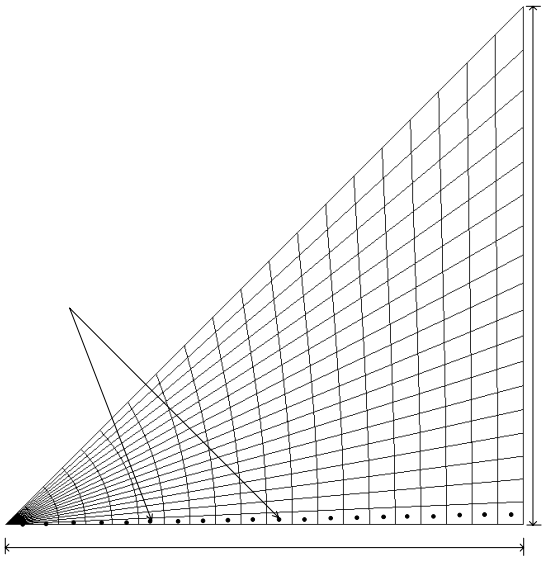

Figure G-6: The inlet flow cross-section as discretisized in radial and circumferential directions.

Table G-1 shows the inlet properties for the cold and hot gas flows to the test section; the data pertains to BETS045. Therefore, the Cartesian grid that resembles the geometric properties of the BETS045 test section was used (Table 4-16). The guessed effective thermal conductivity used was 18.6769 *W/mK*.

Table G-1: Cold and hot gas inlet properties for the volume independence solution.

	Temperature [K]	Pressure [kPa]	Velocity [m/s]
Cold gas	13.518 + 273.15	3800	0.565
Hot gas	55.365 + 273.15	3800	0.573

Table G-2 shows temperature solutions for the four volume sizes that were used with reference to Figure G-1 to Figure G-4. For the same boundary conditions in Table G-1, temperatures values were extracted at D1/3 distance from the outlet face (Figure G-5) and they are given in Table G-2. The full volume has more temperature values than the rest of the volumes because of the bed transverse positions (Figure G-1). The other three have the same number of bed transverse positions (and hence CVs).

Table G-2: Braiding temperature profile temperature values for temperature distribution for different volumes.

Bed transverse position [m]	Full volume [K]	Halve volume [K]	Quarter volume [K]	1/8 volume [K]
-0.1465	286.6722			
-0.1391	286.6751			
-0.1316	286.6827			
-0.1242	286.6993			
-0.1167	286.7333			
-0.1092	286.8004			
-0.1018	286.9272			
-0.0943	287.1571			
-0.0869	287.5543			
-0.0794	288.2062			
-0.0720	289.2173			
-0.0645	290.6923			
-0.0571	292.7049			
-0.0496	295.2603			
-0.0422	298.2626			
-0.0346	301.5568			
-0.0269	304.8321			
-0.0192	307.6810			
-0.0115	309.7788			
-0.0051	310.6979			
0.0051	310.6971	310.6975	310.6837	310.6363
0.0115	309.7771	309.7780	309.7647	309.7753
0.0192	307.6785	307.6797	307.6677	307.7180
0.0269	304.8293	304.8307	304.8209	304.8875
0.0346	301.5538	301.5552	301.5491	301.6159
0.0422	298.2598	298.2612	298.2611	298.3218
0.0496	295.2579	295.2590	295.2637	295.3162
0.0571	292.7030	292.7038	292.7104	292.7523
0.0645	290.6909	290.6914	290.6979	290.7292
0.0720	289.2163	289.2167	289.2221	289.2439
0.0794	288.2055	288.2057	288.2097	288.2242
0.0869	287.5539	287.5540	287.5567	287.5658
0.0943	287.1568	287.1569	287.1587	287.1641
0.1018	286.9271	286.9271	286.9282	286.9313
0.1092	286.8003	286.8003	286.8009	286.8026
0.1167	286.7333	286.7333	286.7336	286.7345
0.1242	286.6993	286.6993	286.6994	286.6999
0.1316	286.6827	286.6827	286.6828	286.6830
0.1391	286.6751	286.6751	286.6751	286.6753
0.1465	286.6722	286.6722	286.6722	286.6723

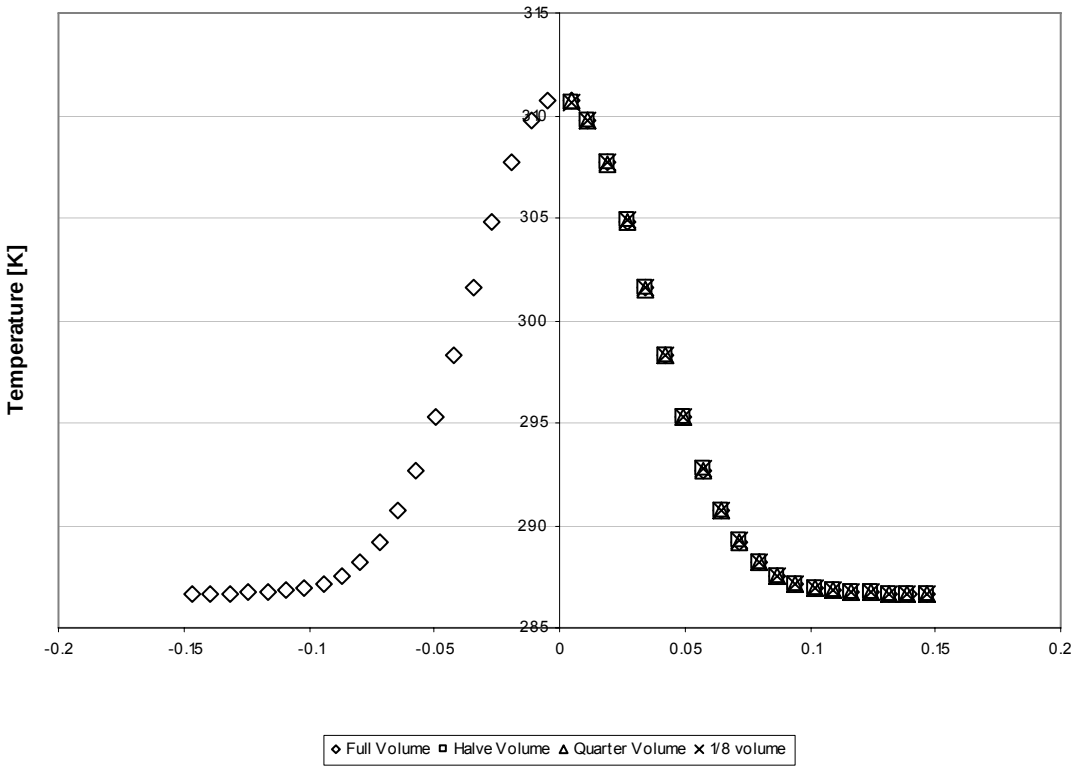

Figure G-7: Comparisons of braiding temperature profiles as the volume of the test section is changed.

Figure G-7 shows that the braiding temperature profiles for all four volumes used stays the same as extracted along the radial lines (bed transverse positions in Table G-2) shown in Figure G-1 to Figure G-4. Therefore, the Cartesian grid that resembled the 1/8 of the total volume was used to generate temperature field solution for all test sections.

The discretization in Figure G-6 was reduced to improve the aspect ratio of the generated CVs; the final resolution is shown in Figure 6-4 and Figure G-8. Boundary conditions in Table G-1 were used and temperature values in for each bed tranverse position were recorded for each Radial line (1 to 5) in Table G-3.

Bed transver

To be certain that temperature values (and hence temperature profile) from any radial line in Figure G-8 could be used for simulation the following equation was used for values in Table G-3 to calculate the percentage difference $\left(Perc\,Diff_{BedTransverse}\right)_{RadialLine1}$ ::

$$\left(Perc\,Diff_{BedTransverse}\right)_{RadialLine1} = \left(1 - \frac{\left(T_{BedTransverse}\right)_{RadialLine1}}{\left(\overline{T}_{BedTransverse}\right)_{RadialLine1\ldots5}}\right) \times 100 \qquad \text{(G.1)}$$

Where for a temperature at a particular bed tranverse position $BedTransverse$ at the Radial line 1 $\left(RadialLine1\right)$ in Figure G-8 and Table G-3:

- $\left(T_{BedTransverse}\right)_{RadialLine1}$ = the temperature calculated at a particular bed tranverse position $BedTransverse$,
- $\left(\overline{T}_{BedTransverse}\right)_{RadialLine1\ldots5}$ = the average temperature calculated at a particular bed tranverse position $BedTransverse$ at all five Radial lines $\left(RadialLine1\ldots5\right)$

Equation (G.1) is applied for each temperature value in Table G-3 and percentage dfferences are tabulated in Table G-4 where an average value of 0.0609% is obtained. This value is satifactory because it is lower than the standard uncertainty percentages in the braiding temperatre profiles from Table C- 1 to Table C- 6 (between 1.5 % and 10.508 %).

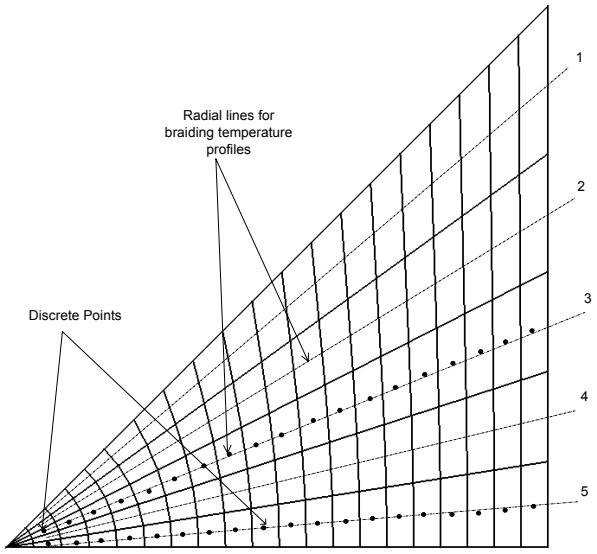

Figure G-8: Discrete points in the structured grid of the gas inflow area of the BETS test section along the corresponding radial lines.

Table G-3: Braiding temperature profile values for different radial lines indicated in Figure G-8

Radial line 1		Radial line 2		Radial line 3		Radial line 4		Radial line 5	
Bed transverse position	Temperature	Bed transverse position	Temperature	Bed transverse position	Temperature	Bed transverse position	Temperature	Bed transverse position	Temperature
[m]	[K]	[m]	[K]	[m]	[K]	[m]	[K]	[m]	[K]
0.005	310.592	0.005	310.594	0.005	310.595	0.005	310.596	0.005	310.596
0.012	309.697	0.012	309.699	0.012	309.700	0.012	309.701	0.012	309.702
0.019	307.621	0.019	307.622	0.019	307.624	0.019	307.625	0.019	307.626
0.027	304.786	0.027	304.789	0.027	304.791	0.027	304.794	0.027	304.795
0.035	301.515	0.035	301.521	0.035	301.528	0.035	301.533	0.035	301.537
0.044	297.514	0.043	297.848	0.043	298.061	0.042	298.189	0.042	298.249
0.054	293.473	0.052	294.261	0.051	294.777	0.050	295.094	0.050	295.244
0.065	290.529	0.061	291.436	0.059	292.077	0.058	292.487	0.057	292.687
0.076	288.662	0.071	289.446	0.067	290.055	0.065	290.468	0.065	290.674
0.086	287.611	0.080	288.175	0.076	288.665	0.073	289.018	0.072	289.202
0.097	287.078	0.089	287.433	0.084	287.780	0.081	288.049	0.079	288.194
0.108	286.831	0.098	287.032	0.092	287.255	0.089	287.441	0.087	287.545
0.118	286.728	0.107	286.831	0.100	286.963	0.096	287.081	0.094	287.151
0.129	286.688	0.117	286.737	0.109	286.809	0.104	286.880	0.102	286.923
0.140	286.674	0.126	286.696	0.117	286.733	0.112	286.773	0.109	286.798
0.150	286.669	0.135	286.678	0.125	286.697	0.120	286.718	0.117	286.732
0.161	286.668	0.144	286.672	0.134	286.680	0.127	286.691	0.124	286.699
0.172	286.668	0.153	286.669	0.142	286.673	0.135	286.678	0.132	286.682
0.182	286.668	0.163	286.668	0.150	286.670	0.143	286.673	0.139	286.675
0.193	286.668	0.172	286.668	0.158	286.669	0.150	286.671	0.147	286.672

Table G-4: Percentage difference in temperatures as determined from Equation (G.1) using temperature values in Table G-3.

Radial line 1		Radial line 2		Radial line 3		Radial line 4		Radial line 5	
Bed transverse position	Percentage Difference	Bed transverse position	Percentage Difference	Bed transverse position	Percentage Difference	Bed transverse position	Percentage Difference	Bed transverse position	Percentage Difference
[m]	[%]	[m]	[%]	[m]	[%]	[m]	[%]	[m]	[%]
0.005	0.0008	0.005	0.0002	0.005	0.0001	0.005	0.0005	0.005	0.0005
0.012	0.0009	0.012	0.0003	0.012	0.0001	0.012	0.0004	0.012	0.0007
0.019	0.0008	0.019	0.0005	0.019	0.0001	0.019	0.0005	0.019	0.0008
0.027	0.0016	0.027	0.0007	0.027	0.0000	0.027	0.0010	0.027	0.0013
0.035	0.0039	0.035	0.0019	0.035	0.0004	0.035	0.0021	0.035	0.0034
0.044	0.1538	0.043	0.0417	0.043	0.0298	0.043	0.0728	0.043	0.0929
0.054	0.3723	0.052	0.1048	0.052	0.0703	0.052	0.1780	0.052	0.2289
0.065	0.4503	0.061	0.1395	0.061	0.0801	0.061	0.2206	0.061	0.2891
0.076	0.4136	0.071	0.1432	0.071	0.0669	0.071	0.2094	0.071	0.2805
0.086	0.3200	0.08	0.1245	0.08	0.0453	0.08	0.1677	0.08	0.2314
0.097	0.2186	0.089	0.0952	0.089	0.0254	0.089	0.1189	0.089	0.1693
0.108	0.1357	0.098	0.0657	0.098	0.0119	0.098	0.0767	0.098	0.1129
0.118	0.0776	0.107	0.0417	0.107	0.0043	0.107	0.0454	0.107	0.0698
0.129	0.0416	0.117	0.0245	0.117	0.0006	0.117	0.0253	0.117	0.0403
0.14	0.0212	0.126	0.0135	0.126	0.0006	0.126	0.0133	0.126	0.0220
0.15	0.0104	0.135	0.0073	0.135	0.0006	0.135	0.0067	0.135	0.0116
0.161	0.0049	0.144	0.0035	0.144	0.0007	0.144	0.0031	0.144	0.0059
0.172	0.0021	0.153	0.0017	0.153	0.0003	0.153	0.0014	0.153	0.0028
0.182	0.0010	0.163	0.0010	0.163	0.0003	0.163	0.0008	0.163	0.0015
0.193	0.0006	0.172	0.0006	0.172	0.0002	0.172	0.0005	0.172	0.0008

The braiding temperature profile values in Table G-3 are plotted in Figure G-9 with their bed transverse position. It is seen in the figure that there's a relatively small change in temperature profile (visually); and this can be confirmed by using Equation (G.2).

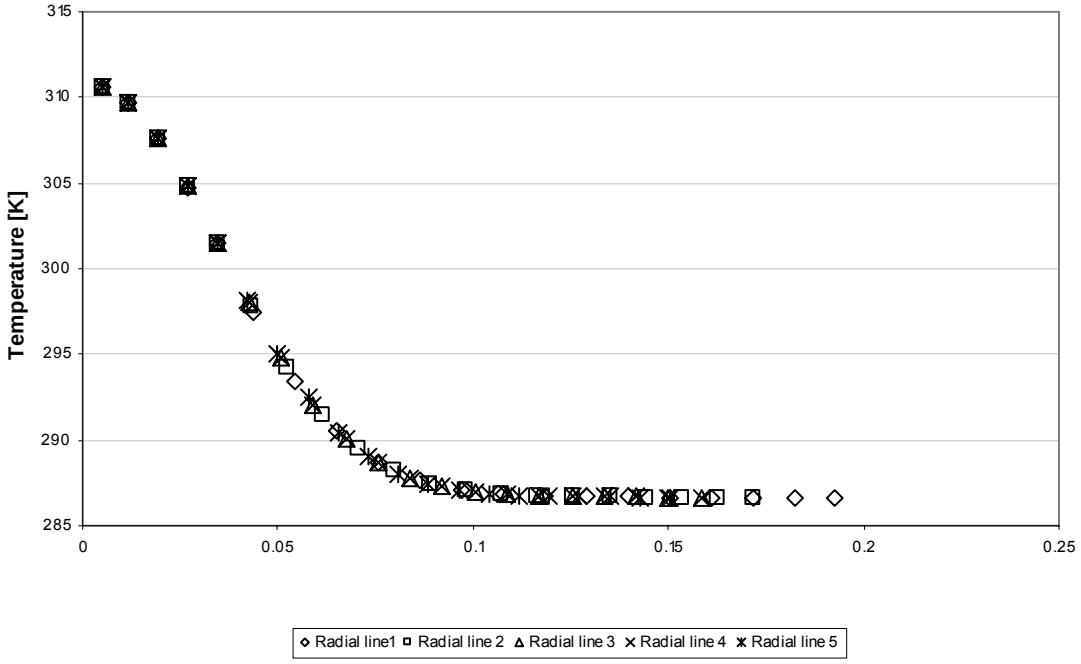

Figure G-9: Comparisons of the braiding temperature profiles at different radial lines.

Bed transve

APPENDIX H: Braiding temperature profile polynomial fit (formulation)

The braiding profile polynomial fit of the experimental results in Appendix F was necessary for the effective thermal conductivity optimization search routine. The search routine (Appendix J) determines the fluid effective thermal conductivity by comparing the experimental polynomial fitted relation with the CFD temperature profiles. As stated before, the customized CFD solution for the BETS geometry was used to predict the calculated CFD temperature profiles at any location in the BETS bed.

The temperature profile of the BETS for measurements done in any of the two measurement layers (Table E-1 to Table E-6) typically has a curved shape as shown in Figure H-1 when plotted against the bed transverse position (also shown in Figure G-7).

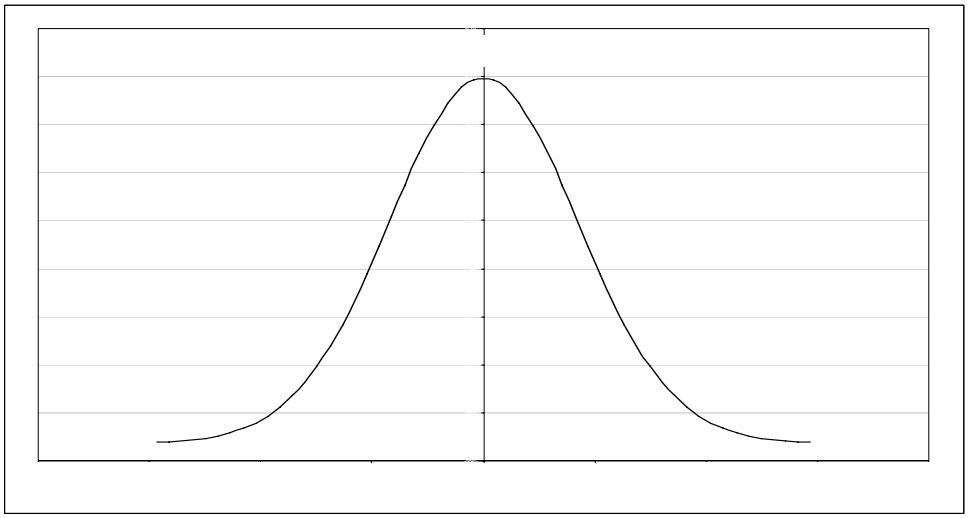

Figure H-1: Braiding temperature profile across the bed.

Theoretically, the radial diffusion between the cold gas and braiding gas is symmetric across the bed i.e. the temperature transverse distribution will be the same in the outward direction from the bed centreline. This is also evident from the CFD generated temperature transverse distribution results in Figure G-7 in Appendix G that are shown to prove volume independence in the braiding temperature profile.

Maximum

The symmetry in the braiding temperature profile for test in the three test sections is evaluated in Appendix I. The symmetry is formulated in Equation (I.1) whereby the calculated value must range between 0 (zero) and 1 (one); which respectively indicates the worst and best symmetry in the measured profile. The calculated values are shown in Table I-1 and they range between 0.93 and 0.99 for all the tests in the three test sections. This implies that the distribution profile can be represented in one quadrant as shown in Figure H-2.

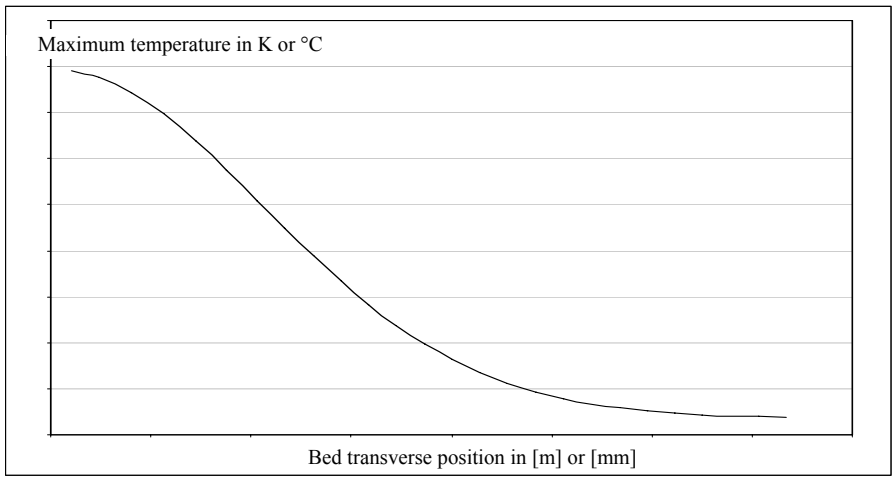

Figure H-2: Braiding temperature profile across the bed (one quadrant representation).

The experimental data given in Appendix F gives a similar braiding temperature profile that is given in Figure H-1. To change the experimental profile to the format in Figure H-2, the following steps were followed:

1. All the negative bed transverse positional values were changed to a positive values,
2. The average temperature were used for measurement points with the same transverse position, and
3. Temperature values were in Kelvin [K].

The above steps have been followed in the spreadsheets that can be found on the accompanying Data CD for each respective BETS test section.

This study found that the correct shape of the curve in Figure H-2 could be represented by a tangent trigonometric function. This was done as follows:

1) A tangent trigonometric function generates a curve that is within the multiples of -90˚ and +90˚ or $-\frac{\pi}{2}$ and $+\frac{\pi}{2}$ in radians. The value of the function will always be zero, and exactly at the midpoint between these limits which are known as asymptotes as indicated in Figure H-3.

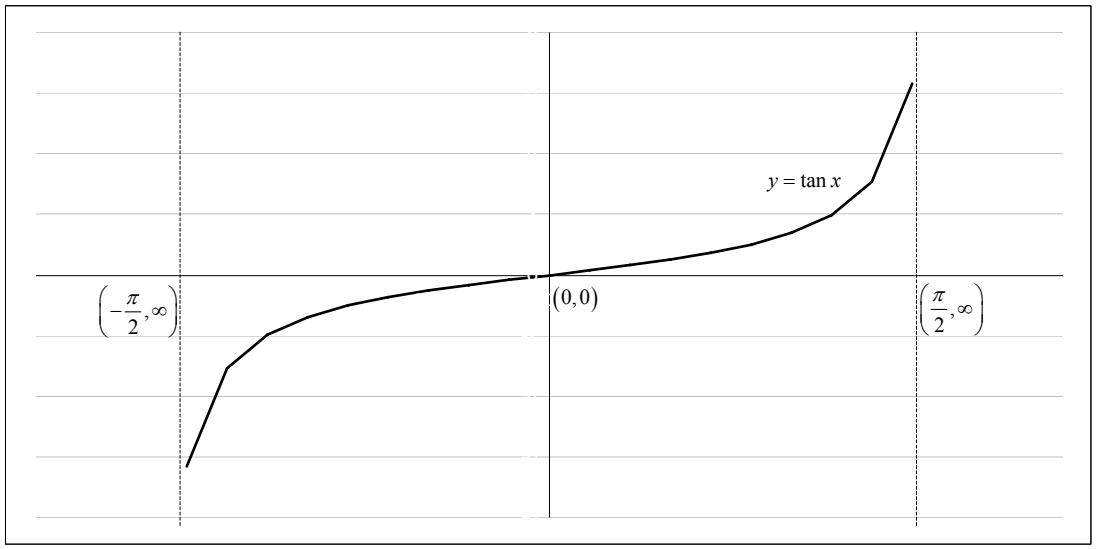

Figure H-3: Tangent trigonometric curve with asymptotes.

The inverse function for the curve in Figure H-3 ($y = \tan x$) generates the curve shown in Figure H-4 ($y = \tan^{-1} x$). The shape of this inverse function generates a curve with the same shape as the temperature braiding profile when multiplied by -1 ($y = -\tan^{-1} x$), as also shown in Figure H-4.

y-axis

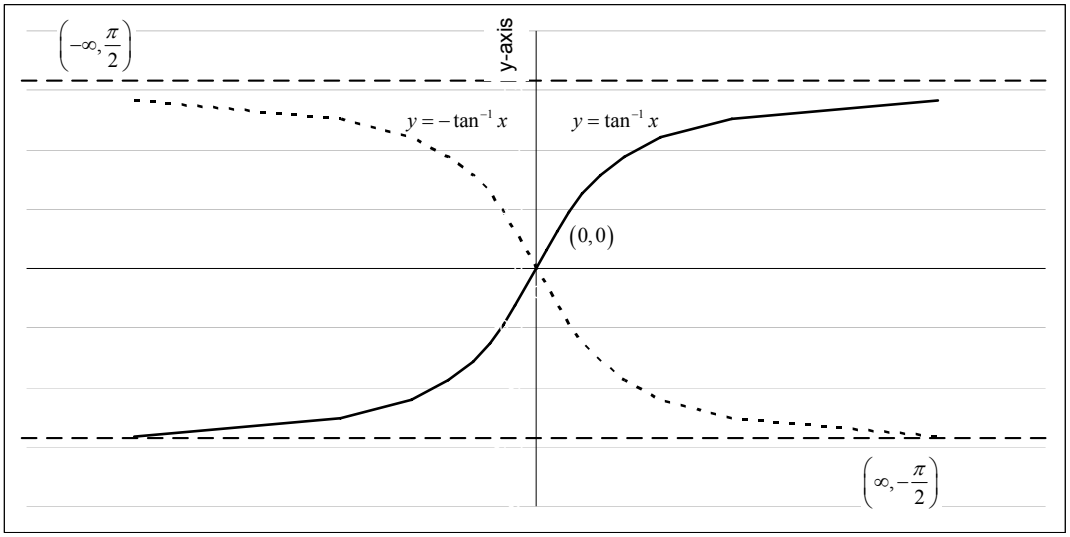

Figure H-4: Arc-tangent trigonometric curves (Inverse functions).

Using the y-axis values as input data, this function can be rewritten as, $x = -\tan y$ and is plotted in Figure H-5.

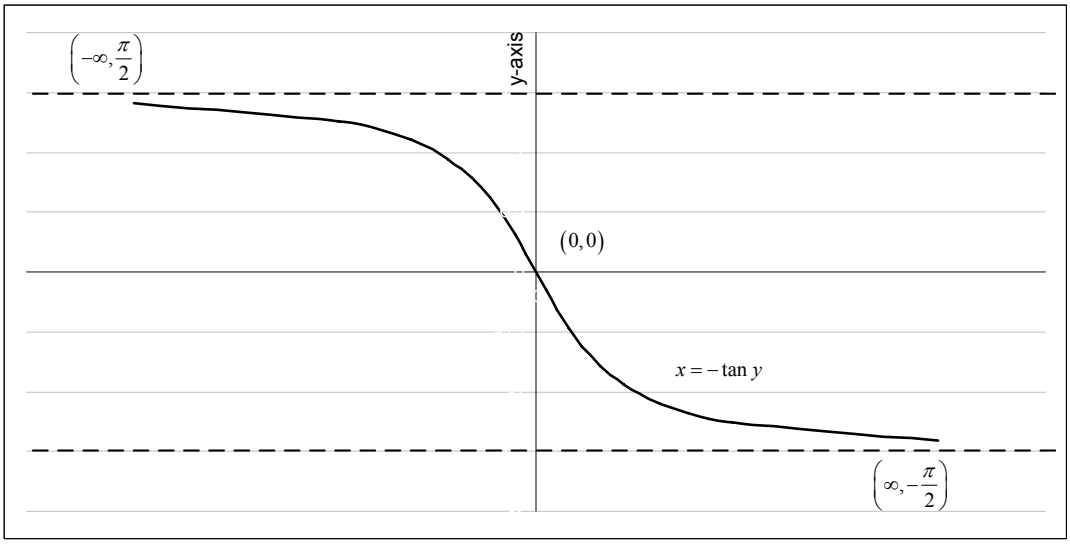

Figure H-5: Tangent trigonometric curve with asymptotes – braiding profile reflection.

2) For illustrative purposes the experimental data for the BETS036 tests at the Reynolds number of 10,000 will be used for the derivation of the final polynomial equation for

the bottom layer. The experimental data is shown in Table H-1 and plotted in Figure H-6.

Table H-1: The experimental data for BETS036 at Reynolds number of 10 000.

BOTTOM LAYER MEASUREMENT	
Bed transverse position	**Temperature Profile**
[m]	[K]
0.02	309.88
0.033	301.50
0.036	306.40
0.048	295.12
0.065	290.61
0.078	289.40
0.094	287.90
0.108	287.70
0.124	287.60
0.139	287.50

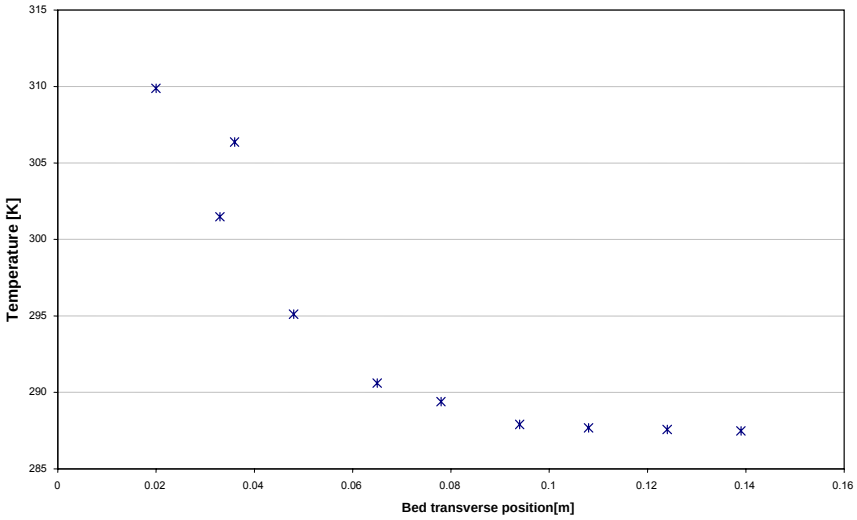

Figure H-6: Braiding temperature profile plot for BETS036 at the Reynolds number of 10 000.

Comparing the plot in Figure H-6 with the curve in Figure H-5 the following can be deduced:

- The limits of the experimental data are in the range of 310 K and 286 K. This implies that the theoretical zero point will be at 298 K. That also implies that the

period between the two asymptotes has decreased from π to $\frac{\pi}{(310-286)} = \frac{\pi}{24}$.

The corresponding *x*-axis (bed transverse position) for the theoretical zero point would be at 0.05 (approximation).

- The zero point (where *x*=*y*) is used to transform the curve in Figure H-5 to the experimental plot curve in Figure H-6 as follows:

$$\begin{aligned} & x = -\tan y \; for \left[-\frac{\pi}{2}, +\frac{\pi}{2} \right] \\ & x - 0.05 \cong -\tan\left((y - 298)\frac{\pi}{24} \right) for \left[286, 310 \right] \\ & \Leftrightarrow x \cong -\tan\left(\frac{\pi}{24}(y - 298) \right) + 0.05 \; for \left[286, 310 \right] \end{aligned} \qquad \text{(H.1)}$$

3) Using the Temperature T for *y*-axis and bed radius r for *x*-axis the experimental curve in Equation (H.1) can be characterized with constants a, b, c and d as follows:

$$r \cong -b \tan\left(a\left(T - c \right) \right) + d \qquad \text{(H.2)}$$

- a = the period of the function,
- b = the amplitude of the function,
- c = the temperature zero point of the curve function, and
- d = the bed radius zero point of the curve function.

Table H-2: The optimized constants for the BETS036 bottom layer experimental data at the Reynolds number of 10, 000.

Constants	Values
a	0.0870407
b	0.014898544
c	303.7650086
d	0.031964811

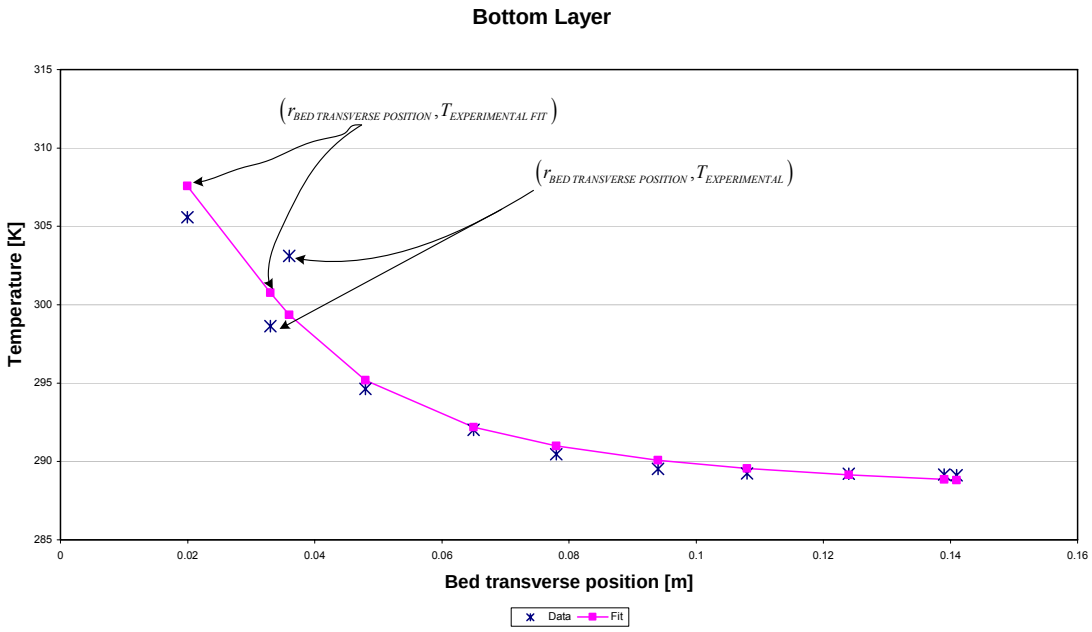

Figure H-7: The polynomial curve fit with the experimental data.

The optimized constants in Table H-2 were calculated by minimizing the difference (errors) between the BETS measured temperature values $T_{EXPERIMENTAL}$ and the calculated temperature values in Equation (H.2). This was done by using bed transverse positions in Table H-1 as input variables (for $r_{BED\,TRANSVERSE\ POSITION}$) to give calculated temperature values $T_{EXPERIMENTAL\,FIT}$; as done in Equation (H.3):

$$T_{EXPERIMENTAL\,FIT} \cong \frac{1}{a}\arctan\left(\frac{d - r_{BED\,TRANSVERSE\ POSITION}}{b}\right) + c \qquad \text{(H.3)}$$

The errors were calculated as follows:

$$error_{EXPERIMENTAL\,FIT} = \left|T_{EXPERIMENTAL} - T_{EXPERIMENTAL\,FIT}\right| \Big/ N \qquad \text{(H.4)}$$

The minimized errors calculated in Equation (H.4) were averaged over the number of points that were fitted at the bottom or top layer measurement N and are summarized in Table H-3 for the three test sections.

Table H-3: Summary of the errors in the polynomial fit for the three test sections.

Reynolds Number [-]	BETS036		BETS039		BETS045	
	Bottom layer measurement	Top layer measurement	Bottom layer measurement	Top layer measurement	Bottom layer measurement	Top layer measurement
1000	0.94	0.41	0.47	0.27	0.28	0.51
2000	0.83	0.46	0.48	0.24	0.33	0.59
3000	0.76	0.50	0.48	0.24	0.34	0.60
4000	0.86	0.50	0.38	0.41	0.39	0.78
5000	0.97	0.51	0.34	0.24	0.38	0.78
6000	1.18	0.53	0.34	0.35	0.34	0.98
7000	1.23	0.56	0.33	0.28	0.36	0.85
8000	1.27	0.53	0.33	0.42	0.59	0.76
9000	1.21	0.58	0.35	0.27	0.60	0.78
10000	1.14	0.55	0.36	0.43	0.60	0.80
20000	1.00	0.62	0.37	0.40	0.55	0.90
30000	0.81	0.65	0.62	0.41	0.71	0.80
40000	0.78	0.53	0.43	0.44	0.48	0.05

The errors are in the range between 0.05 and 1.27.

The so-called R-squared value R^2 in Equation (H.5) was used to evaluate the polynomial fit of the experimental data. For a good fit the defined value must be closer to unity (1).

$$R^2 = 1 - \frac{SSE}{SST} \tag{H.5}$$

Where:

$$SSE = \sum_N \left(T_{EXPERIMENTAL} - T_{EXPERIMENTAL\ FIT} \right)^2,$$

$$SST = \left(\sum_N T_{EXPERIMENTAL}^2 \right) - \frac{\left(\sum_N T_{EXPERIMENTAL} \right)^2}{N},$$

N = number of fitted points at the bottom or top layer measurement.

The R-squared values for the polynomial fit or experimental fit are summarized in Table H-4.

Table H-4: Summary of the R-squared values in the polynomial fit for the three test sections.

Reynolds Number [-]	BETS036		BETS039		BETS045	
	Bottom layer measurement	Top layer measurement	Bottom layer measurement	Top layer measurement	Bottom layer measurement	Top layer measurement
1000	0.94	0.98	0.99	0.99	0.99	0.97
2000	0.94	0.97	0.99	0.99	0.99	0.97
3000	0.94	0.96	0.99	0.99	0.99	0.97
4000	0.95	0.96	0.99	0.97	0.99	0.97
5000	0.95	0.96	0.99	0.99	0.99	0.96
6000	0.94	0.96	0.99	0.99	0.99	0.95
7000	0.92	0.96	0.99	0.99	0.99	0.96
8000	0.92	0.97	0.99	0.98	0.99	0.96
9000	0.93	0.96	0.99	0.99	0.99	0.96
10000	0.94	0.97	0.99	0.97	0.99	0.96
20000	0.96	0.96	0.99	0.98	0.99	0.96
30000	0.96	0.96	0.99	0.98	0.98	0.97
40000	0.96	0.97	0.99	0.98	0.98	0.99

The average value on the calculated R-squared value is 0.99 at all experiments for all three test sections which is satisfactory.

Figure G-8 is redrawn in Figure H-8 and it is important that the following is noted in going forward:

- The temperature T_{CFD} at point $\left(x_{CFD}, y_{CFD}\right)$ in the CFD grid will be located at the radial distance $r_{CFD} = \sqrt{x_{CFD}^2 + y_{CFD}^2}$ (Bed transverse positions in Table G-2 and Table G-3), and
- r_{CFD}, together with the optimized constants $a, b, c \; and \; d$ for the particular experiment, were used to calculate the corresponding experimental temperature value using Equation (H.2); the value was then compared with T_{CFD} for that particular experiment. The comparison is illustrated Appendix J

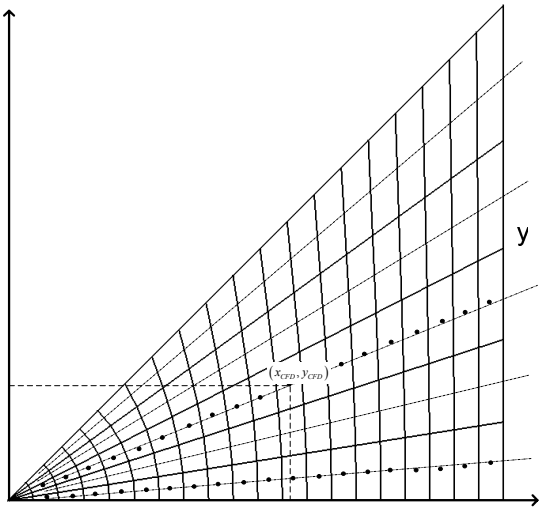

Figure H-8: Discrete points in the structured grid for BETS flow geometry.

APPENDIX I: Braiding temperature profile symmetry

The symmetry in the measured temperature at the point, which is at the bed transverse position $r_{BED\,TRANSVERSE\,POSITION}$ that lies on both sides of the vertical line, is evaluated with the following equation:

$$T_{symm} = \left(1 - \frac{ABS\left(T_{-r_{BED\,TRANSVERSE\,POSITION}} - T_{+r_{BED\,TRANSVERSE\,POSITION}} \right)}{\frac{1}{2}\left(T_{-r_{BED\,TRANSVERSE\,POSITION}} + T_{+r_{BED\,TRANSVERSE\,POSITION}} \right)} \right) \qquad \text{(I.1)}$$

Where,

- $T_{-r_{BED\,TRANSVERSE\,POSITION}}$ = temperature measurements to the left-hand side of the bed vertical line when viewed from the top,
- $T_{+r_{BED\,TRANSVERSE\,POSITION}}$ = temperature measurements to the right-hand side of the bed vertical line when viewed from the top, and

From Equation (I.1), it is deduced that the symmetry value, T_{symm} will be unity if $T_{-r_{BED\,TRANSVERSE\,POSITION}} = T_{+r_{BED\,TRANSVERSE\,POSITION}}$; that will imply that the radial diffusion in the mixture is purely symmetrical. Therefore, the level of symmetry is influenced by the difference between the two measured temperatures.

The measured braiding temperature profiles were normalized by using Equation (5.2); and the calculated values are tabulated in Appendix F from Table F- 1 to Table F- 6. This implies that the normalized values take up values for $T_{EXPERIMENTAL}$ in Figure H-7; and also take up the values of either $T_{-r_{BED\,TRANSVERSE\,POSITION}}$ or $T_{+r_{BED\,TRANSVERSE\,POSITION}}$ for symmetry calculations for the measurements done on both side of the bed vertical line in the top view. Figure A-2 to Figure A-7 in Appendix A show the top views for the three test sections; the thermocouple positioning for $r_{BED\,TRANSVERSE\,POSITION}$ values are also depicted in the figures.

The symmetry values for the normalized temperature values in Table F- 1 to Table F- 6 were calculated using Equation (I.1) and were averaged over the number of points that were fitted at the bottom or top layer of measurement N i.e.:

$$\overline{T}_{symm} = \left(T_{symm1} + T_{symm2} + ... + T_{symmN}\right) \Big/ N \qquad \text{(I.2)}$$

Where,

- $\overline{T}_{symm}$ = averaged symmetrical value for the bottom or top layer of measurement, and
- $T_{symm1}, T_{symm2}, ..., T_{symmN}$ = symmetry values calculated respectively at fitted points $1, 2, ..., N$.

The averaged symmetrical values $\overline{T}_{symm}$ are tabulated in Table I-1 for the three test sections.

Table I-1: Summary in averaged symmetry values calculations in the (normalized) braiding temperature profiles for the three test sections.

Reynolds Number [-]	BETS036		BETS039		BETS045	
	Bottom layer measurement	Top layer measurement	Bottom layer measurement	Top layer measurement	Bottom layer measurement	Top layer measurement
1000	0.96	0.97	0.96	0.98	0.98	0.96
2000	0.95	0.96	0.96	0.99	0.98	0.95
3000	0.95	0.96	0.96	0.99	0.98	0.94
4000	0.95	0.99	0.99	0.99	0.95	0.94
5000	0.94	0.96	0.96	0.99	0.98	0.94
6000	0.94	0.96	0.96	0.99	0.98	0.94
7000	0.95	0.96	0.96	0.99	0.97	0.94
8000	0.95	0.96	0.96	0.99	0.97	0.94
9000	0.95	0.96	0.96	0.97	0.97	0.94
10000	0.94	0.96	0.95	0.97	0.97	0.93
20000	0.94	0.96	0.96	0.94	0.98	0.93
30000	0.94	0.96	0.97	0.96	0.98	0.93
40000	0.95	0.96	0.97	0.98	0.98	0.94

The average symmetry values in the braiding temperature profile range between 0.93 and 0.99 for all tests in all three BETS test sections; the two values are quite close to unity (1) which indicates that the radial diffusion was fairly symmetrical in all experiments.

APPENDIX J: Data search technique

The purpose of the data search technique is to determine the enhanced fluid thermal conductivity in the experimental results by calculating the error between experimental braiding temperature profile and the CFD braiding temperature profile.

Figure J-1 shows the influence of fluid thermal conductivity on the braiding temperature profile as simulated using the CFD model. For particular experimental conditions that are given in Table G-1, two CFD braiding temperature profiles that might fall between the experimental braiding profiles are shown in Figure J-1.

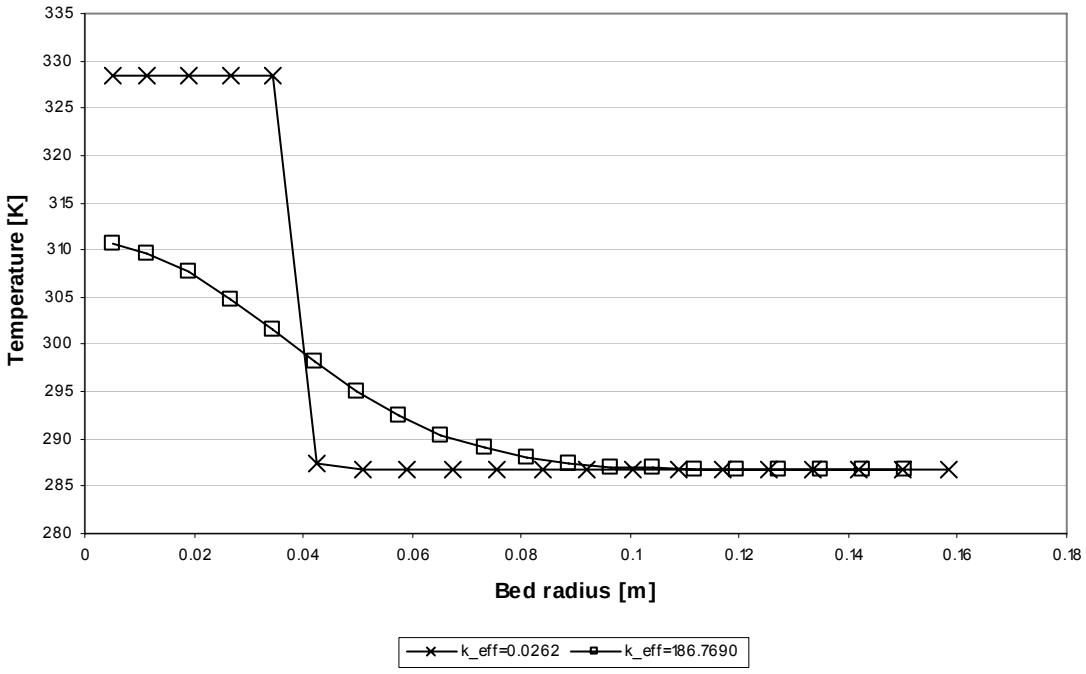

Figure J-1: CFD braiding temperature profiles simulated for different effective conductivity.

The following procedures were followed to calculate the effective thermal conductivity for the experimental results from the CFD model:

- The effective thermal conductivity was randomly chosen (guessed value) to start the CFD simulations,
- The error was calculated between the braiding temperature profiles in the CFD simulations and experimental results,

- The new effective thermal conductivity was formulated as a function of the error calculated in the previous step; this new value was set as a guessed value , and
- The error had to be minimized for an accurate prediction of the final value.

These procedures are summarized in Figure J-2.

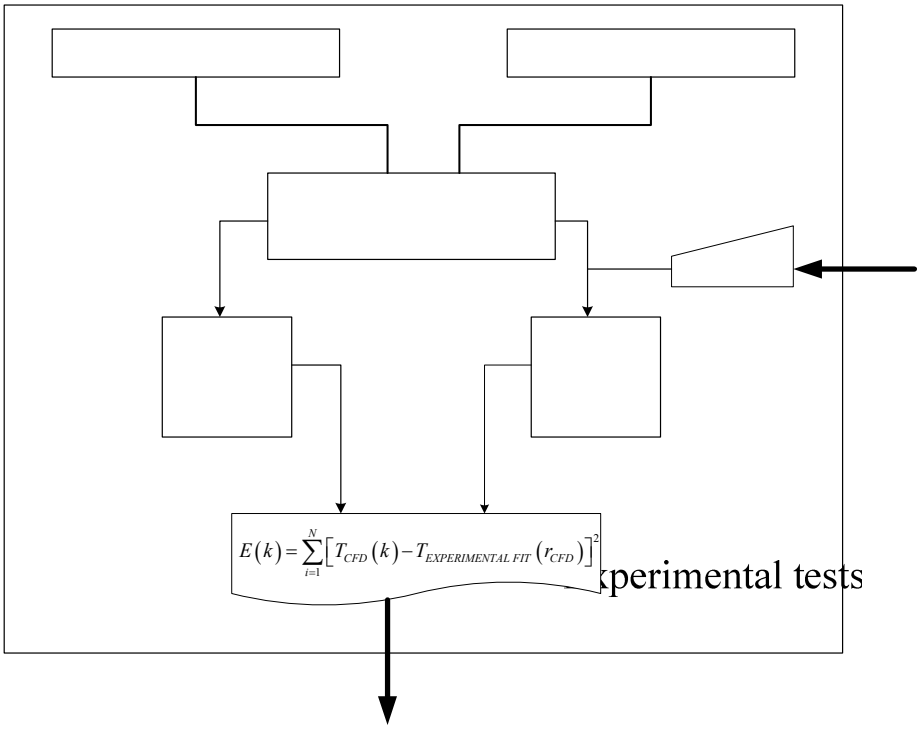

Figure J-2: Flow diagram formulating the calculated error and the guessed effective thermal conductivity.

Figure J-2 shows that the calculated error E can be formulated as a function of the guessed thermal conductivity k, i.e.:

Same boundary conditi

$$E(k)=\sum_{i=1}^{N}\left[T_{CFD}(k)-T_{EXPERIMENTAL\ FIT}(r_{CFD})\right]^2 \qquad \text{(J.1)}$$

The next procedure is to minimize $E(k)$, i.e. finding optimum value of k such that:

$$\frac{\partial E(k)}{\partial k}\cong F(k)\cong 0 \qquad \text{(J.2)}$$

Measured braiding temperature profiles

Where,

- $F(k)$ = derivative function of $E(k)$, and
- Equation (J.2) is illustrated in Figure J-3.

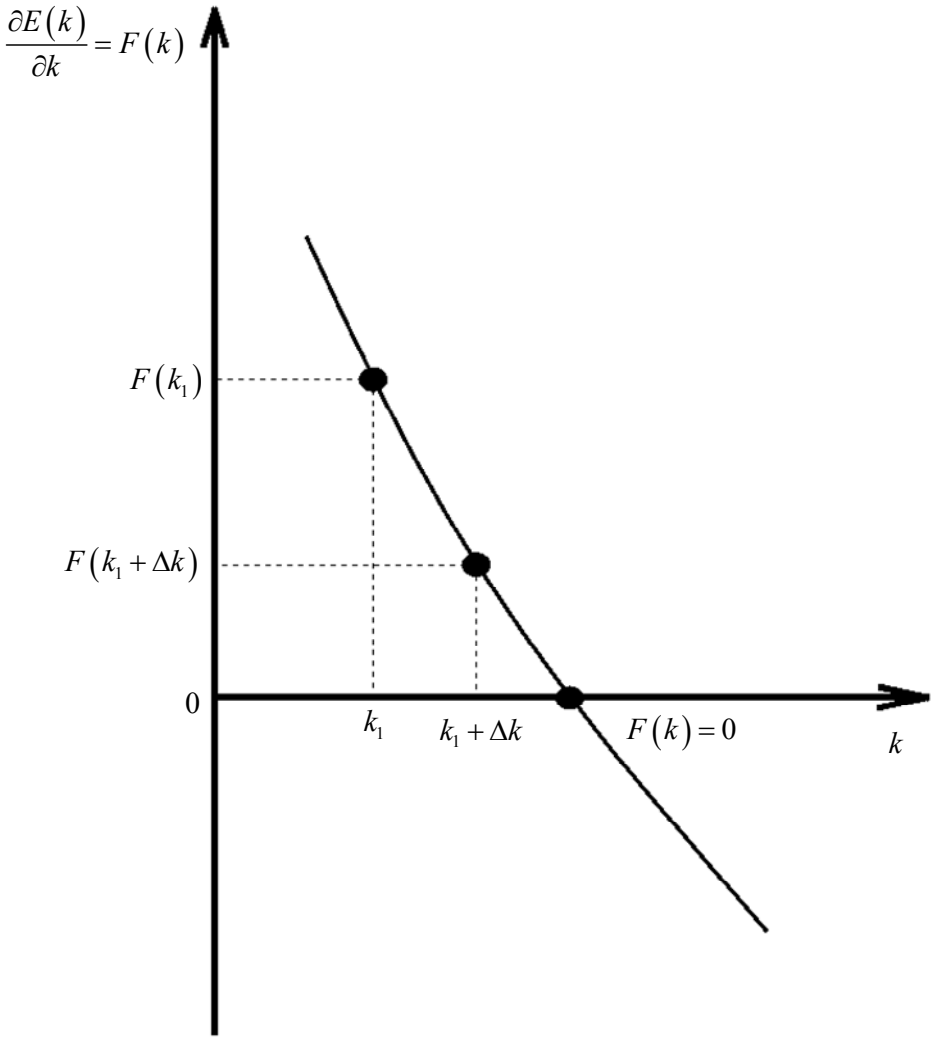

Figure J-3: Graphical representation of the error function.

Figure J-3 shows that, for the first guessed thermal conductivity k_1, the amount Δk by which the thermal conductivity must be adjusted such that Equation (J.2) will be satisfied $\left(F(k) = 0\right)$. The mathematical calculation of the first error function $F(k_1 + \Delta k)$ can be formulated by means of the Taylor series method to:

$$F(k_1 + \Delta k) = F(k_1) + \Delta k \left.\frac{\partial F}{\partial k}\right|_{k=k_1} + (\Delta k)^2 \left.\frac{\partial^2 F}{\partial k^2}\right|_{k=k_1} + \ldots \qquad \text{(J.3)}$$

Therefore, the general error function $F(k + \Delta k)$ is estimated as follows:

$$F\left(k+\Delta k\right) \cong F\left(k\right) + \Delta k \frac{\partial F\left(k\right)}{\partial k} \tag{J.4}$$

The second order terms in the Taylor series in Equation (J.3) have a minimal influence and are omitted in the formulation. The search technique will find Δk such that $F\left(k+\Delta k\right)=0$ i.e:

$$\begin{aligned} & F\left(k\right) + \Delta k \frac{\partial F\left(k\right)}{\partial k} = 0 \\ & \therefore \Delta k = - F\left(k\right) \Big/ \frac{\partial F\left(k\right)}{\partial k} \end{aligned} \tag{J.5}$$

Incorporating Equation (J.1) in the final formulation of Δk in Equation (J.5) leads to the following equation for Δk:

$$\Delta k = - \frac{\partial E\left(k\right)}{\partial k} \Big/ \frac{\partial^2 E\left(k\right)}{\partial k^2} \tag{J.6}$$

Reiterating from the previous statements in this section the search technique will find k such that $\Delta k \cong 0$. This implies that the change in the error due to the change in effective thermal conductivity is zero, i.e. $\frac{\partial E}{\partial k} \cong 0$. Perturbing the guessed thermal conductivity k with a small percentage of its value δk enable the approximation in $\frac{\partial E}{\partial k}$ to be calculated as follows:

$$\frac{\partial E}{\partial k} = \frac{E^{++} - E^{--}}{k^{++} - k^{--}} \tag{J.7}$$

Where:

- $\delta k = \alpha \cdot k$
- $k^{++} = k + \delta k$,
- $k^{--} = k - \delta k$,
- $E^{++} = F\left(k^{++}\right)$, and

- $E^{--} = F\left(k^{--}\right)$.

This implies that $\frac{\partial E}{\partial k}$ is perturbed as follows:

$$\frac{\partial E^{+}}{\partial k} = \frac{E^{++} - E}{k^{++} - k}$$
$$\frac{\partial E^{-}}{\partial k} = \frac{E - E^{--}}{k - k^{--}} \qquad \text{(J.8)}$$

These two perturbed gradients, $\frac{\partial E^{+}}{\partial k}$ and $\frac{\partial E^{-}}{\partial k}$, are mathematically calculated at the midpoint between k and k^{++}, and the midpoint between k and k^{--} respectively. These midpoints can be formulated as follows:

- $k^{+} = k + \frac{1}{2}\delta k$, and
- $k^{-} = k - \frac{1}{2}\delta k$.

The change in these gradients, $\frac{\partial^2 E}{\partial k^2}$, is calculated as follows:

$$\frac{\partial^2 E}{\partial k^2} = \frac{\frac{\partial E^{+}}{\partial k} - \frac{\partial E^{-}}{\partial k}}{k^{+} - k^{-}} \qquad \text{(J.9)}$$

These equations (Equation (J.7) to Equation (J.9)) are illustrated in Figure J-4. It is important to note that α in $\delta k = \alpha \cdot k$ should be kept as small as possible as (say $0 < \alpha < 0.1$).

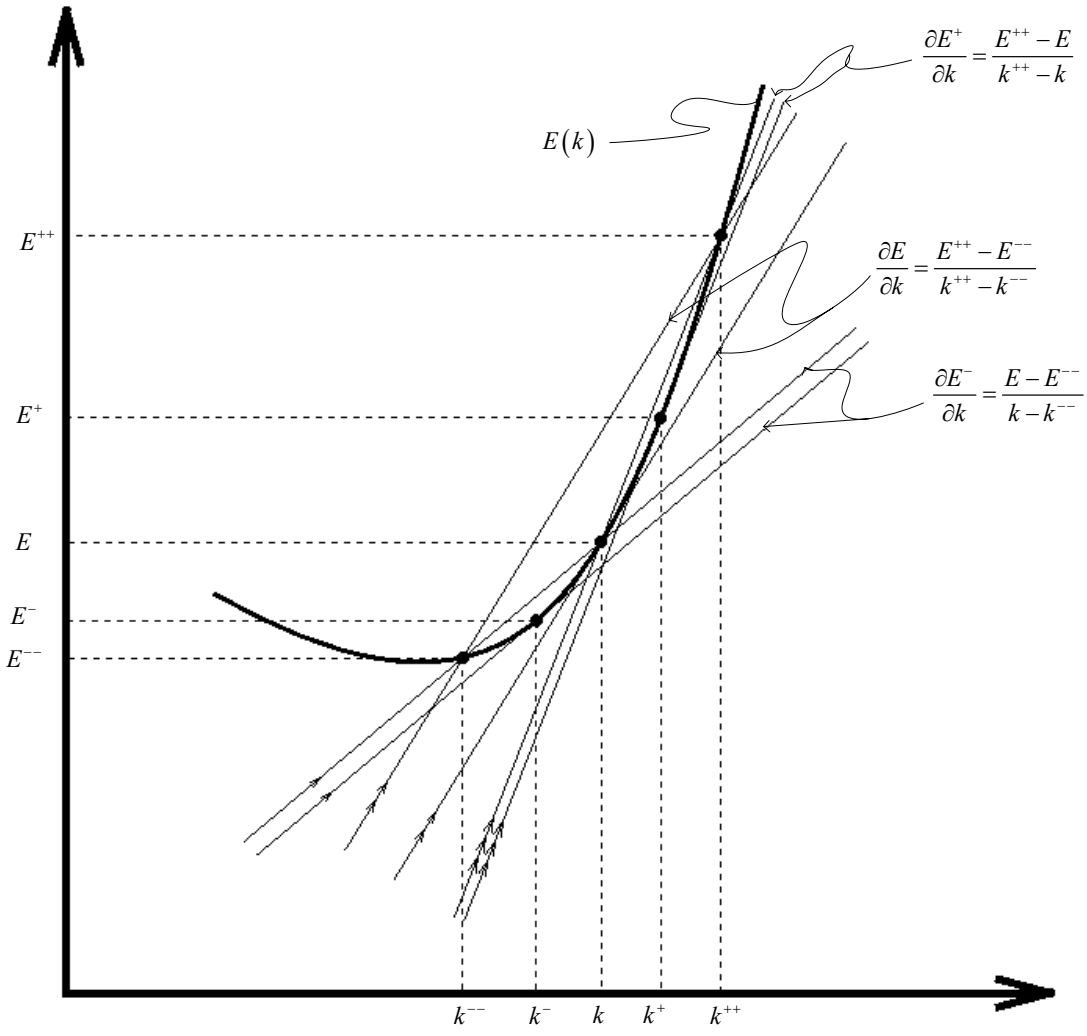

Figure J-4: Graphical representation of the error function perturbation.

Figure J-3 shows that the enhanced effective fluid conductivity Δk has to be calculated iteratively before Equation (J.2) can be reached. Hence, there's a need to develop and implement customized search routine in the CFD program to minimize the error automatically.

The search routine is illustrated in Figure J-5.

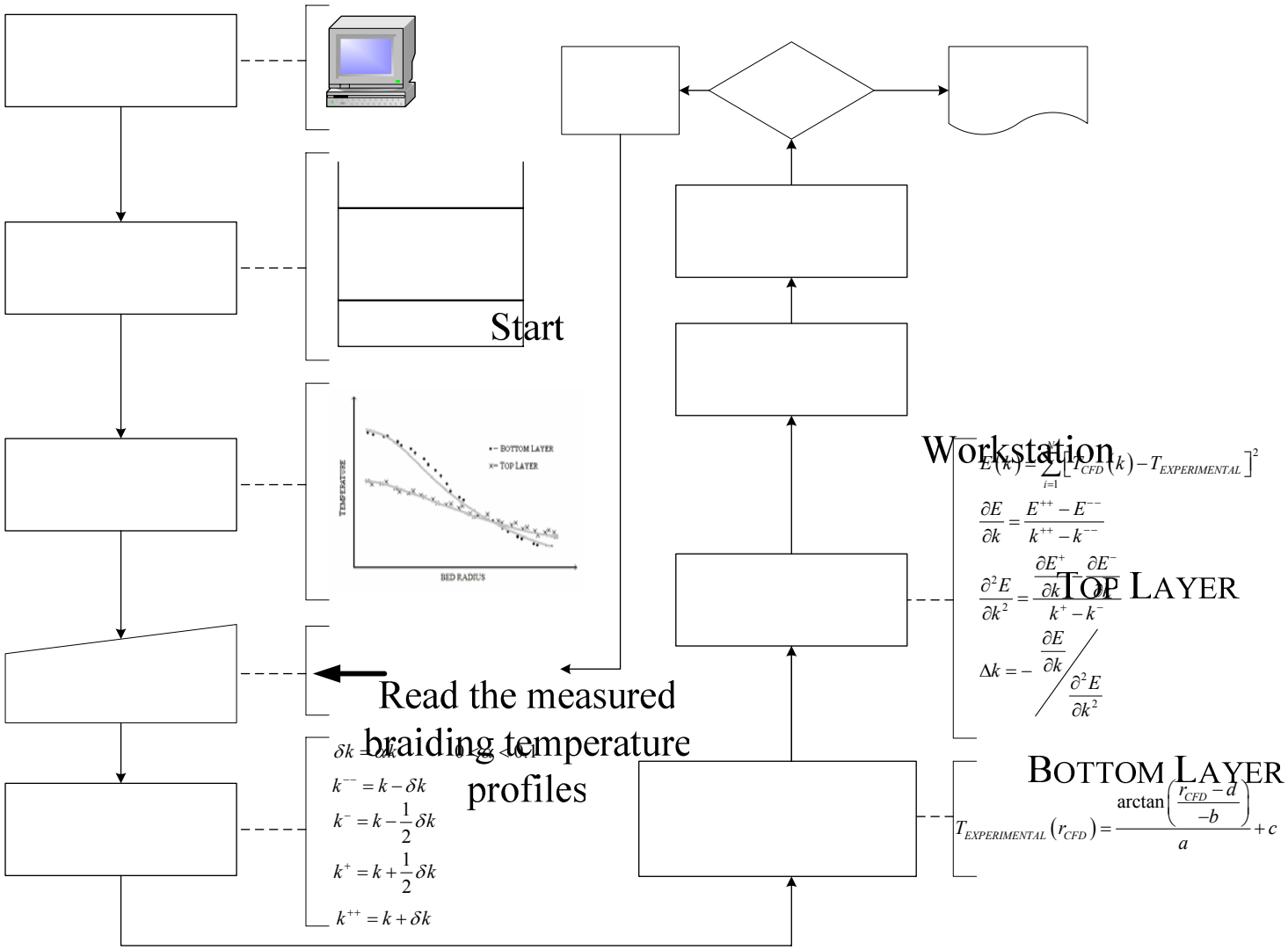

Figure J-5: Illustration of the search routine that was implemented in the CFD program.

The following points are noted with reference to Figure J-5:

- The CFD program needs to simulate the braiding temperature profiles for five perturbed values of the guessed effective thermal conductivity k; the perturbation interval was kept at $\delta k = 0.00625 \times k$, i.e. $\alpha = 0.00625$, to keep the perturbed values of $\frac{\partial E}{\partial k}$ as small as possible and close to each other. This controls the overshooting or down-shooting of the values of $\frac{\partial E}{\partial k}$ as shown in search routine.
- For each perturbed effective conductivity the error is calculated as follows:

$$E(k) = E(k)_{BotLayer} + E(k)_{TopLayer}$$
$$= \left[\sum_{i=1}^{N_{CV}} \left(T_{CFD}(k) - T_{EXPERIMENTAL\ FIT}(r_{CFD}) \right)_i^2 \right]_{BotLayer} + \left[\sum_{i=1}^{N_{CV}} \left(T_{CFD}(k) - T_{EXPERIMENTAL\ FIT}(r_{CFD}) \right)_i^2 \right]_{TopLayer}$$

with:

N_{CV} = number of control volumes discretisized in a radial direction of the flow field in the CFD grid.

APPENDIX K: Grid dependence study

The objective of this grid dependence study was to determine the discretization error in the CFD solution(s). As the grid is refined (grid cells become smaller and the number of cells in the flow domain increase), the spatial discretization errors should asymptotically approach zero, excluding computer round-off error. The method for examining the spatial convergence of the CFD simulations in this study is based on the well-known Richardson extrapolation (see Roache (1998)). In the Richardson extrapolation method a 'relative solution error', E_{rel} is calculated and this parameter was used to determine the grid independence of the solutions. The specific form of E_{rel} that is used is as follows:

$$E_{rel} = \frac{rms\left(f_{i+1} - f_i\right)}{\left[\max\left(f_i\right) - \min\left(f_i\right)\right](r^p - 1)} \qquad \text{(K.1)}$$

Where,

- f_{i+1} and f_i are the solutions on two successively refined meshes,
- r^p is the ratio with which successively meshes are refined and p is the order of the underlying numerical scheme – in this case taken as 1 so that the mesh size can be linearly changed and the CFD simulations are manageable.

The relative solution error E_{rel} gives the normalized change in the solution should the mesh be refined in a next step using the refinement ratio r^p.

Applying the Richardson method on a three-dimensional grid may not be practical for the memory requirements, because increasing the number of grid points in three separate directions simultaneously may quickly exceed the available memory of the computer. In the current case we will show that one of the three grid directions (axial, transverse and azimuthally) is far more sensitive to the number of grid points than the others. This will help in the sense that it will not be necessary to refine the grid in all three grid directions equally but that a coarser mesh point distribution can be used in two of the three grid

directions. By using this information we will be able to successfully apply the Richardson method.

The main heat transfer mechanisms that are active in the current application are those of heat convection and heat conduction. In Flo++, 2nd order numerical discretization is implemented for the heat conduction, whilst the 1st order numerical discretization is implemented for the heat convection. The latter assumes the UPWIND differencing scheme. A 2nd order scheme for the convection terms can be used, provided that the requirement for stability is met, namely that the Peclet number is smaller than 2. The main flow direction in the current application is in the axial direction. This is due to the fact that the geometry together with the porosity of the bed forces the apparent flow in the axial direction due to high Reynolds numbers (1 000 to 40 0000).

A rough estimation of the Peclet number Pe characterized by the plug flow over the full axial distance $D1$ of the packed bed is formulated as follows:

$$Pe = \frac{\left(\rho c_p u_o\right)_{average} D1}{k_g} \qquad \text{(K.2)}$$

Where,

- $\rho_{average}$ = average inlet density for the hot and cold gases,
- $\left(c_p\right)_{average}$ = average inlet specific heat for the hot and cold gases, and
- $\left(u_o\right)_{average}$ = average superficial velocity for the hot and cold gases.

The Peclet numbers were calculated from the experimental results described in Chapter 5 and the k_{eff} values that were evaluated using a mesh distribution for which the results are not grid dependent. The calculated values are shown in Table K-1.

Table K-1: Peclet numbers based on the effective thermal conductivities over the full axial bed distance..

	BETS045		BETS036	
Reynolds Number	k_{eff}	Pe	k_{eff}	Pe
[-]	[W/m K]	[-]	[W/m K]	[-]
1000	1.158	405.577	1.248	356.000
40000	26.386	732.040	39.320	483.424

For Peclet numbers that are larger than or equal to 2, a 1st order UPWIND scheme should be used for convection (Versteeg and Malalasekera (1998)) and for small Peclet numbers (<2) a 2nd order central differencing scheme should be employed. However, this would account for one cell. For the calculated Peclet numbers in Table K-1 the minimum and maximum number of axial cells can be calculated as follows:

$$\begin{aligned} Minimum\ cells &= \frac{Pe_{\min}}{2} = \frac{356.000}{2} \cong 178\ cells \\ Maximum\ cells &= \frac{Pe_{\max}}{2} = \frac{732.040}{2} \cong 366\ cells \end{aligned} \qquad \text{(K.3)}$$

Due to almost negligible convection in the transverse and azimuthal directions one can expect to use a much coarser grid in these directions than the axial direction.Therefore, the strategy for the grid dependence study proceeded as follows:

- A fixed number of grid points in the transverse and azimuthal directions was used while applying the Richardson method (Equation (K.1)) in the axial direction only. The value of $r^p = 1.5$ was used in the current work and was randomly chosen to make a small variance as the mesh size increases.
- Once an optimal number of grid points in the axial direction had been established, the number of grid points transversely and azimuthally was varied to see if there were any significant changes.

A typical temperature solution near the inlet of the geometry is shown in Figure K-1. Appendix G shows that the generated temperature profiles in the grid were volume independent. Therefore, 1/8 of the total volume (Figure G-4) was used.

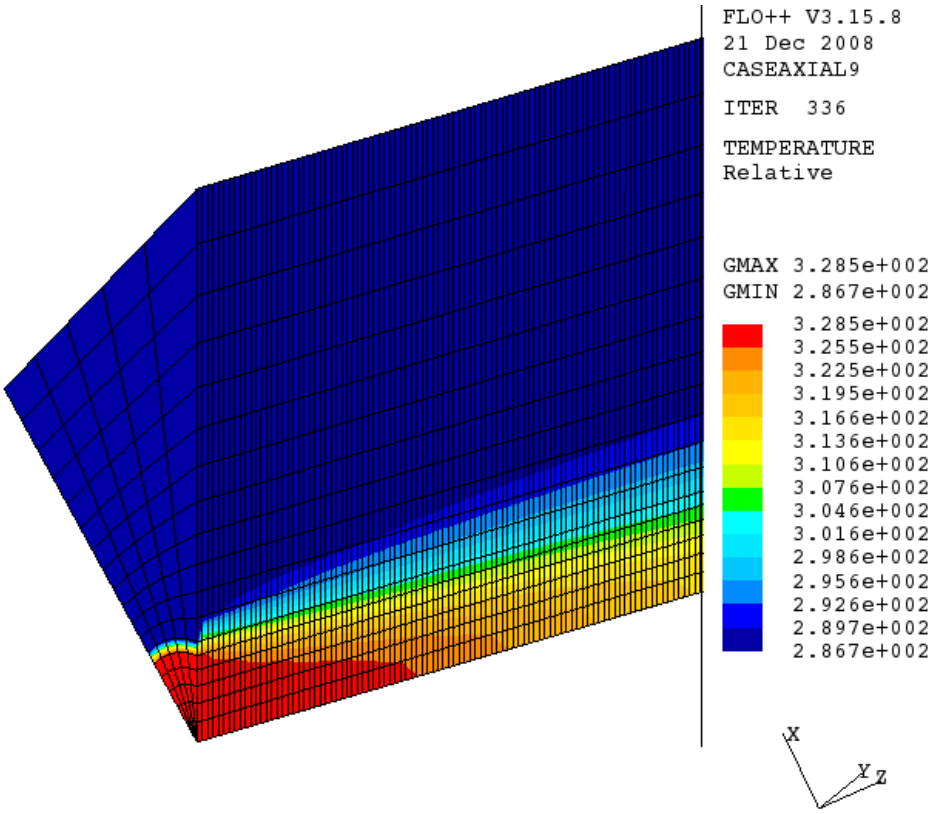

Figure K-1: Typical grid point temperature distribution.

Four cases for the grid refinement were investigated to determine the effect of the number of grid points on Equation (K.1). These cases are as follows:

- **Base case:** It was decided to start with a base case with a fixed number of 5 grid cells azimuthally and 18 cells transversely. A slightly uneven spacing was used transversely to better resolve the diffusion at the hot and cold interface. The grid spacing axially was varied starting with 12 cells and increasing that with a ratio $r^p = 1.5$ for a total of 10 meshes. The QUICK convection discretization scheme was used, which is between 1st and 2nd order accurate (a hybrid between UPWIND and central differencing, but unconditionally stable). The number of grid points for this base case is shown in Table K-2:

Table K-2: Number of the grid points for the base case.

Grid	Angular (azimuthal)	Transverse	Axial
1	5	18	12
2	5	18	18
3	5	18	27
4	5	18	41
5	5	18	61
6	5	18	91
7	5	18	137
8	5	18	205
9	5	18	308
10	5	18	461

- **Transverse refinement:** The sensitivity of the solution was tested to an increase in number of cells in the transverse direction using 36 cells instead of 18 cells. The same grid point densities were used azimuthally and axially as in the base case.
- **Angular or azimuthal refinement:** The sensitivity of the solution was tested to an increase in number of cells in the angular direction using 10 cells instead of 5 cells. The same grid point densities were used transversely and axially as in the base case.
- **UPWIND differencing scheme:** In a last experiment we have taken the base case but used the UPWIND convection discretization scheme (instead of the QUICK scheme), which is 1st order accurate.

K.1 Results

The test results are presented for the Cartesian grid and the cylindrical grid. Results are presented graphically to demonstrate the effect of the relative solution error (Equation (K.1)) as the grid resolution or distribution changes from coarse to fine.

The axial temperature values that were used in the calculations were determined through linear interpolation at the same axial positions as the number of cells increased. Figure K-2 and Figure K-3 show the temperature profiles, taken at the discretisized axial points and

at the linearly interpolated axial positions, respectively. The data shown is for the BETS036 test section geometry and its experimental data at the Re = 1 000.

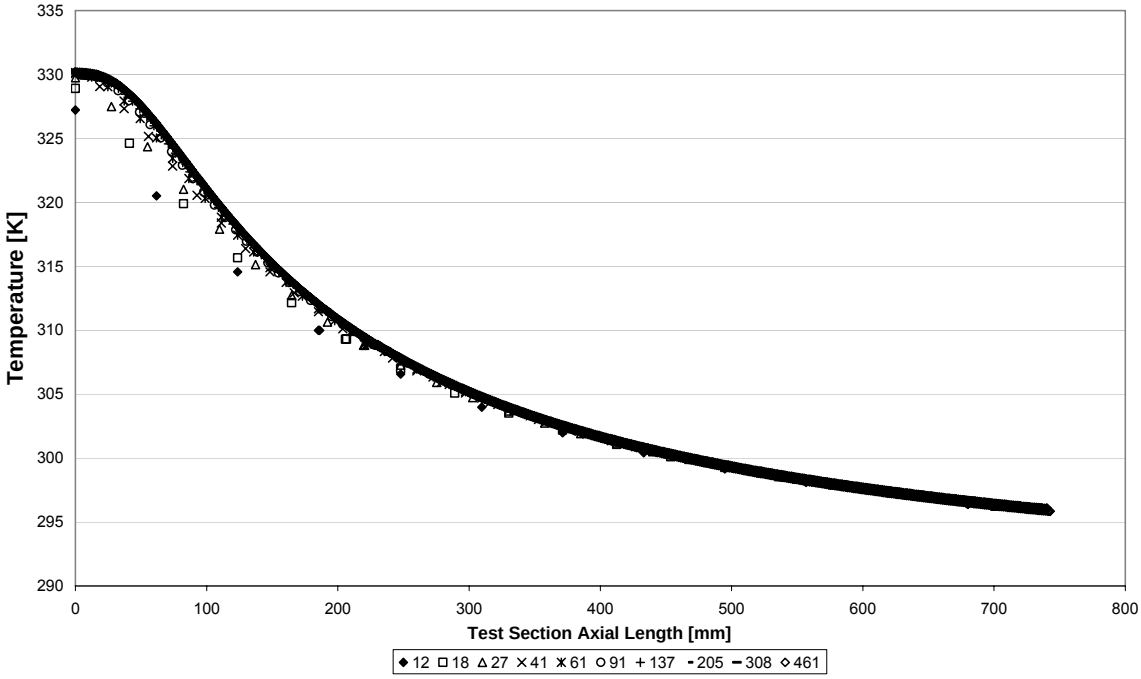

Figure K-2: Temperature profile for different grids as the number of grid points in axial direction increases.

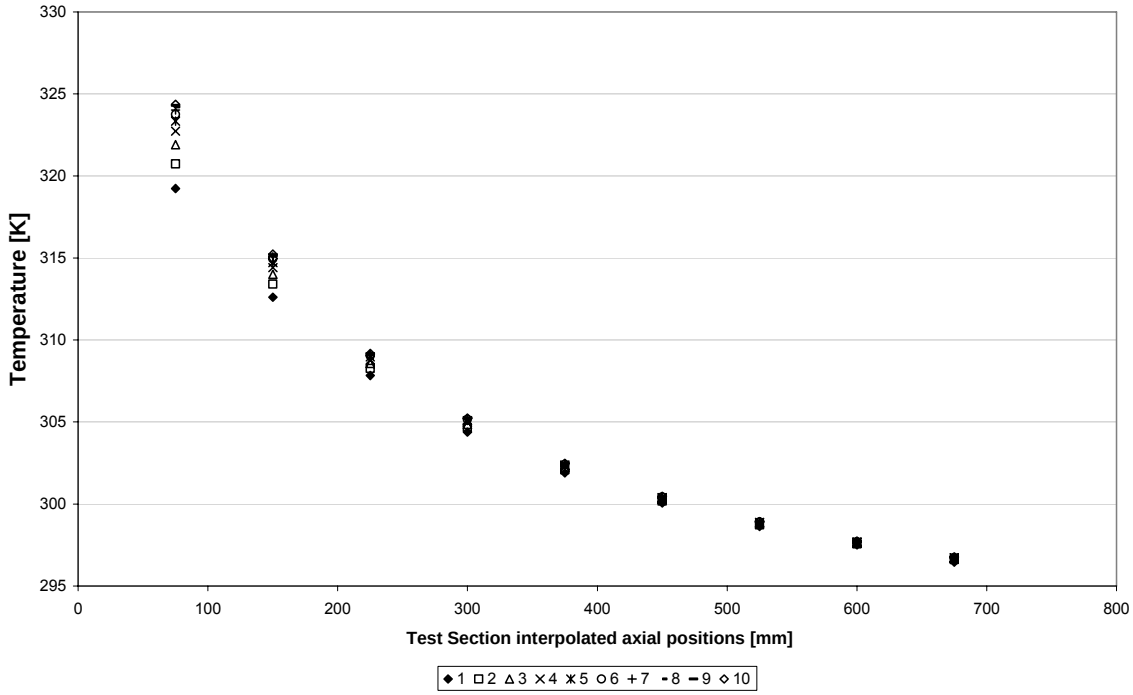

Figure K-3: Temperature profile for different grids at the same interpolated axial positions.

The axial temperature profile starts to become stable at grid point 6 as seen in Figure K-2 and Figure K-3 for 91 grid points in the axial direction.

K.2 Cartesian Grid

Graphs of the relative solution error are shown from Figure K-4 to Figure K-7. The graphs show that the relative solution error decreases as the number of cells increases.

Also evident from the graphs is that refinement in the angular and radial directions has almost no effect on the solution error. This can be attributed to the strong plug flow in the axial direction. There is also not a significant advantage in using the QUICK scheme to that of the UPWIND scheme. Since the grids have a relative small number of grid points it is therefore not very important to spend much time on a selection between UPWIND and higher order convection discretization schemes. By using a finer grid the UPWIND method gives the same results while solution times and memory requirements are well within limits.

It can be seen that the solution expected between grids 5 and 6 has a solution error of less than 0.5% for both test sections, i.e.

$$\begin{aligned} E_{rel} &= \pm 0.01\left(r^{p} - 1\right) \\ &= 0.01\left(1.5 - 1\right) \\ &= 0.01\left(0.5\right) \\ &= 0.005 \end{aligned} \qquad \text{(K.4)}$$

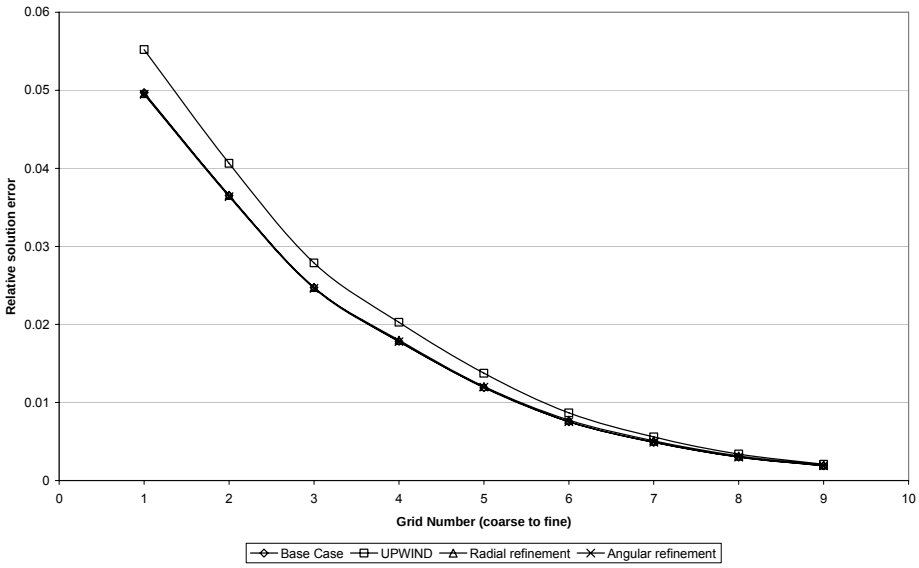

Figure K-4: Relative solution error with varying grid densities (BETS036, Low Reynolds number).

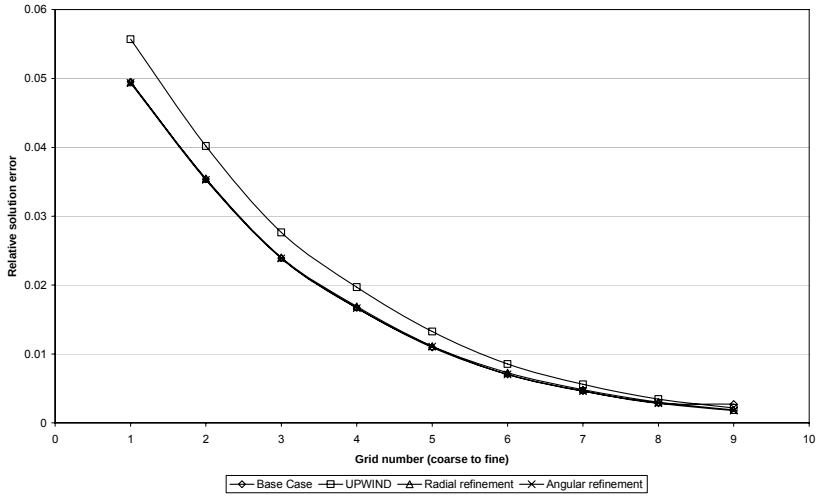

Figure K-5: Relative solution error with varying grid densities (BETS036, High Reynolds number).

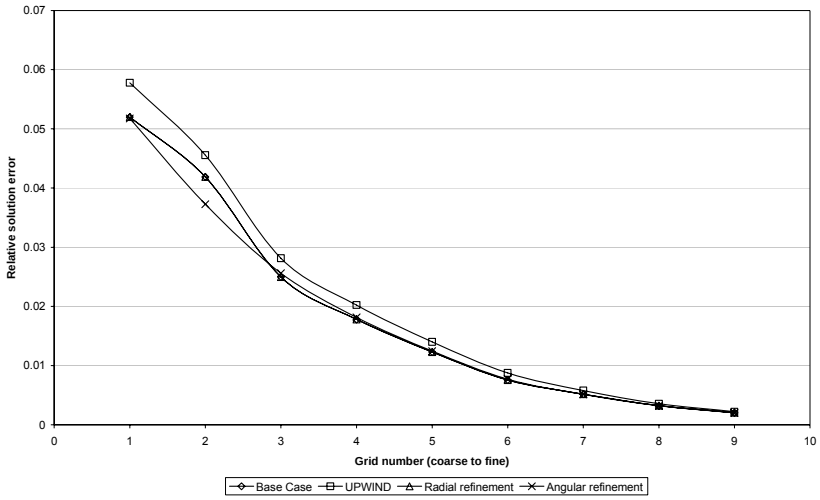

Figure K-6: Relative solution error with varying grid densities (BETS045, Low Reynolds number).

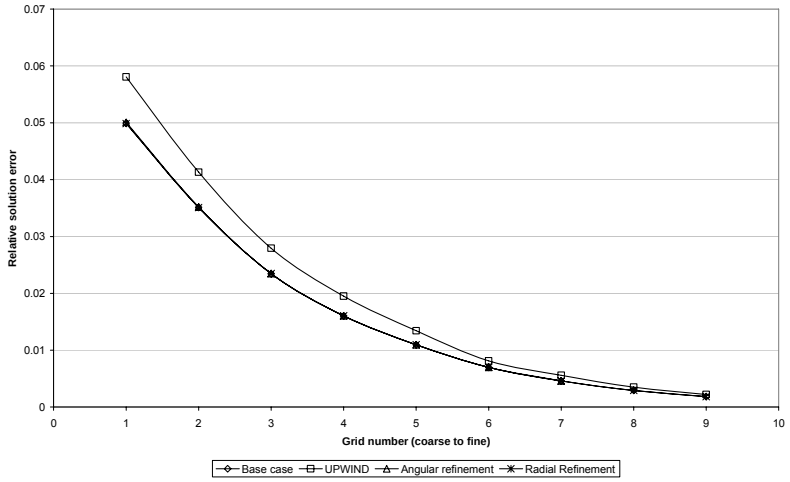

Figure K-7: Relative solution error with varying grid densities (BETS045, High Reynolds number).

K.3 Cylindrical Grid

The Cartesian and cylindrical meshes had the same grid point distribution in the axial and azimuthal directions except for the transverse (for Cartesian grid) and radial (for cylindrical grid) direction. Figure K-8 shows the inflow area indicating the boundaries for both grids. It is seen that the Cartesian grid has one standard side conforming to the cylindrical grid in a radial direction.

Because the experimental test sections have square cross sections, the Cartesian grid is a better representation of the geometry. If the difference or disparities between the results obtained on the Cartesian and cylindrical meshes are small, it simply means that what happens in the corner of the flow (shown in the Figure K-8 as neglected by the cylindrical grid) is not of much significance. Therefore, the same grid point distribution in the Cartesian grid for the final mesh size was used to generate the cylindrical grid.

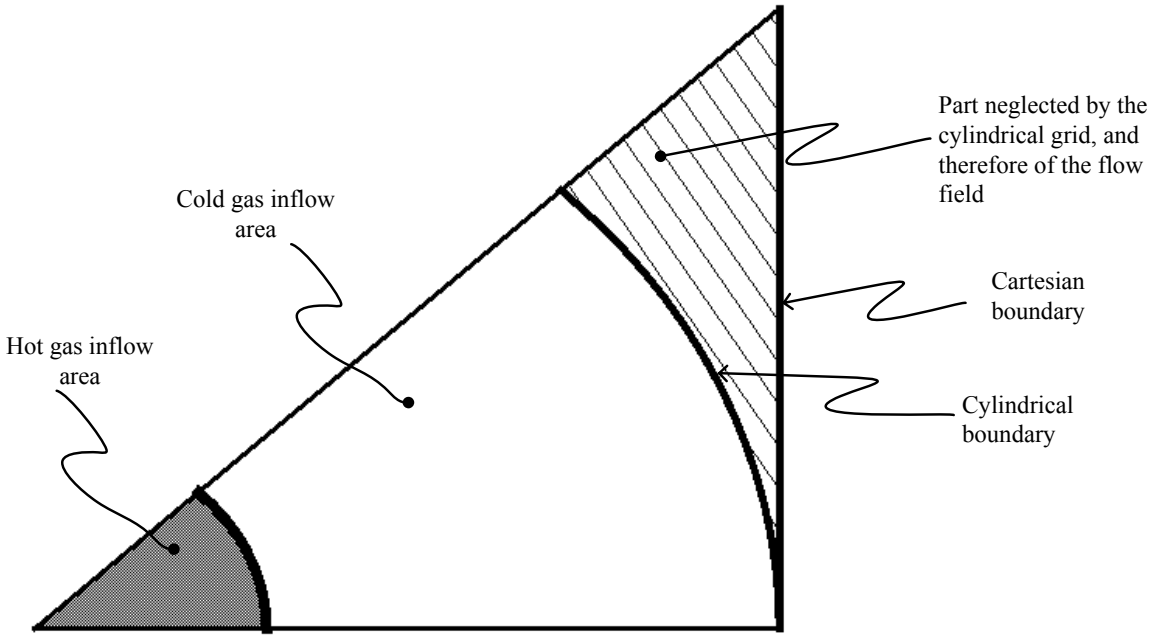

Figure K-8: Variation of inflow areas between the Cartesian and the cylindrical grid.

Raw data for these results are in the excel files that can be found on the Data CD attached at the back of this report.